Signal processing for MIMO radars : detection under gaussian and non-gaussian environments and application to STAP.

Chin Yuan Chong

N° d'ordre : 2011-16-TH

THÈSE DE DOCTORAT

SPECIALITE : PHYSIQUE

Ecole Doctorale « Sciences et Technologies de l'Information des Télécommunications et des Systèmes »

Présentée par :

Chin Yuan CHONG

Sujet :

Signal Processing for MIMO Radars: Detection under Gaussian and non-Gaussian environments and application to STAP

Soutenue le 18 novembre 2011 devant les membres du jury :

M. Olivier BESSON	ISAE Toulouse	Rapporteur
M. Gilles FLEURY	SUPELEC	Président du jury
M. Braham HIMED	Air Force Research Laboratory	Rapporteur
M. William LAU	DSO National Laboratories	Examinateur
M. François LE CHEVALIER	Thalès / Delft University of Technology	Examinateur
M. Marc LESTURGIE	ONERA / SONDRA	Directeur de thèse
Mme Sylvie MARCOS	CNRS / LSS / SUPELEC	Examinateur
M. Frédéric PASCAL	SONDRA / SUPELEC	Examinateur

Acknowledgements

First of all, I would like to thank all my supervisors, formal and informal, for their guidance and trust in letting me work independently: Marc Lesturgie, my thesis director as well as the director of SONDRA; Frédéric Pascal, my "dear" supervisor aka Agnès B model; Jean-Philippe Ovarlez, always willing to discuss and answer any question even if he is busy and Leonard Tan who never ends to amaze me with his ability to understand diverse subjects.

Next, I would like to express my gratitude to DSO National Laboratories for giving me the opportunity to go to SONDRA for attachment and subsequently a scholarship to fund this PhD.

I have spent some of the best years of my life in France and this would not have been possible without SONDRA and others in SUPELEC. I would like to thank especially: Tonio, my first office-mate who taught me French and French Culture 101; Fredou who then so patiently helped me improve my French and showed me the other and real side of Paris; Karimou (together with Fredou), we have spent such wonderful times as office-mates; Danny, my PhD-mate who can be so irritating and likable at the same time; gentle and kind Anne-Hélène and Laetitia who add the feminine and motherly touch to SONDRA; Rami who stops at nothing to help a friend; charismatic Rémi who surprised me by showing his softer side at times; Pierre and Mélanie who took over the baton in creating ambiance in SONDRA; crazy Chiara who has grown up so much over the years; sportive Luc who has improved our work-life balance as a member of CE; Régis who introduced me to the world of sports climbing; Dr Lambert who cares in his own way; Bernard who tirelessly manages the coffee account; Alex and Gillaume for making my conference trips so enjoyable. There are so many others, thank you so much for these memorable years!

Finally, a big THANK YOU to my loving family who has always been supportive of me: my parents who care for me in very different ways, my two sisters who have almost set up a fan club for me, my adorable nephews who rank me as their favorite, my little brother whom I care for deeply and my two brother-in-laws who are working quietly behind the scene.

Contents

Acronyms and Abbreviations

AMF	Adaptive Matched Filter
CCM	Clutter Covariance Matrix
CFAR	Constant False Alarm Rate
CLT	Central Limit Theorem
CNR	Clutter-to-Noise Ratio
CPI	Coherent Processing Interval
DDMA	Doppler Division Multiple Access
DOA	Direction Of Arrival
DoF	Degree-of-Freedom
ECEF	Earth-Centered, Earth-Fixed
FPE	Fixed Point Estimate
GLRT	Generalized Likelihood Ratio Test
GLRT-LQ	Generalized Likelihood Ratio Test - Linear Quadratic
GMTI	Ground Moving Target Indication
GPS	Global Positioning System
HF	High Frequency
HFSWR	High Frequency Surface Wave Radar
HMPAR	Hybrid MIMO Phased-Array Radar
i.i.d.	Independent and Identically Distributed
MDV	Minimum Detectable Velocity
MI	Mutual Information
MIMO	Multi-Input Multi-Output
MISO	Multi-Input Single-Output
ML	Maximum Likelihood
MSD	Matched Subspace Detector
MTI	Moving Target Indication
NED	North-East-Down
NSCM	Normalized Sample Covariance Matrix
LOS	Line-Of-Sight
OGD	Optimum Gaussian Detector
OTHR	Over-The-Horizon Radar
PDF	Probability Density Function
PRF	Pulse Repetition Frequency
PRI	Pulse Repetition Interval
RCS	Radar Cross Section
SAR	Synthetic Aperture Radar
SCM	Sample Covariance Matrix
SIMO	Single-Input Multi-Output

SIR	Signal-to-Interference Ratio
SIRV	Spherically Invariant Random Vector
SISO	Single-Input Single-Output
SNR	Signal-to-Noise Ratio
STAP	Space-Time Adaptive Processing
STC	Space-Time Coding
TS-MIMO	Transmit Subaperturing MIMO
UAV	Unmanned Aerial Vehicle
XLOS	Cross Line-Of-Sight

Symbols and Notations

M	Number of receive elements where there is only one receive subarray
N	Number of transmit elements where there is only one transmit subarray
$\tilde{M}$	Number of receive subarrays
$\tilde{N}$	Number of transmit subarrays
N_{rx}	Total number of receive elements
N_{tx}	Total number of transmit elements
M_m	Number of elements in m-th receive subarray
N_n	Number of elements in n-th transmit subarray
N_p	Total physical number of elements
N_e	Total effective number of elements
$N_{e,i}$	Effective number of elements in the i-th subarray
N_s	Number of target-free i.i.d. secondary data
$N_{s,i}$	Number of target-free i.i.d. secondary data for the i-th subarray
K_e	Effective number of subarrays
K_p	Physical number of subarrays
L	Number of pulses
L_a	Effective aperture size
d_r	Spacing between elements in the receive subarray
d_t	Spacing between elements in the transmit subarray
θ_r	Receive angle
θ_t	Transmit angle
f_d	Relative Doppler frequency
f_t	Target Doppler frequency
σ^2	Interference power per element
σ_t^2	Target power per element
N_{MC}	Number of runs for Monte-Carlo simulations
$\mathrm{SIR}_{\mathrm{pre}}$	Average SIR per element before processing
$\mathrm{SIR}_{\mathrm{post}}$	Total equivalent SIR of the entire system after processing
$\mathrm{SIR}_{\mathrm{g}}$	Gain in SIR due to processing
P_{fa}	Probability of false alarm
P_d	Probability of detection
λ, η	Detection threshold
$\mathbf{M}$	Interference covariance matrix
$\mathbf{M}_c$	Clutter covariance matrix
$\widehat{\mathbf{M}}_{SCM}$	Sample Covariance Matrix
$\widehat{\mathbf{M}}_{FP}$	Fixed Point Estimate

$\mathbf{I}$	Identity matrix
$\mathbf{I}_n$	Identity matrix of size n
$\mathrm{tr}(\cdot)$	Trace of a matrix
$\|\cdot\|$	Determinant of a matrix
$E(\cdot)$	Expectation of a matrix
$\otimes$	Kronecker product
$\sim$	to be distributed as
$\stackrel{d}{=}$	equal in distribution as
$\mathcal{CN}$	Complex Normal distribution
χ^2_k	chi-square distribution with k DoF
$(\cdot)^\dagger$	conjugate transpose or Hermitian operator
$(\cdot)^T$	transpose
$\Re(\cdot)$	real part
$\Im(\cdot)$	imaginary part
$\Gamma(n)$	Gamma function
$\Gamma(n,a)$	Upper incomple Gamma function
$Q_k(a,b)$	Marcum Q-function
$B(a,b)$	Beta function
$I_x(a,b)$	Regularized incomplete beta function
J	Jacobian
$\mathbb{1}_{[0,1]}(x)$	Indicator function

List of Figures

List of Tables

Résumé

I Introduction

Le Multiple-Input Multiple-Output (MIMO) est une technique utilisée dans les communications [1] qui a récemment été adoptée pour des applications radar. Les systèmes de communication MIMO surmontent les problèmes causés par le *fading* en emettant des flux d'informations différents avec plusieurs émetteurs décorrélés. Les différents signaux subissent donc un *fading* indépendant et le récepteur a un rapport signal sur bruit (SNR) moyen qui est plus ou moins constant, tandis que dans les systèmes conventionnels qui transmettent toute leur énergie sur une seule voie, le SNR varie considérablement.

Dans le contexte du radar, un radar MIMO est celui où les émetteurs envoient des formes d'ondes différentes (orthogonales ou partiellement corrélées) qui peuvent être séparées à la réception. Cela permet la diversité de forme d'onde. En outre, les émetteurs et récepteurs peuvent être suffisamment séparés de manière à assurer la diversité spatiale. Cela réduit les fluctuations de la surface équivalente radar (RCS) parce que la cible est vue sous différentes incidences par chaque paire d'émetteur-récepteur [2].

La plupart des travaux récents sur les radars MIMO considèrent deux configurations principales, appelées MIMO *statistique* et *cohérente*, comme illustrées dans la figure I. Le radar MIMO statistique [3] a une configuration où tous les éléments d'antenne sont largement séparés et donnent une image diversifiée de la cible, améliorant ainsi la robustesse de la détection des cibles étendues [4]. D'autre part, pour le radar MIMO cohérent [5], tous les éléments sont étroitement espacés dans un sous-réseau de telle sorte que le goniométrie est possible. La diversité provient des formes d'ondes différentes émises par les émetteurs. Dans ce cas, l'espacement peut être clairsemé dans le sous-réseau pour améliorer la résolution.

Dans cette thèse, nous nous concentrons sur les performances de détection des radars MIMO et également à l'utilisation de techniques MIMO pour le Space-Time Adaptive Processing (STAP) qui est une application radar importante.

I.1 Configurations

Nous commençons avec un résumé des différentes configurations où il y a la diversité de forme d'onde et/ou la diversité spatiale. La diversité de forme d'onde vient des formes d'ondes différentes et séparables transmises par chaque élément d'émission tandis que la diversité spatiale est due à l'espacement important entre les sous-réseaux de telle sorte que la cible est vue sous différentes incidences. En raison de

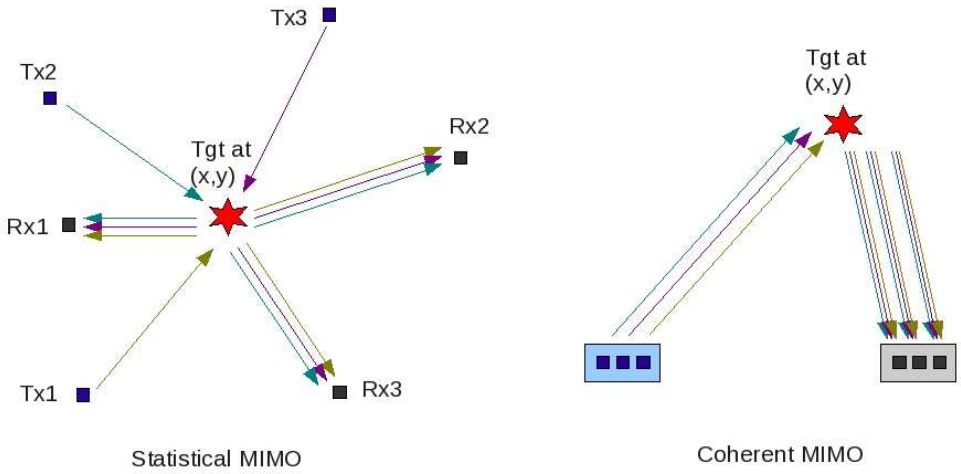

Figure I: Illustration des concepts des radars MIMO statistique et cohérent.

la décorrélation des RCS de la cible, le traitement non cohérent doit être fait entre les sous-réseaux et le goniométrie n'est pas possible.

Ici, les entrées et/ou sorties sont définies en fonction de la diversité spatiale des sous-réseaux d'émission et/ou de réception. On suppose qu'il y a diversité de forme d'onde tant qu'il y a plus d'un élément d'émission. Cela signifie que même s'il n'y a qu'un seul sous-réseau d'émission, on peut encore avoir la diversité de forme d'onde, s'il y a plus d'un élément dans le sous-réseau d'émission. Les différentes configurations SISO, SIMO, MISO et MIMO sont résumées dans le tableau I. $\tilde{N}$ est le nombre de sous-réseaux d'émission et $\tilde{M}$ est le nombre de sous-réseaux de réception. Le n-ième sous-réseau d'émission et le m-ième sous-réseau de réception contiennent N_n et M_m éléments, respectivement, pour $n = 1, \ldots, \tilde{N}$ et $m = 1, \ldots, \tilde{M}$. Le nombre total des éléments d'émission et de réception sont $N_{tx} = \sum_{n=1}^{\tilde{N}} N_n$ et $N_{rx} = \sum_{m=1}^{\tilde{M}} M_m$, respectivement. Le nombre total (réel) d'éléments est donc $N_p = N_{tx} + N_{rx}$.

Config	$\tilde{N}$	N_n	$\tilde{M}$	M_m
SISO	1	≥ 1	1	≥ 1
SIMO	1	≥ 1	> 1	≥ 1
MISO	> 1	≥ 1	1	≥ 1
MIMO	> 1	≥ 1	> 1	≥ 1

Table I: Les différentes configurations possibles.

Pour être le plus générique que possible, nous définissons ici la configuration hybride qui englobe toutes les configurations différentes: SISO, SIMO, MISO et

MIMO. Aucune hypothèse n'est faite sur le nombre de sous-réseaux d'émission et de réception et le nombre d'éléments dans chaque sous-réseau. La seule hypothèse faite est que chaque élément d'émission transmet une forme d'onde différente qui peut être séparée à la réception. Un exemple de cette configuration MIMO hybride est donné dans la figure II. Notez que les flèches en gras indiquent que plusieurs formes d'ondes sont transmises.

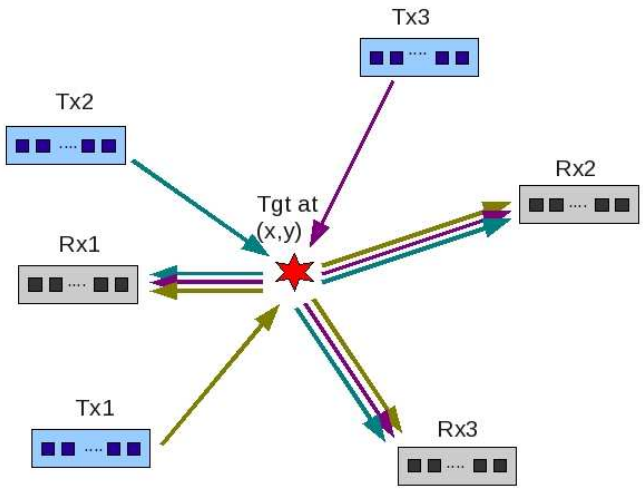

Figure II: Un exemple de la configuration hybride avec $\tilde{N} = \tilde{M} = 3$.

Dans les sous-réseaux, les éléments sont supposés être rapprochés mais aucune hypothèse n'est faite sur la disposition et l'espacement des éléments. L'espacement entre les éléments dans chaque sous-réseau peut être plus grand que $\frac{\lambda}{2}$, mais il doit être inférieur à l'espacement nécessaire pour la décorrélation des RCS de la cible. Le signal reçu par les éléments étant corrélés, le traitement cohérent peut être fait et chaque sous-réseau a des capacités de goniométrie.

L'espacement clairsemé améliore la résolution en grandissant la taille de l'ouverture effective mais il provoque des lobes de réseau. Pour éviter les lobes de réseau, soit les émetteurs soit les récepteurs doivent être rapprochés de telle sorte que les premiers zéros du faisceau annulent les lobes de réseau. Une autre option consiste à utiliser un réseau aléatoire. Cela permettrait de supprimer les lobes de réseau, mais également d'augmenter le niveau des lobes secondaires.

En raison de la diversité spatiale, la cible est vue par le radar MIMO sous $K_e = \tilde{N}\tilde{M}$ ($K_e = 9$ dans l'exemple donnée dans la figure II) différentes incidences. Cela signifie que nous avons un nombre effectif K_e de sous-réseaux qui est plus grand que le nombre réel de sous-réseaux $K_p = \tilde{N} + \tilde{M} = 6$. Lorsque nous avons plus d'un sous-réseau d'émission et plus d'un sous-réseau de réception, nous augmentons K_e tel que $K_e \geq \tilde{N} + \tilde{M}$ en raison de gain de diversité.

Le nombre effectif d'éléments est donné par $N_e = \sum_{m=1}^{\tilde{M}} \sum_{n=1}^{\tilde{N}} M_m N_n$. L'un des

avantages de la diversité de forme d'onde en MIMO est qu'il peut augmenter le nombre effectif d'éléments de telle sorte qu'il est plus grand que le nombre d'éléments réel, N_p. Cela est vrai lorsque $N_{tx} > 1$ et $N_{rx} > 1$. Ce comportement est normal car quand $N_{tx} = 1$, il n'y a qu'une seule forme d'onde alors que quand $N_{rx} = 1$, la diversité de forme d'onde n'est pas exploitée car elle est reçue uniquement par un seul récepteur. Le nombre effectif maximum d'éléments est obtenu quand il y a autant récepteurs que d'émetteurs ($N_{tx} = N_{rx}$), *quelque soit la configuration.*

De plus, le gain en SIR est proportionnel à $N_e = N_{rx}N_{tx}$. Ce gain provient de deux parties: le gain de traitement cohérent au sein des sous-réseaux de réception (N_{rx}) et le gain en puissance avec N_{tx} éléments d'émission. C'est le cas pour le système de puissance illimitée, où chaque élément d'émission transmet la même quantité d'énergie, tel que la puissance totale d'émission est proportionnelle au nombre d'éléments d'émission (et non pas le nombre de sous-réseaux d'émission $\tilde{M}$). Cela permet la réciprocité entre les éléments d'émission et de réception parce qu'il y a une symétrie sur les performances du radar MIMO entre ces éléments. C'est-à-dire qu'un radar MIMO avec a éléments d'émission et b éléments de réception est équivalent en termes de performance à un radar avec b éléments d'émission et a éléments de réception. Avec cette réciprocité, nous pouvons étudier les configurations en fonction de K_e et N_e seulement. En outre, nous verrons dans la partie sur le STAP que pour le cas SISO, la taille de l'ouverture effective (et donc la précision de l'estimation) dépend également de N_e et non pas seulement de N_{rx} ou N_{tx}.

D'autre part, dans un système de puissance limitée, où la puissance totale est répartie entre tous les éléments d'émission, le gain SIR est proportionnel au nombre d'éléments de réception.

Il est important de toujours maximiser N_e. Comme mentionné précédemment, afin d'avoir $N_e > N_p$, il est nécessaire de choisir $N_{rx} > 1$ et $N_{tx} > 1$. Du point de vue énergétique, étant donné le choix entre deux configurations où N_e est le même (une avec plus d'éléments d'émission et l'autre avec plus d'éléments de réception en raison de la symétrie), il est préférable de choisir celle avec plus de récepteur.

II Détection en Environnement Gaussien et Non Gaussien

II.1 Motivation

Les algorithmes pour traiter les signaux des radars MIMO ont été largement étudiés dans le cas d'interférences additives et gaussiennes. Dans [6, 4, 3], les auteurs étudient la performance de détection pour des antennes largement séparées tandis que dans [5, 7] les auteurs considèrent des antennes colocalisées. Le cas hybride où les sous-réseaux sont largement séparés et contiennent un ou plusieurs éléments est étudié dans [8].

Selon [4], les sous-réseaux doivent être suffisamment espacés afin de décorréler les signaux reçus par chaque sous-réseau. Il n'est pas toujours possible de respecter cette condition, en particulier si l'on considère le MIMO-STAP où les sous-réseaux d'émission et/ou de réception sont en mouvement. En outre, des formes d'ondes

parfaitement orthogonales n'existent pas [9], en particulier en présence de décalage Doppler.

Dans la première partie de ce travail, nous supposons que l'espacement entre sous-réseaux est insuffisant et que l'orthogonalité imparfaite des formes d'onde introduisent une corrélation non nulle des signaux entre les sous-réseaux. Cependant, les interférences sont toujours gaussiennes. L'objectif est de développer un détecteur robuste et optimal même si les sous-réseaux sont corrélés. Etant donné que les performances des radars MIMO est très dépendante de la configuration et du scénario, nous considérons un modèle de signal qui est très général de sorte que nous pouvons étudier les effets des différents paramètres afin de trouver les configurations qui maximisent les performances de détection.

Dans la deuxième partie du travail, nous ne pouvons plus supposer que les intérferences sont gaussiennes. Il y a deux raisons principales pour utiliser des modèles non-gaussiens. Premièrement comme mentionné précédemment, l'un des avantages d'un radar MIMO est une meilleure résolution. Habituellement dans chaque cellule de résolution, il y a un grand nombre de diffuseurs. Selon le théorème central limite (CLT), la puissance des interférences dans chaque cellule est presque constante et suit une distribution gaussienne. Toutefois, quand la cellule de résolution devient plus petite, elle contient moins de diffuseurs et le CLT ne s'applique plus. Les modèles non gaussiens qui tiennent compte de la variation de la puissance des interférences doivent être utilisés. En outre, comme la cellule de résolution devient plus petite, il est plus probable que la zone éclairée soit non-homogène.

Deuxièmement, pour les configurations avec des sous-réseaux très éloignés, les RCS vues par chaque sous-réseau sont différentes, réduisant ainsi les fluctuations de la RCS. De même, les signaux reçus d'interférences varient d'un sous-réseau à un autre. Par conséquent, il est important d'utiliser des modèles non gaussiens qui reflètent mieux les fluctuations de puissance des interférences. En effet, des mesures expérimentales [10, 11, 12, 13] ont montré que les interférences sont bien représentées par les modèles statistiques non-gaussiens, notamment le modèle Spherically Invariant Random Vector (SIRV) [14, 15, 16] qui a été largement étudié dans [17, 18, 19] surtout en termes de détection.

II.2 Détecteur Gaussien avec Interférences connues

Un modèle de signal général est utilisé de façon à représenter la configuration hybride décrite précédemment. Supposons qu'il y ait $\tilde{N}$ sous-réseaux d'émission et $\tilde{M}$ sous-réseaux de réception et qu'ils sont tous très éloignés. Différentes (mais pas nécessairement orthogonales) formes d'ondes sont transmises par chaque élément d'émission, même par ceux appartenant au même sous-réseau. Cela signifie que bien qu'il y ait une configuration rapprochée dans le sous-réseau, il y a encore la diversité des formes d'ondes dans le sous-réseau. Cela permet la séparation des signaux transmis à la réception de telle sorte que l'information angulaire peut être obtenue.

En raison de l'espacement large, la RCS de la cible vue par chaque sous-réseau

est supposée différente, mais déterministe. Les éléments au sein de chaque sous-réseau sont rapprochés telles que la RCS reste la même. Grâce à cette diversité spatiale, avoir $\tilde{N}$ sous-réseaux d'émission et $\tilde{M}$ sous-réseaux de réception est équivalent à avoir K_e sous-réseaux effectifs. Le signal reçu après le filtrage adapté peut être exprimé comme:

$$\mathbf{y}_i = \alpha_i \mathbf{p}_i + \mathbf{z}_i, \qquad \forall\ i = 1, \ldots, K_e, \tag{1}$$

où $\mathbf{y}_i$, $\mathbf{p}_i$ et $\mathbf{z}_i$ sont respectivement le signal reçu, le vecteur de pointage bistatique et le vecteur d'interférence pour le i-ième sous-réseau. α_i est la RCS de la cible vue par le i-ième sous-réseau.

Il n'est pas toujours possible d'atteindre l'espacement nécessaire pour que les interférences soient non-corrélées et les formes d'ondes parfaitement orthogonales n'existent pas. Nous supposons que ces facteurs entraînent la corrélation entre les signaux reçus des sous-réseaux différents. Par conséquent, nous considérons le modèle de signal suivant qui ne suppose pas l'indépendance entre les sous-réseaux différents.

$$\mathbf{y} = \mathbf{P}\boldsymbol{\alpha} + \mathbf{z},$$

où les vecteurs $\mathbf{y}$, $\boldsymbol{\alpha}$ and $\mathbf{z}$ sont respectivement les concaténations de tous les signaux reçus, des RCS et des signaux des interférences. $\mathbf{P}$ est une matrice de taille N_exK_e contenant tous les vecteurs de pointage.

La matrice de covariance de chaque $\mathbf{z}_i$ est $\mathbf{M}_{ii}$ et la matrice de inter-correlation entre $\mathbf{z}_i$ et $\mathbf{z}_j$ est $\mathbf{M}_{ij}$ telle que $\mathbf{z} \sim \mathcal{CN}(\mathbf{0}, \mathbf{M})$ où $\mathbf{M}$ est une matrice de taille N_exN_e, composant les matrices $\mathbf{M}_{ij}$ $\forall\ i, j \in \{1, \ldots, K_e\}$.

II.2.1 Détection

En supposant que les paramètres d'interférence sont connus, le détecteur optimal pour le critère de Neyman-Pearson est [C3]:

$$\begin{aligned} \ln \Lambda(\mathbf{y}) &= 2\Re(\mathbf{y}^\dagger \mathbf{M}^{-1}\mathbf{P}\hat{\boldsymbol{\alpha}}) - \hat{\boldsymbol{\alpha}}^\dagger \mathbf{P}^\dagger \mathbf{M}^{-1}\mathbf{P}\hat{\boldsymbol{\alpha}}, \\ &= \mathbf{y}^\dagger \mathbf{M}^{-1}\mathbf{P}(\mathbf{P}^\dagger \mathbf{M}^{-1}\mathbf{P})^{-1}\mathbf{P}^\dagger \mathbf{M}^{-1}\mathbf{y}. \end{aligned}$$

Ce détecteur a une structure classique qui est constitué d'un projecteur sur le sous-espace du signal utile. Il est essentiellement la version multi-dimensionnelle du détecteur optimal gaussien (OGD). Ce détecteur prend en considération la corrélation possible entre les sous-réseaux et est donc robuste aux problèmes tels que l'espacement des sous-réseaux et l'orthogonalité imparfaite des formes d'ondes. Dans le cas particulier où il n'y a pas de corrélation entre les sous-réseaux, ce détecteur devient le MIMO OGD comme proposé dans [4, 20].

II.2.2 Résultats des Simulations

Afin de comparer les configurations différentes et d'étudier les paramètres (K_e, N_{tx}, N_{rx}, etc), nous allons considérer deux cas: le cas MISO qui a la diversité spatiale en émission et la diversité de forme d'onde et le cas SIMO qui ne dispose que la

diversité spatiale en réception. La RCS de la cible est modélisée comme une variable aléatoire gaussienne. Les résultats les plus importants sont résumés ici.

Le cas MISO On considère K_e éléments d'émission largement espacés et un seul sous-réseau de réception avec M éléments. N_p est fixe, ce qui signifie que plus il y a d'éléments d'émission (créant ainsi plus de sous-réseaux effectif), moins il y aura d'éléments dans le sous-réseau de réception. Cela affecte le nombre effectif total d'éléments qui à son tour affecte le gain en SIR.

Dans la figure III, nous avons tracé la probabilité de détection P_d en fonction du SIR. Dans les régions à faible SIR, les performances de détection se dégradent avec l'augmentation de K_e en raison de l'augmentation des seuils de détection quand les dégrés de liberté (DoF) augmentent. Toutefois, dans les régions à SIR élevés, les performances de détection pour $K_e = 3$ sont les plus mauvaises car le cas K_e est la plus sensible aux fluctuations de la RCS. En prenant en compte les gains en SIR, $K_e = 6$ a un net avantage sur $K_e = 3$. Bien que le cas $K_e = 12$ soit robuste aux fluctuations de la RCS, il n'y a pas de gain en SIR et son seuil de détection est trop élevé. Ainsi, ses performances de détection restent pire que celles des $K_e = 3, 6$.

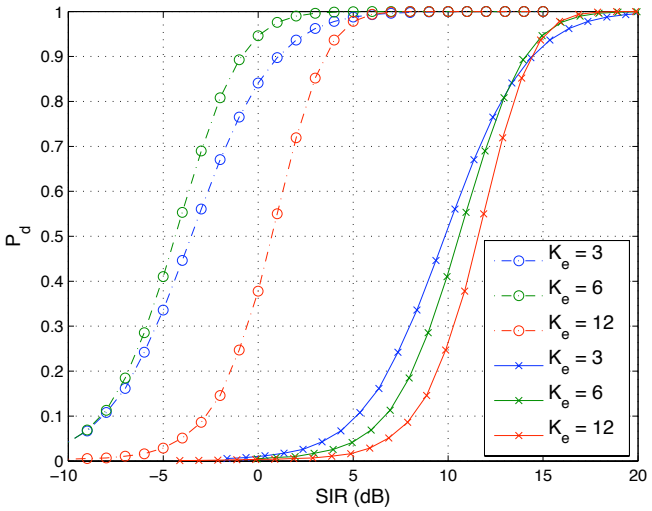

Figure III: P_d en fonction du SIR_{pre} (lignes en pointillées et tirets) et SIR_{post} (lignes pleines) pour le cas MISO.

Le cas SIMO On considère un unique élément d'émission. La diversité spatiale vient seulement des sous-réseaux de réception qui contiennent chacun $\frac{N_p-1}{K_e}$ éléments. Notez que N_e reste le même pour différents K_e car $N_{tx} = 1$ tel que $N_e = N_{rx}$. Par ailleurs, comme il n'y a qu'un élément d'émission, il n'y a pas de diversité de forme d'onde et $N_e = N_p - 1 < N_p$.

On trace la P_d en fontion du SIR dans la figure IV pour $K_e = 3, 6, 12$ et $N_p = 13$

dans le cas SIMO. Comme prévu, les performances de détection sont meilleures pour les petits K_e dans les régions à SIR faible et l'inverse dans les régions à SIR élévés.

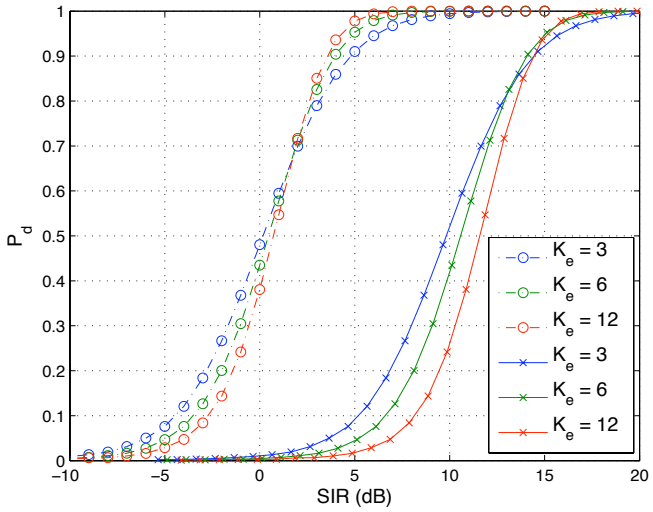

Figure IV: P_d en fonction du SIR_{pre} (lignes en pointillées et tirets) et SIR_{post} (lignes pleines) pour le cas SIMO.

II.3 Détecteur Gaussien et Adaptatif

Comme la matrice de covariance est généralement inconnue dans la réalité, nous considérons dans cette section la version adaptative du détecteur. Basé sur le test de Kelly [21] dans lequel la distribution de l'ensemble des données est prise en compte, le test de Kelly MIMO se calcule de la manière suivante [C3]:

$$\frac{\mathbf{y}^\dagger \widehat{\mathbf{M}}_{SCM}^{-1}\mathbf{P}(\mathbf{P}^\dagger \widehat{\mathbf{M}}_{SCM}^{-1}\mathbf{P})^{-1}\mathbf{P}^\dagger \widehat{\mathbf{M}}_{SCM}^{-1}\mathbf{y}}{N_s + \mathbf{y}^\dagger \widehat{\mathbf{M}}_{SCM}^{-1}\mathbf{y}}.$$

où $\widehat{\mathbf{M}}_{SCM}$ est la Sample Covariance Matrix (SCM) de $\mathbf{M}$:

$$\widehat{\mathbf{M}}_{SCM} = \frac{1}{N_s}\sum_{l=1}^{N_s}\mathbf{z}(l)\mathbf{z}(l)^\dagger.$$

L'estimation de la matrice de covariance cause une perte en SIR. Cette perte est réprésentée par un facteur de perte l_f qui est β-distribuée avec les paramètres $N_s - N_e + K_e + 1$ et $N_e - K_e$. Lorsque $N_e = K_e$, bien qu'il n'y ait aucun gain cohérent, car il n'y a qu'un élément par sous-réseau, il n'y pas de perte en SIR. C'est parce que le sous-espace de cible occupe l'ensemble d'espace de signal et donc le sous-espace d'interférence est nul. Puisque le sous-espace d'interférence n'est pas estimé, il n'y a aucune perte due à l'estimation en SIR. Par conséquent, l_f n'est plus une variable aléatoire et $l_f = 1$ [C5].

La moyenne de l_f est donnée par $E(l_f) = \frac{N_s - N_e + K_e + 1}{N_s + 1}$:

- Étant donné N_s fixe, il pourrait être préférable de choisir un nombre N_e petit et un nombre K_e grand pour minimiser la perte due à l'estimation.
- Pour limiter la perte à 3 dB, c'est-à-dire $E(l_f) > 0,5$, nous avons besoin de $N_s > 2N_e - 2K_e - 1$, à condition que $N_s \geq N_e$ pour que la SCM soit de rang plein.
- Pour le réseau d'antennes à commande de phase où $K_e = 1$, on obtient $N_s > 2N_e - 3$ qui est la règle bien connue de Reed-Mallett-Brennan [22].

Les moyennes du facteur de perte $E(l_f)$ pour les cas SIMO et MISO sont tracées dans la figure V. Notez que $l_f \in [0, 1]$. N_s est choisi de telle sorte qu'il varie entre $\max(N_e)$ et $5\max(N_e)$. Pour le cas SIMO, N_e reste le même pour toutes les valeurs de K_e. Ainsi, nous voyons une nette augmentation de $E(l_f)$ avec l'augmentation de K_e et N_s. D'autre part, N_e change pour le cas MISO. Comme N_e est plus grand que K_e, $E(l_f)$ dépend plus de N_e et $E(l_f)$ atteint son minimum pour $K_e \approx \frac{N_p}{2}$.

II.3.1 Résultats des Simulations

On utilise les mêmes paramètres et les mêmes configurations que précédemment, sauf qu'un modèle de cible stationnaire est utilisé pour mieux étudier l'effet de l'estimation de la matrice de covariance. La P_d est tracée en fonction du SIR dans la figure VI en utilisant $N_s = 20$ données secondaires pour le cas SIMO. Sans les gains en SIR et les pertes dues à l'estimation, les performances de détection (lignes pleines) se dégradent avec l'augmentation de K_e en raison de seuils plus élevés, comme dans le cas du détecteur non-adaptatif. Ici, le gain en SIR est fondamentalement le même pour tous les K_e parce que N_e reste le même. Cependant, $E(l_f)$ augmente avec K_e (voir la figure V(a)) surtout quand il y a peu de données secondaires ($N_s = 20 < 2N_e$). Après avoir pris en compte la perte due à l'estimation, les performances de détection (lignes en pointillées et tirets) sont améliorées avec l'augmentation de K_e.

Dans la figure VII, nous avons tracé la P_d en fonction du $\mathrm{SIR}_{\mathrm{pre}}$ pour les différents K_e et pour $N_s = 50, 80$. Il y a plusieurs facteurs qui peuvent affecter les performances de détection. Comme mentionné précédemment, l'augmentation du seuil avec l'augmentation de K_e dégrade les performances de détection. Le gain en SIR est proportionnel à N_e et il atteint son maximum pour $K_e \approx \frac{N_p}{2}$ et son minimum pour $K_e = 1$ et $K_e = N_p - 1$. Enfin, la perte due à l'estimation est opposée au gain en SIR : cette perte augmente quand N_e est grand pour N_s fixe. On note que les différences sont plus grandes lorsque N_s est petit que quand N_s est grand (voir la figure V(b)).

En effet, quand $N_s = 50$ (Fig. VII(a)), nous obtenons les moins bonnes performances de détection pour $K_e = 6, 7$ car le gain en SIR pour N_e grand n'est pas suffisant pour compenser $E(l_f)$ petit dû au fait que $N_s \approx N_e$. Par ailleurs les performances de détection sont meilleures pour des K_e petits.

D'autre part, quand $N_s = 80$ (Fig. VII(b)), il y a assez de données sécondaires tel que $N_s \approx 2N_e$ pour tous les K_e. Par conséquent, les performances de détection

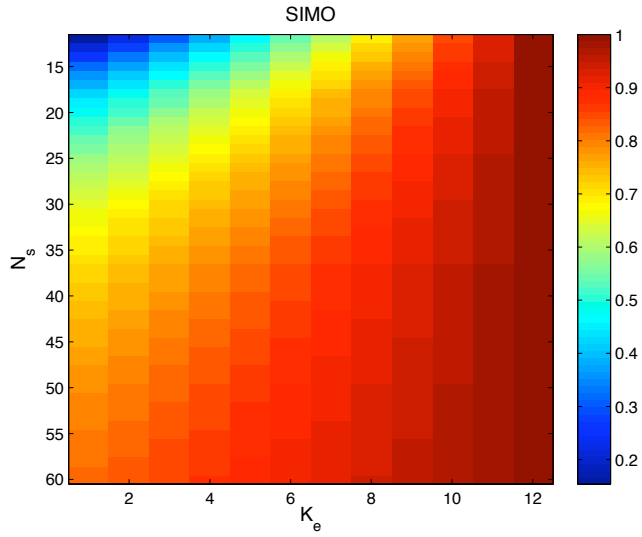

(a) Cas SIMO

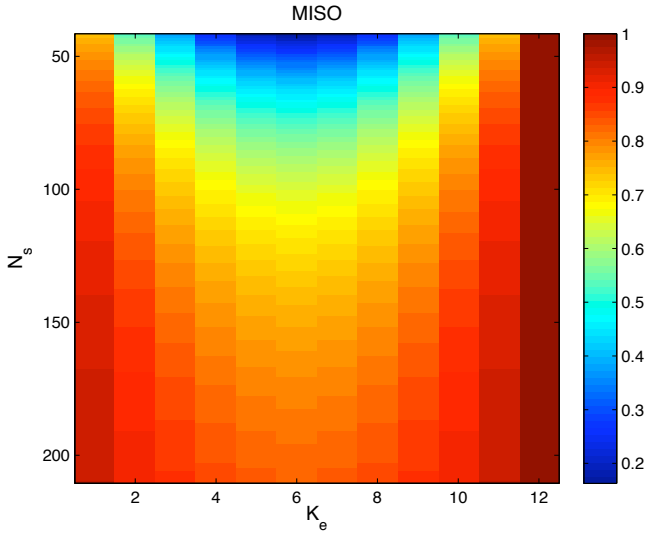

(b) Cas MISO

Figure V: La moyenne du facteur de perte $E(l_f)$ en fonction du K_e et N_s.

sont comparables pour la plupart des valeurs de K_e sauf pour les plus grands K_e qui sont pénalisés par un seuil de détection trop élévé.

II.4 Détecteur Non Gaussien avec Interférences connues

Dans cette section, nous considérons des interférences non gaussiennes, dont la puissance est différente et indépendante pour chaque sous-réseau. Le modèle de signal donné par l'équation (1) est utilisé mais les interférences sont modélisées par

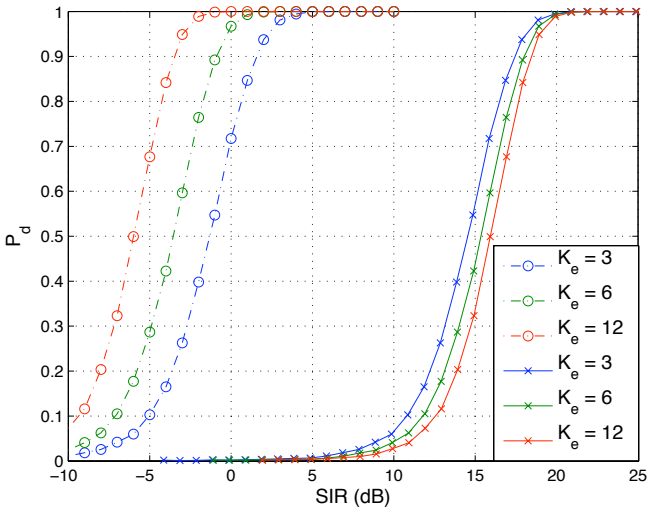

Figure VI: P_d en fonction du SIR_{pre} (lignes en pointillées et tirets) et SIR_{post} (lignes pleines) pour le cas SIMO. $N_s = 20$.

le modèle SIRV [14, 15, 16]. Ce modèle décrit les interférences comme le produit d'un processus gaussien complexe aléatoire $\mathbf{x}$ (le *speckle*) et la racine carrée d'une variable aléatoire positive τ (la *texture*):

$$\mathbf{z} = \sqrt{\tau}\mathbf{x}.$$

Le vecteur $\mathbf{x}$ a une moyenne nulle et sa matrice de covariance est notée $\mathbf{M}$. La matrice de covariance $\mathbf{M} = E(\mathbf{x}\mathbf{x}^\dagger)$ est normalisée de sorte que $tr(\mathbf{M}) = N_x$ où N_x est la dimension de $\mathbf{x}$ pour des considérations d'identifiabilité [23].

Le speckle modélise les fluctuations temporelles des interférences tandis que la texture modélise les fluctuations spatiales de la puissance des interférences. Le SIRV peut modèliser les différentes interférences non gaussiennes en fonction de la texture choisie. Les interférences gaussiennes sont un cas particulier où la texture est une constante.

Pour de telles interférences, le Generalized Likelihood Ratio Test - Linear Quadratic (GLRT-LQ) est intéressant car il a la propriété désirable d'être homogène en termes de $\mathbf{p}$, $\mathbf{M}$ et $\mathbf{y}$: il est invariant à l'échelle des données. Par conséquent, la texture s'annule sous l'hypothèse H_0 et le détecteur est à taux constant de fausse alarme (CFAR) par rapport à la texture. Le GLRT-LQ est étendu au cas MIMO [J1]:

$$\begin{aligned}\Lambda(\mathbf{y}) &= \prod_{i=1}^{K_e}\left[1 - \frac{|\mathbf{p}_i^\dagger \mathbf{M}_i^{-1}\mathbf{y}_i|^2}{(\mathbf{p}_i^\dagger \mathbf{M}_i^{-1}\mathbf{p}_i)(\mathbf{y}_i^\dagger \mathbf{M}_i^{-1}\mathbf{y}_i)}\right]^{-N_{e,i}}, \\ &= \prod_{i=1}^{K_e}\Lambda_i(\mathbf{y}_i)^{N_{e,i}},\end{aligned}$$

où $\mathbf{M}_i$ est la matrice de covariance de $\mathbf{y}_i$.

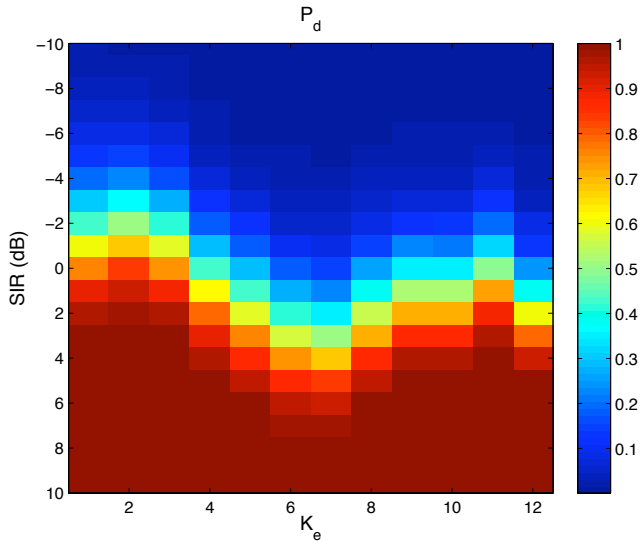

(a) $N_s = 50$

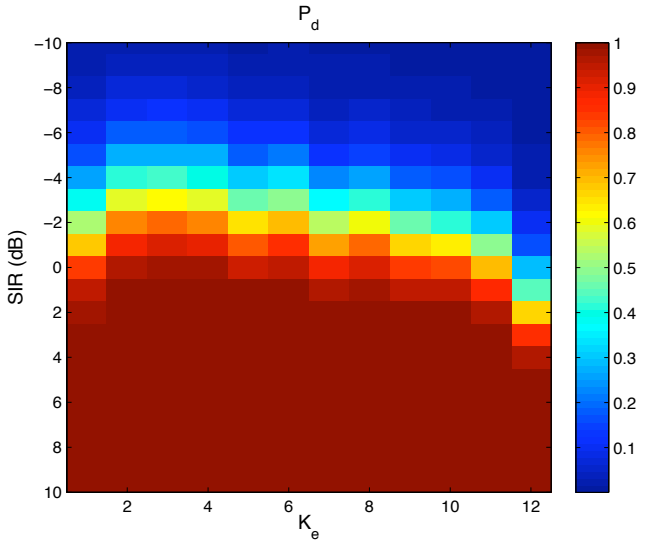

(b) $N_s = 80$

Figure VII: P_d en fonction du $\mathrm{SIR}_{\mathrm{pre}}$ pour le cas MISO.

Pour un système de radar MIMO contenant K_e sous-réseaux et $N_{e,0}$ ($N_{e,0} > 1$) éléments dans chaque sous-réseau, la probabilité de fausse alarme P_{fa} du MIMO GLRT-LQ est donnée par [J1]:

$$P_{fa} = \lambda^{-N_{e,0}+1} \sum_{k=0}^{K_e-1} \frac{(N_{e,0}-1)^k}{k!} (\ln \lambda)^k.$$

Notez que la P_{fa} ne dépend que de K_e et de $N_{e,0}$ (et non pas sur des paramètres des interférences) ; ceci démontre la propriété texture-CFAR du MIMO GLRT-LQ.

II.4.1 Résultats des Simulations

La configuration utilisée pour les simulations de Monte-Carlo est présentée dans le tableau II. Nous utilisons à la fois le modèle de cible fixe et le modèle de cible fluctuante, la P_{fa} est fixée à 0,001 et $N_{MC} = 10^4$.

$\tilde{M}$	$\tilde{N}$	M_m	N_n	$K_e = \tilde{M}\tilde{N}$	$N_{e,0} = M_m N_n$
3	2	4	3	6	12

Table II: La configuration des simulations de Monte-Carlo.

Nous commençons par le cas où les interférences sont gaussiennes. Dans la figure VIII, la P_d en fonction du SIR_{pre} est tracée pour le MIMO GLRT-LQ et le MIMO OGD. Premièrement, nous notons que le MIMO GLRT-LQ perd environ 0,5 dB par rapport au MIMO OGD pour les deux modèles de cible parce que le MIMO OGD est le détecteur optimal sous l'interférence gaussienne. Cela peut être considérée comme une perte CFAR, c'est-à-dire une perte supplémentaire subie par le MIMO GLRT-LQ par rapport au cas optimal, et due à la propriété de texture-CFAR. Deuxièmement, sous l'interférence gaussienne, le MIMO GLRT-LQ et le MIMO OGD sont autant influencés par les fluctuations de la RCS. Ils perdent environ 4 dB de SIR. Cependant, la forme des courbes de détection reste presque inchangée parce qu'il y a six sous-réseaux, c'est-à-dire six vues de la cible indépendantes.

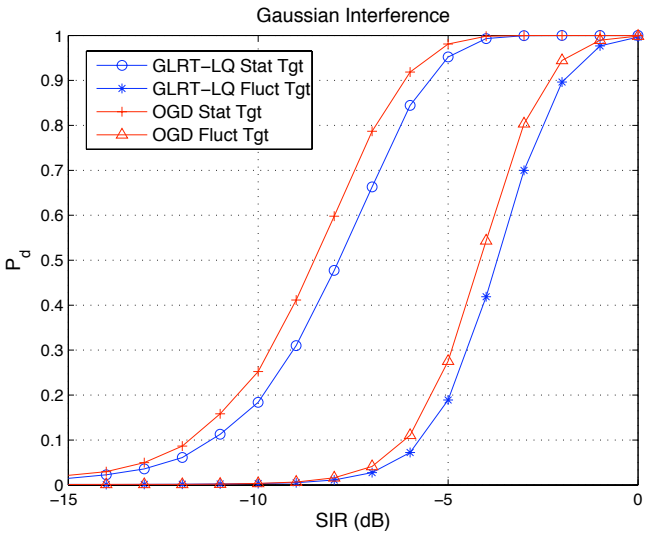

Figure VIII: P_d en fonction du SIR_{pre} où les interférences sont gaussiennes, considérant à la fois des cibles fixes et fluctuantes et pour le MIMO GLRT-LQ et le MIMO OGD.

Les performances de détection pour le MIMO GLRT-LQ et le MIMO OGD sous les interférences impulsives et K-distribuées ($\tau \sim \Gamma(0,5,2)$) sont montrées dans la figure IX. Lorsque l'interférence est impulsive, le MIMO GLRT-LQ est plus

performant que le MIMO OGD. Pour le MIMO OGD, la grande variation de la puissance de l'interférence résulte à un seuil de détection plus élevé pour maintenir la même P_{fa}.

D'autre part, les termes $\mathbf{y}_i^\dagger \mathbf{M}_i^{-1} \mathbf{y}_i$ du MIMO GLRT-LQ prennent en compte cette variation de puissance dans la régulation des fausses alarmes. Par ailleurs, le MIMO GLRT-LQ peut détecter des cibles très faibles ($P_d = 0,25$ pour un SIR $= -25$dB) grâce à la prise en compte de cette variation. Cependant, cet avantage du MIMO GLRT-LQ est réduit lorsque la cible est fluctuante. Pour des interférences non gaussiennes, les performances de détection du MIMO GLRT-LQ sont meilleures que celles du MIMO OGD quel que soit le modèle de cible.

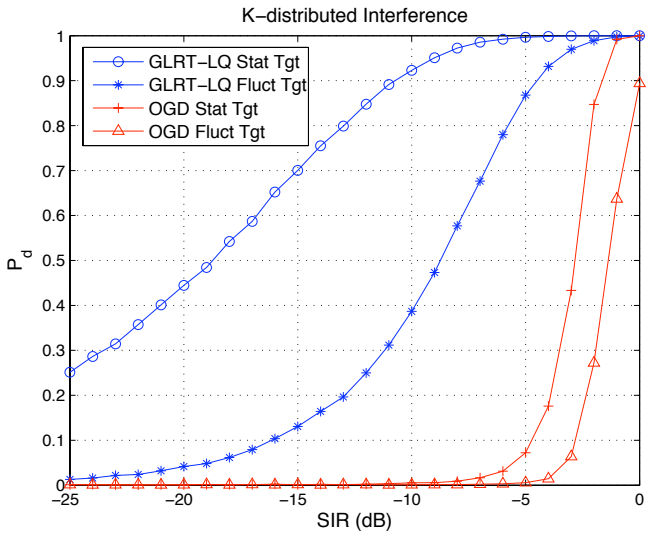

Figure IX: P_d en fonction du SIR_{pre} où les interférences sont impulsives et K-distribuées, considérant à la fois les modèles de cible fixe et fluctuante et pour le MIMO GLRT-LQ et le MIMO OGD.

II.5 Détecteur Non Gaussien et Adaptatif

La version adaptative du détecteur est obtenue en remplaçant la matrice de covariance $\mathbf{M}_i$ par son estimateur $\widehat{\mathbf{M}}_i$:

$$\hat{\Lambda}(\mathbf{y}) = \prod_{i=1}^{K_e} \hat{\Lambda}_i(\mathbf{y}_i)^{N_{e,i}} = \prod_{i=1}^{K_e} \left[1 - \frac{|\mathbf{p}_i^\dagger \widehat{\mathbf{M}}_i^{-1} \mathbf{y}_i|^2}{(\mathbf{p}_i^\dagger \widehat{\mathbf{M}}_i^{-1} \mathbf{p}_i)(\mathbf{y}_i^\dagger \widehat{\mathbf{M}}_i^{-1} \mathbf{y}_i)} \right]^{-N_{e,i}}.$$

Quand les interférences sont non gaussiennes, la SCM n'est plus l'estimateur du maximum de vraisemblance (ML). Donc, nous considérons ici l'estimateur du point fixe (FPE) qui a été introduit dans [23, 24] et ensuite analysé dans [25, 26]. Le FPE est l'estimateur ML exact où la texture est déterministe et inconnue [25]. D'autre part, quand τ est une variable aléatoire positive, le FPE est un estimateur ML approché [23, 24].

II.5.1 Résultats des Simulations

Dans la figure X, nous avons tracé les performances de détection du MIMO GLRT-LQ adaptatif utilisant le FPE, le MIMO AMF utilisant SCM et le test de Kelly MIMO pour des interférences gaussiennes. Seul le modèle de cible fixe est utilisé pour mieux étudier les effets de l'estimation de la matrice de covariance.

Lorsque $N_{s,i}$ est grand, les performances du MIMO AMF sont comparables à celles du test de Kelly MIMO car il y a suffisamment de données secondaires pour estimer la matrice de covariance. Le MIMO GLRT-LQ adaptatif subit une petite perte CFAR d'environ 1 dB, un compromis pour la robustesse aux variations de la puissance des interférences.

Toutefois, lorsque $N_{s,i}$ est petit, le MIMO AMF perd 1 dB par rapport au test de Kelly MIMO, qui profite des $\mathbf{y}_i$ pour augmenter le nombre de données secondaires disponibles. Ce qui est intéressant est que le MIMO GLRT-LQ adaptatif est aussi un peu meilleur que le MIMO AMF. C'est parce que quand $N_{s,i} = 2N_{e,i}$, le terme $\mathbf{y}_i^\dagger \widehat{\mathbf{M}}_{SCM,i}^{-1} \mathbf{y}_i$ n'est plus négligeable et le test de Kelly MIMO devient plus semblable au MIMO GLRT-LQ adaptatif.

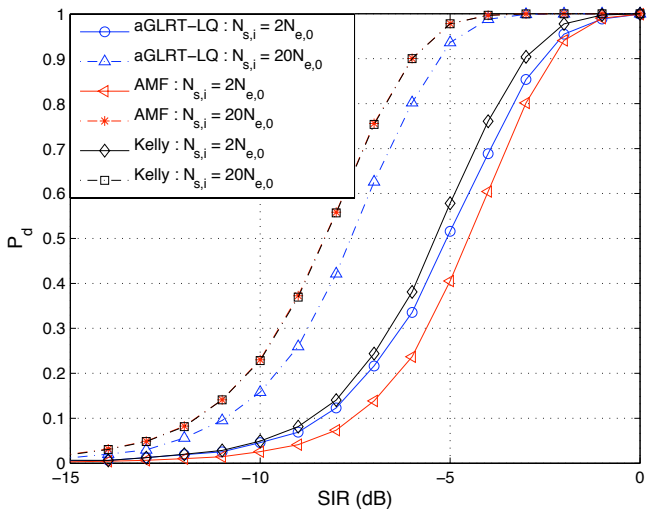

Figure X: P_d en fonction du SIR_{pre} pour le MIMO GLRT-LQ adaptatif utilisant le FPE, le MIMO AMF utilisant la SCM et le test de Kelly MIMO pour des interférences gaussiennes.

La figure XI montre les performances de détection lorsque les interférences sont impulsives et K-distribuées. Comme prévu, le MIMO GLRT-LQ adaptatif est plus performant que le MIMO AMF et le test de Kelly MIMO quand l'interférence est impulsive. Le test de Kelly MIMO est comparable au MIMO GLRT-LQ adaptatif quand $N_{s,i}$ est petit parce que $N_{s,i} + \mathbf{y}_i^\dagger \widehat{\mathbf{M}}_{SCM,i}^{-1} \mathbf{y}_i \approx y_i^\dagger \widehat{\mathbf{M}}_{SCM,i}^{-1} \mathbf{y}_i$. Ainsi il est robuste aux variations de puissance des interférences. Toutefois lorsque $N_{s,i}$ est grand, le test de Kelly MIMO ne peut plus prendre en compte les variations de puissance. Ainsi, le test de Kelly MIMO a des meilleures performances de détection

lorsque $N_{s,i}$ est petit. On note cependant qu'il perd quand même beaucoup de SIR par rapport au MIMO GLRT-LQ adaptatif, la SCM n'étant plus l'estimateur ML pour des interférences non gaussiennes. Les performances de détection du MIMO AMF sont les plus mauvaises comparées à celles des deux autres détecteurs.

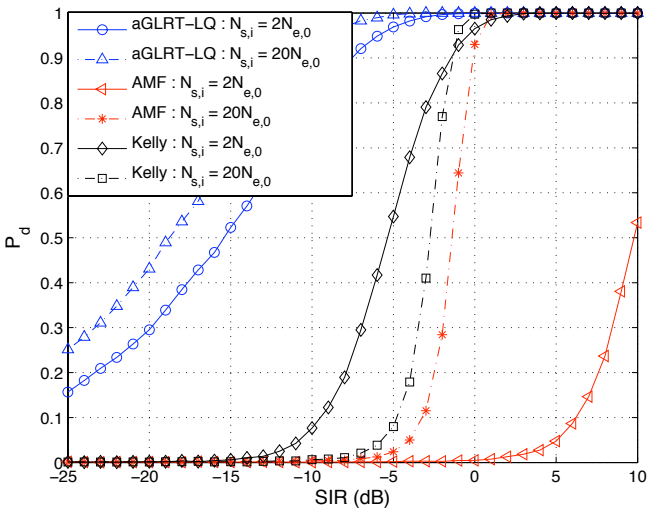

Figure XI: P_d en fonction du SIR_{pre} pour le MIMO GLRT-LQ adaptatif utilisant le FPE, le MIMO AMF utilisant la SCM et le test de Kelly MIMO pour des interférences impulsives et K-distribuées.

III Application: STAP

III.1 Motivation

Le STAP est une technique [27, 28, 29] souvent utilisée par les radars aéroportés pour détecter des cibles qui se déplacent lentement et qui se trouvent dans des interférences comme le fouillis de sol ou un brouillage fort. Alors que les radars classiques sont capables de détecter des cibles à la fois dans le domaine temporel lié à la position de la cible et dans le domaine fréquentiel lié à la vitesse de la cible, le STAP utilise un domaine supplémentaire (l'espace) lié à la localisation angulaire de la cible. On obtient alors une technique de filtrage adaptatif en deux dimensions qui utilise conjointement les dimensions temporel et spatial pour supprimer les interférences, ce qui permet la détection de ces cibles. Le principe du STAP est illustré dans la figure XII (source: [30]). Avec l'utilisation de configurations MIMO, les performances du radar peuvent être améliorées, notamment celles de l'estimation de la position angulaire et la vitesse minimale détectable (MDV).

Dans cette partie des travaux, nous considérons deux configurations différentes: le SISO-STAP où il n'y a pas de diversité spatiale et le MISO-STAP où il y a une diversité spatiale. Il existe une diversité de forme d'onde dans les deux cas. La

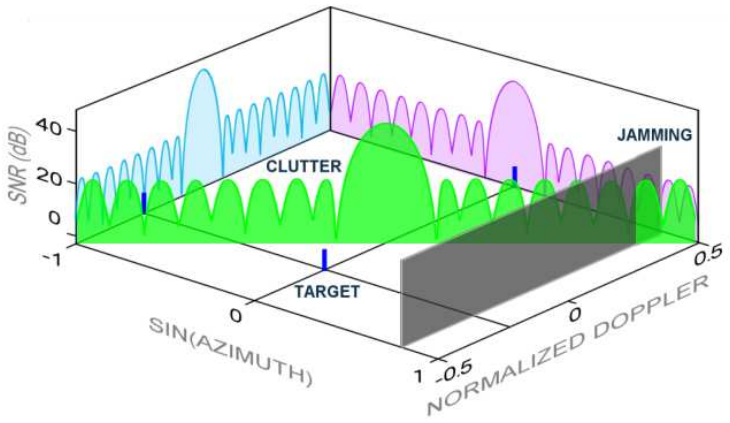

Figure XII: Illustration de la concept STAP: le traitement conjoint des dimensions temporel et spatial permet la détection des cibles lentes.

configuration SISO, ou MIMO cohérente, est bien adaptée au STAP. Avec seulement la diversité de forme d'onde, la configuration SISO est capable d'augmenter N_e, qui à son tour augmente le gain en SIR qui conduit à une meilleure performance de détection et d'estimation. En plus, elle augmente la taille de l'ouverture virtuelle qui limite le fouillis dans une cellule de résolution angulaire plus petite, facilitant ainsi la suppression du fouillis et la réduction de la MDV.

Beaucoup de travaux ont été fait sur le SISO-STAP [31, 32, 33]. Cependant, ces derniers ne traitent pas le problème de la conception de la configuration pour optimiser les performances de détection et d'estimation. Dans la première partie, nous étudions différentes configurations SISO en fonction des performances de détection et d'estimation. Nous considérons deux situations différentes. Tout d'abord, nous faisons varier le nombre d'éléments d'émission et de réception en gardant le nombre total d'éléments fixe. Ensuite, nous changons l'espacement entre les éléments d'émission et de réception. En fait, en plus de l'amélioration des performances de détection et d'estimation, nous verrons que la conception de configuration peut également réduire le rang de la matrice de covariance du fouillis facilitant ainsi son estimation, surtout quand il y a peu de données secondaires disponibles.

Notez qu'ici l'intervalle du traitement cohérent (CPI) est supposé constant mais le CPI pour les configurations SISO peut être augmenté puisque le balayage de faisceau n'est pas nécessaire. Un CPI plus long améliore la résolution Doppler et rend plus facile la suppression du fouilllis.

Les systèmes d'antennes peuvent détecter uniquement les cibles dont la vitesse en ligne de visée (LOS) ou la vitesse radiale est non-nulle. La direction LOS est définie comme la direction perpendiculaire aux contours isorange tandis que l'opposée de la direction LOS (XLOS) est tangente aux contours isorange. Pour les radars bistatiques, les sous-réseaux d'émission et de réception ont des LOS et XLOS différentes, donc nous considérons les LOS et XLOS équivalentes monostatiques. Si une cible se déplace dans le sens XLOS, sa position radar ne change pas

et sa fréquence Doppler est nulle. Ainsi, elle apparaît comme du fouillis pour le radar.

La diversité spatiale est utile car une cible mobile peut avoir une vitesse LOS nulle par rapport à une antenne, mais il est impossible pour elle d'avoir une vitesse LOS nulle pour toutes les antennes simultanément. Donc, la possibilité que la cible soit confondue avec le fouillis est réduite. Cet avantage est parfois appelé le *geometry gain* dans la littérature. Par ailleurs, plusieurs antennes largement espacées nous permettent d'obtenir des informations complètes sur la vitesse de la cible de telle sorte que la vitesse peut être uniquement déterminée.

De plus comme précédemment, la diversité spatiale rend la détection plus robuste aux fluctuations de la RCS puisque les sous-réseaux voient la cible des angles différents et il est peu probable que tous les sous-réseaux voient une faible RCS en même temps. Ce gain est souvent appelé *diversity gain* dans la littérature. Toutefois, de telles configurations signifient une configuration bistatique pour chaque sous-réseau et les configurations bistatiques sont en général défavorable pour les applications STAP à cause de l'augmentation du rang et la non stationnarité de la matrice de covariance du fouillis. Cette augmentation peut être considérée comme un écart de puissance du fouillis sur plus de dégrés de liberté que dans le cas monostatique.

Une solution possible, telle que proposée dans [34], est d'utiliser la configuration multistatique, c'est-à-dire chaque sous-réseau se compose d'un sous-réseau différent d'émission et de réception. Cela signifie qu'il n'y a pas d'augmentation du nombre effectif de sous-réseaux et d'éléments, il n'est donc pas considéré comme une configuration MIMO. Chaque sous-réseau est dans une configuration monostatique (les sous-réseaux d'émission et de réception sont co-situés) et ne reçoit que son propre signal transmis. Notez que les signaux doivent être suffisamment séparés pour éviter toute interférence.

Dans [35], les auteurs ont utilisé la configuration SIMO et il n'y a qu'un seul élément d'émission tel qu'il n'y a pas de diversité de forme d'onde, seulement une diversité spatiale. Ils proposent l'utilisation des techniques classiques de STAP bistatique [36] pour compenser la non-stationnarité du fouillis. Dans la deuxième partie de ce travail, nous supposons également que ces techniques sont appliquées à chaque sous-réseau de telle sorte que le fouillis peut être considéré comme stationnaire. Cependant, nous adoptons une configuration différente, le MISO. Nous considérons qu'il y a un seul sous-réseau de réception dont les éléments sont étroitement espacés de telle sorte que la formation de faisceaux est possible. La diversité spatiale vient des éléments d'émission qui sont tous très éloignés. Cette configuration réduit le nombre d'éléments requis pour avoir le même N_e comparé à [35] et elle ne nécessite pas beaucoup de différentes formes d'onde orthogonales. En outre, cette configuration est facile à réaliser en utilisant un radar classique, en particulier la partie réception. Les sous-réseaux d'émission peuvent être montés sur des plate-formes petites et légères car il n'y a qu'un seul élément par sous-réseau.

III.2 SISO-STAP

Nous considérons la configuration MIMO cohérente. Supposons qu'il y ait N éléments d'émission et M éléments de réception et que ces éléments soient étroitement espacés tels que la RCS de la cible est la même. La détection est effectuée avec L impulsions. Après le filtrage adapté en distance radar, en supposant que les sous-réseaux d'émission et de réception sont co-localisés de telle sorte que l'angle d'émission et de réception sont les mêmes ($\theta_r = \theta_t = \theta$), le signal reçu peut être exprimé comme:

$$\begin{aligned} \mathbf{y} &= ae^{j\phi}\mathbf{a}(\theta) \otimes \mathbf{b}(\theta) \otimes \mathbf{v}(f_d) + \mathbf{c} + \mathbf{n}, \\ &= ae^{j\phi}\mathbf{p} + \mathbf{c} + \mathbf{n}, \end{aligned}$$

où $ae^{j\phi}\mathbf{p}$ caractérise une cible avec une RCS de $ae^{j\phi}$. Les vecteur de pointage de réception, d'émission et Doppler sont:

$$\begin{aligned} \mathbf{a}(\theta) &= \left[1 \ \cdots \ \exp(j2\pi\frac{(M-1)d_r}{\lambda}\sin\theta)\right]^T, \\ \mathbf{b}(\theta) &= \left[1 \ \cdots \ \exp(j2\pi\frac{(N-1)d_t}{\lambda}\sin\theta)\right]^T, \\ \mathbf{v}(f_d) &= [1 \ \cdots \ \exp(j2\pi(L-1)\mathrm{PRI}\cdot f_d)]^T, \end{aligned}$$

où f_d est la fréquence Doppler, λ est la longueur d'onde du radar et le PRI est l'intervalle de répétition des impulsions. d_r et d_t sont respectivement les espacement entre les élément d'émission et de réception. Le radar étant en mouvement, la fréquence Doppler réelle de la cible f_t est donnée par:

$$f_t = f_d + \frac{2v}{\lambda}\sin\theta,$$

où v est la vitesse du radar.

Les échos indésirables se composent du fouillis et du bruit. Le fouillis est réprésenté par un vecteur gaussien $\mathbf{c} \sim \mathcal{CN}(\mathbf{0}, \mathbf{M}_c)$. $\mathbf{M}_c$ est la matrice de covariance du fouillis (CCM) et elle est de rang faible. Le bruit est réprésenté par un vecteur gaussien $\mathbf{n} \sim \mathcal{CN}(\mathbf{0}, \sigma^2\mathbf{I})$ et σ^2 est la puissance du bruit. La matrice de covariance des intérférences $\mathbf{M}$ est donc donnée par: $\mathbf{M} = \mathbf{M}_c + \sigma^2\mathbf{I}$.

III.2.1 Détection

Lorsque les paramètres d'interférence sont connus, le détecteur CFAR optimal est l'OGD:

$$\Lambda(\mathbf{y}) = \frac{|\mathbf{p}^\dagger\mathbf{M}^{-1}\mathbf{y}|^2}{\mathbf{p}^\dagger\mathbf{M}^{-1}\mathbf{p}}.$$

Dans le cas du STAP, la puissance du fouillis est très localisée (le long des *clutter ridges*) et le fouillis est beaucoup plus fort que le bruit. Par conséquent, le

SIR effectif varie considérablement selon la position et la vitesse de la cible. Une mesure de performance qui est utile pour illustrer cet effet est la perte en SIR qui est définie comme la perte de SIR par rapport au cas idéal où il n'y a que du bruit:

$$\begin{aligned} \text{SIR loss} &= \frac{a^2 \mathbf{p}^\dagger \mathbf{M}^{-1} \mathbf{p}}{\frac{a^2}{\sigma^2} MNL}, \\ &= \frac{\sigma^2 \mathbf{p}^\dagger \mathbf{M}^{-1} \mathbf{p}}{MNL}. \end{aligned}$$

Dans le cas où les paramètres d'interférence sont inconnus, nous supposons que nous avons accès à N_s données secondaires (indépendantes et identiquement distribuées) pour estimer $\mathbf{M}$ que nous notons $\mathbf{y}_1, \ldots, \mathbf{y}_{N_s}$. Le détecteur optimal adaptatif est le test de Kelly qui s'écrit [21]:

$$\hat{\Lambda}(\mathbf{y}) = \frac{|\mathbf{p}^\dagger \widehat{\mathbf{M}}_{\text{SCM}}^{-1} \mathbf{y}|^2}{(\mathbf{p}^\dagger \widehat{\mathbf{M}}_{\text{SCM}}^{-1} \mathbf{p})(N_s + \mathbf{y}^\dagger \widehat{\mathbf{M}}_{\text{SCM}}^{-1} \mathbf{y})}.$$

III.2.2 Estimation

L'avantage principal du MIMO cohérent est l'augmentation de la résolution angulaire, c'est-à-dire de ses performances d'estimation. En théorie de l'estimation [37], la borne de Cramér-Rao (CRB) exprime une borne inférieure sur la variance des estimateurs d'un paramètre déterministe. Pour l'estimation *après* détection, nous obtenons la CRB pour θ et f_t:

$$\begin{aligned} \text{CRB}_{\theta\theta} &= \frac{1}{2a^2} \left(\frac{\mathbf{d}_f{}^\dagger \mathbf{M}^{-1} \mathbf{d}_f}{(\mathbf{d}_s{}^\dagger \mathbf{M}^{-1} \mathbf{d}_s)(\mathbf{d}_f{}^\dagger \mathbf{M}^{-1} \mathbf{d}_f) - \Re(\mathbf{d}_s{}^\dagger \mathbf{M}^{-1} \mathbf{d}_f)^2} \right), \\ \text{CRB}_{f_t f_t} &= \frac{1}{2a^2} \left(\frac{\mathbf{d}_s{}^\dagger \mathbf{M}^{-1} \mathbf{d}_s}{(\mathbf{d}_s{}^\dagger \mathbf{M}^{-1} \mathbf{d}_s)(\mathbf{d}_f{}^\dagger \mathbf{M}^{-1} \mathbf{d}_f) - \Re(\mathbf{d}_s{}^\dagger \mathbf{M}^{-1} \mathbf{d}_f)^2} \right). \end{aligned}$$

III.2.3 Configurations

Nombre d'éléments d'émission et de réception Un avantage de la diversité dans les radars MIMO est qu'elle peut augmenter le nombre d'éléments effectif (virtuel) $N_e = MN$ de telle sorte qu'il soit plus grand que le nombre réel d'éléments $N_p = M + N$. Le maximum du nombre effectif d'éléments est atteint lorsque le nombre d'éléments d'émission est égal au nombre d'éléments de réception. Par ailleurs, la taille de l'ouverture effective est donnée par: $L_a = (N-1)d_t + (M-1)d_r$.

Selon [38], si $d_r = \frac{\lambda}{2}$, un espacement $d_t = Md_r$ permet de maximiser la taille d'ouverture tout en maintenant l'échantillonnage critique. Dans ce cas, nous aurons une taille d'ouverture de $L_a = [(N-1)M + (M-1)]\frac{\lambda}{2} = (MN-1)\frac{\lambda}{2}$. Cela correspond à un réseau virtuel avec des éléments MN rapprochés tout en utilisant seulement $N + M$ éléments.

Étant donné un nombre fixe d'éléments réels N_p, la taille de l'ouverture maximale possible en respectant l'échantillonnage critique est $L_a^{max} = (N_e^{max} - 1)\frac{\lambda}{2} \leq$

$(\frac{{N_p}^2}{4} - 1)\frac{\lambda}{2}$. Nous considérons quatre configurations avec $N_p = 10$ éléments réels, qui sont résumées dans le tableau III. Le cas classique (Config 1) est inclus pour comparaison. La Config 3 optimise à la fois N_e et L_a.

Config	N	M	N_e	L_a/λ
1	1	9	9	4
2	2	8	16	7.5
3	5	5	25	12
4	8	2	16	7.5

Table III: Les configurations pour la répartition d'éléments.

Espacement entre les éléments d'émission et de réception Après avoir fixé la répartition des éléments, nous avons encore d'autres paramètres de conception tels que les espacements d'éléments dans les sous-réseaux qui peuvent être exploités pour améliorer les performances de détection et d'estimation ainsi que pour réduire le rang de la CCM.

Avant de présenter les différentes configurations, nous commençons par la présentation de la règle généralisée de Brennan en MIMO qui peut être utilisée pour estimer le rang de la CCM dans le cas où les éléments ne sont pas nécessairement espacés à $\lambda/2$.

Theorem (La règle généralisée de Brennan en MIMO [J2])**.** *On définit α, β et γ comme suit:*

$$\begin{aligned} \alpha &= \frac{d_r}{\lambda/2}, \\ \beta &= \frac{2v\mathrm{PRI}}{\lambda/2}, \\ \gamma &= \frac{d_t}{\lambda/2}. \end{aligned}$$

Dans le cas où α, β et γ sont des nombres entiers, le rang de la CCM r est donné par le nombre des valeurs distinctes (entières) N_d tel que:

$$m\alpha + n\gamma + l\beta, \quad \forall \quad \begin{cases} m = 0, \ldots, M-1, \\ n = 0, \ldots, N-1, \\ l = 0, \ldots, L-1. \end{cases}$$

Si α, β and γ ne sont pas des nombres entiers, seulement N_d valeurs propres de la CCM sont importantes et le rang de la CCM est approximativement N_d [39].

Les configurations que nous allons étudier sont résumées dans le tableau IV, en prenant la Config 3 comme exemple. α et γ varient tout en gardant $\beta = 2$.

Un problème important du MIMO-STAP est l'augmentation du rang du fouillis. Cependant, lorsqu'il y a une ambiguïté dans le domaine Doppler (e.g. $\beta = 2$ ici), il peut être intéressant d'introduire de l'ambiguïté dans le domaine spatial afin de réduire la largeur des *clutter ridges* et le rang du fouillis (Config b et d). Les *clutter ridges* supplémentaires causés par l'ambiguïté spatiale se produisent au même endroit que ceux causés par l'ambiguïté Doppler ; il n'y a donc pas d'augmentation du nombre de *clutter ridge*. Le rang du fouillis réduit permet également de réduire le nombre de données secondaires nécessaires pour l'estimation de la CCM. Les algorithmes de rang réduit peuvent alors être mis en œuvre lorsque le rang du fouillis est faible.

Config	α	γ	rang de $\mathbf{M}_c$
a	1	1	39
b	2	2	24
c	1	αM=5	55
d	2	αM=10	40

Table IV: Les configurations pour l'espacement d'éléments, en utilisant la Config 3 comme exemple.

III.2.4 Résultats des Simulations

Les paramètres suivants sont considérés pour les simulations. Le radar se trouve à l'origine. La distance radar de la cible est de 70 km et $\theta = 0$. La fréquence centrale du radar est de 15 MHz ($\lambda = 20$ m) et le PRI est de 5 s. Le SNR est de 0 dB par élément et par impulsion. Le rapport fouillis sur bruit (CNR) est de 60 dB par élément et par impulsion. Le nombre d'impulsions est $L = 16$.

Pour étudier les performances de détection, nous considérons deux cibles à $\theta = 0$ et de fréquences Doppler normalisées $\omega_t = 0,01$ (T1) et 0,2 (T2). Cela nous permet de comparer les performances de détection des configurations différentes avec et sans fouillis. La P_{fa} est fixée à 10^{-3}.

Dans la figure XIII(a), nous montrons la P_d en fonction du SNR pour les Config 1-4. Les courbes pour les Config 2 et 4 coïncident. Comme la fréquence Doppler pour la cible 2 est loin de celle du fouillis, le SIR effectif est approximativement égal au SNRxMNL. Nous constatons que les configurations MIMO (Config 2-4) nous donnent de meilleures performances de détection que la configuration du STAP classique (Config 1) parce que ces configurations augmentent le MNL.

En raison de la perte en SIR (voir la figure XIII(b)), les courbes de détection de la cible 1 sont décalées vers le droite. Les configurations MIMO ont une perte en SIR plus petite grâce à un plus grand MNL qui augmente également la taille de l'ouverture virtuelle, qui à son tour réduit la largeur du *clutter ridge*. Ainsi pour la cible 1, les différences de performances sont encore plus évidentes.

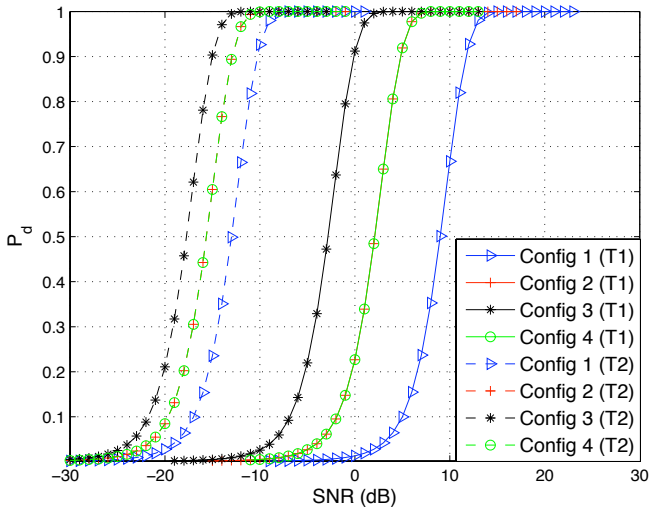

(a) P_d en fonction du SNR

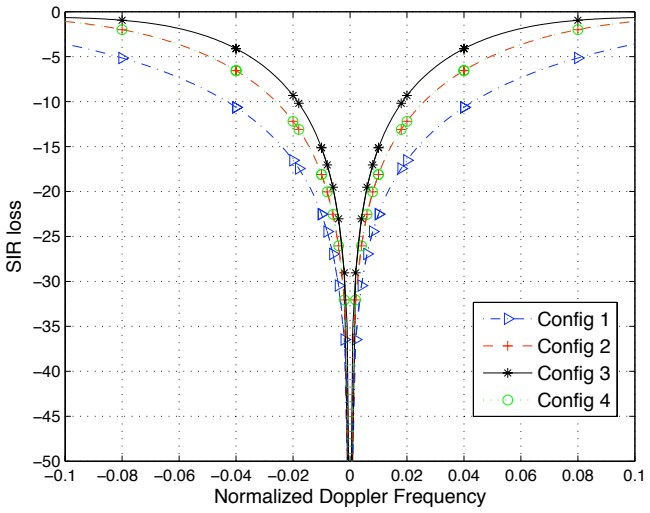

(b) Pertes en SIR en fonction de ω_t

Figure XIII: P_d en fonction du SNR et pertes en SIR en fonction de ω_t pour les Config 1-4. Dans tous les cas, $\theta = 0$ et on utilise la Config c.

La figure XIV montre les courbes correspondantes aux Config a-d. Ici, MNL est le même (Config 3). Ainsi, nous voyons dans la figure XIV(a) que les performances de détection de la cible 2 sont presque similaires pour toutes les configurations sauf pour la Config a qui perd 1 dB de SIR, même à $\omega_t = 0,2$. Pour la cible 1, les différences des performances de détection proviennent des différences de taille d'ouvertures virtuelles L_a en raison de l'espacement entre les éléments. Nous constatons que les configurations clairsemées (Config c et d) donnent de meilleures

performances que les configurations étroitement espacées (Config a et b). Selon la figure XIV(b), les pertes en SIR pour la cible 1 sont respectivement de 24,5 dB, 19 dB, 15 dB et 12,5 dB pour les Config a-d. Dans le cas où il y a l'ambiguïté Doppler $\beta > 1$ ($\beta = 2$ dans ce cas), elle peut être exploitée pour améliorer les performances de détection (comparer Config c avec Config d).

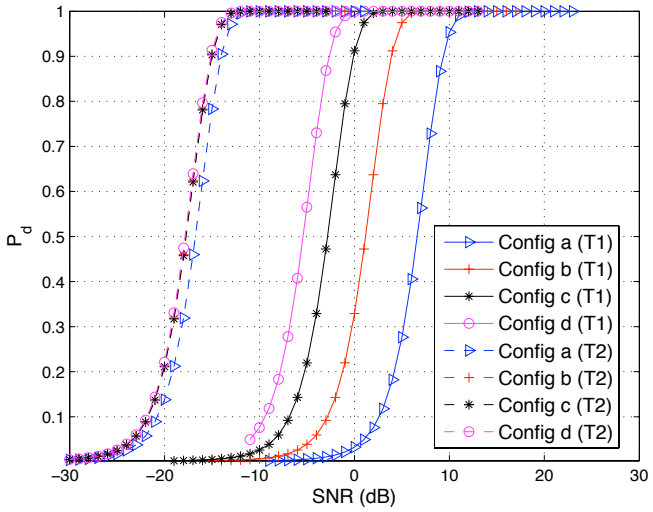

(a) P_d en fonction du SNR

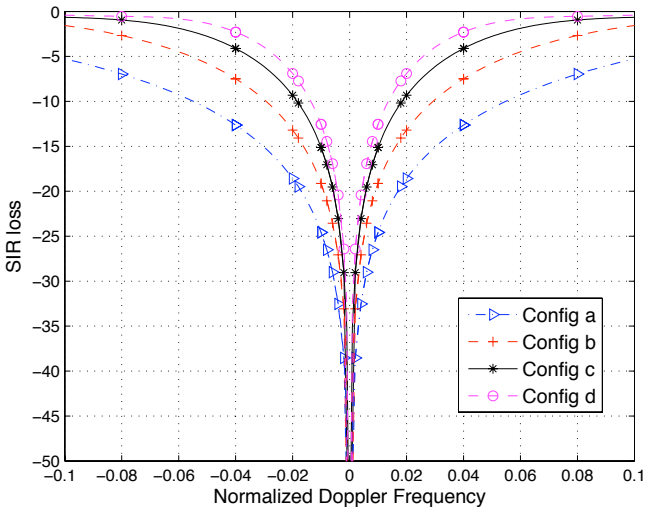

(b) Pertes en SIR en fonction de ω_t

Figure XIV: P_d en fonction du SNR et pertes en SIR en fonction de ω_t pour les Config a-d. Dans tous les cas, $\theta = 0$ et on utilise la Config 3.

Dans la figure XV, nous avons la P_d en fonction du SNR pour les Config 1-4 pour le cas adaptatif où $\mathbf{M}$ est estimée en utilisant $N_s = 500$ données secondaires.

L'estimation adaptative cause une dégradation des performances de détection pour toutes les configurations. Toutefois la dégradation est la plus importante pour la Config 3 parce que la dimension de $\mathbf{M}$ est la plus grande ce qui nécessite plus de données secondaires pour l'estimation de la matrice de covariance. C'est pourquoi sa performance de détection est la plus mauvaise pour la cible 2. Toutefois, le *clutter ridge* est plus étroit pour la Config 3 que pour la Config 1 et comparable à ceux des Config 2 et 4. Ainsi pour la cible 1, la Config 3 est toujours la meilleure en raison de N_e et L_a grands. Cependant, son avantage sur les Config 2 et 4 a diminué par rapport au cas où $\mathbf{M}$ est connue.

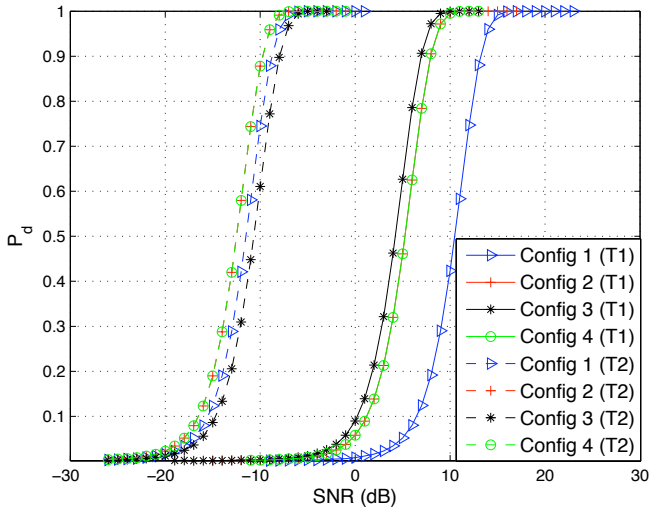

Figure XV: P_d en fonction du SNR pour les Config 1-4. Dans tous les cas, $\theta = 0$ et on utilise la Config c avec $N_s = 500$.

Les courbes correspondantes aux Config a-d (en utilisant la Config 3) sont montrées dans la figure XVI. L'estimation de la matrice de covariance cause une perte d'environ 7 dB pour toutes les configurations. La perte est la même parce que les configurations ont les mêmes MNL et N_s.

Maintenant nous regardons les performances d'estimation. Tout d'abord, nous comparons les Config 1-4 pour $\alpha = 1$, $\gamma = M$ et $\beta = 2$. Dans la figure XVII, les CRBs pour θ et f_t sont tracées en dB en fonction de la fréquence Doppler normalisée ω_t. Encore une fois, les courbes des Config 2 et 4 coïncident (la courbe de Config 2 n'est pas visible). En général, nous voyons que la CRB est faible loin du *clutter ridge* alors qu'elle devient beaucoup plus élevée au *clutter ridge* ($\omega_t = 0$) en raison de la présence du fouillis. La Config 3 a la CRB la plus basse en général et donne donc une meilleure précision de l'estimation et aussi une MDV beaucoup plus petite. Plus important encore, toutes les configurations MIMO (Config 2-4) améliorent la performance d'estimation par rapport à la configuration du STAP classique (Config 1).

Ensuite, nous comparons les Config a-d en utilisant la Config 3 ($N_{tx} = N_{rx} = 5$).

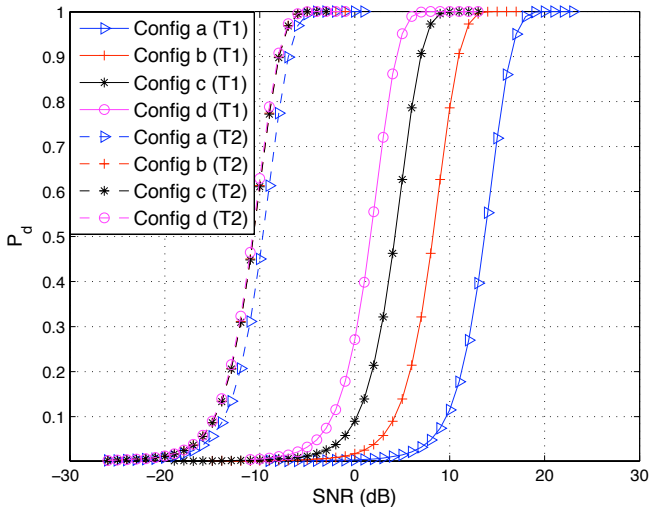

Figure XVI: P_d en fonction du SNR pour les Config a-d. Dans tous les cas, $\theta = 0$ et on utilise la Config 3 avec $N_s = 500$.

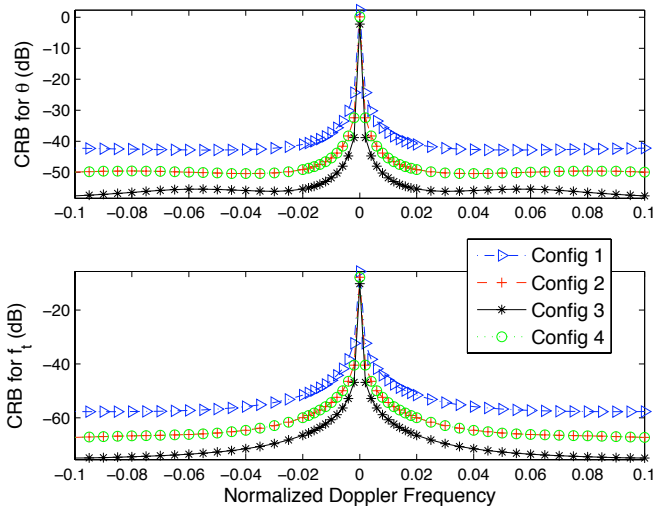

Figure XVII: Les CRBs en dB pour θ (en haut) et f_t (en bas) pour les Config 1-4. $\beta = 2$.

Notez qu'il n'y a pas de *clutter ridge* supplémentaire même si $\alpha > 1$ et $\gamma > 1$, car les paramètres sont choisis tels que les *clutter ridges* coïncident avec ceux dus à $\beta = 2$. Dans la figure XVIII, nous avons les CRBs en dB pour θ et f_t. Les améliorations des CRBs sont proportionnelles à l'augmentation de L_a. Avec L_a grand, les cellules de résolution angulaire sont plus petites, il y a donc plusieurs cellules de résolution entre le fouillis et la cible pour une même fréquence Doppler, ce qui rend la suppression du fouillis plus facile. Les améliorations des CRBs sont

plus importantes pour θ que pour f_t.

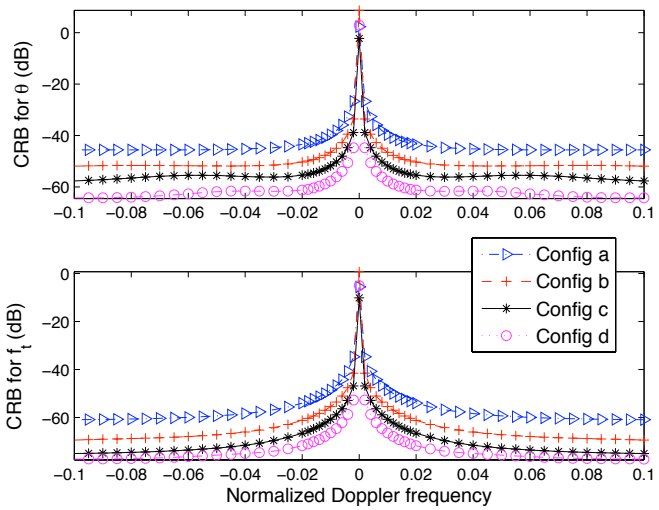

Figure XVIII: Les CRBs en dB pour θ (en haut) et f_t (en bas) pour les Config a-d. $\beta = 2$.

III.3 MISO-STAP

Nous supposons qu'il y a un seul sous-réseau de réception dont les éléments sont étroitement espacés et K_e sous-réseaux d'émission contenant un seul élément chacun. Ces derniers sont largement séparés afin de s'assurer que les retours sont non corrélés. Chaque paire de sous-réseau (d'émission et de réception) est dans une configuration bistatique et la RCS de la cible vue par chaque paire est aussi différente, donnée par $\boldsymbol{\alpha} = [a_1 e^{j\phi_1} \ \cdots \ a_{K_e} e^{j\phi_{K_e}}]^T$. Nous supposons que la cible reste dans la cellule sous test lors du CPI et que la RCS ne change pas d'une impulsion à une autre, bien qu'elle soit différente pour chaque sous-réseau.

Le signal reçu peut être exprimé comme suit:

$$\begin{aligned} \mathbf{y}_i &= a_i e^{j\phi_i} \mathbf{a}(\theta_r) \otimes \mathbf{v}(f_{d,i}) + \mathbf{c}_i + \mathbf{n}_i, \\ &= a_i e^{j\phi_i} \mathbf{p}_i + \mathbf{c}_i + \mathbf{n}_i, \end{aligned}$$

où $\mathbf{p}_i$ est le vecteur de pointage du i-ième sous-réseau constitué des vecteurs de pointage de réception et Doppler. Comme il n'y a qu'un seul sous-réseau de réception, le vecteur de réception est le même pour tous les sous-réseaux. Le vecteur Doppler varie de sous-réseau à sous-réseau car $f_{d,i}$ est différente pour chaque sous-réseau en raison de la position relative et la vitesse des sous-réseaux par rapport à la cible. Il n'y a qu'un seul élément dans chaque sous-réseau d'émission, donc il n'y a pas de vecteur d'émission. $\mathbf{c}_i$ et $\mathbf{n}_i$ sont respectivement les vecteurs de fouillis et de bruit.

Comme les interférences reçues par les différents sous-réseaux sont non corrélées et gaussiennes, le détecteur optimal est le MIMO OGD:

$$\ln \Lambda(\mathbf{y}) = \sum_{i=1}^{K_e} \frac{|\mathbf{p}_i^\dagger \mathbf{M}_i^{-1} \mathbf{y}_i|^2}{\mathbf{p}_i^\dagger \mathbf{M}_i^{-1} \mathbf{p}_i}.$$

III.3.1 Résultats des Simulations

Pour les simulations, nous considérons trois cas: $K_e = 1, 2, 5$. $K_e = 1$ est le cas classique et il est inclus pour comparaison. La position et la vitesse des sous-réseaux d'émission et de réception, ainsi que celles de la cible, sont présentées dans le tableau V. La configuration pour $K_e = 5$ est illustrée dans la figure XIX. Les autres paramètres sont les mêmes que précédemment.

x-position du récepteur (km)	0
y-position du récepteur (km)	0
x-vitesse du récepteur (m/s)	2
y-vitesse du récepteur (m/s)	0
x-position des émetteurs (km)	$70 \cdot \cos((-K_e:-1)\frac{\pi}{K_e+1})$
y-position des émetteurs (km)	$70 \cdot \sin((-K_e:-1)\frac{\pi}{K_e+1})$
x-vitesse des émetteurs (m/s)	2
y-vitesse des émetteurs (m/s)	0
x-position de la cible (km)	0
y-position de la cible (km)	70

Table V: La configuration pour les simulations MISO-STAP.

Afin de démontrer la robustesse du MISO-STAP aux fluctuations de la RCS et de la vitesse selon la direction, nous considérons deux cibles avec des vitesses absolues différentes: 0,1 m/s (T1) et 1,5 m/s (T2). Cependant, leurs directions varient aléatoirement selon une distribution uniforme entre 0 et 2π. Leurs RCS vues par chaque sous-réseau sont représentées par une distribution gaussienne: $\boldsymbol{\alpha} \sim \mathcal{CN}(\mathbf{0}, \sigma_t^2 \mathbf{I})$ et σ_t^2 est la puissance de la cible.

Dans la figure XX, nous avons les courbes P_d en fonction du SNR pour $K_e = 1, 2, 5$. $K_e = 1$ est le STAP classique. Pour les deux cibles, les performances de détection sont meilleures pour K_e grand malgré la nécessité d'un seuil élévé pour maintenir la même P_{fa}. Ceci est principalement dû à l'augmentation de N_e et aussi à la diversité spatiale. Avec celle-ci, les fluctuations de la RCS sont moyennées. Par ailleurs en raison de la diversité des directions LOS, il est impossible pour une cible mobile d'avoir une vitesse LOS nulle pour toutes les sous-réseaux simultanément. Ceci explique pourquoi les courbes de détection de $K_e = 2, 5$ convergent plus rapidement vers 1 que pour $K_e = 1$.

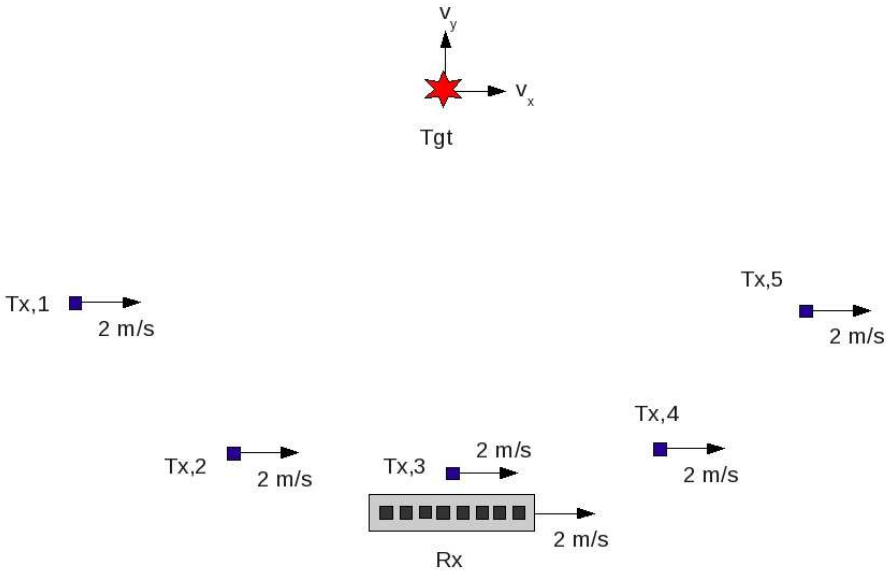

Figure XIX: La configuration des simulations MISO-STAP ($K_e = 5$).

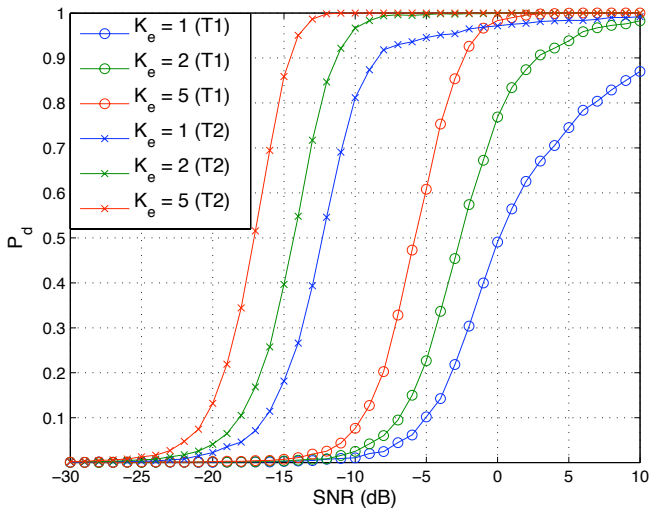

Figure XX: P_d en fonction du SNR pour le MISO-STAP avec $K_e = 1, 2, 5$.

Ensuite, nous comparons les performances de détection du MISO-STAP avec $K_e = 2$ et celles du SISO-STAP avec $N = 2$ (Fig. XXI). Les deux systèmes ont un sous-réseau de réception avec 8 éléments espacés de la moitié de la longueur d'onde et avec deux éléments d'émission. Dans le cas MISO, les éléments d'émission sont placés selon le tableau V alors que dans le cas SISO, les éléments d'émission sont espacés à $M \cdot \frac{\lambda}{2} = 4\lambda$. Les deux configurations ont le même nombre d'éléments

$N_p = 10$ et le même nombre effectif d'éléments $N_e = 16$.

Comme prévu, les performances de détection sont meilleures pour le cas SISO à faible SNR en raison de la meilleure résolution. Toutefois, la configuration SISO n'est pas robuste aux fluctuations de la RCS et aux changements de direction du mouvement de la cible ce qui explique la lente convergence de la P_d vers 1. Ainsi, le cas MISO donne de meilleurs résultats pour des P_d élévées.

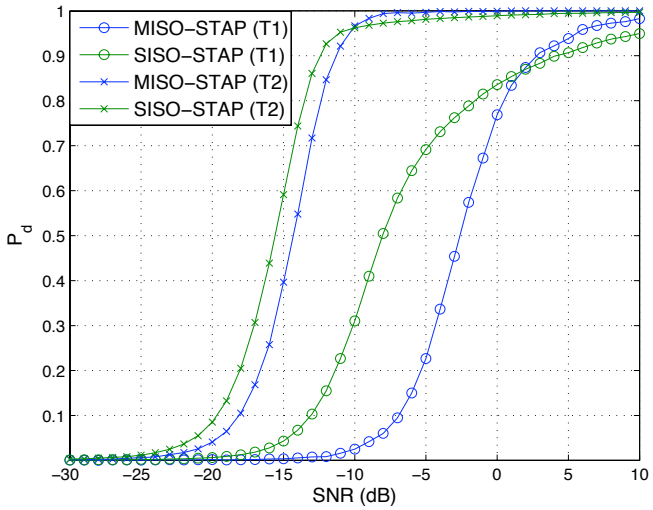

Figure XXI: P_d en fonction du SNR pour le MISO-STAP ($K_e = 2$) et pour SISO-STAP ($N = 2$).

IV Conclusion

IV.1 Détecteur Gaussien

Un nouveau détecteur MIMO gaussien qui prend en considération la corrélation possible entre les sous-réseaux a été développé. Il devient le classique MIMO OGD lorsque les sous-réseaux ne sont pas corrélés (la matrice de covariance est alors diagonale par bloc). Les propriétés statistiques de ce nouveau détecteur ne varient pas sous l'hypothèse H_0 même si les sous-réseaux sont corrélés. Ce nouveau détecteur est ainsi robuste aux paramètres des interférences. La version adaptative de ce détecteur basée sur le test de Kelly est également calculée.

Les propriétés du détecteur sont étudiées pour différents paramètres, par exemple le nombre effectif de sous-réseaux K_e et le nombre effectif d'éléments N_e. Avoir le même nombre d'éléments d'émission et de réception maximise N_e, indépendamment du nombre de sous-réseaux d'émission et de réception. Il est important de maximiser N_e, car il affecte le gain SIR. Avoir un nombre K_e plus grand augmente la robustesse aux fluctuations de la RCS, mais il augmente également le seuil de

détection requis pour maintenir la même P_{fa}, causant une perte en SIR. Des simulations sont effectuées pour comparer les performances de détection pour différents K_e et N_e.

Pour la version adaptative, nous avons discuté du facteur de perte l_f qui est dû à l'estimation de la matrice de covariance et du nombre de données secondaires N_s nécessaire. Selon la distribution statistique de l_f, on peut constater que pour un N_s fixe, il est préférable de choisir un nombre N_e plus petit et un nombre K_e plus grand pour réduire les pertes . Pour limiter cette perte à 3 dB, nous avons besoin de $N_s > 2N_e - 2K_e - 1$ en assurant que $N_s \geq N_e$ de telle sorte que la SCM soit de rang plein. Des simulations sont ensuite effectuées pour comparer les performances de détection pour différents K_e ainsi que pour différents N_s.

IV.2 Détecteur Non Gaussien

Le détecteur GLRT-LQ dédié à la détection sous des interférences non gaussienes a été étendu au cas MIMO. Les performances théoriques du MIMO GLRT-LQ ont été calculées et validées avec des simulations. Les performances de détection sont ensuite analysées par des simulations. Par rapport au détecteur classique MIMO OGD, le nouveau détecteur améliore significativement les performances de détection sous des interférences non gaussiennes, en particulier quand les interférences sont très impulsives. Il a une légère perte de performance lorsque les interférences sont gaussiennes. Cela est attendu puisque le MIMO OGD est le détecteur optimal sous des interférences gaussiennes. Toutefois, la robustesse du détecteur MIMO GLRT-LQ sous différentes interférences non gaussiennes (K-distribuées, Weibull-texturées) compense cette légère perte sous des interférences gaussiennes. Nous avons également étudié la dégradation des performances de détection en fonction des fluctuations de la RCS.

Ensuite, la version adaptative de ce détecteur est considérée. Le FPE est utilisé pour estimer la matrice de covariance puisque la SCM n'est plus ML sous des interférences non gaussiennes. Les propriétés texture-CFAR et matrice-CFAR du MIMO GLRT-LQ adaptatif sont montrées théoriquement pour le cas où il n'y a qu'un seul sous-réseau. En raison de la complexité des calculs, le cas où il y a plus d'un sous-réseau est étudié de façon empirique avec l'aide des simulations.

Les performances de détection du MIMO GLRT-LQ adaptatif utilisant le FPE sont ensuite comparées au MIMO AMF utilisant la SCM et le test de Kelly MIMO. Comme prévu, le nouveau détecteur possède de bien meilleures performances sous des interférences non gaussiennes, en particulier lorsque les interférences sont très impulsives. En raison de la ressemblance du test de Kelly MIMO et du MIMO GLRT-LQ adaptatif surtout quand il y a peu de données secondaires, le test de Kelly MIMO subit moins de perte de performances que le MIMO AMF sous des interférences non gaussiennes. En outre, le MIMO GLRT-LQ adaptatif a des performances comparables quand les interférences sont gaussiennes.

La principale conclusion est qu'il est toujours préférable d'utiliser le MIMO GLRT-LQ adaptatif avec le FPE, quelle que soit la distribution des interférences,

en raison de la robustesse de ces outils par rapport à la matrice de covariance et à la texture. Même dans le cas où l'interférence est gaussienne pour tous les sous-réseaux, la puissance de l'interférence pour chaque sous-réseau est probablement différente, c'est-à-dire les textures sont différentes mais déterministes.

IV.3 SISO-STAP

Dans la première partie du travail, nous avons étudié les performances de détection et d'estimation du MIMO-STAP monostatique et cohérent (SISO-STAP) en termes de probabilités de détection pour une P_{fa} fixe, ainsi que la CRB qui donne la borne inférieure des variances des estimateurs. Nous considérons différentes configurations. La répartition des éléments entre les sous-réseaux d'émission et de réception varie (Config 1-4) tout en gardant un nombre d'éléments réels fixe. Il se trouve que lorsque les nombres d'éléments d'émission et de réception sont égaux, le nombre effectif d'éléments N_e et la taille de l'ouverture effective (pour l'échantillonnage critique) sont maximisés. Les espacements entre les éléments d'émission et de réception sont ensuite analysés (Config a-d) pour augmenter encore plus la taille de l'ouverture effective. La règle de Brennan en MIMO est également généralisée à des espacements entre les éléments qui ne sont pas nécessairement égaux à la moitié de longueur d'onde.

Pour la partie sur la détection, un N_e plus grand augmente la P_d pour une P_{fa} fixe lorsque la cible est loin du fouillis tel que le SIR final est presque proportionnel à N_eL . D'autre part, lorsque la cible est proche du fouillis, la maximisation de L_a est plus importante car elle permet de réduire la perte en SIR et donc la MDV pour des P_d et P_{fa} données. Les configurations clairsemées (Config b et d) peuvent augmenter L_a et donc réduire la MDV. Il n'y aura pas des ambiguïtés supplémentaires si les ambiguïtés spatiales sont choisies pour coïncider avec les ambiguïtés Doppler.

Toutefois, lorsque N_e est grand, un plus grand nombre de données secondaires est nécessaire pour estimer $\mathbf{M}$, ce qui n'est pas toujours possible d'avoir. Dans ce cas, il est préférable de choisir une configuration avec un N_e plus petit afin de limiter la perte due à l'estimation. En outre, en utilisant la règle généralisée de Brennan en MIMO, nous avons également constaté que les configurations clairsemées (Config b et d) peuvent aussi réduire le rang de la CCM. Le rang réduit peut être exploité pour réduire le nombre de données secondaires requis en utilisant des algorithmes de rang réduit.

Pour la partie estimation, les CRBs et MDV sont plus faibles si nous n'estimons pas la RCS de la cible simultanément (pour l'identification et la classification des cibles). En outre, l'augmentation de L_a améliore la précision en général, surtout loin du fouillis et permet également de réduire la MDV. Les bornes peuvent être encore abaissées sans ambiguïtés supplémentaires en augmentant les espacement d'éléments de certaines façons.

IV.4 MISO-STAP

Dans la deuxième partie du travail, une étude préliminaire est effectuée sur l'application des configurations MISO au STAP (MISO-STAP). La configuration utilisée est constitué d'un seul sous-réseau de réception et de plusieurs éléments d'émission. Cette configuration est intéressante car elle est réalisable facilement en ajoutant des éléments d'émission aux systèmes STAP existants.

En raison de la diversité angulaire du MISO-STAP, le radar est robuste aux fluctuations de la RCS et à la variation de la vitesse de la cible par rapport à l'angle d'incidence du signal émis et reçu. Les performances du MISO-STAP dépendent beaucoup de la configuration, non seulement sur le nombre de sous-réseaux et d'éléments, mais aussi sur la position et la vitesse de chaque sous-réseau. Même avec le même nombre de sous-réseaux et d'éléments, nous pouvons changer la pente du *clutter ridge* en changeant la position et la vitesse de chaque sous-réseau par rapport à la cible.

Enfin, une comparaison entre le MISO-STAP et le SISO-STAP est faite en termes de probabilités de détection et en gardant les mêmes N_p et N_e. Le SISO-STAP est meilleur que le MISO-STAP en général dû à une meilleure résolution, mais sa probabilité de détection converge lentement vers 1 parce qu'il n'est pas robuste aux fluctuations de la RCS et aux variations de direction du mouvement de la cible. Ainsi, pour des P_d élévées, le MISO-STAP est meilleur que le SISO-STAP.

V Perspectives

Le traitement du signal pour les radars MIMO est un sujet relativement nouveau pour lequel il y a encore beaucoup de travail à faire. Quelques suites possibles à cette thèse sont proposées ci-dessous.

Le modèle du signal peut être davantage développé en incluant les formes d'ondes et la distance radar, ainsi qu'un modèle de cible fluctuante. Par ailleurs en raison de la nature multidimensionnelle du MIMO, il pourrait être plus efficace d'utiliser des tenseurs pour la représentation des signaux et pour les différents traitements utilisés. Dans une configuration avec plusieurs sous-réseaux largement séparés, la RCS de la cible perçue par chaque sous-réseau est différente et dépend de l'angle d'incidence du signal émis et reçu; il est alors possible de caractériser une cible par son diagramme RCS permettant ensuite la classification.

Un algorithme en deux étapes peut être utilisé pour des tests d'hypothèse utilisant les meilleurs sous-réseaux en termes de SIR. Une pondération adaptative peut aussi être introduite pour pénaliser les sous-réseaux avec un SIR faible. De même, seulement des sous-réseaux avec un SIR élevé doivent être utilisés pour l'estimation.

Le rang réduit des configurations clairsemées (Config b et d) peut être exploité en utilisant des méthodes de rang faible pour estimer la matrice de covariance. De telles méthodes ont déjà été étudiées en détail pour le STAP classique et il serait intéressant d'étendre celles-ci au MIMO. D'autres méthodes classiques telle que le diagonal loading ou encore les méthodes auto-régressives peuvent aussi être

considérées pour surmonter le manque de données secondaires.

Pour l'étude du CRB, il faudrait inclure le seuil SIR qui définit le seuil pour lequel la performance de l'estimateur approche la CRB. Par ailleurs, d'autres bornes qui sont plus précises pourraient être considérées au lieu de la CRB. Enfin, des mesures expérimentales valideraient les résultats théoriques et de simulation obtenus dans cette thèse.

Introduction

Multiple-Input Multiple-Output (MIMO) is a technique used in communications that has recently been adopted for radar applications [1]. MIMO communication systems overcome the problems caused by fading by transmitting different streams of information from several decorrelated transmitters. The different signals undergo independent fading as the transmitters are decorrelated. The receiver thus has an average (over all the information streams) Signal-to-Noise Ratio (SNR) which is more or less constant; whereas in conventional systems which transmit all their energy over a single channel, the received SNR varies considerably.

In the context of radar, a MIMO radar is one where the transmit elements send different (orthogonal or partially correlated) waveforms which can be separated at the receive end. This provides waveform diversity. Moreover, the transmit and receive elements can be sufficiently separated so as to provide spatial diversity. This reduces the fluctuations of the target Radar Cross Section (RCS) due to the different target aspects seen by each pair of transmit-receive elements [2].

Most recent works in MIMO radars consider two main configurations, denoted as *statistical* and *coherent* MIMO radars, as illustrated in Fig. 1. Statistical or distributed MIMO radars [3] have a configuration where all antenna elements are widely separated and give a diversified view of the target, thus improving stability in the detection of extended targets [4]. On the other hand, for coherent or co-located MIMO radars [5], all the elements are closely spaced in a subarray such that direction-finding is possible. The diversity comes from the different waveforms transmitted by each transmit element. In this case, sparse arrangement is possible within the subarray, hence improving resolutions. These configurations are further explained in Chapter 1 which contains an overview of recent works on MIMO radars.

In Chapter 2, we focus on the detection performance of MIMO radars while in Chapter 3, we consider the use of MIMO techniques for an important radar application: Space-Time Adaptive Processing (STAP). The main motivations for this thesis are given below.

Motivation for Chapter 2

MIMO procedures for radar have been widely studied for the case of additive Gaussian interferences. In [6, 4, 3], the authors considered the detection performance for widely separated antennas while in [5, 7] the authors considered co-located antennas. The combined case of having widely separated antenna subarrays which contain colocated antenna elements is considered in [8]. This is the case that is used in Chapter 2.

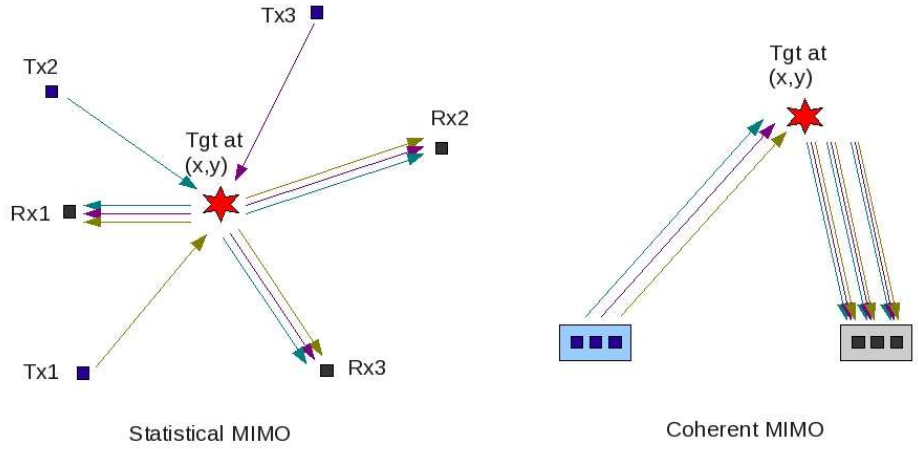

Figure 1: Illustration of the statistical and coherent MIMO radar concepts.

According to [4], the subarrays have to be sufficiently spaced in order to decorrelate the signal returns in each subarray. It might not be possible to respect this condition, especially when we consider MIMO-STAP where the transmit and/or receive subarrays are moving. Moreover, perfectly orthogonal waveforms do not exist [9], especially in the presence of Doppler frequency.

In the first part of Chapter 2, we assume that insufficient spacing between subarrays and imperfect orthogonality of the transmitted waveforms introduce correlation between the subarrays. However, the interference is still Gaussian. The aim is to derive a robust detector that is able to obtain optimum results in the Maximum Likelihood (ML) sense whether the subarrays are uncorrelated or not. As the performance of MIMO radars is very dependent on configuration and scenario, we consider a signal model which is very general so that we are able to study the various parameters for configuration design to maximize the detection results.

In the second part of Chapter 2, we no longer assume that the interference is Gaussian. There are two main reasons for considering non-Gaussian models. Firstly, as mentioned earlier, one advantage of a MIMO imaging radar is improved resolution. Usually, in each resolution cell, there is a large number of scatterers. According to the Central Limit Theorem (CLT), the interference power in each cell is almost constant and the interference is considered to follow a Gaussian distribution. However, as the resolution cell becomes smaller, it contains fewer scatterers and the CLT no longer applies. Therefore, non-Gaussian models which take into account the variations in interference power have to be used. Moreover, as the resolution cell becomes smaller, it is more likely for the illuminated area to be non-homogeneous.

Secondly, for configurations with widely separated subarrays, the target returns received by each subarray are different due to different aspect angles, thus reducing target RCS fluctuations. Similarly, the interference returns vary from subarray to

subarray. Hence, it is important to use non-Gaussian models which better reflect the interference power fluctuations. Indeed, experimental radar interference measurements [10, 11, 12, 13] have been found to fit non-Gaussian statistical models such as the well-known Spherically Invariant Random Vector (SIRV) model [14, 15, 16] which has been widely studied, particularly in terms of detection [17, 18, 19].

Motivation for Chapter 3

STAP is a technique [27, 28, 29] used in airborne phased-array radar to detect slow-moving targets embedded in an interference background such as jamming or strong ground clutter. While conventional radars are capable of detecting targets both in the time domain related to the target range and in the frequency domain related to the target velocity, STAP uses an additional domain (space) related to the target angular localization. The consequence is a two-dimensional adaptive filtering technique which uses the temporal and spatial dimensions jointly to suppress interference, hence enabling these targets to be detected. This is illustrated in Fig. 2 (source: [30]).

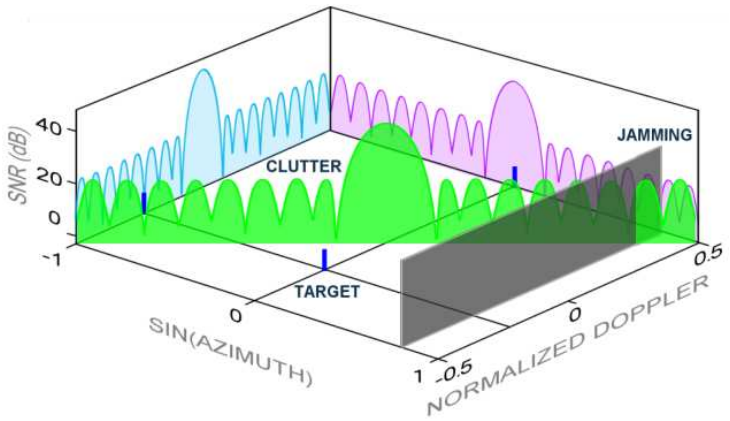

Figure 2: Illustration of the STAP concept: joint processing of temporal and spatial dimension enables the detection of slow-moving targets.

The main use of STAP is Ground Moving Target Indication (GMTI). The ground targets of interest are usually slow moving and are often buried in clutter returns. The clutter arising from airborne radar systems has angle-Doppler dependence, enabling it to be differentiated from moving targets, thus even slow moving targets can be detected. With the use of MIMO configurations, the performance of the radar can be further enhanced, such as the angle-estimation performance and Minimum Detectable Velocity (MDV).

In Chapter 3, we consider two different configurations: Single-Input Single-Output (SISO) where there is no spatial diversity and Multiple-Input Single-Output (MISO) where there is spatial diversity. There is waveform diversity in both cases. The SISO configuration, commonly known as coherent MIMO in the literature,

is well-suited to the STAP application. With only waveform diversity, the SISO configuration is able to increase the effective number of elements N_e which in turn increases the Signal-to-Interference Ratio (SIR) gain, resulting in improved detection and estimation. More importantly, it increases the virtual aperture size which confines the clutter to within a smaller angular resolution cell, hence facilitating clutter suppression and lowering MDV.

Much work has been done on SISO-STAP [31, 32, 33]. However, these works do not treat the problem of configuration design to maximize detection and estimation performance. In Section 3.1, we study different SISO configurations in terms of the detection and estimation performance. We consider two different situations. Firstly, we vary the number of transmit and receive elements given a fixed number of elements. Secondly, we change the spacing between the transmit and receive elements given a fixed radar velocity. In fact, other than improvement in detection and estimation performance, we will see in Section 3.1.4 that configuration design can also be applied to reduce clutter rank, hence facilitating the estimation of the interference covariance matrix, especially when there are few secondary data available.

Note that the Coherent Processing Interval (CPI) is assumed to be constant here. However, SISO configurations have the potential to improve detection and estimation performance further as longer CPI can be applied since beam scanning is not required. Longer CPI improves the Doppler resolution which increases the separation between the clutter and target in the spatial-Doppler domain, hence making clutter suppression easier.

Radar systems can detect only targets with non-zero Line-Of-Sight (LOS) or radial velocity. The LOS direction is defined as the direction perpendicular to the isorange contours while the Cross LOS (XLOS) direction is tangential to the isorange contours, as illustrated in Fig 3 for both monostatic and bistatic radars. Note that for bistatic radars, as the transmit and receive subarrays have different LOS and XLOS velocities, we consider the equivalent monostatic LOS and XLOS velocities. If a target is moving in the XLOS direction, its range does not change and it has zero Doppler frequency. Thus, it appears as part of the clutter to the radar.

Having spatial diversity is useful as a moving target may have zero LOS speed with respect to one radar system but it is impossible for it to have zero LOS speed for all radar systems simultaneously. Hence, having widely separated radar systems reduces the possibility of the target being buried in stationary ground clutter. This advantage is sometimes called the *geometry* gain in the literature. Moreover, having multiple radar systems enables us to obtain full information on the target velocity such that the velocity is determined uniquely.

Furthermore and as it will be discussed in Chapter 2, having spatial diversity increases the robustness against fluctuating targets as different aspects of the target are seen by the subarrays and it is unlikely that all subarrays see low target RCS at the same time. This gain is commonly called *diversity* gain in the literature. However, such configurations inherently mean bistatic configurations for each sub-

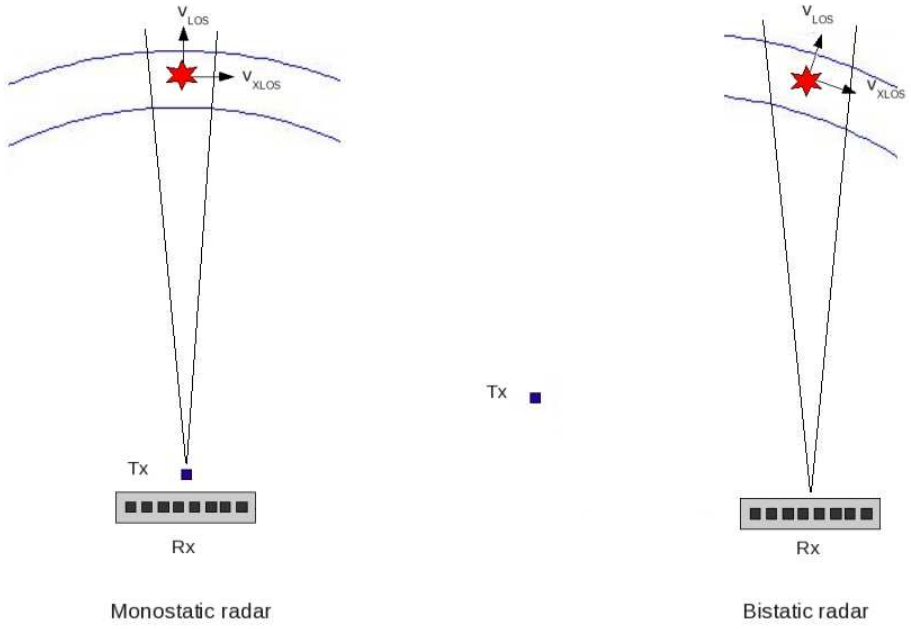

Figure 3: Illustration of LOS and XLOS velocity in a monostatic and a bistatic radar.

array. Bistatic configurations are not in general favorable for STAP applications due to the increased clutter rank. This increase in clutter rank can be seen as a spread of clutter power over more Degrees-of-Freedom (DoF) than for the monostatic case. Moreover, the clutter properties become range dependent, i.e. the clutter is non-stationary.

One possible way to overcome this problem, as proposed in [34] is to use the multistatic configuration, i.e. each subarray consists of a different transmit and receive subarray. This means that there is no increase in the effective numbers of subarrays and elements, hence it is not considered a MIMO configuration. Each subarray is in a monostatic configuration (co-located transmit and receive) and it receives only its own transmitted signal. Note that the waveforms still need to be sufficiently separated to avoid interference.

In [35], the authors used the Single-Input Multiple-Output (SIMO) configuration and there is only one transmit element such that there is no waveform diversity, only spatial diversity. They propose the use of classical bistatic STAP techniques [36] to compensate for clutter non-stationarity. In Section 3.2, we assume also that such techniques are applied to each transmit-receive pair such that the clutter can be considered stationary. However, we will adopt a different configuration: MISO. We consider that there is only one receive subarray with closely spaced elements such that beamforming can be done. Spatial diversity comes from the transmit elements which are all widely separated. This configuration reduces the number

of elements required to achieve the same N_e as compared to [35], yet it does not require many different orthogonal waveforms. Moreover, it is easy to achieve this configuration using existing hardware, especially the receive part. Additional transmit elements can be mounted on small light-weight platforms like Unmanned Aerial Vehicle (UAV) since no beamforming is required as there is only one element per transmit subarray.

Chapter 1

Overview of MIMO Radars

In this chapter, a short overview of recent developments in MIMO radars is given. We begin by introducing the concept of MIMO in terms of communications, before defining MIMO radars in Section 1.1. Most works on MIMO radars can be broadly divided into two categories: statistical MIMO and coherent MIMO. These two types of MIMO radars are described and distinguished from multistatic radars and phased-array radars. We define also a third category: hybrid MIMO for configurations which are a hybrid between the first two types of MIMO radars. The advantages and disadvantages of MIMO radars are described briefly. MIMO communications and MIMO radars are also compared.

Recent works on statistical MIMO, coherent MIMO and hybrid MIMO are then described further in Section 1.2, Section 1.3 and Section 1.4, respectively. Note that only the most representative works are included but this list is by no means exhaustive. Note also that imaging using MIMO techniques is not included in this chapter.

1.1 Overview

In communications, MIMO is the use of multiple antennas at both the transmit and receive ends to increase data throughput and link range without additional bandwidth or transmit power (see Fig. 1.1). On one hand, the MIMO structure adds as a spatial multiplexer, thus allowing much higher transmission rates than that of a SISO channel, resulting in higher spectral efficiency. Basically, the spatial dimension is used to complement the bandwidth requirement, enabling narrowband MIMO communication systems to perform like wideband systems without MIMO. On the other hand, the MIMO structure also offers multiple propagation paths, hence overcoming fading effects and increasing link reliability.

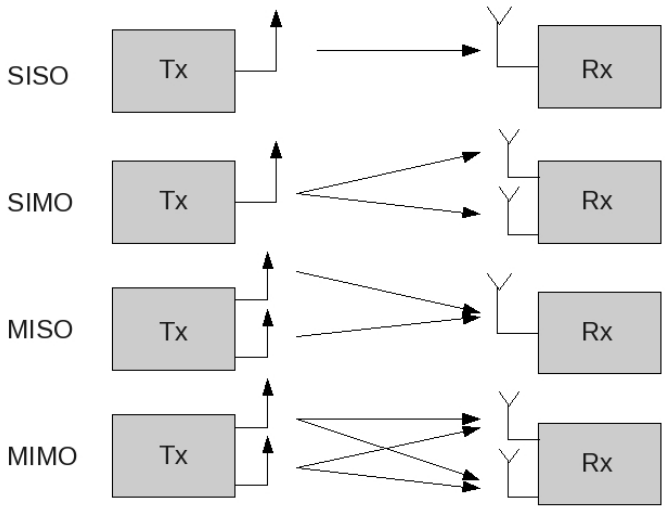

Figure 1.1: Illustration of the MIMO concept.

Recently, the radar community is starting to look into the use of MIMO techniques in radar applications [40, 5, 3, 1]. A MIMO radar can be broadly defined as a radar system employing multiple transmit waveforms and having the ability to jointly process signals received at multiple receive antennas [3]. These waveforms can be orthogonal, resulting in omnidirectional transmission; or correlated, resulting in diverse beam patterns depending on the design objectives.

In terms of configurations, the antennas can be widely-separated or co-located. One important difference between the two configurations is the signal model: widely-separated antennas take advantage of the spatial properties of extended targets while the target is modeled as a point with no spatial property for co-located antennas. In other words, widely-separated antennas see different independent aspects of the target while the co-located antennas see the same target RCS up to some known relative delay due to the geometries of the antennas.

1.1.1 Statistical MIMO

Each configuration and model has its advantages and challenges. The *statistical MIMO* configuration, a term commonly used to describe the widely-separated configuration, focuses on spatial diversity. With spatial diversity, the antennas see different aspects of the same target. This reduces the fluctuations in detection and estimation performance that depend on the RCS of the target. This is often called the *diversity gain* in the literature. Another advantage of spatial diversity is that we are able to do target characterization and classification with sufficient number of antennas looking at different aspects of a complex target. This can also be considered as anti-stealth technique as stealth is usually effective only in the monostatic backscatter configuration.

In the case of Moving Target Indication (MTI), having widely-separated antennas reduces the possibility of the target being buried in stationary ground clutter. This is because even if a moving target has zero LOS speed with respect to one antenna, it cannot have zero LOS speed for all antennas simultaneously. This advantage is sometimes called the *geometry* gain in the literature. Moreover, multiple widely-separated antennas enable us to determine the velocity uniquely. However, in the case of GMTI applications where ground clutter is the main interference, additional pre-processing is needed to compensate for non-stationary clutter arising from bistatic configurations.

Due to the decorrelation of the target RCS, non-coherent processing is usually done for statistical MIMO radars. This means that only time synchronization is needed between antennas and this is generally done in practice through ranging. In the case of a simple target where the target RCS remains correlated, coherent processing has been proposed at both the transmit and receive antennas to achieve high resolution. However, this means that additional phase synchronization is required and this is much harder to realize due to the wide separation. Moreover, there is the need to deal with ambiguities stemming from the large separations between antennas.

One closely related radar system is the multistatic radar [34] which also consists of widely-separated antennas. For multistatic radars, each receive antenna receives only the signals transmitted by the corresponding transmit antenna. To minimize the communication bandwidth required to share raw data among sensors, decentralized methods are often employed. Each sensor implements its own detection test with local thresholds which are coupled between sensors.

Conversely, the joint processing of *all* transmit and receive antennas is done for statistical MIMO radars such that the effective number of antennas is more than the physical number of transmit and receive antennas. There is a higher degree of cooperation between the antennas due to the centralized detection strategy of the statistical MIMO radar. This difference is illustrated in Fig. 1.2.

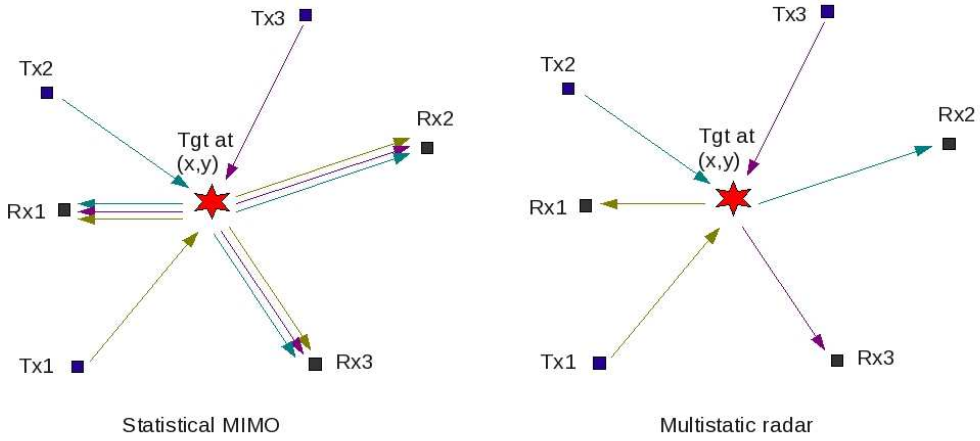

Figure 1.2: Comparison between statistical MIMO radars and multistatic radars.

1.1.2 Coherent MIMO

The *coherent MIMO* configuration, the corresponding term to describe the co-located configuration, concentrates on improving angular resolution. As the target RCS at each receive element is correlated, coherent processing is possible. With sparse element arrangement, a virtual array of $N_{rx}N_{tx}$ elements can be obtained using only $N_{rx} + N_{tx}$ elements where N_{rx} and N_{tx} are the number of receive and transmit elements, respectively. This gain in virtual aperture size increases angular resolution. Parameter identifiability is also improved by up to a factor of N_{tx} as compared to the case where only one single waveform is transmitted [41]. This means that more targets can be detected and identified.

Phased-arrays with multiple transmit elements have the same structure as the coherent MIMO radars. However, as the same waveform is transmitted at each transmit element, phased-arrays are able to cohere and steer the transmitted energy to form a focused beam. Coherent MIMO radars transmit orthogonal waveforms at each transmit element, hence illuminating the scene of interest uniformly. While this means that no beam scanning is necessary, transmit processing gain from a focused beam is lost. This difference is illustrated in Fig. 1.3. Note however that more and more MIMO radar researchers are now considering beam pattern design to trade off between coverage and transmit processing gain. This will be described in more details in Section 1.3.

1.1.3 Hybrid MIMO

Most recent works concentrate on the advantages of either the statistical or coherent MIMO configurations. There are few papers which propose hybrid configurations that encompass both statistical MIMO and coherent MIMO. Essentially in these

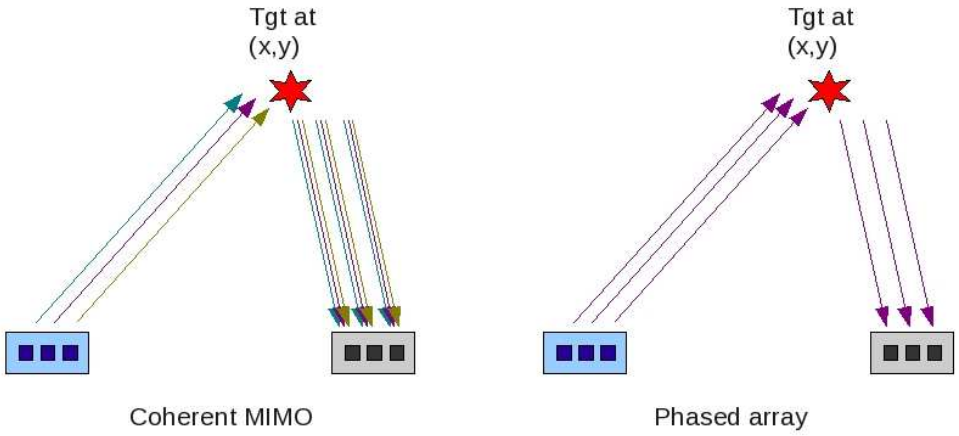

Figure 1.3: Comparison between coherent MIMO radars and phased-arrays.

hybrid configurations, there are multiple elements in some or all subarrays to enable beamforming capability. Note that some papers consider other techniques like transmit subaperturing to create a hybrid configuration. These will be described further in Section 1.4. While the hybrid configurations enjoy the advantages of both types of MIMO radars, they have the main disadvantage of increased complexity. The hybrid MIMO configuration is illustrated in Fig 1.4. Note that the bold arrows indicate that multiple waveforms are transmitted from each transmit subarray.

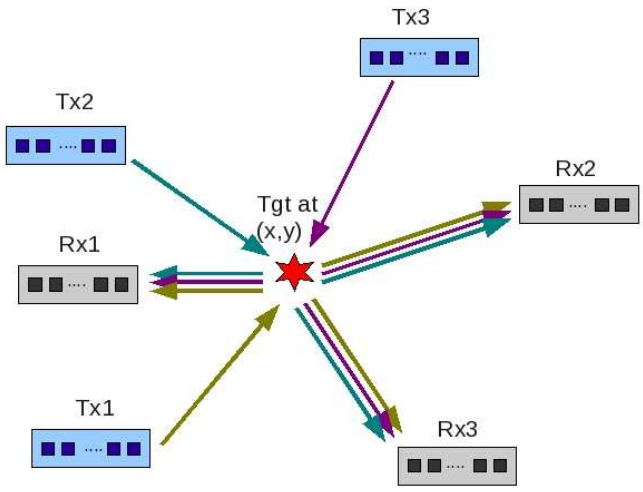

Figure 1.4: An illustration of a hybrid MIMO system.

1.1.4 Notation and Definition

Note that in MIMO communications, MI- and -MO refer to the channel carrying the signals and not the device itself. In the radar problem, the target serves as the "channel". Hence we consider MI- or -MO only when the configuration results in a different target RCS. This arises when the receive/transmit elements/subarrays are widely-separated. With this definition, statistical MIMO remains classified as MIMO while coherent MIMO will be classified under SISO together with phased-arrays. This will be further explained in Section 2.2. This definition has also been adopted in [2, 42]. Note that some authors define SIMO as the phased-array radar.

1.1.5 Advantages and Disadvantages of MIMO

There are many reasons why MIMO configurations are interesting:

- Improvement in performance in detection and estimation due to increased aperture size;
- More robust performance as well as anti-stealth properties due to spatial diversity;
- Overcome space constraints by spreading antennas;
- Target characterization possible;
- Increased number of resolvable targets.

Some of these advantages will be explained further in the following sections.

While MIMO techniques have captured the attention of many researchers and research institutes, there are also critics about the actual usefulness of MIMO and even on the quality of papers on MIMO radars. The most critical paper is the one by Daum and Huang from Raytheon [9]. Firstly, they pointed out that MIMO radars suffer a substantial loss in SIR compared to phased-arrays, owing to the loss of transmit processing gain. However, this loss can be compensated by longer on-target integration time as MIMO radars transmit omnidirectional beam and do not need to do scanning. Note also that the transmit processing gain is lost only if beamforming is done on receive, i.e. it is done after incoherent processing. Therefore there is much on-going research on transmit beamforming and waveform design to mitigate this problem.

Secondly, they pointed out that the maximum useful area of the range-Doppler space is reduced by a factor of N_{tx} for a MIMO radar employing N_{tx} orthogonal waveforms. For this reason, MIMO techniques are more suitable for High Frequency (HF) radars which have more useful Doppler space as compared to microwave radars. Work has been done to apply MIMO techniques and configurations to Over-The-Horizon Radars (OTHR) [43, 44] and High Frequency Surface Wave Radars (HFSWR) [45].

Another main problem is the fact that perfectly orthogonal waveforms do not exist. Even modulations induced by complex target reflections (Doppler shifts) can cause a degradation in the orthogonality of waveforms. While this is a relatively strong assumption (indeed this assumption is made in some sections of this thesis), there is on-going research on quasi-orthogonal waveforms. Moreover, current research assuming orthogonal waveforms can be extended to include the effects of correlated waveforms by adding the transmitted waveforms in the signal model.

1.1.6 MIMO communications Vs MIMO radars

Before going into details of recent works on MIMO radars, it is interesting to compare MIMO communications and MIMO radars. According to [9], the relevant differences can be summarized as shown in Table 1.1. Despite these fundamental differences, many techniques and algorithms developed in communications can still be applied to radar and should be considered.

Communications	Radar
High tolerance and desirability for low transmit processing gain	Low tolerance and desirability for low transmit processing gain
Zero tolerance for a hiatus in transmission	High tolerance for a hiatus in target detections
Importance of bandwidth and channel capacity	Importance of SIR, detection probability, range and Doppler resolution and measurement accuracy

Table 1.1: Differences between communications and radar.

1.2 Statistical MIMO

It is well-known that a target RCS is rapidly changing as a function of the target aspect. Both experimental measurements and theoretical results demonstrate that scintillations of 10 dB or more in the reflected energy can occur by changing the target aspect by as little as one milliradian [46]. This can be seen in Fig 1.5 which shows the variations of the target RCS with respect to aspect angle for a complex target (source: [46]). This results in signal fading which can degrade the system's detection and estimation performances significantly.

The statistical MIMO radar [3] has a configuration where all the antenna elements are widely-separated and give a diversified view of the target. Statistical target models are often used to model the fluctuations of the target RCS, hence the name *statistical*. As the received signal of the statistical MIMO radar is a superposition of independently faded signal, its average SIR remains more or less constant, thus improving stability in the detection of extended targets [4]. On the other

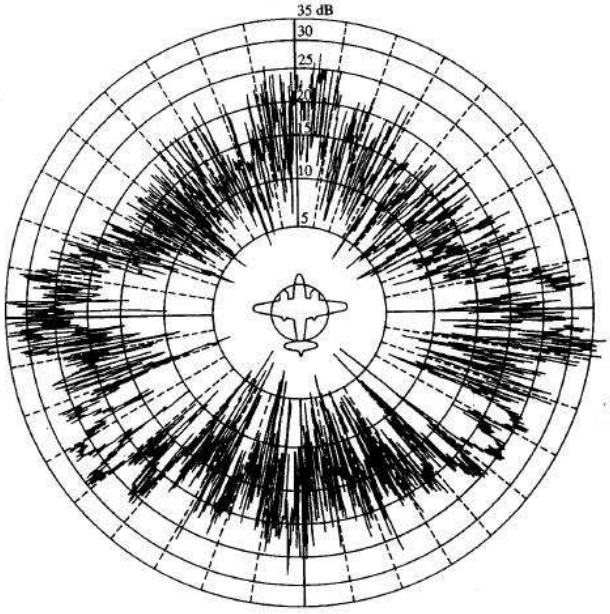

Figure 1.5: RCS of a complex target with respect to aspect angle.

hand, the conventional radar suffers from large variations in the received power under fluctuating target models.

1.2.1 Spatial Decorrelation and Diversity Gain

Let there be a target at $(0, 0)$ and its dimensions in the x and y axes be D_x and D_y, respectively. The m-th receiver and n-th transmitter are located at $(x_{r,m}, y_{r,m})$ and $(x_{t,n}, y_{t,n})$, respectively and λ is the carrier wavelength. According to [4], if at least one of the following four conditions are met:

$$\begin{aligned}
\frac{x_{t,m}}{\sqrt{x_{t,m}^2 + y_{t,m}^2}} - \frac{x_{t,m'}}{\sqrt{x_{t,m'}^2 + y_{t,m'}^2}} &> \frac{\lambda}{D_x}, \\
\frac{y_{t,m}}{\sqrt{x_{t,m}^2 + y_{t,m}^2}} - \frac{y_{t,m'}}{\sqrt{x_{t,m'}^2 + y_{t,m'}^2}} &> \frac{\lambda}{D_y}, \\
\frac{x_{r,n}}{\sqrt{x_{r,n}^2 + y_{r,n}^2}} - \frac{x_{r,n'}}{\sqrt{x_{r,n'}^2 + y_{r,n'}^2}} &> \frac{\lambda}{D_x}, \\
\frac{y_{r,n}}{\sqrt{x_{r,n}^2 + y_{r,n}^2}} - \frac{y_{r,n'}}{\sqrt{x_{r,n'}^2 + y_{r,n'}^2}} &> \frac{\lambda}{D_y},
\end{aligned}$$

then the mn-th and $m'n'$-th elements of the channel matrix are uncorrelated. Basically, this means that the antennas are so widely-separated that they fall in different beamwidths originating from the target, as illustrated in Fig. 1.6.

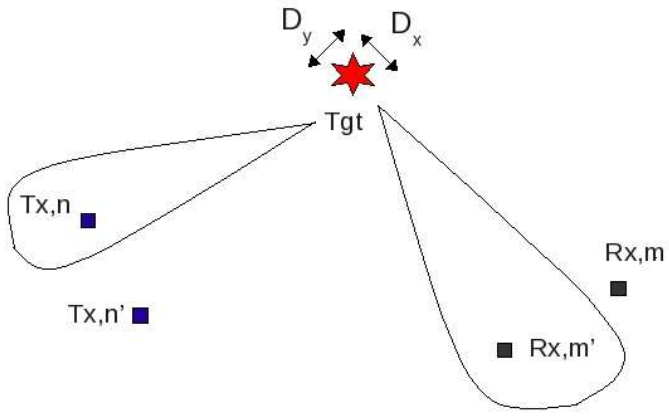

Figure 1.6: Illustration of how the target RCS decorrelates as its beamwidth cannot illuminate two antennas simultaneously.

It has been shown that for rich scattering conditions, i.e. the complex target to be detected is composed of a large number of scatterers Q, the diversity gain is equal to $N_{rx}N_{tx}$ which is the maximum diversity gain obtainable. However, in the limiting case where rich scattering is lacking, it is shown that the diversity gain is only equal or less than $\min(Q, N_{rx}N_{tx})$ [47]. In the extreme case of a point target, the elements of the channel matrix become correlated.

1.2.2 Common Reference Frame

In a conventional monostatic radar, system-centric measurements such as range, Doppler frequency and Direction Of Arrival (DOA) are used to estimate target position and velocity. For statistical MIMO radars, as in the case of multistatic radars, each transmit-receive pair has a different reference frame (range, Doppler frequency and DOA). Hence to merge all information, it is necessary to adopt a common frame and the most convenient frame to use is the North-East-Down (NED) coordinate system with the origin referenced to Earth-Centered, Earth-Fixed (ECEF) coordinates, as illustrated in Fig. 1.7.

A realizable approximation to the ML estimate of target position and velocity then involves a fine grid search over a two-dimensional (x and y for target position and v_x and v_y for target velocity) cost surface resulting from the non-coherently summed outputs from each transmit-receive pair. This means that target localization can be done by triangulation alone, i.e. it is not necessary to have multiple closely-spaced elements for direction-finding. Hence it is possible to have only one element at each location, processing multiple pulses instead. This will reduce the dimension of MIMO multi-pulse radar, e.g. MIMO-STAP. However, for MIMO-STAP, this configuration means that fully coherent space-time algorithms are not possible as incoherent processing has to be done between elements due to the wide

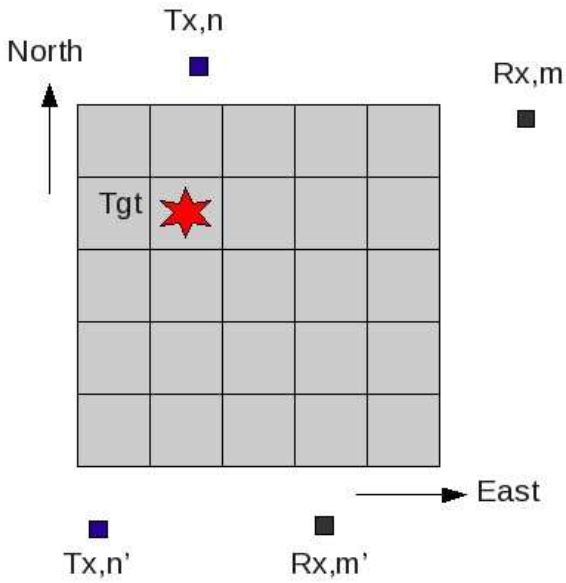

Figure 1.7: Use of a North-East-Down coordinate system as common reference frame for statistical MIMO radars. Note that only North and East are illustrated here.

separation. One major issue with this configuration is that the resolution is different depending on the transmit-receive pair, an issue addressed in [38].

In [48], the authors have demonstrated that this two-dimensional search gives better detection performance than an one-dimensional (in Doppler frequency) search for each transmit-receive path individually. This is because the joint maximization approach imposes more restrictions on the test statistic and thus effectively reduces false alarms. However, this approach also results in higher complexity.

1.2.3 Configuration studies

Some of the first questions that come into mind when we talk about statistical MIMO radars are:

1. Statistical MIMO radars or phased-arrays?
2. How to choose the number of transmitters and receivers?
3. What is the optimal way to place the antennas?

The first question has been treated in [2, 49] which found that in terms of detection performance, it is better to use the phased-array at low SIR and the statistical MIMO radar at high SIR.

The authors considered the second question in [50] in terms of relative entrophy. They found that when the number of transmitters is fixed, it is always better to

have more receivers. However, when the number of receivers is fixed, it is better to have fewer transmitters for low SIR and more transmitters for high SIR. In [51], the authors used the Cramér-Rao Bound (CRB) to study this question. Considering a fixed number of elements N_p, they found that it is better to have the same number of receivers and transmitters if the power transmitted per transmitter is fixed; it is better to have more than one transmitter and more receivers than transmitters if the total transmit power is fixed.

Finally, the third question is answered in [52] where it is found that symmetrically placing all the transmitters and receivers gives the best achievable performance in terms of CRB. The relative positions between the transmitters and receivers do not affect results if orthogonal waveforms are transmitted.

1.2.4 Waveform design

According to [53], estimation and classification capabilities of the radar can be improved by maximizing the Mutual Information (MI) between the target impulse response and reflected radar signals. In [54], the authors used this criterion to design optimal codes for MIMO radars using Space-Time Coding (STC) to achieve diversity. They obtained the same results using the Chernoff bound for the detection probability as the design criterion.

The authors then added two different constraints in the maximization of the MI [55]. The first was on the average received signal-to-disturbance ratio to reflect a power unlimited system and the second was on the total transmitted energy to reflect a power limited system. Using these design criteria, the rank of the code matrix can be used to trade energy integration (low rank) for transmit diversity (high rank). The authors found that high rank coding should be used for high SIR while low rank coding is more advantageous for low SIR. This reflects the results in Section 1.2.3 which say that energy integration (through the use of phased-arrays) is more important for low SIR and diversity is more significant for high SIR.

The work of [54] is further investigated in [56, 57]. In [56], the authors used a non-Gaussian model instead of a Gaussian model to describe the target while the authors considered colored noise instead of white Gaussian noise in [57]. In [58], the authors studied the use of STC codes to reduce waveform cross-correlation in order to improve range resolutions.

1.3 Coherent MIMO

Coherent MIMO radars [5] contain closely-spaced elements in a single subarray such that all elements see the same or correlated target RCS. Note that the transmit and receive subarrays are not necessarily co-located: they can be in a bistatic configuration. As the target RCS is correlated, direction-finding is possible. Diversity comes from the different waveforms transmitted by each transmit element. In this case, sparse arrangement is possible within the subarray, hence improving resolutions further. The main advantages of the coherent MIMO radar are:

- Improved angular resolutions (Section 1.3.1);
- Virtual spatial tapering of the virtual array, resulting in lower sidelobes (Section 1.3.1);
- Increased parameter identifiability [41], i.e. increased number of targets that can be detected and localized by the array;
- Direct application of adaptive techniques for parameter estimation as the signals reflected back by the target are linearly independent [7];
- Ability to null mainbeam jamming and robustness to multipath [9];
- Reduced interference to neighbouring systems and more covert operation due to the reduced spatial transmit power density of omnidirectional transmission [59];
- Flexibility for transmit beampattern design (Section 1.3.4).

1.3.1 Virtual Array

The most significant improvement in detection and estimation performance comes from the increase in virtual array size. The virtual array pattern achieved by the coherent MIMO radar is given by the convolution of the actual positions of the transmit and receive elements. For example, in Fig. 1.8, with N_{tx} sparsely-spaced transmit elements and N_{rx} closely-spaced (at say $\lambda/2$) receive elements, we are able to obtain a longer effective aperture of $(N_{rx}N_{tx} - 1) \cdot \lambda/2$. The same result can be obtained by having the transmit elements closely-spaced and the receive elements sparsely-spaced. The increase in aperture size results in improved angular resolutions.

Alternatively, the transmit elements can be closely-spaced in one direction and the receive elements in another direction such that a 2-D virtual array containing $N_{rx}N_{tx}$ elements can be formed using only two 1-D subarrays containing N_{tx} and N_{rx} elements, respectively (see Fig. 1.9).

Next, we consider closely-spaced configurations for both the transmit and receive subarrays. Let there be four elements in each subarray. The uniform array weighting can be represented by [1 1 1 1]. The equivalent MIMO virtual array weighting is then given by: [1 2 3 4 3 2 1]. This corresponds to an array of seven elements, larger than the transmit and receive subarays individually. More importantly, the virtual array weightings act like a spatial taper, resulting in lower sidelobes.

1.3.2 MIMO-STAP

One of the most important applications of the coherent MIMO technique is STAP. This application will be explored further in Chapter 3, not just in coherent MIMO configuration, but also for MISO configuration. The main advantage of coherent

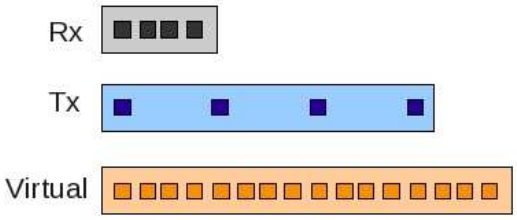

Figure 1.8: Virtual array formed from closely-spaced receive subarray and sparse transmit subarray.

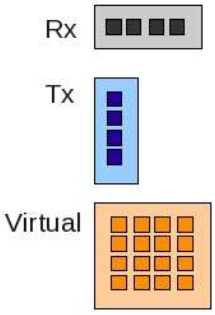

Figure 1.9: 2-D virtual array formed from closely-spaced 1-D receive and transmit subarrays.

MIMO is improved angular resolution which is very important for STAP as it reduces the MDV.

In the case where orthogonal waveforms are transmitted, it illuminates all angles uniformly, there is no need for beam scanning. The CPI can thus be increased, resulting in better Doppler resolution which lowers the MDV further. Moreover, with uniform illumination, the clutter covariance matrix remains the same for all angles. Hence this matrix has to be estimated and inverted only once whereas for the classical case, this has to be done for each angle that the beam illuminates.

The use of orthogonal waveforms also results in additional DoFs which can be used to filter out more clutter subspace with minimum effect on SIR. Note however that the extra dimension created by the orthogonal waveforms increases the rank of the clutter subspace, making STAP more complex. To reduce the computational complexity, the authors exploited the geometry of the problem instead of the data in [39]. This is done by representing the clutter subspace using prolate spheroidal wavefunctions. However, this method is sensitive to clutter subspace mismatch since it is data independent.

In [60, 31, 61, 62], the authors proposed the Doppler Division Multiple Access (DDMA) method. Basically, conventional waveforms are used and orthogonality is achieved by phase coding from pulse to pulse, i.e. the waveforms are orthogonal over one CPI and not for each pulse. This method is easy to implement as it requires only the addition of phase shifters at the transmit end. No change is needed for the receive range pulse compression. Hence, this can be achieved by using existing STAP radars. However, it is equivalent to scanning different Doppler zones such that there is a loss of target SIR when the Doppler zone containing the target is not "illuminated".

In this method, as the Pulse Repetition Frequency (PRF) has to be divided by the number of orthogonal channels, it has to be increased, resulting in reduced unambigious range. If the PRF is not high enough, high-speed targets might potentially be aliased into blind zones associated with the clutter. Hence, in [63], the author proposed modifying DDMA by adding code permutations and random phases to remove ambiguities and eliminate blind speeds. The MIMO-STAP concept using DDMA has been demonstrated in [32] using a small-scale experimental testbed containing four transmit and four receive elements.

1.3.3 Waveform design

There has been much work done on MIMO waveform design, using different criteria for optimization. In [64], the authors focused on optimizing two criteria: maximization of MI and minimization of the minimum mean square error. These criteria lead to the same solution under the same total power constraint. Note that the authors considered extended targets with large D_x and/or D_y such that the target returns are decorrelated although the coherent MIMO configuration is used. Hence, the target model is similar to that for the statistical MIMO configuration. In a subsequent paper [65], the minimax robust waveform design is investigated and this leads to different optimal waveforms despite using the same criteria as above. In [66], the authors proposed an iterative optimization algorithm based on the alternating projection method to solve the optimization problem in [64, 65] numerically instead of a closed-form solution.

Other design criteria have been used. In [67, 68], the authors designed MIMO waveforms by minimizing the trace of the CRB matrix while in [69], the MIMO ambiguity functions are used to design good waveforms. In [70], the author designed waveforms by matching them to the target or clutter subspace and compared the detection results using these waveforms and orthogonal waveforms. With some prior knowledge of the target or clutter statistics, it is possible to improve detection performance.

1.3.4 Transmit Beamforming

Another interesting area of research is the use of the transmit covariance matrix to control the transmit beam. Many papers assume the transmit covariance matrix

to be the identity matrix, i.e. the transmitted waveforms are perfectly orthogonal. This results in an omnidirectional beampattern. In the case of phased-array, the transmit covariance matrix has rank one, i.e. all transmitted waveforms are identical or fully correlated, resulting in a focused transmit beam. This is illustrated in Fig. 1.10. By controlling signal cross-correlation, diverse beampatterns that lie between the two extremes of high-directionality to omnidirectionality can be created.

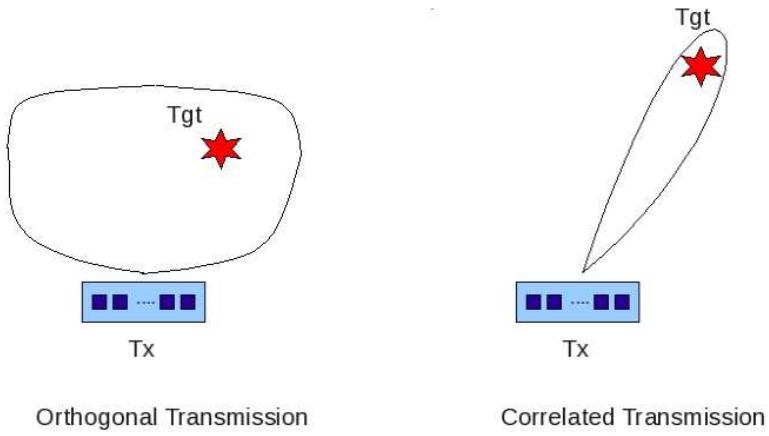

Figure 1.10: Illustration of the different beams obtained by orthogonal and correlated transmission.

In [71], the authors used convex optimization techniques to find an arbitrary transmit covariance matrix so as to achieve a desired spatial transmit beampattern. This is extended in [72] to the rank-deficient case which arises when the number of available waveforms is smaller than the number of transmitters. In [73], the aim is to maximize the power around the locations of the targets of interest and also to minimize the cross-correlation of the signals reflected back to the radar by the targets of interest. The authors proposed a two-step solution to obtain the desired transmit covariance matrix which can be rank deficient as well. The main disadvantage of these techniques is that it requires complex optimization techniques. The resulting waveforms are complicated and do not have a constant envelope, making it difficult for synthesis and power amplification.

In general, when the SIR is low, correlated waveforms should be transmitted, i.e. more towards phased-array kind of operation. This is similar to the results obtained for statistical MIMO radars (see Section 1.2.3 and Section 1.2.4). On the other hand, when the SIR is high, less correlated waveforms should be transmitted to maximize DoFs for separating targets from interference and also to allow the use of larger, sparsely spaced arrays while avoiding the potential ambiguities [74].

1.4 Hybrid MIMO

In this section, we consider hybrid MIMO configurations. The most general signal model has been proposed in [8, 75] where the authors considered widely-separated subarrays and there can be one or more elements in each subarray. This model encompasses both the statistical and coherent MIMO configurations and many others. This is also the model that we adopt in Chapter 2. In [8, 75], an iterative Generalized Likelihood Ratio Test (GLRT) is proposed to detect and estimate multiple targets.

In [76], the authors applied tensor algebra and multidimensional harmonic retrieval techniques to do target localization using the general hybrid configuration. On top of that, they considered L pulses. They showed that the maximum number of targets that can be identified, provided that $L > 3$, is upper bounded by:

$$\min\left(\left\lfloor\frac{N_{rx}}{\tilde{M}}\right\rfloor, \left\lfloor\frac{N_{tx}}{\tilde{N}}\right\rfloor\right),$$

where $\tilde{M}$ and $\tilde{N}$ are the number of receive and transmit subarrays, respectively.

The authors proposed a hybrid configuration in [77] to perform direct position determination using all collected data together rather than doing triangulation based on the angle of arrival of each receive subarray. Note that the configuration used consists of widely-separated transmit elements, widely-separated receive subarrays with multiple elements and L pulses. This method improves localization performance especially when the SIR is low.

1.4.1 Performance under different Swerling models

In [42], the authors studied the detection and direction-finding performance of different configurations under Swerling target models [46] (Cases I-IV). A summary of the Swerling target models in terms of their Probability Density Function (PDF) and fluctuation pattern is shown in Table 1.2 (α and $\bar{\alpha}$ are the target RCS and the average target RCS, respectively).

Case	PDF of target RCS α, $f(\alpha)$	Fluctuation
I	$\frac{1}{\bar{\alpha}}e^{-\alpha/\bar{\alpha}}$	Scan-to-scan
II	$\frac{1}{\bar{\alpha}}e^{-\alpha/\bar{\alpha}}$	Pulse-to-pulse
III	$\frac{4\alpha}{\bar{\alpha}^2}e^{-2\alpha/\bar{\alpha}}$	Scan-to-scan
IV	$\frac{4\alpha}{\bar{\alpha}^2}e^{-2\alpha/\bar{\alpha}}$	Pulse-to-pulse

Table 1.2: Summary of Swerling target models.

In this case, the transmit elements are *all* either closely-spaced or widely-separated, resulting in the SI- or MI- configurations. Similarly, the receive elements

are *all* either closely-spaced or widely-separated, resulting in the -SO or -MO configurations.

For single-pulse detection, it is better to employ beamforming than to exploit diversity when SIR is low and vice versa when SIR is high, for all Swerling target types. This is consistent with the results found in [4] for Swerling cases I and II. Moreover, when multiple pulses are used, this is equivalent to having temporal diversity for Swerling cases II and IV since the target RCS changes from pulse-to-pulse. This temporal diversity benefits more systems with low spatial diversity. On the other hand, this is equivalent to SIR improvement for Swerling cases I and III as the target RCS remains constant for the entire scan. This is more beneficial for MIMO configurations.

For direction-finding, the authors found that the angular diversity improves estimation performance in terms of CRB for the Swerling case I and to some extent case III but not cases II and IV.

1.4.2 MISO Configurations

One of the configurations that has been widely studied is the MISO configuration. This is because it contains the characteristics of both phased-arrays (in the receive part) and statistical MIMO radars (in the transmit part). In [2], the authors found that the detection performance of MISO radars is between that of phased-arrays and statistical MIMO radars. MISO radars are better than statistical MIMO radars but worse than phased-arrays when SIR is low. On the other hand, MISO radars are better than phased-arrays but worse than statistical MIMO radars when SIR is high.

Similarly, the authors considered in [6] the direction-finding capability of the MISO configurations where there are widely-separated transmit elements and one single receive subarray. In [78], the authors showed how several illuminators of opportunity can be used to detect targets passively with a single receiver subarray in a MISO configuration. This is done using subspace methods and compressed sensing techniques.

1.4.3 Phased-MIMO, Transmit Subaperturing MIMO and Hybrid MIMO Phased-Array Radar

The idea of partitioning the transmit array has been introduced in [79] and further developed in [80, 81, 82]. In [80], the scheme is called phased-MIMO radar, it is called Transmit Subaperturing MIMO (TS-MIMO) in [81] while in [82], it is called Hybrid MIMO Phased-Array Radar (HMPAR). Strictly speaking, these schemes should be classified under coherent MIMO as radar systems containing co-located antennas are considered. However, it is classified under hybrid MIMO as it combines the coherent MIMO radar and the phased-array.

Basically, in these schemes, the transmit array is divided into K_e subarrays of different sizes. These subarrays can be disjoint or overlapping such that $1 \leq K_e \leq$

N_{tx}. $K_e = 1$ becomes the phased-array while $K_e = N_{tx}$ becomes the coherent MIMO radar. Each element in a subarray transmits the same waveform such that a focused beam can be formed as in the case of phased-arrays. At the same time, different subarrays transmit different orthogonal waveforms such that there is waveform diversity. If $K_e < N_{tx}$, it can be considered that these hybrid MIMO radars transmit correlated waveforms such that the rank of the transmit covariance matrix is K_e. These schemes are closely related to the transmit beamforming designs described in Section 1.3.4. However, these hybrid schemes are simpler as no complex optimization is required.

Chapter 2

MIMO Detectors

This chapter is organized as follows. We begin by describing and classifying different MIMO configurations in Section 2.2 according to their spatial diversity. Next, we present a general signal model for MIMO radar (Section 2.3.1). Instead of considering a single element at each location, we assume that there is a subarray containing one or more elements. Moreover, no assumption is made on the independence of the individual subarrays.

Section 2.3.2 shows the derivation of the optimum MIMO Gaussian detector based on the above signal model such that it takes into consideration possible correlation between subarrays. It becomes the classical MIMO Optimum Gaussian Detector (OGD) when the subarrays are uncorrelated such that the covariance matrix is block diagonal. Its statistical properties are summarized in Section 2.3.3.

In Section 2.3.4, the simulation configurations and parameters are presented. We consider two main configurations: one where the effective number of element N_e is varying and one where N_e is constant. The total number of physical elements N_p remains constant for both cases. In Section 2.3.5, we see how the detection performance varies according to N_e and the effective number of subarrays K_e.

The adaptive version of this detector is then derived based on Kelly's Test in Section 2.4.1 while in Section 2.4.2, we study its statistical properties, especially the loss factor which is the loss in SIR due to the estimation of the covariance matrix. In Section 2.4.3, the effects of K_e, N_e and the number of secondary data N_s on the loss factor and consequently on the detection performance are studied through simulations.

In Section 2.5.1, we consider non-Gaussian interference, modeled by the SIRV model which is a non-homogeneous and non-Gaussian process with random power. Note that we consider that the subarrays are independent in this section. A new MIMO non-Gaussian detector is then derived in Section 2.5.2. Its statistical properties are derived in Section 2.5.3. The detection performance is then analyzed through Monte-Carlo simulations and compared to that of the MIMO OGD under both Gaussian and non-Gaussian interference (Section 2.5.5).

Next, in Section 2.6.1, the adaptive version of the non-Gaussian detector is considered, using the Fixed Point Estimate (FPE) as the covariance matrix estimate. The effects of the covariance matrix estimation on the detection performance are then investigated using Monte-Carlo simulations in Section 2.6.3. Finally, a brief summary of the contributions of this chapter is given in Section 2.7.

2.1 Definition

In the remaining chapters, the following notations will be adopted: *array* denotes the whole system except where it is used to explain concepts like *virtual array* and *synthetic array* in Chapter 3. *Subarray* refers to a grouping of antenna elements that are closely-spaced or sparse such that they see the same target RCS. It is possible to have only one element in a subarray.

We consider that there are $\tilde{N}$ transmit subarrays and $\tilde{M}$ receive subarrays in the array. The total *physical* number of subarrays is then $K_p = \tilde{N} + \tilde{M}$. On the other hand, an effective subarray consists of one transmit subarray and one receive subarray. In the case of MIMO where the transmitted waveforms from different transmit subarrays can be received and separated at each receive subarray, the total *effective* (virtual) number of subarrays becomes $K_e = \tilde{N}\tilde{M}$.

Let there be N_n and M_m elements in the n-th transmit and m-th receive subarrays, respectively. There are then $N_{tx} = \sum_{n=1}^{\tilde{N}} N_n$ transmit elements and $N_{rx} = \sum_{m=1}^{\tilde{M}} M_m$ receive elements in the array. The total number of physical elements in all subarrays (both transmit and receive) is given by $N_p = N_{tx} + N_{rx}$.

Similarly, $N_{e,i} = N_n M_m$ is the effective number of elements in the i-th effective subarray formed by the n-th transmit subarray and the m-th receive subarray. The total effective number of elements is then:

$$N_e = \sum_{i=1}^{K_e} N_{e,i} = \sum_{n=1}^{\tilde{N}} \sum_{m=1}^{\tilde{M}} N_n M_m = N_{tx} N_{rx}.$$

2.2 Configurations

In this section, we give an overview of the different configurations which can have waveform and/or spatial diversity. Waveform diversity is given by the different separable waveforms transmitted by each transmit element while spatial diversity is due to the wide spacing between subarrays such that different aspects of the target are seen. Due to the decorrelation of the target returns, non-coherent processing has to be done between subarrays and direction-finding is not possible.

Within subarrays, the elements are assumed to be closely-spaced though no assumption is made on the arrangement and actual spacing of the elements. Each subarray can be sparse, i.e. the spacing between elements is greater than $\frac{\lambda}{2}$ but smaller than the spacing needed to decorrelate so that the elements still see the same aspect of the target. As the signal received at the elements are correlated, coherent processing can be done and each subarray has direction-finding capabilities. An example of this general MIMO configuration (where $\tilde{N} = \tilde{M} = 3$) is given in Fig. 2.1. The bold arrows indicate that multiple waveforms are transmitted from each transmit subarray.

The sparse spacing increases resolution due to the increase in effective aperture size but it causes grating lobes. To avoid grating lobes, either the receive or transmit subarray should be closely-spaced such that the first zeros of the beam pattern

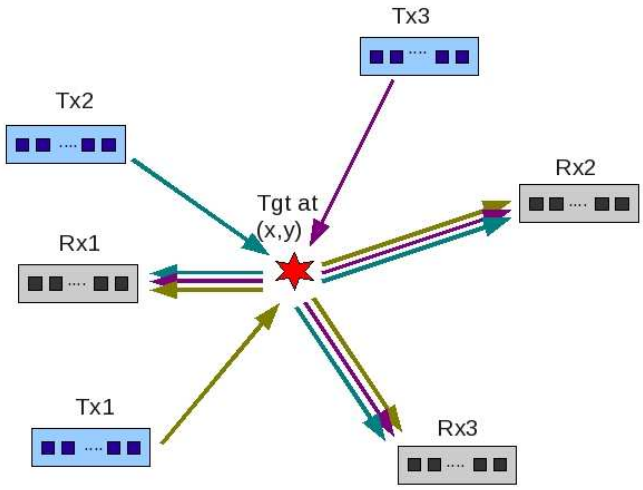

Figure 2.1: The configuration where $\tilde{N} = \tilde{M} = 3$.

cancel out the grating lobes of the sparse array. Another option is to use a random thinned array. This would remove the grating lobes but increase the sidelobe levels.

Here, *multiple* input and/or output is defined according to the spatial diversity for the transmit and/or receive end. Waveform diversity is assumed as long as there is more than one transmit element. That means that even if there is no transmit spatial diversity (only one transmit subarray), there can still be waveform diversity if there are more than one element in the transmit subarray. The different configurations SISO, SIMO, MISO and MIMO are summarized in Table 2.1.

Config	$\tilde{N}$	N_n	$\tilde{M}$	M_m
SISO	1	≥ 1	1	≥ 1
SIMO	1	≥ 1	> 1	≥ 1
MISO	> 1	≥ 1	1	≥ 1
MIMO	> 1	≥ 1	> 1	≥ 1

Table 2.1: Different possible configurations.

2.2.1 Effective number of Subarrays and Elements

Due to spatial diversity, the MIMO radar sees $K_e = \tilde{N}\tilde{M}$ ($K_e = 9$ in the example given in Fig. 2.1) different aspects of the target. This means that we have an effective number of subarrays K_e which is more than the actual number of subarrays $K_p = \tilde{N} + \tilde{M} = 6$. When we have more than one transmit subarray and more than one receive subarray, $K_e \geq \tilde{N} + \tilde{M}$ due to diversity gain.

The effective number of elements is given by $N_e = \sum_{m=1}^{\tilde{M}} \sum_{n=1}^{\tilde{N}} M_m N_n$. One of the advantages of waveform diversity in MIMO is that it can increase the effective number of elements such that it is greater than the physical number of elements, N_p. This is true when $N_{tx} > 1$ and $N_{rx} > 1$. This is expected because when $N_{tx} = 1$, there is only one waveform while when $N_{rx} = 1$, the waveform diversity is not exploited as it is received only by a single receive element.

Interestingly, the maximum effective number of elements is obtained when there is an equal number of receive and transmit elements ($N_{tx} = N_{rx}$), *regardless* of the configuration. Given a fixed N_p and if N_p is odd, it is not possible to have an equal number of transmit and receive elements. In such cases, the maximum N_e is given when $N_{tx} = \frac{N_p-1}{2}$ and $N_{rx} = \frac{N_p+1}{2}$ or vice versa.

Remark 2.1. *Given a fixed N_p, the maximum possible effective number of elements is given by:*

$$N_e^{max} = \begin{cases} (\frac{N_p}{2})^2 = \frac{N_p^2}{4}, & N_p \text{ even}, \\ (\frac{N_p-1}{2})(\frac{N_p+1}{2}) = \frac{N_p^2-1}{4}, & N_p \text{ odd}. \end{cases}$$

The derivation is given in Appendix B.1.

2.2.2 SIR Gain

We define the pre-processing SIR, SIR_{pre} to be the average SIR per element before processing:

$$\begin{aligned} \text{SIR}_{\text{pre}} &= \frac{|\alpha|_{ave}^2}{\sigma^2}, \\ &= \frac{\boldsymbol{\alpha}^\dagger \boldsymbol{\alpha}/K_e}{\sigma^2}, \end{aligned}$$

where σ^2 is the interference power per element such that $\text{tr}(\mathbf{M}) = \sigma^2 N_e$ and $\mathbf{M}$ is the interference covariance matrix. $|\alpha|_{ave}^2$ is the average power of the target RCS $\boldsymbol{\alpha}$ and is given by: $\boldsymbol{\alpha}^\dagger \boldsymbol{\alpha}/K_e$.

The post-processing SIR, SIR_{post} is defined to be the total equivalent SIR of the entire system after processing:

$$\text{SIR}_{\text{post}} = \boldsymbol{\alpha}^\dagger \mathbf{P}^\dagger \mathbf{M}^{-1} \mathbf{P} \boldsymbol{\alpha}, \tag{2.1}$$

where $\mathbf{P}$ is the $N_e \text{x} K_e$ matrix containing all the steering vectors as defined in Eqn. (2.4).

The SIR gain is then defined as the gain in SIR after processing:

$$\begin{aligned}\text{SIR gain} &= \frac{\text{SIR}_{\text{post}}}{\text{SIR}_{\text{pre}}},\\ &= \frac{\boldsymbol{\alpha}^{\dagger}\mathbf{P}^{\dagger}\mathbf{M}^{-1}\mathbf{P}\boldsymbol{\alpha}}{\frac{|\alpha|^2_{ave}}{\sigma^2}},\\ &= \frac{\boldsymbol{\alpha}^{\dagger}\mathbf{P}^{\dagger}\mathbf{M}^{-1}_{norm}\mathbf{P}\boldsymbol{\alpha}}{|\alpha|^2_{ave}},\\ &\approx \frac{\sum_{i=1}^{K_e} N_{e,i}|\alpha|^2_{ave}}{|\alpha|^2_{ave}} = N_e,\end{aligned}$$

where $\mathbf{M}_{norm} = \frac{1}{\sigma^2}\mathbf{M}$ and $N_{e,i}$ is the effective number of elements in the i-th subarray.

So the SIR gain is proportional to $N_e = N_{rx}N_{tx}$. This gain comes from two parts: coherent processing gain within the subarrays (N_{rx}) and the power gain from having N_{tx} transmit elements. This is the case for power unlimited system where each transmit element transmits the same amount of power, such that the total transmit power is proportional to the number of transmit elements (not the number of transmit subarrays $\tilde{M}$). This allows for the reciprocity of the transmit and receive elements because there is a symmetry between the transmit and receive elements on the performance of the MIMO radar. This means that a MIMO radar system with a transmit elements and b receive elements is equivalent to one with b transmit elements and a receive elements, in terms of performance. With this reciprocity, we are able to study the configurations in the subsequent sections in terms of only K_e and N_e. Moreover, we see in Chapter 3 that for the SISO case, the effective aperture size (and hence estimation accuracy) depends also on N_e and not just N_{rx} or N_{tx}.

On the other hand, in a power limited system where the total power is divided among all transmit elements, the SIR gain is proportional to the number of receive elements. *This means that it is advantageous to have more receive elements for SIR gain.*

It is important to always maximize N_e. As mentioned earlier, in order to have $N_e > N_p$, it is necessary to choose $N_{rx} > 1$ and $N_{tx} > 1$. From the energy point of view, given a choice between two configurations where N_e is the same (one with more receive elements and the other with more transmit elements due to the symmetry), it is better to choose the one with larger N_{rx}.

2.2.3 Comparisons

2.2.3.1 SISO

For the SISO configuration, there is only one transmit and one receive subarray and this is equivalent to the configuration of *coherent MIMO* radars. The transmit and receive subarrays can be co-located or in a bistatic configuration. Furthermore, if there is only one transmit element (N_1=1) and there are several receive elements

($M_1 > 1$), this becomes the classical phased array. In this case, there is only one transmitted waveform, i.e. no waveform diversity.

There is no spatial diversity and hence this configuration is sensitive to target fluctuations, like conventional radars. Its diversity comes from the transmitted waveforms. Its main advantage lies in the increased resolution and direction-finding capabilities due to coherent processing of signals from all elements.

2.2.3.2 MIMO

There are several transmit and receive subarrays to give spatial diversity and subarrays that contain more than one element will have direction-finding capability and also coherent processing gain. If there is only one element in each transmit and receive subarray ($N_n = 1$ and $M_m = 1$), this becomes the *statistical MIMO* radars.

For this configuration, there are both spatial and waveform diversity. Given a fixed number of antenna elements, having more subarrays increases robustness to target fluctuations. However, this comes at the cost of reduced resolution as the signals from different subarrays are decorrelated and non-coherent processing has to be done instead of coherent processing.

2.2.3.3 SIMO and MISO

These two configurations are combinations of SISO and MIMO. For SIMO, there is only one transmit subarray and several receive subarrays. The advantage of this configuration is the possibility of implementing the receive subarrays on small platforms like UAV while the bulky transmit subarray can be implemented on a larger platform.

On the other hand, there are several transmit subarrays and only one receive subarray for the MISO configuration. One famous example of MISO configuration is the Global Positioning System (GPS). The satellites are the transmit subarrays while the GPS receiver is the receive subarray. With several transmitters, it is possible to do ranging by triangulation, hence a single transmit element is sufficient in each subarray and similarly for the receive subarray. The advantage of this configuration is obvious: with one simple receiver, the user is already able to make use of the navigation system.

2.2.3.4 Hybrid Configuration

We define here the hybrid configuration as a generic configuration which encompasses all the different configurations: SISO, SIMO, MISO and MIMO. No assumption is made on the number of transmit and receive subarrays and the number of elements in each subarray. The only assumption made is that each transmit element transmits a different waveform that can be separated at the receive end. This is the setup that will be considered in the following sections.

2.3 Gaussian Detector with Known Interference Parameters

2.3.1 Signal Model

In this section, the signal model that will be used to derive the detector is presented. This signal model is very general so as to represent the hybrid configuration described in Section 2.2. We consider a target located at (x, y). Let there be $\tilde{N}$ transmit subarrays and $\tilde{M}$ receive subarrays and they are all widely separated. The n-th transmit and m-th receive subarray contain N_n and M_m elements respectively, for $n = 1, \ldots, \tilde{N}$ and $m = 1, \ldots, \tilde{M}$.

Due to the wide separation, the target RCS seen by each receive-transmit subarray pair are assumed to be different but deterministic. The elements within each subarray are assumed to be closely-spaced such that the target RCS is the same.

Remark 2.2 (On the transmitted waveforms)**.** *Different (but not necessarily orthogonal) waveforms are assumed to be transmitted from every transmit element, even those belonging to the same subarray. As explained in Section 2.2, this means that while there is a closely-spaced configuration within the subarray, there is still diversity of waveform within the subarray. This enables the received signal from each transmit element to be separated such that transmit angular information can be obtained.*

Let $\mathbf{v}(\theta_{t,n})$ and $\mathbf{a}(\theta_{r,m})$ be the steering vectors and $\theta_{t,n}$ and $\theta_{r,m}$ the angular location for the target for the n-th transmit and m-th receive subarray, respectively. The received signal after matched filtering can be expressed as:

$$\mathbf{y}_{m,n} = B_{m,n}\mathbf{p}_{m,n} + \mathbf{z}_{m,n}, \quad \begin{cases} m = 1, \ldots, \tilde{M}, \\ n = 1, \ldots, \tilde{N}, \end{cases} \tag{2.2}$$

where $\mathbf{B}$ is the $\tilde{M}\text{x}\tilde{N}$ matrix containing the target RCS such that $B_{m,n}$ is the target RCS seen by the m-th receive and n-th transmit subarray pair. The vector $\mathbf{p}_{m,n}$ is the $M_m N_n$x1 bistatic angular steering vector which is equal to $\mathbf{a}(\theta_{r,m}) \otimes \mathbf{v}(\theta_{t,n})$ and $\mathbf{z}_{m,n}$ is the $M_m N_n$x1 vector containing interference returns.

Note that the corresponding time-delay for the $m-n$ receive-transmit pair $t_{m,n}$ is assumed to be known. This is the case for radars where the area of interest is divided into small cells and the detection test is applied at each cell to check for the presence of a target.

For each radar parameter to be determined, a steering vector is required. The resulting steering vector is simply the Kronecker product of all the steering vectors. In the multistatic case, as the transmit and receive angles are no longer the same, a separate steering vector is required for transmit ($\mathbf{v}(\theta_{t,n})$) and receive ($\mathbf{a}(\theta_{r,m})$). Note that only one pulse is considered in this chapter but this model can easily be extended for a pulsed-radar, as is the case in Chapter 3.

With spatial diversity, having $\tilde{N}$ transmit subarrays and $\tilde{M}$ receive subarrays is equivalent to having K_e effective subarrays. Thus, Eqn. (2.2) becomes:

$$\mathbf{y}_i = \alpha_i \mathbf{p}_i + \mathbf{z}_i, \qquad \forall\ i = 1, \ldots, K_e, \tag{2.3}$$

where

$$\begin{aligned} \alpha_i &= B_{m,n}, \\ \mathbf{p}_i &= \mathbf{p}_{m,n}, \\ \mathbf{z}_i &= \mathbf{z}_{m,n}, \end{aligned}$$

and $N_{e,i}$ is the length of the i-th steering vector $\mathbf{p}_i$. It is also the effective number of elements in the i-th subarray. $\mathbf{z}_i$ is the i-th interference vector. The total effective number of elements N_e is thus $N_e = \sum_{i=1}^{K_e} N_{e,i} = N_{tx}N_{rx} = \sum_{m=1}^{\tilde{M}} \sum_{n=1}^{\tilde{N}} M_m N_n$.

Remark 2.3 (Problem of spacing and non-orthogonality of waveforms)**.** *According to [4], the required spacing between the subarrays for the target returns to be uncorrelated depends on the size of the target. Similarly, for the interference returns to be uncorrelated, the required spacing depends on the resolution cell size. It is not always possible to achieve these spacings, especially in the case where the transmit or receive subarrays are moving. More importantly, perfectly orthogonal waveforms do not exist. We assume that these factors cause the return signals from different subarrays to be correlated.*

Due to Rem. 2.3, we consider the following signal model that does not assume the independence of the different subarrays.

$$\mathbf{y} = \mathbf{P}\boldsymbol{\alpha} + \mathbf{z},$$

where the vectors $\mathbf{y}$, $\boldsymbol{\alpha}$ and $\mathbf{z}$ are the concatenation of all the received signals, target RCS and interference returns, respectively:

$$\mathbf{y} = \begin{bmatrix} \mathbf{y}_1 \\ \vdots \\ \mathbf{y}_{K_e} \end{bmatrix}, \qquad \boldsymbol{\alpha} = \begin{bmatrix} \alpha_1 \\ \vdots \\ \alpha_{K_e} \end{bmatrix}, \qquad \mathbf{z} = \begin{bmatrix} \mathbf{z}_1 \\ \vdots \\ \mathbf{z}_{K_e} \end{bmatrix},$$

and $\mathbf{P}$ contains all the steering vectors and is a N_exK_e matrix since $N_e = \sum_i^{K_e} N_{e,i}$:

$$\mathbf{P} = \begin{bmatrix} \mathbf{p}_1 & & \mathbf{0} \\ & \ddots & \\ \mathbf{0} & & \mathbf{p}_{K_e} \end{bmatrix}. \tag{2.4}$$

The covariance matrix of each $\mathbf{z}_i$ is given by $\mathbf{M}_{ii}$ while the inter-correlation matrix between $\mathbf{z}_i$ and $\mathbf{z}_j$ is denoted as $\mathbf{M}_{ij}$ such that $\mathbf{z} \sim \mathcal{CN}(\mathbf{0}, \mathbf{M})$ where $\mathbf{M}$ is a N_exN_e matrix composed of the block matrices $\mathbf{M}_{ij}\ \forall\ i, j \in \{1, \ldots, K_e\}$. Note that $N_e \geq K_e$ and $\mathbf{P}$ has full column rank K_e due to the K_e different aspects of the target.

2.3.2 Derivation

Under Gaussian assumptions with known interference parameters, the problem of detecting a target corrupted by an additive interference with a MIMO radar can be formulated using a binary hypothesis test:

$$\begin{cases} \mathrm{H}_0: & \mathbf{y} = \mathbf{z}, \\ \mathrm{H}_1: & \mathbf{y} = \mathbf{P}\boldsymbol{\alpha} + \mathbf{z}. \end{cases}$$

Under the hypothesis H_0, it is assumed that the received signal contains only interference returns and hence there is no target. Under the hypothesis H_1, it is assumed that the received signal contains a deterministic complex signal on top of the interference returns and hence a target is present.

Two important figures of merit related to the binary hypothesis test are the probability of false alarm and the probability of detection. The probability of false alarm P_{fa} is the probability of choosing H_1 when the target is absent (H_0) while the probability of detection P_d is the probability of choosing H_1 correctly when the target is present.

According to the Neyman-Pearson criterion, the optimum solution to the hypothesis testing problem is the likelihood ratio test which is given by:

$$\Lambda(\mathbf{y}) = \frac{f(\mathbf{y}|\mathrm{H}_1)}{f(\mathbf{y}|\mathrm{H}_0)} \underset{\mathrm{H}_0}{\overset{\mathrm{H}_1}{\gtrless}} \lambda, \tag{2.5}$$

where λ is the detection threshold chosen to ensure that $\mathrm{P}(\Lambda(\mathbf{y}) > \lambda|\mathrm{H}_0) = P_{fa}$.

Given that $\mathbf{z} \sim \mathcal{CN}(\mathbf{0}, \mathbf{M})$ and $\mathbf{M}$ is known, after some simple manipulations, the GLRT becomes:

$$\ln \Lambda(\mathbf{y}) = -(\mathbf{y} - \mathbf{P}\boldsymbol{\alpha})^\dagger \mathbf{M}^{-1}(\mathbf{y} - \mathbf{P}\boldsymbol{\alpha}) + \mathbf{y}^\dagger \mathbf{M}^{-1}\mathbf{y}.$$

Although $\mathbf{p}_i$ is generally not known in advance, it can be found by sweeping through the possible values and finding the maximum. Hence, $\mathbf{p}_i$ is considered to be known and not estimated. On the other hand, the target RCS are unknown and we have to find their ML estimates: $\hat{\boldsymbol{\alpha}} = [\hat{\alpha}_1 \dots \hat{\alpha}_{K_e}]^T$. For each α_i,

$$\begin{aligned} \frac{\partial \ln \Lambda(\mathbf{y})}{\partial \alpha_i} &= \mathrm{tr}\left[\left(\frac{\partial \ln \Lambda(\mathbf{y})}{\partial \boldsymbol{\alpha}}\right)^\dagger \frac{\partial \boldsymbol{\alpha}}{\partial \alpha_i}\right], \\ &= \left[2\mathbf{P}^\dagger \mathbf{M}^{-1}(\mathbf{y} - \mathbf{P}\boldsymbol{\alpha})\right]^\dagger \mathbf{b}_i = 0, \end{aligned}$$

and $\mathbf{b}_i$ is the K_ex1 vector where

$$\mathbf{b}_i(i') = \begin{cases} 1, & i = i', \\ 0, & i \neq i'. \end{cases}$$

Considering all α_i, this gives:

$$\mathbf{P}^\dagger \mathbf{M}^{-1}\mathbf{y} = \mathbf{P}^\dagger \mathbf{M}^{-1}\mathbf{P}\boldsymbol{\alpha}.$$

As $\mathbf{P}$ is of full column rank and $\mathbf{M}$ is of full rank, $\mathbf{P}^\dagger\mathbf{M}^{-1}\mathbf{P}$ is of full rank and thus invertible. Hence the ML estimate of $\boldsymbol{\alpha}$ is given by:

$$\hat{\boldsymbol{\alpha}} = (\mathbf{P}^\dagger\mathbf{M}^{-1}\mathbf{P})^{-1}\mathbf{P}^\dagger\mathbf{M}^{-1}\mathbf{y}. \tag{2.6}$$

Using Eqn. (2.6), the detector can be expressed as:

$$\begin{aligned} \ln\Lambda(\mathbf{y}) &= 2\Re(\mathbf{y}^\dagger\mathbf{M}^{-1}\mathbf{P}\hat{\boldsymbol{\alpha}}) - \hat{\boldsymbol{\alpha}}^\dagger\mathbf{P}^\dagger\mathbf{M}^{-1}\mathbf{P}\hat{\boldsymbol{\alpha}}, \\ &= \mathbf{y}^\dagger\mathbf{M}^{-1}\mathbf{P}(\mathbf{P}^\dagger\mathbf{M}^{-1}\mathbf{P})^{-1}\mathbf{P}^\dagger\mathbf{M}^{-1}\mathbf{y}. \end{aligned} \tag{2.7}$$

This detector has a classical structure which consists of a projector projecting the received signal onto the useful signal subspace. It is basically the multidimensional version of the OGD. As this detector takes into consideration the possible correlation of the subarrays and is thus robust to problems like subarray spacing and imperfect orthogonality of the waveforms as explained in Rem 2.3, it will be referred to as the Robust MIMO OGD (R-MIMO OGD) detector [C3].

Remark 2.4. *In the particular case where there is no correlation between the subarrays, the R-MIMO OGD detector becomes:*

$$\ln\Lambda(\mathbf{y}) = \sum_{i=1}^{K_e} \frac{|\mathbf{p}_i^\dagger\mathbf{M}_{ii}^{-1}\mathbf{y}_i|^2}{\mathbf{p}_i^\dagger\mathbf{M}_{ii}^{-1}\mathbf{p}_i}. \tag{2.8}$$

This is the same equation as that obtained for MIMO OGD, as proposed in [4, 20].

Indeed, when the subarrays are uncorrelated, $\mathbf{M}$ is block diagonal:

$$\mathbf{M} = \begin{bmatrix} \mathbf{M}_{11} & \dots & \mathbf{0} \\ \vdots & \ddots & \vdots \\ \mathbf{0} & \dots & \mathbf{M}_{K_eK_e} \end{bmatrix}.$$

Its inverse is also block diagonal. $\mathbf{P}^\dagger\mathbf{M}^{-1}\mathbf{P}$ becomes:

$$\mathbf{P}^\dagger\mathbf{M}^{-1}\mathbf{P} = \begin{bmatrix} \mathbf{p}_1^\dagger\mathbf{M}_{11}^{-1}\mathbf{p}_1 & \dots & \mathbf{0} \\ \vdots & \ddots & \vdots \\ \mathbf{0} & \dots & \mathbf{p}_{K_e}^\dagger\mathbf{M}_{K_eK_e}^{-1}\mathbf{p}_{K_e} \end{bmatrix}.$$

Thus the R-MIMO OGD detector becomes like that in Eqn. (2.8).

2.3.3 Statistical Properties

Consider the whitened received signal $\mathbf{x} = \mathbf{M}^{-1/2}\mathbf{y}$, the detector becomes:

$$\ln\Lambda(\mathbf{x}) = \mathbf{x}^\dagger\mathbf{M}^{-1/2}\mathbf{P}(\mathbf{P}^\dagger\mathbf{M}^{-1}\mathbf{P})^{-1}\mathbf{P}^\dagger\mathbf{M}^{-1/2}\mathbf{x}.$$

The matrices $\mathbf{M}$ and $\mathbf{P}^\dagger\mathbf{M}^{-1}\mathbf{P}$ are of full rank while $\mathbf{P}$ is of full column rank and the minimum rank among these matrices is K_e. Hence the rank of the matrix

$\mathbf{M}^{-1/2}\mathbf{P}(\mathbf{P}^\dagger\mathbf{M}^{-1}\mathbf{P})^{-1}\mathbf{P}^\dagger\mathbf{M}^{-1/2}$ is also K_e. Under H_0, $\mathbf{x} \sim \mathcal{CN}(\mathbf{0}, \mathbf{I})$, the distribution of the detector is simply the central chi-square with $2K_e$ DoF, denoted by $\chi^2_{2K_e}(0)$. This is the same as the distribution of the MIMO OGD detector where the subarrays are not correlated. Under H_1, $\mathbf{x} \sim \mathcal{CN}(\mathbf{M}^{-1/2}\mathbf{P}\boldsymbol{\alpha}, \mathbf{I})$ and the distribution of the detector becomes the non-central chi-square with a non-centrality parameter of $2\boldsymbol{\alpha}^\dagger\mathbf{P}^\dagger\mathbf{M}^{-1}\mathbf{P}\boldsymbol{\alpha}$, denoted by $\chi^2_{2K_e}(2\boldsymbol{\alpha}^\dagger\mathbf{P}^\dagger\mathbf{M}^{-1}\mathbf{P}\boldsymbol{\alpha})$. Note that the non-centrality parameter in the distribution of the detector under H_1 is $2\mathrm{SIR}_{\mathrm{post}}$ as defined in Eqn.(2.1). The factor 2 comes from the fact that the interference power is divided equally between its real and imaginary part such that it is halved for DoF.

The distribution of the R-MIMO OGD detector given by Eqn. (2.7) can be summarized as belows:

$$\ln \Lambda(\mathbf{y}) \overset{d}{=} \begin{cases} \mathrm{H}_0: & \frac{1}{2}\chi^2_{2K_e}(0), \\ \mathrm{H}_1: & \frac{1}{2}\chi^2_{2K_e}(2\boldsymbol{\alpha}^\dagger\mathbf{P}^\dagger\mathbf{M}^{-1}\mathbf{P}\boldsymbol{\alpha}). \end{cases}$$

More importantly, the distribution does not depend on the correlation between the subarrays under H_0. This shows the **M**-Constant False Alarm Rate (**M**-CFAR) property of the R-MIMO OGD detector. This property is very useful as it means that the requirement of independence between subarrays can be relaxed using this detector. Note that the detector still depends on the actual covariance matrix but its PDF under H_0 does not.

The effective number of subarrays is given by: $K_e = \tilde{N}\tilde{M}$. It determines the DoF in the distribution of the detector. Given the same SIR, detection performance deteriorates with increasing DoF, as a higher threshold λ is required to maintain the same P_{fa} (see Appendix B.2). However, with fewer subarrays, SIR can vary greatly due to the fluctuations of the target RCS. Hence the choice of K_e will depend on the applications, e.g. large K_e for surveillance and small K_e for direction finding. Indeed, it is shown in [83] that there is an inherent tradeoff between the number of transmit diversity paths and amount of energy integration along each path.

For a detector with a central chi-square distribution under H_0, its P_{fa} is given by:

$$\begin{aligned} P_{fa} &= \mathrm{P}(\Lambda(\mathbf{y}) > \lambda | \mathrm{H}_0), \\ &= \frac{\Gamma(K_e, \lambda)}{\Gamma(K_e)}, \\ &= \mathrm{e}^{-\lambda} \sum_{k=0}^{K_e-1} \frac{\lambda^k}{k!}. \end{aligned} \tag{2.9}$$

For a detector with a non-central chi-square distribution under H_1, its P_d is given by:

$$P_d = Q_{K_e}(\sqrt{2\boldsymbol{\alpha}^\dagger\mathbf{P}^\dagger\mathbf{M}^{-1}\mathbf{P}\boldsymbol{\alpha}}, \sqrt{2\lambda}), \tag{2.10}$$

where $Q_{K_e}(a, b)$ is the Marcum Q-function [84].

2.3.4 Simulation Configurations and Parameters

2.3.4.1 Simulation Configurations

In order to compare different configurations and to study different design parameters (K_e, N_{tx}, N_{rx} etc), we will consider two cases: MISO case which has both transmit spatial diversity and waveform diversity and SIMO case which has only receive spatial diversity.

MISO Case Let there be K_e widely-spaced transmit elements (i.e. only one element per subarray) and one receive subarray with M elements such that the spatial diversity comes from transmit subarrays. The total number of elements N_p is kept the same, i.e. if there are more transmit elements (thus creating more effective subarrays), there will be fewer elements in the receive subarray. This affects the effective total number of elements N_e which in turn affects the SIR gain.

SIMO Case On the other hand, there is only one transmit element for the SIMO case. The spatial diversity comes only from the receive subarrays. With N_p total number of elements, there are $\frac{N_p-1}{K_e}$ elements in each receive subarray (where $\frac{N_p-1}{K_e}$ is an integer) such that $M = M_1 = \cdots = M_{K_e}$. We assume that there is an equal number of receive elements in each receive subarray for simplicity. Having different M_m does not change N_e as it depends only on the total number of receive elements N_{rx}. Similarly, the total effective number of elements remains the same for different K_e since N_{tx} remains one such that $N_e = N_{rx}$. Moreover, as there is only one transmit element, there is no waveform diversity and $N_e = N_p - 1 < N_p$.

The configurations are summarized in Table 2.2 and the variation of N_e with K_e for both cases (MISO and SIMO) is shown in Fig. 2.2. For the MISO configuration, as there is only one element per transmit subarray, $K_e = N_{tx}$. Hence, as discussed in Section 2.2.1, $N_e^{max} = \frac{N_p^2-1}{4} = 42$ is reached when $N_{tx} = \frac{N_p-1}{2} = 6$ and when $N_{tx} = \frac{N_p+1}{2} = 7$. Furthermore, N_e is greater than N_p only when $N_{tx} > 1$ and $N_{rx} > 1$. Hence, $N_e = N_p - 1 < N_p$ when $K_e = 1, 12$ for MISO.

Note that the variation of N_e depends only on N_{tx} and N_{rx}. It does not matter whether the configuration is SIMO or MISO.

2.3.4.2 Generation of Covariance Matrix

The covariance matrix $\mathbf{M}_{ii}$ of each $\mathbf{z}_i$, without loss of generalities, is chosen identically. It is spatially colored and its elements are given by:

$$\mathrm{M}_{ii}(p,q) = \rho^{|p-q|} e^{j\frac{\pi}{2}(p-q)}.$$

The correlation coefficient ρ is chosen to be 0.2 such that there is a slight correlation between different elements of the subarray.

	SIMO	MISO
N_p	13	13
No. of tx subarrays	1	K_e
No. of rx subarrays	K_e	1
No. of elements per tx subarray	1	1
No. of elements per rx subarray	$\frac{N_p-1}{K_e}$	$N_p - K_e$
N_e	$N_p - 1$	$(N_p - K_e)K_e$

Table 2.2: Simulation configurations.

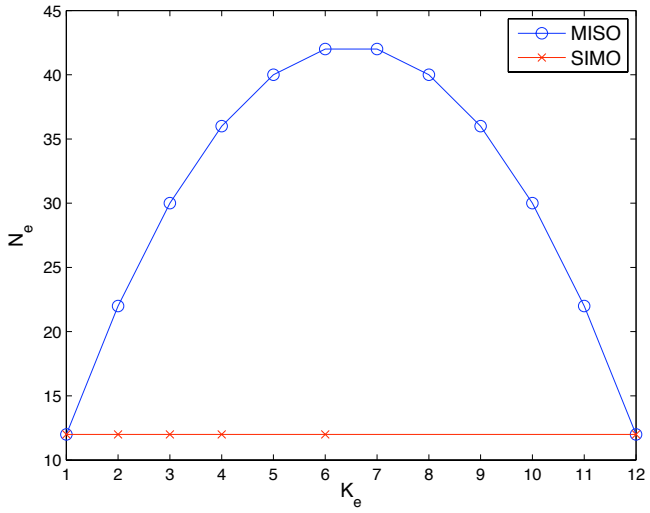

Figure 2.2: Variation of N_e with K_e for MISO and SIMO cases. $N_p = 13$.

For the case where the subarrays are considered to be uncorrelated, the inter-correlation matrices are null matrices. For the case where the subarrays are correlated, the inter-correlation matrices are generated using uniformly distributed variables:

$$\mathrm{M}_{ii'}(p,q) = \tau_{ii'}\rho_{ii'}^{|p-q|}e^{j\frac{\pi}{2}(p-q)}.$$

where $\tau_{ii'}$ and $\rho_{ii'}$ are uniformly distributed in the interval $[0, 0.4]$. Thus, the mean of $\rho_{ii'}$ is equal to ρ. The inclusion of $\tau_{ii'}$ is to make the power of the intercorrelation matrices $M_{ii'}$ smaller than that of the correlation matrices M_{ii}.

2.3.4.3 Generation of Target RCS

Consider the well-known Swerling I target model where the RCS of the target fluctuates from scan to scan according to a Gaussian distribution. In the MIMO configuration where the subarrays are widely separated, the RCS of the target seen

by each subarray pair can also be represented by a Gaussian distribution, i.e. each element of $\boldsymbol{\alpha}$ is independent and identically distributed (i.i.d.) such that

$$\boldsymbol{\alpha} \sim \mathcal{CN}(\mathbf{0}, \sigma_t^2 \mathbf{I}),$$

where σ_t^2 is the power of the target. This is consistent with the target model given in [2]. Hence the MIMO-version of Swerling I target is one which is modeled as a Gaussian process which fluctuates independently from subarray to subarray and also from scan to scan. Within the subarrays, the elements are closely-spaced such that the target RCS is the same for all elements in the same subarray.

Note that while the target RCS is assumed to be different but *deterministic* in the derivation of the detector, it can also be extended to the stochastic case by replacing the $f(\mathbf{y}|\mathrm{H}_1)$ by the conditional density $f(\mathbf{y}|\mathrm{H}_1, \boldsymbol{\alpha})$ in Eqn. (2.5). This means that Eqn. (2.10) is the conditional P_d, given $\boldsymbol{\alpha}$. The unconditional P_d is then obtained by averaging the conditional P_d over the PDF of $\boldsymbol{\alpha}$.

For comparison purposes, we include the case of a stationary isotropic target, i.e.

$$\alpha_i^* \alpha_i = \sigma_t^2, \qquad \forall\ i = 1, \ldots, K_e.$$

Note that the phase of target RCS is different for each subarray while the amplitude is identical for all subarrays.

2.3.5 Simulation Results

2.3.5.1 P_{fa}

To confirm that correlation between subarrays is indeed CFAR under H_0, Monte-Carlo simulations (10^6 runs) are carried out. The number of subarrays K_e is set to be 3 and the number of elements in each subarray $N_{e,i}$ is set to be identical and equal to $N_{e,0} = 6$. The covariance matrix is generated according to Section 2.3.4.2. In Fig. 2.3, we have plotted the curves for P_{fa} against detection threshold λ for the R-MIMO OGD detector when the subarrays are correlated and when they are uncorrelated, as well as the theoretical curve according to Eqn. (2.9). We see that there is perfect agreement between the curves showing that the curves do not depend on the correlation between the subarrays, i.e. it does not depend on the covariance matrix. This confirms the **M**-CFAR property of the new R-MIMO OGD detector.

2.3.5.2 P_d - SIMO

We begin by looking at the case where the target is stationary as described in Section 2.3.4.3. The subarrays are assumed to be correlated according to Section. 2.3.4.2. In Fig. 2.4, P_d against $\mathrm{SIR}_{\mathrm{pre}}$ (dash-dotted lines) and $\mathrm{SIR}_{\mathrm{post}}$ (solid lines) are plotted for $K_e = 3, 6, 12$ and $N_p = 13$ for the SIMO case. Note that the $P_d - \mathrm{SIR}_{\mathrm{pre}}$ curves show the detection performance *with* processing gains while the $P_d - \mathrm{SIR}_{\mathrm{post}}$ curves show the corresponding detection performance if there is no processing gain.

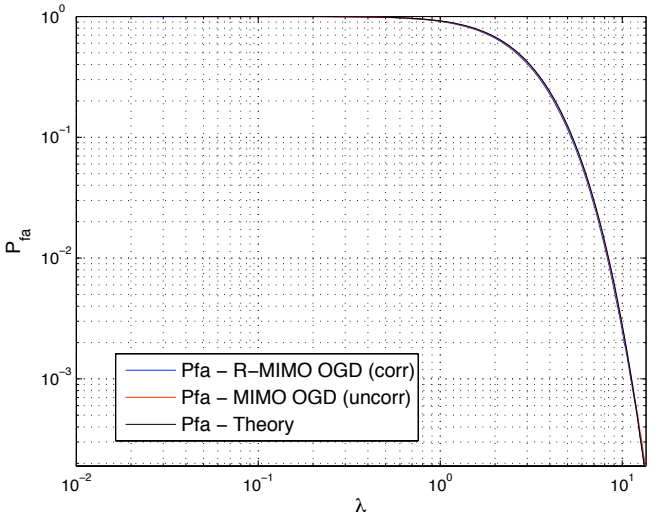

Figure 2.3: P_{fa} against detection threshold λ for Monte-Carlo simulations under Gaussian interference under R-MIMO OGD for correlated and uncorrelated subarrays, as well as theoretical curve.

Here, the effective number of elements remains the same. Hence the SIR gain is almost the same for all K_e. However, with increasing DoF, the detection performance degrades.

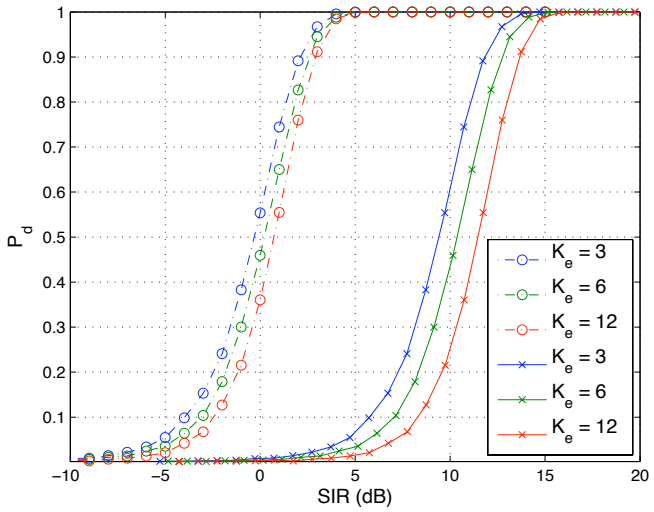

Figure 2.4: P_d against SIR_{pre} (dash-dotted lines) and SIR_{post} (solid lines) under Gaussian interference for correlated subarrays. $P_{fa} = 10^{-3}$. SIMO case. Stationary target model.

When the target is fluctuating, we obtain the plot in Fig. 2.5. As expected, the curves for $K_e = 12$ have hardly changed while the curves for $K_e = 3$ are the

most affected, especially in the high SIR regions. Hence, in the low SIR regions, the detection performance degrades with increasing DoF as before while in the high SIR regions, the detection performance actually improves with increasing DoF.

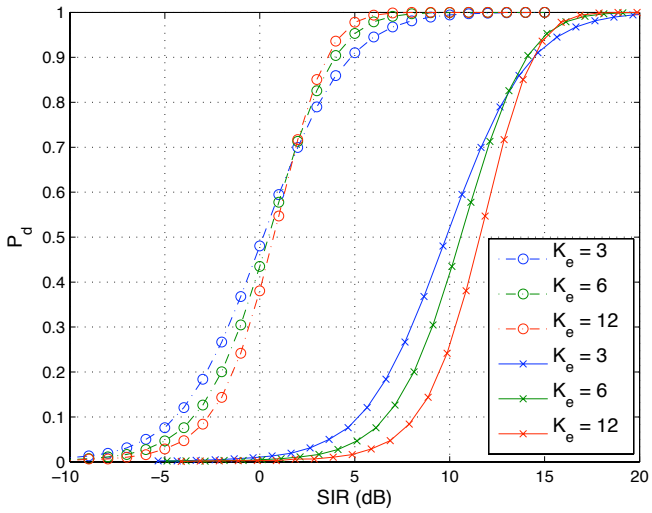

Figure 2.5: P_d against SIR_{pre} (dash-dotted lines) and SIR_{post} (solid lines) under Gaussian interference for correlated subarrays. $P_{fa} = 10^{-3}$. SIMO case. Fluctuating target model.

2.3.5.3 P_d - MISO

As before, we start with the stationary target model. In Fig. 2.6, P_d against SIR_{pre} (dash-dotted lines) and SIR_{post} (solid lines) are plotted for $K_e = 3, 6, 12$ and $N_p = 13$ for the MISO case. Without taking into consideration processing gains, we see from the solid lines that the detection performance degrades with increasing DoF K_e due to the increased threshold. However, after taking into account processing gains (dash-dotted lines), the detection performance for $K_e = 6$ becomes almost identical to that for $K_e = 3$. This is because the effective number of elements N_e changes depending on K_e. According to Fig. 2.2, N_e is larger for $K_e = 6$ than for $K_e = 3$, resulting in a higher SIR gain for $K_e = 6$ to compensate for its higher detection threshold.

In Fig. 2.7, we have plotted the corresponding plot for the fluctuating target model. As expected, the curves for $K_e = 12$ have hardly changed while those for $K_e = 3$ are the most affected, especially for high SIRs. Taking into account processing gains, $K_e = 6$ now has a clear advantage over $K_e = 3$ although they are almost the same when the target is stationary. Although $K_e = 12$ is robust to target fluctuations, it has no processing gain and has a high DoF, resulting in a high threshold. Hence, its detection performance remains worse than that for $K_e = 3, 6$. This, together with results presented in Section 2.3.5.2 generalizes results obtained in [2, 49, 50, 51] where only the statistical MIMO configuration is considered.

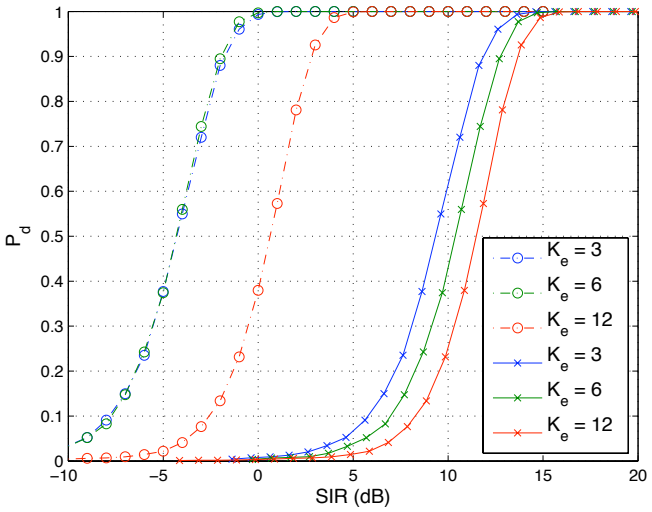

Figure 2.6: P_d against SIR_{pre} (dash-dotted lines) and SIR_{post} (solid lines) under Gaussian interference for correlated subarrays. $P_{fa} = 10^{-3}$. MISO case. Stationary target model.

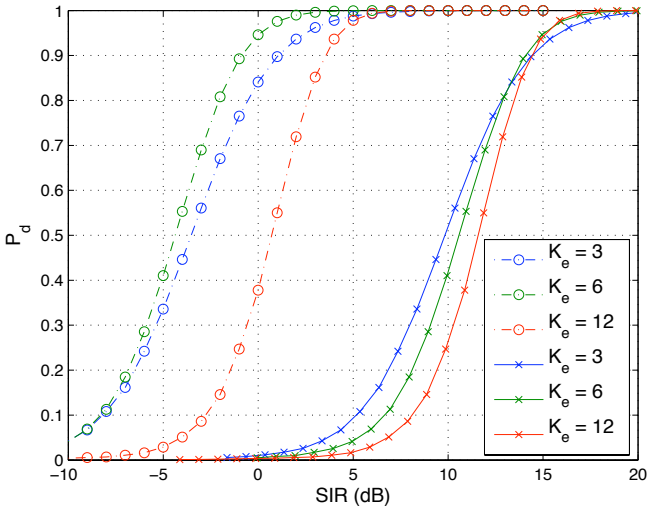

Figure 2.7: P_d against SIR_{pre} (dash-dotted lines) and SIR_{post} (solid lines) under Gaussian interference for correlated subarrays. $P_{fa} = 10^{-3}$. MISO case. Fluctuating target model.

2.4 Adaptive Gaussian Detector

2.4.1 Derivation

In the previous section, we assumed that the covariance matrix was known. As the covariance matrix is usually unknown in reality, we consider in this section the adaptive version of the detector. One common technique of obtaining the adaptive

version is the ad-hoc method of replacing the covariance matrix by its estimate. It is often difficult to obtain sufficient secondary data which contain only interference with the same statistics as that in the test cell. This is especially true for MIMO radars due to its increased dimensions and improved resolutions. In this case, it is better to include the secondary data in the derivation of the detector, as in the case of Kelly's Test proposed in [21]. This is because by including the secondary data in the derivation, both primary and secondary data are used to estimate the covariance matrix. Indeed, it is shown in [21] that for the classical phased-array radar, Kelly's Test has better performance than the ad-hoc adaptive detector when there are few secondary data. Similarly, we derive here the adaptive version of the detector, taking into account the likelihood of all the secondary data.

Assume that we have access to N_s secondary data (containing only interference returns), denoted as: $\mathbf{z}(1), \ldots, \mathbf{z}(N_s)$. Taking into consideration the likelihood of both the received signal and the secondary data, the likelihood ratio test can be written as:

$$\hat{\Lambda}(\mathbf{y}) = \frac{\max\limits_{\mathbf{M},\boldsymbol{\alpha}} f(\mathbf{y}, \mathbf{z}(1), \ldots, \mathbf{z}(N_s)|\mathrm{H}_1)}{\max\limits_{\mathbf{M}} f(\mathbf{y}, \mathbf{z}(1), \ldots, \mathbf{z}(N_s)|\mathrm{H}_0)}.$$

Define the matrices $\mathbf{T}_0$ and $\mathbf{T}_1$ as below:

$$\begin{aligned}
\mathbf{T}_0 &= \frac{1}{N_s+1}\left(\mathbf{y}\mathbf{y}^\dagger + \sum_{l=1}^{N_s}\mathbf{z}(l)\mathbf{z}(l)^\dagger\right), \\
&= \frac{1}{N_s+1}\left(\mathbf{y}\mathbf{y}^\dagger + N_s\widehat{\mathbf{M}}_{SCM}\right), \\
\mathbf{T}_1 &= \frac{1}{N_s+1}\left((\mathbf{y}-\mathbf{P}\boldsymbol{\alpha})(\mathbf{y}-\mathbf{P}\boldsymbol{\alpha})^\dagger + \sum_{l=1}^{N_s}\mathbf{z}(l)\mathbf{z}(l)^\dagger\right), \\
&= \frac{1}{N_s+1}\left((\mathbf{y}-\mathbf{P}\boldsymbol{\alpha})(\mathbf{y}-\mathbf{P}\boldsymbol{\alpha})^\dagger + N_s\widehat{\mathbf{M}}_{SCM}\right),
\end{aligned}$$

where $\widehat{\mathbf{M}}_{SCM}$ is the Sample Covariance Matrix (SCM) of $\mathbf{M}$ and is given by:

$$\widehat{\mathbf{M}}_{SCM} = \frac{1}{N_s}\sum_{l=1}^{N_s}\mathbf{z}(l)\mathbf{z}(l)^\dagger. \tag{2.11}$$

Under H_0, we have

$$\begin{aligned}
f(\mathbf{y}, \mathbf{z}(1), \ldots, \mathbf{z}(N_s)|\mathrm{H}_0) &= \frac{\pi^{-N_e(N_s+1)}}{\|\mathbf{M}\|^{N_s+1}}\exp\left(-\mathbf{y}^\dagger\mathbf{M}^{-1}\mathbf{y} - \sum_{l=1}^{N_s}\mathbf{z}^\dagger(l)\mathbf{M}^{-1}\mathbf{z}(l)\right), \\
&= \left[\frac{1}{\pi^{N_e}\|\mathbf{M}\|}\exp\left(-\mathrm{tr}(\mathbf{M}^{-1}\mathbf{T}_0)\right)\right]^{N_s+1},
\end{aligned}$$

where the second equality is obtained using the identity $\mathrm{tr}(\mathbf{AB}) = \mathrm{tr}(\mathbf{BA})$ [85].

Similarly, under H_1, we have

$$f(\mathbf{y}, \mathbf{z}(1), \ldots, \mathbf{z}(N_s)|\mathrm{H}_1) = \left[\frac{1}{\pi^{N_e}\|\mathbf{M}\|}\exp\left(-\mathrm{tr}(\mathbf{M}^{-1}\mathbf{T}_1)\right)\right]^{N_s+1}.$$

Maximizing with respect to $\mathbf{M}$, we obtain:

$$\begin{aligned}
\max_{\mathbf{M}} f(\mathbf{y}, \mathbf{z}(1), \ldots, \mathbf{z}(N_s)|\mathrm{H}_0) &= f(\mathbf{y}, \mathbf{z}(1), \ldots, \mathbf{z}(N_s)|\mathrm{H}_0)|_{\widehat{\mathbf{M}}=\mathbf{T}_0}, \\
&= \left[\frac{1}{(\pi e)^{N_e}\|\mathbf{T}_0\|}\right]^{N_s+1}. \\
\max_{\mathbf{M}} f(\mathbf{y}, \mathbf{z}(1), \ldots, \mathbf{z}(N_s)|\mathrm{H}_1) &= f(\mathbf{y}, \mathbf{z}(1), \ldots, \mathbf{z}(N_s)|\mathrm{H}_1)|_{\widehat{\mathbf{M}}=\mathbf{T}_1}, \\
&= \left[\frac{1}{(\pi e)^{N_e}\|\mathbf{T}_1\|}\right]^{N_s+1}.
\end{aligned}$$

The detector can also be expressed as:

$$\hat{\Lambda}(\mathbf{y})' = \hat{\Lambda}(\mathbf{y})^{\frac{1}{N_s+1}} = \frac{\|\mathbf{T}_0\|}{\max_{\boldsymbol{\alpha}}\|\mathbf{T}_1\|}. \tag{2.12}$$

Taking the determinant of $\mathbf{T}_0$, we have:

$$\begin{aligned}
\|\mathbf{T}_0\| &= \left(\frac{1}{N_s+1}\right)^{N_e}\|\mathbf{y}\mathbf{y}^\dagger + N_s\widehat{\mathbf{M}}_{SCM}\|, \\
&= \left(\frac{1}{N_s+1}\right)^{N_e}\|\frac{1}{N_s}\mathbf{y}\mathbf{y}^\dagger\widehat{\mathbf{M}}_{SCM}^{-1} + \mathbf{I}\| \cdot \|N_s\widehat{\mathbf{M}}_{SCM}\|, \\
&= \left(\frac{N_s}{N_s+1}\right)^{N_e}\|\widehat{\mathbf{M}}_{SCM}\|\left(1 + \frac{1}{N_s}\mathbf{y}^\dagger\widehat{\mathbf{M}}_{SCM}^{-1}\mathbf{y}\right),
\end{aligned} \tag{2.13}$$

using identities from [85].

Similarly, the determinants of $\mathbf{T}_1$ can be expressed as below:

$$\|\mathbf{T}_1\| = \left(\frac{N_s}{N_s+1}\right)^{N_e}\|\widehat{\mathbf{M}}_{SCM}\|\left(1 + \frac{1}{N_s}(\mathbf{y}-\mathbf{P}\boldsymbol{\alpha})^\dagger\widehat{\mathbf{M}}_{SCM}^{-1}(\mathbf{y}-\mathbf{P}\boldsymbol{\alpha})\right). \tag{2.14}$$

Inserting them in Eqn. (2.12), we get:

$$\begin{aligned}
\hat{\Lambda}(\mathbf{y})' &= \frac{1 + \frac{1}{N_s}\mathbf{y}^\dagger\widehat{\mathbf{M}}_{SCM}^{-1}\mathbf{y}}{\max_{\boldsymbol{\alpha}}(1 + \frac{1}{N_s}(\mathbf{y}-\mathbf{P}\boldsymbol{\alpha})^\dagger\widehat{\mathbf{M}}_{SCM}^{-1}(\mathbf{y}-\mathbf{P}\boldsymbol{\alpha}))}, \\
&= \frac{1 + \frac{1}{N_s}\mathbf{y}^\dagger\widehat{\mathbf{M}}_{SCM}^{-1}\mathbf{y}}{1 + \frac{1}{N_s}\mathbf{y}^\dagger\widehat{\mathbf{M}}_{SCM}^{-1}\mathbf{y} - \frac{1}{N_s}\mathbf{y}^\dagger\widehat{\mathbf{M}}_{SCM}^{-1}\mathbf{P}(\mathbf{P}^\dagger\widehat{\mathbf{M}}_{SCM}^{-1}\mathbf{P})^{-1}\mathbf{P}^\dagger\widehat{\mathbf{M}}_{SCM}^{-1}\mathbf{y}},
\end{aligned}$$

where the second equality is obtained by using the ML estimate of $\boldsymbol{\alpha}$ given by Eqn. (2.6). Note that it is assumed that $N_s \geq N_e$ such that $\widehat{\mathbf{M}}_{SCM}$ is invertible. Re-arranging the equation, we obtain MIMO Kelly's Test [C3]:

$$\frac{\mathbf{y}^\dagger\widehat{\mathbf{M}}_{SCM}^{-1}\mathbf{P}(\mathbf{P}^\dagger\widehat{\mathbf{M}}_{SCM}^{-1}\mathbf{P})^{-1}\mathbf{P}^\dagger\widehat{\mathbf{M}}_{SCM}^{-1}\mathbf{y}}{N_s + \mathbf{y}^\dagger\widehat{\mathbf{M}}_{SCM}^{-1}\mathbf{y}}. \tag{2.15}$$

Remark 2.5.

- *If there is only one subarray, Eqn. (2.15) becomes Kelly's Test [21].*
- *If the covariance matrix* $\mathbf{M}$ *is block diagonal, i.e. the subarrays are uncorrelated, and if this prior information is used in the estimation of* $\mathbf{M}$*, this results in another version of MIMO Kelly's Test:*

$$\prod_{i=1}^{K_e}\left[1-\frac{|\mathbf{p}_i^\dagger\widehat{\mathbf{M}}_{SCM,ii}^{-1}\mathbf{y}_i|^2}{(\mathbf{p}_i^\dagger\widehat{\mathbf{M}}_{SCM,ii}^{-1}\mathbf{p}_i)(N_{s,i}+\mathbf{y}_i^\dagger\widehat{\mathbf{M}}_{SCM,ii}^{-1}\mathbf{y}_i)}\right]^{-N_{s,i}}, \tag{2.16}$$

where $N_{s,i}$ *is the number of secondary data used for the* i*-th subarray and* $N_s=\sum_{i=1}^{K_e}N_{s,i}$*. See Appendix B.3 for derivation and its statistical properties.*

2.4.2 Statistical Properties

The distribution of MIMO Kelly's Test given by Eqn. (2.15) is:

$$\hat{\Lambda}(\mathbf{y})\overset{d}{=}\begin{cases}\mathrm{H}_0: & \beta_{K_e,N_s-N_e+1}(0),\\ \mathrm{H}_1: & \beta_{K_e,N_s-N_e+1}(\gamma_{nc}),\end{cases}$$

where β_{K_e,N_s-N_e+1} is a beta-distributed random variable with parameters K_e and N_s-N_e+1. The beta-distributed random variable is central under H_0 and non-central with non-centrality parameter γ_{nc} under H_1. γ_{nc} is conditional on l_f which is also beta-distributed with parameters $N_s-N_e+K_e+1$ and N_e-K_e:

$$\gamma_{nc}=2\mathrm{SIR}_{\mathrm{post}}\cdot l_f,\qquad l_f\sim\beta_{N_s-N_e+K_e+1,\ N_e-K_e}.$$

The random variable l_f can be considered as a loss factor on $\mathrm{SIR}_{\mathrm{post}}$ due to the estimation of the covariance matrix. We can consider that the total DoF is N_s+1 (primary and secondary data) but N_e-K_e is used to estimate the interference space, hence the resulting DoF is $N_s-N_e+K_e+1$. The average loss is then the ratio between the available DoF and the total DoF. The resulting DoF is split between the target part and the interference part, resulting in the distribution β_{K_e,N_s-N_e+1}.

Remark 2.6.

- *The distribution of the detector* $\beta_{K_e,\ N_s-N_e+1}$ *is valid only when the two parameters* K_e *and* N_s-N_e+1 *are positive (they are integers by definition). Hence we have:*

$$N_s-N_e+1\geq 1\Rightarrow N_s\geq N_e.$$

This is a necessary condition for the SCM to be of full rank.

- *Similarly, for the distribution of the loss factor to be valid, we have*

$$N_e-K_e\geq 1\Rightarrow N_e\geq K_e+1.$$

When $N_e=K_e$*,* l_f *is no longer a random variable.*

Theorem 2.1. *In the case where there is only one effective element per subarray such that $N_e = K_e$, the loss factor becomes one and the non-centrality parameter is simply [C5]:*

$$\gamma_{nc} = 2\ \mathrm{SIR}_{\mathrm{post}}.$$

The proof can be found in Appendix B.4.

It is interesting to note that when $N_e = K_e$, although there is no coherent gain as there is only one effective element per subarray, there is also no loss in the target SIR. This is because the target subspace spans the entire signal space and thus the orthogonal subspace (interference) is null. Since the interference subspace is not estimated, there is no estimation loss on SIR.

The mean or expected value of l_f is given by:

$$E(l_f) = \frac{N_s - N_e + K_e + 1}{N_s + 1}.$$

- Given a fixed N_s, it might be better to choose a smaller N_e and a bigger K_e to have a bigger loss factor (less loss).
- To limit the loss to 3 dB, i.e. $E(l_f) > 0.5$, we need $N_s > 2N_e - 2K_e - 1$, providing $N_s \geq N_e$ is fulfilled such that the SCM is of full rank.
- For the classical phased-array case where $K_e = 1$, we obtain $N_s > 2N_e - 3$ which is the well-known Reed-Mallett-Brennan's rule [22].

The mean of the loss factor $E(l_f)$ for SIMO and MISO cases as defined in Section 2.2 are plotted in Fig. 2.8. Note that $l_f \in [0, 1]$ and there is no SIR loss if $l_f = 1$. N_s is chosen such that it varies between $\max(N_e)$ and $5\max(N_e)$. For the SIMO case, there are some values of K_e that are not possible as it will result in non-integral number of elements in each subarray. For the SIMO case, N_e remains the same for all values of K_e. Hence, we see a clear increase in $E(l_f)$ with increasing K_e and N_s. On the other hand, N_e changes for the MISO case (see Fig. 2.2). As N_e is larger than K_e, we see a clear dependence of $E(l_f)$ on N_e, causing $E(l_f)$ to reach its minimum for $K_e \approx \frac{N_p}{2}$.

The probability of false alarm for the adaptive version is given by:

$$P_{fa} = 1 - I_\lambda(K_e, N_s - N_e + 1),$$

where $I_x(a, b)$ is the regularized incomplete beta function as defined in [86] and λ is the detection threshold. According to Eqn. (8.17.20) in [87], we have:

$$I_x(a, b) = I_x(a + 1, b) + \frac{x^a(1 - x)^b}{aB(a, b)}, \tag{2.17}$$

where $B(a, b)$ is the beta function. As the second term in Eqn. (2.17) is positive, $I_x(a, b) > I_x(a + 1, b)$, i.e. for the same threshold, P_{fa} is higher for larger K_e. More importantly, for the same P_{fa}, a higher threshold is required for larger K_e as in the case of the detector with known interference parameters.

A simple analytical expression for P_d cannot be found as the non-centrality parameter γ_{nc} is conditional on another beta-distributed random variable.

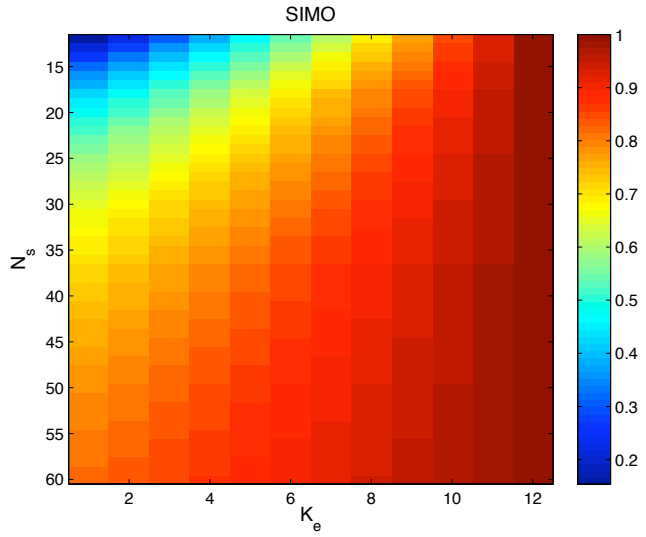

(a) SIMO case

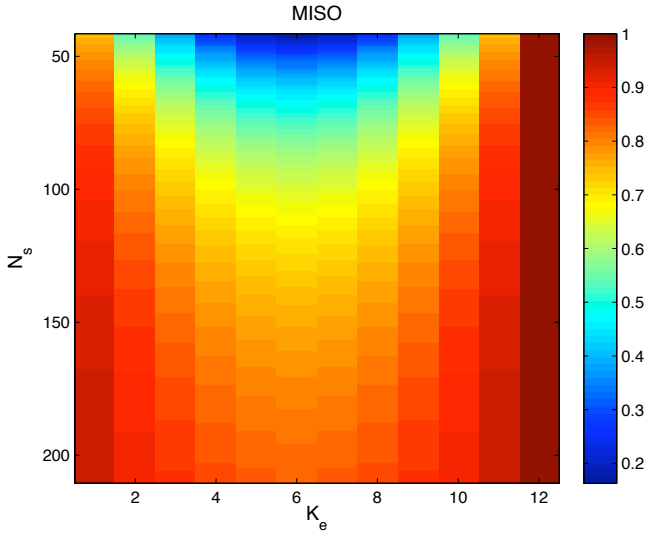

(b) MISO case

Figure 2.8: Mean value of loss factor $E(l_f)$ against K_e and N_s.

2.4.3 Simulation Results

In this section, we consider only the stationary target model so as to better study the effects of changing different parameters like K_e, N_e and N_s. However, we expect the adaptive detector to be more robust to target fluctuations with large K_e.

2.4.3.1 P_d - SIMO

P_d is plotted against SIR_{pre} (dash-dotted lines) and SIR_{post} (solid lines) in Fig. 2.9 for $K_e = 3, 6, 12$ and $N_p = 13$ using the stationary target model. $N_s = 20$ secondary data are used to estimate the covariance matrix. Without taking into consideration processing gains and estimation loss, the detection performance (solid lines) degrades with increasing K_e due to increased threshold, as for the case of the non-adaptive detector. Here, the effective number of elements remains the same. Hence the SIR gain is almost the same for all K_e. However, $E(l_f)$ increases with increasing K_e (see Fig. 2.8(a)), especially when there are few secondary data ($N_s = 20 < 2N_e$). After taking into account the estimation loss, the detection performance (dashed-dotted lines) actually improves with increasing K_e.

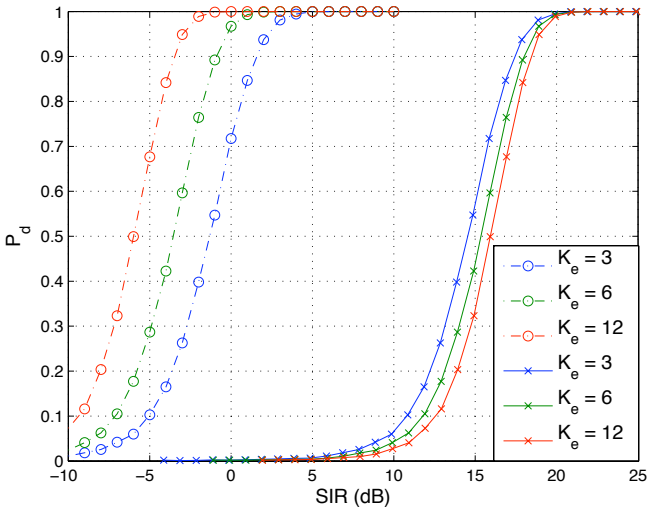

Figure 2.9: P_d against SIR_{pre} (dash-dotted lines) and SIR_{post} (solid lines) under Gaussian interference for correlated subarrays. $P_{fa} = 10^{-3}$. SIMO case. Stationary target model. $N_s = 20$.

2.4.3.2 P_d - MISO

In Fig. 2.10, we have plotted P_d against SIR_{pre} for different K_e, using the stationary target model and with $N_p = 13$ and $N_s = 50, 80$. There are several factors that can affect the detection performance. As mentioned earlier, the threshold increases with increasing K_e for the same P_{fa}, hence deteriorating the detection performance. The SIR gain is proportional to N_e and it reaches its maximum at $K_e \approx \frac{N_p}{2}$ and its minimum at $K_e = 1$ and $K_e = N_p - 1$. Finally, the estimation loss is inversely proportional to the SIR gain as l_f is smaller when N_e is large, given a fixed N_s. Note that the differences are larger when N_s is small than when N_s is large (see Fig. 2.8(b)).

Indeed, when $N_s = 50$ (Fig. 2.10(a)), $K_e = 6, 7$ have the worst detection performance as the SIR gain from having large N_e is not enough to compensate for its small $E(l_f)$ as $N_s \approx N_e$. Moreover, detection performance is better for smaller K_e than for bigger K_e. On the other hand, when $N_s = 80$ (Fig. 2.10(b)), $N_s \approx 2N_e$ even for $K_e = 6, 7$, resulting in a reasonably good $E(l_f)$ which is then compensated for by their large SIR gain. In fact, the detection performance is quite similar for most values of K_e except for large K_e which are penalized too much by their high threshold.

Next, we have plotted P_d against SIR_{pre} for different N_s/N_e, $K_e = 3$ and $N_p = 13$ in Fig. 2.11. As before, the stationary target model is considered. We see that the minimum number of secondary data required is $N_s/N_e = 2$. While the detection performance improves with increasing N_s, the improvement is no longer significant for $N_s/N_e > 3$.

2.5 Non-Gaussian Detector with Known Interference Parameters

2.5.1 Signal Model

In this section, we consider non-Gaussian interference where the power of the interference is different and independent for each subarray. We recall here the signal model after matched filtering given by Eqn. (2.3):

$$\mathbf{y}_i = \alpha_i \mathbf{p}_i + \mathbf{z}_i, \qquad \forall\ i = 1, \ldots, K_e,$$

where $\mathbf{y}_i$, $\mathbf{p}_i$ and $\mathbf{z}_i$ are the received signal, the bistatic steering vector and the interference returns for the i-th subarray, respectively. α_i is the target RCS seen by the i-th subarray. $K_e = \tilde{M}\tilde{N}$ is the effective number of subarrays while $N_{e,i}$ is the effective number of elements in the i-th subarray and the total effective number of elements N_e is $N_e = \sum_{i=1}^{K_e} N_{e,i}$.

As mentioned earlier, non-Gaussian interference is considered in this section. The non-Gaussian statistical model we use is the SIRV model [14, 15, 16]. This model writes interference returns as the product of a complex Gaussian random process $\mathbf{x}$ (*speckle*) and the square-root of a positive random variable τ (*texture*):

$$\mathbf{z} = \sqrt{\tau}\mathbf{x}.$$

The vector $\mathbf{x}$ has zero mean and covariance matrix $\mathbf{M}$, denoted by $\mathcal{CN}(\mathbf{0}, \mathbf{M})$. The matrix $\mathbf{M} = E(\mathbf{x}\mathbf{x}^\dagger)$ is assumed to be normalized such that $tr(\mathbf{M}) = N_x$ where N_x is the length of $\mathbf{x}$ for identifiability considerations [23]. The PDF of a SIRV is then given by:

$$p_{\mathbf{z}}(\mathbf{z}) = \int_0^\infty g_{\mathbf{z}}(\mathbf{z}, \tau) p(\tau) d\tau,$$

where $p(\tau)$ is the unknown texture PDF and

$$g_{\mathbf{z}}(\mathbf{z}, \tau) = \frac{1}{(\pi\tau)^{N_x}|\mathbf{M}|} \exp\left(-\frac{\mathbf{z}^\dagger \mathbf{M}^{-1}\mathbf{z}}{\tau}\right).$$

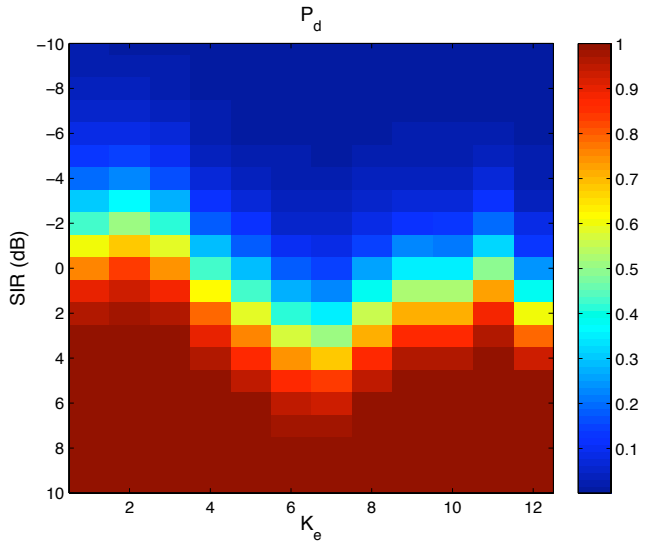

(a) $N_s = 50$

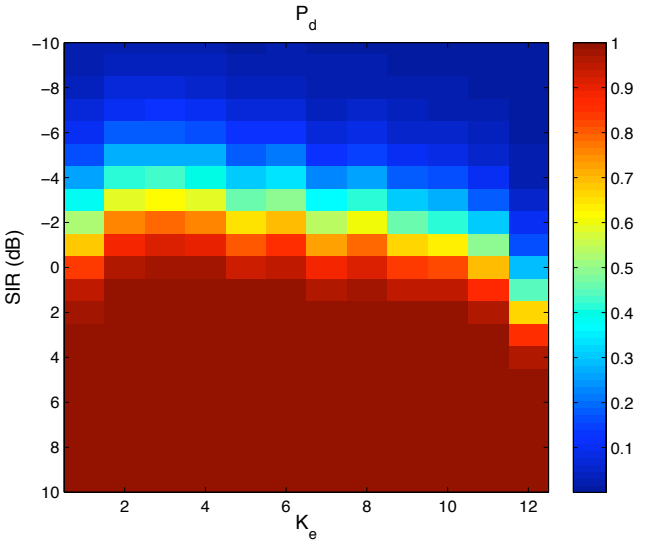

(b) $N_s = 80$

Figure 2.10: P_d against $\mathrm{SIR}_{\mathrm{pre}}$ and K_e under Gaussian interference for correlated subarrays. $P_{fa} = 10^{-3}$ and $N_p = 13$. MISO case. Stationary target model.

The speckle models temporal fluctuations of interference while the texture models spatial fluctuations of interference power. The SIRV can model different non-Gaussian interference depending on the chosen texture, with Gaussian interference as the special case where the texture is a constant. Experimental radar interference measurements [10, 11, 12, 13] have been shown to fit the SIRV model well. Furthermore, it also has a Gaussian kernel which means that certain classical results can still be applied. For example, the ML estimates of target parameters are given

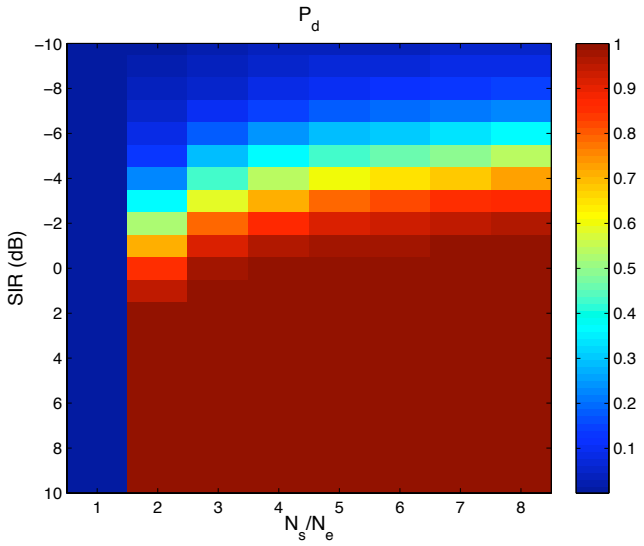

Figure 2.11: P_d against SIR_{pre} and N_s/N_e under Gaussian interference for correlated subarrays. $P_{fa} = 10^{-3}$ and $K_e = 3$. MISO case. Stationary target model.

by the maximization of the traditional matched filter.

2.5.2 Derivation

As before, we consider the detection problem as a binary hypothesis test:

$$\begin{cases} \text{H}_0: & \mathbf{y}_i = \mathbf{z}_i, \\ \text{H}_1: & \mathbf{y}_i = \alpha_i \mathbf{p}_i + \mathbf{z}_i, \end{cases} \qquad i = 1, \ldots, K_e.$$

Under the hypothesis H_0, it is assumed that the received signal contains only interference returns and hence there is no target. Under the hypothesis H_1, it is assumed that the received signal contains a deterministic signal on top of the interference returns and hence a target is present at the location (x, y). It is assumed here that the covariance matrices of all subarrays are known. Note that while the dimension of the received signal, $N_{e,i}$ can be one, its steering vector does not give any information if its length is one. Hence it is assumed that at least one $N_{e,i}$ is greater than one.

We begin with the case where $K_e = 1$ ($\tilde{M} = 1$ and $\tilde{N} = 1$). The dimension of the received signal is $N_{e,1} = M_1 N_1$. The classical likelihood ratio test is given by:

$$\Lambda(\mathbf{y}_1) = \frac{f(\mathbf{y}_1|\text{H}_1)}{f(\mathbf{y}_1|\text{H}_0)} \underset{\text{H}_0}{\overset{\text{H}_1}{\gtrless}} \eta_1,$$

where η_1 is the detection threshold.

If we assume that the covariance matrix $\mathbf{M}_1$ is known and according to [19], $f(\mathbf{y}_1|\text{H}_1)$ and $f(\mathbf{y}_1|\text{H}_0)$ are replaced by their estimates and asymptotically, we ob-

tain:

$$\Lambda_1(\mathbf{y}_1)^{N_{e,1}} = \left[1 - \frac{|\mathbf{p}_1^\dagger \mathbf{M}_1^{-1}\mathbf{y}_1|^2}{(\mathbf{p}_1^\dagger \mathbf{M}_1^{-1}\mathbf{p}_1)(\mathbf{y}_1^\dagger \mathbf{M}_1^{-1}\mathbf{y}_1)}\right]^{-N_{e,1}} \underset{\mathrm{H}_0}{\overset{\mathrm{H}_1}{\gtrless}} \eta_1, \tag{2.18}$$

which is equivalent to:

$$1 - \frac{1}{\Lambda_1(\mathbf{y}_1)} = \frac{|\mathbf{p}_1^\dagger \mathbf{M}_1^{-1}\mathbf{y}_1|^2}{(\mathbf{p}_1^\dagger \mathbf{M}_1^{-1}\mathbf{p}_1)(\mathbf{y}_1^\dagger \mathbf{M}_1^{-1}\mathbf{y}_1)} \underset{\mathrm{H}_0}{\overset{\mathrm{H}_1}{\gtrless}} \frac{\sqrt[N_{e,1}]{\eta_1} - 1}{\sqrt[N_{e,1}]{\eta_1}},$$

and leads to the GLRT-Linear Quadratic (GLRT-LQ) test. The same test is derived in [17] through an asymptotic development of the test statistic in the GLRT and in [18] it is based on the ML estimation of the interference power.

Considering *Gaussian* interference with unknown power, the authors [88] included the ML estimate for interference variance in the derivation of the GLRT, resulting in the CFAR Matched Subspace Detector (MSD) which has the same form as the GLRT-LQ test. Being a "cosine-squared" statistic that measures the fraction of energy the measurement has in the signal subspace [89], the CFAR MSD is invariant to data scaling.

Remark 2.7. *The GLRT-LQ or CFAR MSD detector has the desirable property of being homogeneous in terms of* $\mathbf{p}$, $\mathbf{M}$ *and* $\mathbf{y}$ *such that it is invariant to data scaling. Consequently, the texture of the non-Gaussian interference cancels out under* H_0 *such that the detector is texture-CFAR.*

Note that no explicit form on the steering vector is assumed in the derivation of the GLRT-LQ. Thus, these detectors can also be applied to our case where $\mathbf{p}_1 = \mathbf{a}(\theta_{r,1}) \otimes \mathbf{v}(\theta_{t,1})$.

We consider now the general case where $\tilde{M} \geq 1$ and $\tilde{N} \geq 1$. As the transmit-receive subarrays are widely separated, the interference returns can be considered to be independent, hence $\mathbf{z}_i$ are independent and the likelihood ratio test becomes:

$$\begin{aligned}
\Lambda(\mathbf{y}) &= \frac{f(\mathbf{y}|\mathrm{H}_1)}{f(\mathbf{y}|\mathrm{H}_0)}, \\
&= \frac{\prod_{i=1}^{K_e} f(\mathbf{y}_i|\mathrm{H}_1)}{\prod_{i=1}^{K_e} f(\mathbf{y}_i|\mathrm{H}_0)}, \\
&= \prod_{i=1}^{K_e} \frac{f(\mathbf{y}_i|\mathrm{H}_1)}{f(\mathbf{y}_i|\mathrm{H}_0)} \underset{\mathrm{H}_0}{\overset{\mathrm{H}_1}{\gtrless}} \eta,
\end{aligned}$$

where $\mathbf{y}$ is the concatenation of all the received signals $\mathbf{y} = [\mathbf{y}_1^T, \cdots, \mathbf{y}_{K_e}^T]^T$.

Using Eqn. (2.18), the GLRT-LQ extended to the MIMO case is given by:

$$\begin{aligned}\Lambda(\mathbf{y}) &= \prod_{i=1}^{K_e}\left[1-\frac{|\mathbf{p}_i^\dagger\mathbf{M}_i^{-1}\mathbf{y}_i|^2}{(\mathbf{p}_i^\dagger\mathbf{M}_i^{-1}\mathbf{p}_i)(\mathbf{y}_i^\dagger\mathbf{M}_i^{-1}\mathbf{y}_i)}\right]^{-N_{e,i}}, \\ &= \prod_{i=1}^{K_e}\Lambda_i(\mathbf{y}_i)^{N_{e,i}}, \end{aligned} \tag{2.19}$$

where $\mathbf{M}_i$ is the covariance matrix of $\mathbf{y}_i$. It is interesting to note that the detector of each subarray $\Lambda_i(\mathbf{y}_i)$ has a power of $N_{e,i}$. It acts as a weighting factor for each subarray. Subarrays with larger $N_{e,i}$ have higher SIR gain and consequently the corresponding detectors has a better detection performance. It is logical that these detectors contribute more to the resulting final detector through the weighting factor.

2.5.3 Statistical Properties

Under H_0, the received signal contains only interference returns:

$$\mathbf{y}_i = \mathbf{z}_i = \sqrt{\tau_i}\mathbf{x}_i,$$

where $\mathbf{x}_i \sim \mathcal{CN}(\mathbf{0}, \mathbf{M}_i)$. As τ_i is cancelled out in Eqn. (2.19), $\Lambda_i(\mathbf{y}_i) = \Lambda_i(\mathbf{x}_i)$, i.e. the detector remains the same under Gaussian and non-Gaussian interference. This means that the distribution of the detector remains the same under H_0.

According to [89], the GLRT-LQ or CFAR MSD detector under *Gaussian* interference can be expressed in terms of an F-statistics:

$$\frac{|\mathbf{p}_i^\dagger\mathbf{M}_i^{-1}\mathbf{y}_i|^2}{(\mathbf{p}_i^\dagger\mathbf{M}_i^{-1}\mathbf{p}_i)(\mathbf{y}_i^\dagger\mathbf{M}_i^{-1}\mathbf{y}_i)} \overset{d}{=} \frac{t_i}{t_i+1},$$

where $(N_{e,i}-1)t_i$ is a centralized F-distributed random variable with parameters 2 and $2N_{e,i}-2$. Note that the distribution of $\frac{t_i}{t_i+1}$ can also be expressed in terms of a beta distribution: $\beta_{1,N_{e,i}-1}$.

From Eqn. (2.19), we see that when the number of elements in each subarray $N_{e,i}$ is not a constant, the expression for MIMO GLRT-LQ is very complicated and it is difficult for its detection performance to be analyzed theoretically. Monte-Carlo simulations have to be run in such cases to obtain the detection performance. Instead, in this section, we will consider the particular case where $N_{e,i} = N_{e,0}$ is a constant such that the distribution of all the individual detectors is the same.

Let the number of elements in each transmit and receive subarray be the same, i.e.

$$\begin{cases} M_m = M_{m'}, & m \neq m', \\ N_n = N_{n'}, & n \neq n', \end{cases}$$

such that the effective number of elements in each subarray is the same:

$$M_m N_n = N_{e,0}, \qquad \begin{cases} m = 1, \ldots, \tilde{M}, \\ n = 1, \ldots, \tilde{N}. \end{cases}$$

Eqn. (2.19) can thus be simplified to be:

$$\prod_{i=1}^{K_e} \Lambda_i(\mathbf{y}_i) \underset{\mathrm{H}_0}{\overset{\mathrm{H}_1}{\gtrless}} \eta^{1/N_{e,0}} = \lambda, \tag{2.20}$$

where

$$\Lambda_i(\mathbf{y}_i) = \left[\frac{1}{1 - \frac{|\mathbf{p}_i^\dagger \mathbf{M}_i^{-1} \mathbf{y}_i|^2}{(\mathbf{p}_i^\dagger \mathbf{M}_i^{-1} \mathbf{p}_i)(\mathbf{y}_i^\dagger \mathbf{M}_i^{-1} \mathbf{y}_i)}} \right].$$

Note that the distribution of all the individual detectors is now the same.

Theorem 2.2 (P_{fa} of the new MIMO GLRT-LQ detector)**.** *Given a MIMO radar system containing K_e subarrays and $N_{e,0}$ elements ($N_{e,0} > 1$) in each subarray and using the detector given in Eqn. (2.20), the probability of false alarm is given by [J1]:*

$$P_{fa} = \lambda^{-N_{e,0}+1} \sum_{k=0}^{K_e-1} \frac{(N_{e,0}-1)^k}{k!} (\ln \lambda)^k. \tag{2.21}$$

The proof of Theorem 2.2 can be found in Appendix B.5.

Remark 2.8.

- *When there is only one subarray ($K_e = 1$), the probability of false alarm is given by $P_{fa} = \lambda^{-N_{e,0}+1}$. This is equivalent to the expression derived in [17]. When there is only one element in the subarray ($N_e = 1$), this gives us $P_{fa} = 1$. This implies that the test breaks down as more than one element is required to estimate the interference power. Note however that it is possible to estimate the interference power with only one element if multiple pulses are considered.*
- *P_{fa} depends only on K_e and $N_{e,0}$ and not on the interference parameters, hence showing the texture-CFAR property of the test given by Eqn. (2.20). Moreover, it is clear that the detector does not depend on the covariance matrices which can be different for each transmit-receive subarray.*
- *The closed-form expression is useful for the analysis of detection performance. Using Eqn. (2.21), the threshold to be used in the detection test is theoretically set to ensure a given P_{fa}.*

Even with the simplifying assumption that $N_{e,i} = N_{e,0}$ is a constant, a simple analytical expression of P_d cannot be found as the detector is not invariant to the interference properties under H_1.

2.5.4 Simulation Configurations and Parameters

The parameters used for the Monte-Carlo simulations are presented in Table 2.3. The generation of target RCS is as described in Section 2.3.4.3.

$\tilde{M}$	$\tilde{N}$	M_m	N_n	$K_e = \tilde{M}\tilde{N}$	$N_{e,0} = M_m N_n$
3	2	4	3	6	12

Table 2.3: Parameters used for Monte-Carlo simulations.

Due to Remark 2.8, the covariance matrix $\mathbf{M}_i$ of each $\mathbf{y}_i$, without loss of generalities, is chosen identically and equal to $\mathbf{M}$. $\mathbf{M}$ is spatially colored and its elements are given by:

$$\mathrm{M}(p,q) = \rho^{|p-q|} e^{j\frac{\pi}{2}(p-q)},$$

where ρ is the correlation coefficient and it is chosen to be 0.2 such that there is a slight correlation between different elements of the subarray.

Experimental radar interference measurements have shown that the texture can be distributed according to a Gamma distribution [11, 12] or a Weibull one [90, 91]. When the texture is Gamma-distributed, the resulting interference corresponds to one that is K-distributed. This has been widely studied in the literature, see e.g. [18, 92, 93]. The PDF and mean of the Gamma and Weibull distributions are given in Appendix A.6 and Appendix A.7, respectively.

The interference power for each element, σ^2, is given by:

$$\sigma^2 = E(\tau).$$

In order to keep σ^2 constant, the two parameters of the distributions are set such that the statistical mean of the texture remains the same. In this simulation, σ^2 is chosen to be one. The parameters used to simulate the texture are shown in Table 2.4. The parameters are chosen such that for each texture, the first case is an instance of impulsive interference while the second one is more similar to the Gaussian case. For comparison purposes, the Gaussian case where $p(\tau) = \sigma^2\delta(\tau-1)$, is also simulated. In this case, σ^2 is also equal to one. The different types of interference are plotted in Fig. 2.12. The K-distributed interference with $a = 0.5$ and Weibull-textured interference with $b = 0.658$ contain many spikes with high power although the average power is the same as that of the Gaussian interference.

	Texture distribution	a	b
1	Gamma	0.5	$\frac{\sigma^2}{a} = 2$
2	Gamma	2	$\frac{\sigma^2}{a} = 0.5$
1	Weibull	$\frac{\sigma^2}{\Gamma(1+\frac{1}{b})} = 0.7418$	0.658
2	Weibull	$\frac{\sigma^2}{\Gamma(1+\frac{1}{b})} = 1.1233$	1.763

Table 2.4: Texture parameters used for Monte-Carlo simulations.

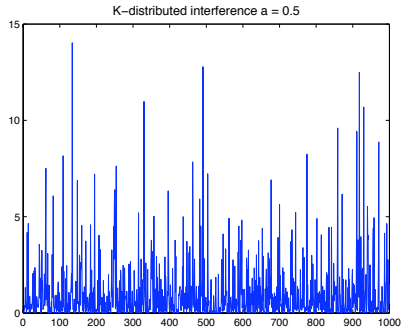

(a) K-distributed, $a = 0.5$

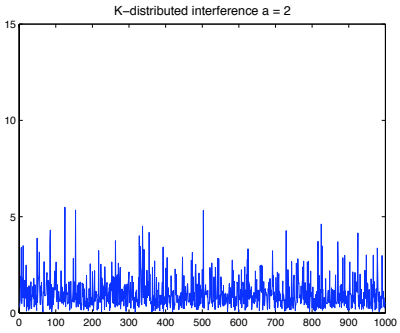

(b) K-distributed, $a = 2$

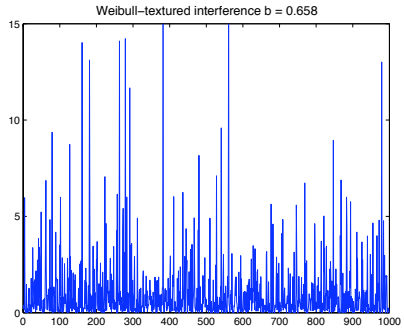

(c) Weibull-textured, $b = 0.658$

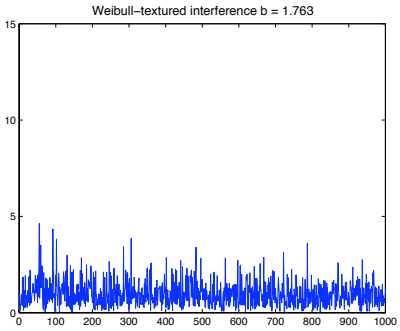

(d) Weibull-textured, $b = 1.763$

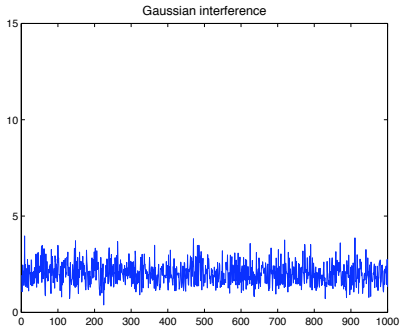

(e) Gaussian

Figure 2.12: Power against samples for the different types of interference. $2\sigma^2 = 2$ for all cases.

2.5.5 Simulation Results

2.5.5.1 P_{fa}

To verify Theorem 2.2, Monte-Carlo simulations ($N_{MC} = 10^6$) are carried out. On Fig. 2.13, we have plotted the curves P_{fa} against the detection threshold λ for different types of interference: Gaussian, K-distributed and Weibull-textured.

We see that there is perfect agreement between the theory given by Theorem 2.2 and the simulation. The texture-CFAR property can also be seen clearly since the curves do not depend on the distribution of the texture.

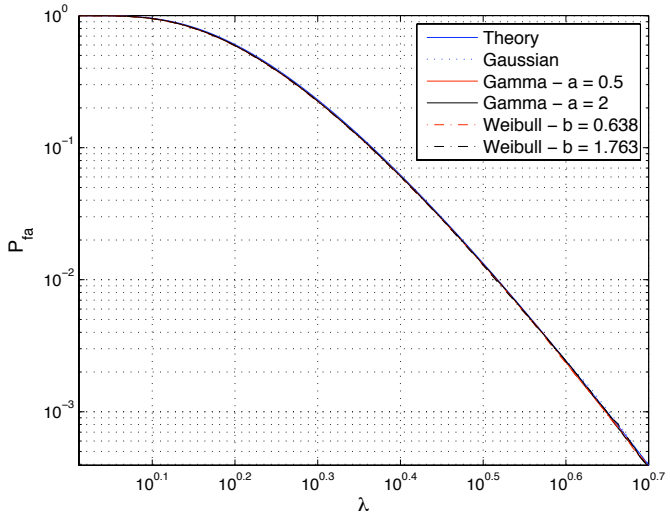

Figure 2.13: P_{fa} against detection threshold λ for theoretical calculations and Monte-Carlo simulations under Gaussian interference and non-Gaussian interference with Gamma and Weibull textures.

2.5.5.2 P_d - Gaussian Interference

Only one configuration has been defined in Section 2.5.4 as the aim of the simulations is not to study the different configurations but rather to compare the detection performance of the non-Gaussian detector MIMO GLRT-LQ to the Gaussian one under different types of interference. For comparison purposes, the MIMO-OGD detector which is optimum under Gaussian interference is considered (see Eqn. (2.8)):

$$\Lambda(\mathbf{y}) = \sum_{i=1}^{K_e} \frac{|\mathbf{p}_i^\dagger \mathbf{M}_i^{-1} \mathbf{y}_i|^2}{\mathbf{p}_i^\dagger \mathbf{M}_i^{-1} \mathbf{p}_i}. \tag{2.22}$$

We begin by considering Gaussian interference. In Fig. 2.14, P_d against SIR_{pre} is plotted for MIMO GLRT-LQ and MIMO OGD, considering both stationary and fluctuating target models as described in Section 2.3.4.3. P_{fa} is set to be 0.001 and $N_{MC} = 10^4$.

Firstly, we note that the MIMO GLRT-LQ incurs a loss of about 0.5 dB of SIR compared to MIMO OGD for both targets. This is expected since MIMO OGD is the optimum detector under Gaussian interference. This can be considered to be a CFAR loss, i.e. the additional loss suffered by MIMO GLRT-LQ compared to the optimum case in exchange for its texture-CFAR properties.

Secondly, we see that under Gaussian interference, both MIMO GLRT-LQ and MIMO OGD are almost equally affected by the fluctuations of the target, both losing about 4 dB of SIR. However, the shape of detection curve remains almost unchanged as there are six subarrays, i.e. six independent target aspects.

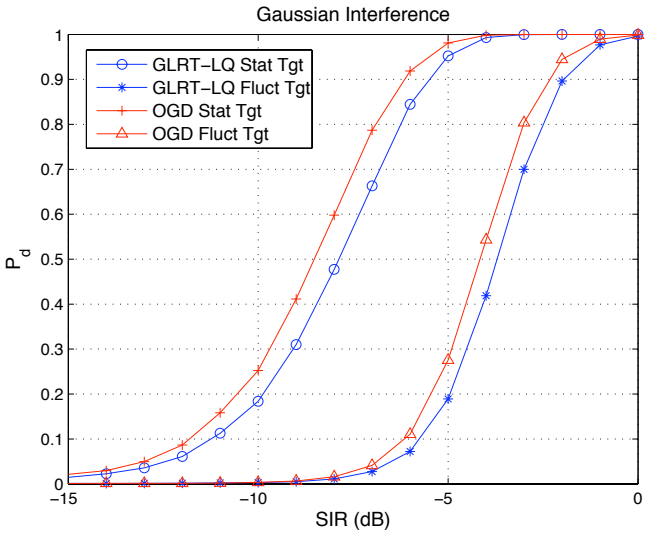

Figure 2.14: P_d against SIR_{pre} where the interference is Gaussian, considering both stationary and fluctuating targets and both MIMO GLRT-LQ and MIMO OGD. $P_{fa} = 0.001$.

2.5.5.3 P_d - Non-Gaussian Interference

The detection performance for MIMO GLRT-LQ and MIMO OGD under K-distributed interference is shown in Fig. 2.15. The interference is more impulsive for smaller values of a. We see that when $a = 0.5$, MIMO GLRT-LQ performs much better than MIMO OGD. This is because for MIMO OGD, the big variation of interference power results in a high detection threshold to maintain the same P_{fa}, as seen from Table 2.5. The increase in threshold results in a drop in detection performance.

a	0.5	2
λ	45.327	25.713

Table 2.5: Detection threshold for MIMO OGD under K-distributed interference for different a.

On the other hand, there are normalizing terms $\mathbf{y}_i^\dagger \mathbf{M}_i^{-1} \mathbf{y}_i$ in MIMO GLRT-LQ to take into account this variation in the regulation of false alarms such that the threshold remains constant at $\lambda = 4.463$. Moreover, the big variation of interference power enables the MIMO GLRT-LQ to detect very weak targets ($P_d = 0.25$ at

SIR $= -25$dB) as the interference power is sometimes much lower than the expected value. However, this advantage of MIMO GLRT-LQ is slightly offset when the target is fluctuating. This is because the target power can also be lower than the expected value (the variation in target power is much smaller though since it is modeled as a Gaussian variable). Overall, when the target is fluctuating, MIMO GLRT-LQ is more affected than MIMO OGD when the interference is impulsive and the difference becomes small when the interference is less impulsive. *However, the detection performance of MIMO GLRT-LQ remains better under non-Gaussian interference, regardless of the target model.*

The performance results for interference with Weibull-distributed texture can be seen in Fig. 2.16. For this case, the interference is more impulsive for smaller values of b. As before, the detection threshold for MIMO OGD increases greatly when the interference is impulsive ($b = 0.658$) as seen in Table 2.6 while that for MIMO GLRT-LQ remains the same at $\lambda = 4.463$, regardless of the texture.

As expected, MIMO GLRT-LQ performs much better than MIMO OGD when the interference is impulsive and almost the same when the interference is less impulsive. This shows the advantage of the MIMO GLRT-LQ: its robustness to different types of non-Gaussian interference that can be modeled by the SIRV. We observe also the same effects of fluctuating targets as in the previous case.

b	0.658	1.763
λ	51.8113	22.344

Table 2.6: Detection threshold for MIMO OGD under Weibull-textured interference for different b.

2.6 Adaptive Non-Gaussian Detector

2.6.1 Derivation

In this section, we consider the adaptive version of the detector which is obtained by the ad-hoc method of replacing the covariance matrix $\mathbf{M}_i$ by its estimate $\widehat{\mathbf{M}}_i$:

$$\hat{\Lambda}(\mathbf{y}) = \prod_{i=1}^{K_e} \hat{\Lambda}_i(\mathbf{y}_i)^{N_{e,i}} = \prod_{i=1}^{K_e} \left[1 - \frac{|\mathbf{p}_i^\dagger \widehat{\mathbf{M}}_i^{-1} \mathbf{y}_i|^2}{(\mathbf{p}_i^\dagger \widehat{\mathbf{M}}_i^{-1} \mathbf{p}_i)(\mathbf{y}_i^\dagger \widehat{\mathbf{M}}_i^{-1} \mathbf{y}_i)} \right]^{-N_{e,i}}. \tag{2.23}$$

The ad-hoc method is employed here due to the increased complexity of the non-Gaussian detector. Moreover, it is a good approximation as it has been shown in [89] for $K_e = 1$ that Eqn. (2.23) is obtained if the texture is unknown but *deterministic* and the likelihood functions are maximized over this additional parameter.

Under Gaussian interference, the classical SCM (defined previously in Eqn. (2.11))

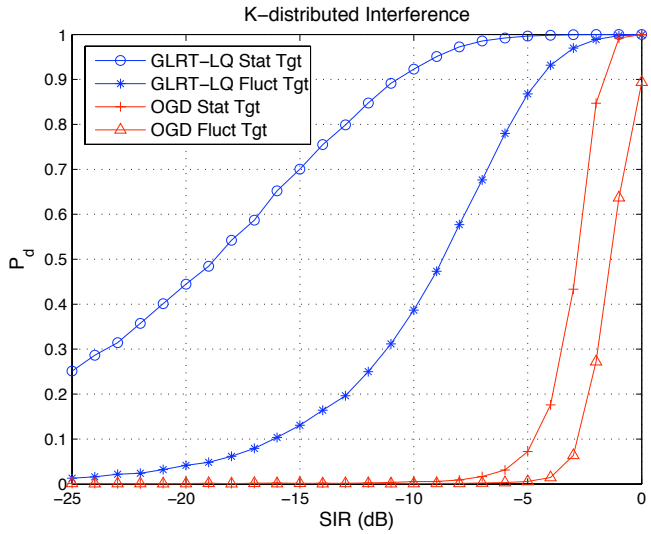

(a) K-distributed, $a = 0.5$

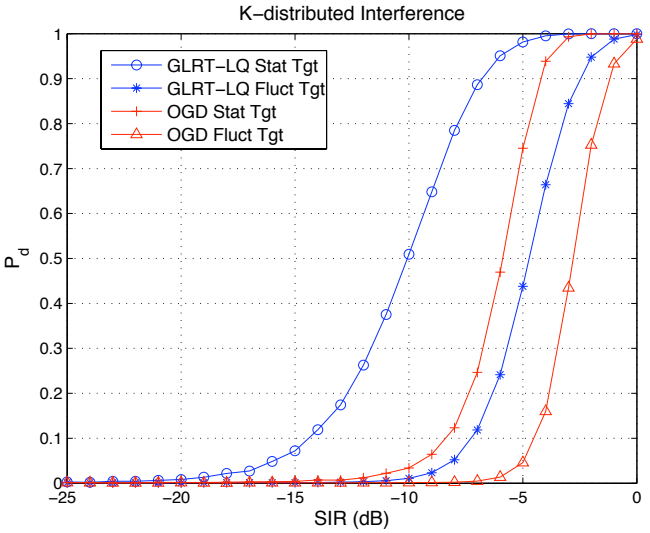

(b) K-distributed, $a = 2$

Figure 2.15: P_d against SIR_{pre}, considering both the stationary and fluctuating targets and both MIMO GLRT-LQ and MIMO OGD. $P_{fa} = 0.001$.

is the ML estimate, given by:

$$\widehat{\mathbf{M}}_{SCM,i} = \frac{1}{N_{s,i}} \sum_{l=1}^{N_{s,i}} \mathbf{x}_i(l)\mathbf{x}_i^{\dagger}(l), \tag{2.24}$$

where $\mathbf{x}_i(l) \sim \mathcal{CN}(\mathbf{0}, \mathbf{M}_i)$ are the i.i.d. secondary data and $N_{s,i}$ is the number of secondary data used to estimate the SCM for the i-th subarray. The SCM follows the complex Wishart distribution, denoted as $\mathcal{CW}(N_{s,i}, N_{e,i}; \mathbf{M}_i)$.

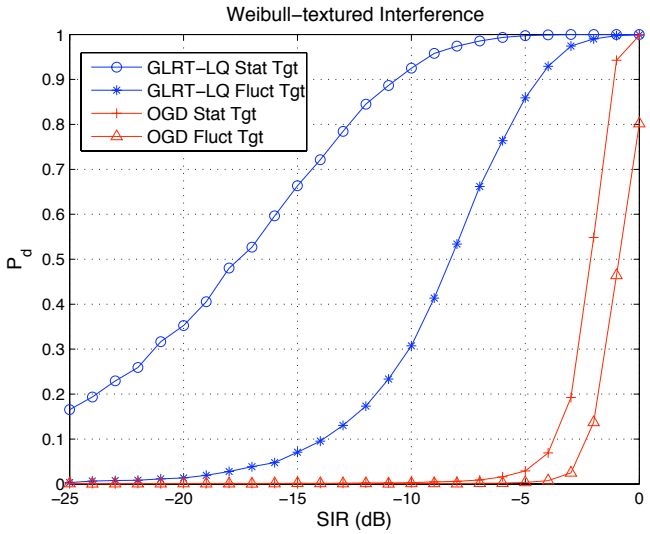

(a) Weibull-textured, $b = 0.658$

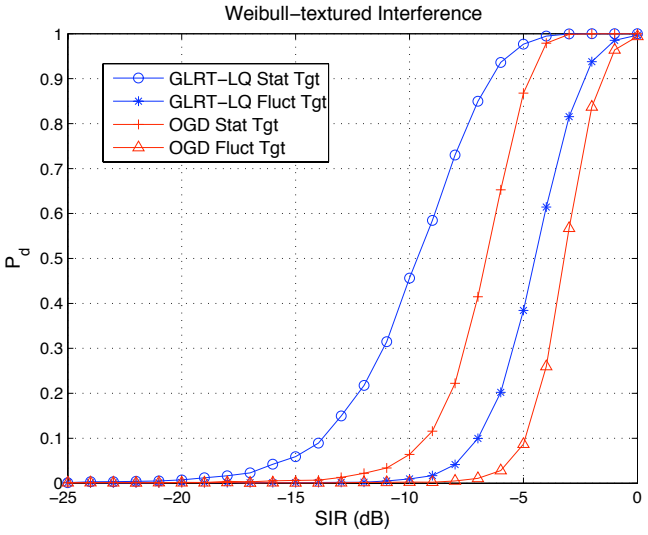

(b) Weibull-textured, $b = 1.763$

Figure 2.16: P_d against SIR_{pre} where the texture has a Weibull distribution with different parameters, considering both the stationary and fluctuating targets and both MIMO GLRT-LQ and MIMO OGD. $P_{fa} = 0.001$.

However, under non-Gaussian interference, $\mathbf{y}_i(l) = \sqrt{\tau_i}\mathbf{x}_i(l)$:

$$\begin{aligned}\widehat{\mathbf{M}}_{SCM,i} &= \frac{1}{N_{s,i}}\sum_{l=1}^{N_{s,i}}\mathbf{y}_i(l)\mathbf{y}_i^{\dagger}(l),\\ &= \frac{1}{N_{s,i}}\sum_{l=1}^{N_{s,i}}\tau_i\mathbf{x}_i(l)\mathbf{x}_i^{\dagger}(l),\end{aligned}$$

we see that the SCM is no longer the ML estimate. Instead, we consider the FPE which was first introduced in [23, 24] and then fully analyzed in [25, 26]. The FPE is the exact ML estimate when the texture is assumed to be deterministic and unknown [25]. On the other hand, when τ is a positive random variable, the FPE is an approximate ML estimate [23, 24]. In [25], it has been shown that the FPE is unique up to a scalar factor. Here, due to the matrix normalization $\text{tr}(\widehat{\mathbf{M}}_{FP,i}) = N_{e,i}$, the resulting FPE is unique and it is defined as the unique solution of the equation:

$$\widehat{\mathbf{M}}_{FP,i} = \frac{N_{e,i}}{N_{s,i}} \sum_{l=1}^{N_{s,i}} \frac{\mathbf{y}_i(l)\mathbf{y}_i^\dagger(l)}{\mathbf{y}_i^\dagger(l)\widehat{\mathbf{M}}_{FP,i}^{-1}\mathbf{y}_i(l)}.$$

Due to the normalizing term in the denominator, the FPE does not depend on the texture of the interference. The FPE is computed using the following iterative algorithm:

$$\widehat{\mathbf{M}}_{FP,i}(k+1) = \frac{N_{e,i}}{N_{s,i}} \sum_{l=1}^{N_{s,i}} \frac{\mathbf{y}_i(l)\mathbf{y}_i^\dagger(l)}{\mathbf{y}_i^\dagger(l)\widehat{\mathbf{M}}_{FP,i}^{-1}(k)\mathbf{y}_i(l)}. \tag{2.25}$$

It has been shown in [25] that 4 or 5 iterations are sufficient to achieve a relative error of 10^{-2}. More importantly, the solution converges towards the FPE regardless of the choice of the initial matrix $\widehat{\mathbf{M}}_{FP,i}(0)$ [25]. One obvious choice is $\mathbf{I}$ which will give the Normalized SCM (NSCM) after the first iteration:

$$\widehat{\mathbf{M}}_{NSCM,i} = \frac{N_{e,i}}{N_{s,i}} \sum_{l=1}^{N_{s,i}} \frac{\mathbf{y}_i(l)\mathbf{y}_i^\dagger(l)}{\mathbf{y}_i^\dagger(l)\mathbf{y}_i(l)}.$$

Consequently, the detector is also matrix-CFAR when the FPE is used [94]. Moreover, it has been shown in [26] that the asymptotic distribution of $\widehat{\mathbf{M}}_{FP}$ is the same as that of the SCM with $\frac{N_{e,i}}{N_{e,i}+1}N_{s,i}$ secondary data under *Gaussian* interference.

2.6.2 Statistical Properties

As before, we note that under H_0, the received signal contains only interference returns and τ_i cancels out in Eqn. (2.23) for the case where the covariance matrix is estimated by the FPE. As a result, $\hat{\Lambda}_i(\mathbf{y}_i) = \hat{\Lambda}_i(\mathbf{x}_i)$, i.e. the detector remains the same under Gaussian and non-Gaussian interference. This means that the distribution of the detector remains the same under H_0.

According to [89], under H_0, considering *Gaussian* interference and using the SCM as the estimated covariance matrix, $\hat{\Lambda}_i(\mathbf{y}_i)$ can be expressed with a random variable B_i which in turn depends on another random variable $l_{f,i}$:

$$\hat{\Lambda}_i(\mathbf{y}_i) \overset{d}{=} 1 + B_i|l_{f,i}.$$

The distributions of the two variables are as follows: $B_i|l_{f,i} \sim \beta'_{1,N_{s,i}-N_{e,i}+1}$ and $l_{f,i} \sim \beta_{N_{s,i}-N_{e,i}+2,N_{e,i}-1}$. The PDF of the beta and beta prime distributions are given in Appendix A.4.

Here, we consider non-Gaussian interference modeled as a SIRV. Using the FPE, $\hat{\Lambda}_i(\mathbf{y}_i)$ can still be expressed asymptotically with a conditional random variable $B_i|l_{f,i}$ but with $N_{s,i}$ replaced by $\frac{N_{e,i}}{N_{e,i}+1}N_{s,i}$. Hence the distribution becomes:

$$\hat{\Lambda}_i(\mathbf{y}_i) \overset{d}{=} 1 + B_i|l_{f,i}, \qquad \begin{cases} B_i|l_{f,i} \sim \beta'_{1,n_{a,i}-1}, \\ l_{f,i} \sim \beta_{n_{a,i},n_{b,i}-n_{a,i}-1}, \end{cases}$$

where

$$\begin{aligned} n_{a,i} &= \frac{N_{e,i}}{N_{e,i}+1}N_{s,i} - N_{e,i} + 2, \\ n_{b,i} &= \frac{N_{e,i}}{N_{e,i}+1}N_{s,i} + 2. \end{aligned}$$

Under H_1, if the texture is deterministic, $l_{f,i}$ is also the loss factor for the i-th subarray. The mean of $l_{f,i}$ is given by:

$$\begin{aligned} E(l_{f,i}) &= \frac{\frac{N_{e,i}}{N_{e,i}+1}N_{s,i} - N_{e,i} + 2}{\frac{N_{e,i}}{N_{e,i}+1}N_{s,i} + 1}, \\ &= \frac{N_{e,i}N_{s,i} - N_{e,i}^2 + N_{e,i} + 2}{N_{e,i}N_{s,i} + N_{e,i} + 1}, \end{aligned}$$

assuming that the FPE is used to estimate the covariance matrix. To limit the loss to 3 dB, i.e. $E(l_{f,i}) > 0.5$, we need:

$$N_{s,i} > 2N_{e,i} - 1 - \frac{3}{N_{e,i}}.$$

Although this is no longer the case when the texture is random, it is a useful rule of thumb to select $N_{s,i} \approx 2N_{e,i}$ as in [22].

The P_{fa} of the adaptive detector is derived in Appendix B.6 for the case $K_e = 1$. However, as shown in Appendix B.6, due to the complexity of the equations, an analytical expression of P_{fa} for the general case $K_e \geq 1$ has not been obtained. Instead, P_{fa} will be computed empirically using Monte Carlo simulations. Similarly, P_d will be calculated from Monte Carlo simulations.

2.6.3 Simulation Results

The same parameters as before (Table 2.3 and 2.4) are used. Only the stationary isotropic target model as described in Section 2.3.4.3 will be considered in these simulations to separate the effects due to fluctuating target from those due to the estimation of the covariance matrix.

To study the effects of the estimation of the covariance matrix on the detection performance, we consider 2 cases: $N_{s,i} = 2N_{e,i}$ and $N_{s,i} = 20N_{e,i}$ to compute $\widehat{\mathbf{M}}_i$ using the Fixed Point algorithm, and compare them to the case where $\mathbf{M}_i$ is known. Note that for simplicity we have $N_{e,i} = N_{e,0}$ for all subarrays but there is no constraint for them to be the same.

As discussed in Section 2.6.2, $N_{s,i}$ has to be about $2N_{e,i}$ to get a loss of approximately 3 dB in detection performance. On the other hand, $N_{s,i} = 20N_{e,i}$ has been chosen to approach the asymptotic case where $\mathbf{M}_i$ is known.

The FPE is obtained using Eqn. (2.25) with 10 iterations. However, from an operational point of view, it suffices to compute the estimate with 4 or 5 iterations to achieve a relative error of 10^{-2} [25]. As expected, when $N_{s,i}$ is large, the detection performance of the adaptive detector tends towards that of the detector where the covariance matrices are known (Fig. 2.17).

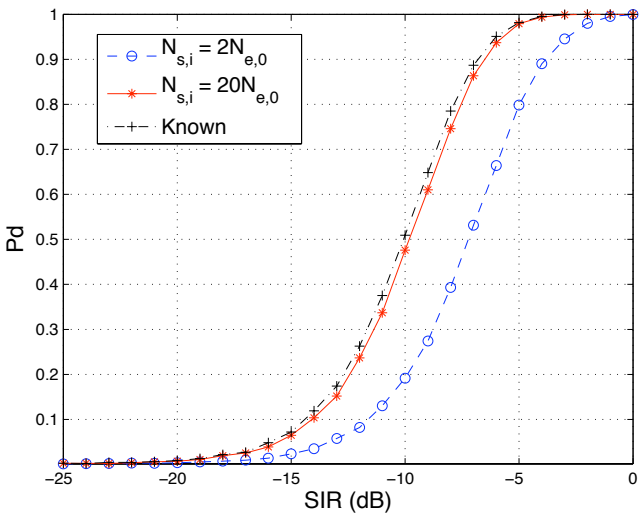

Figure 2.17: P_d against SIR_{pre} with the adaptive MIMO GLRT-LQ using FPE and interference with Gamma-distributed texture ($a = 2$). Stationary target model.

2.6.3.1 P_d - Gaussian Interference

We begin by looking at the detection performance when the interference is Gaussian. For comparison purposes, the MIMO Adaptive Matched Filter (AMF) which is the adaptive version of the MIMO OGD, has been considered. It is obtained simply by replacing the covariance matrix by its estimate in Eqn. (2.22):

$$\hat{\Lambda}(\mathbf{y}) = \sum_{i=1}^{K_e} \frac{|\mathbf{p}_i^\dagger \widehat{\mathbf{M}}_i^{-1} \mathbf{y}_i|^2}{\mathbf{p}_i^\dagger \widehat{\mathbf{M}}_i^{-1} \mathbf{p}_i}.$$

The SCM given in Eqn. (2.24) is used in the MIMO AMF since it is the ML estimate under Gaussian interference. We consider also MIMO Kelly's Test derived

in Section 2.4.1 for uncorrelated subarrays as given by Eqn. (2.16):

$$\prod_{i=1}^{K_e}\left[1-\frac{|\mathbf{p}_i^{\dagger}\widehat{\mathbf{M}}_{SCM,i}^{-1}\mathbf{y}_i|^2}{(\mathbf{p}_i^{\dagger}\widehat{\mathbf{M}}_{SCM,i}^{-1}\mathbf{p}_i)(N_{s,i}+\mathbf{y}_i^{\dagger}\widehat{\mathbf{M}}_{SCM,i}^{-1}\mathbf{y}_i)}\right]^{-N_{s,i}}.$$

Note that MIMO Kelly's Test is the optimum test when the interference is Gaussian and also that the covariance matrix estimate used is always the SCM according to the derivation in Appendix B.3.

According to [95], for the case where $K_e = 1$, as the signal vector $\mathbf{y}_i$ is not used in the estimation of the covariance matrix, the AMF is expected to perform worse than Kelly's Test. In the case where $K_e \gg 1$, MIMO Kelly's Test is expected to be much better than the MIMO AMF especially when there are few secondary data.

In Fig. 2.18, we have plotted the detection performance under Gaussian interference of the adaptive MIMO GLRT-LQ using FPE, the MIMO AMF using SCM and MIMO Kelly's Test using SCM, all considering stationary target model.

When $N_{s,i}$ is large, the performance of the MIMO AMF is similar to that of MIMO Kelly's Test as there are sufficient secondary data to estimate the covariance matrix and the addition of $\mathbf{y}_i$ does not improve the performance of Kelly's Test any further. However, the adaptive MIMO GLRT-LQ suffers a small CFAR loss of about 1 dB, a trade-off for robustness against variations of interference power.

However, when $N_{s,i}$ is small, the MIMO AMF incurs a loss of 1 dB of detection performance compared to MIMO Kelly's Test which takes advantage of $\mathbf{y}_i$ to increase the number of available secondary data. More interestingly, the adaptive MIMO GLRT-LQ actually performs slightly better than the MIMO AMF as well. This is because when $N_{s,i} = 2N_{e,i}$, the term $\mathbf{y}_i^{\dagger}\widehat{\mathbf{M}}_{SCM,i}^{-1}\mathbf{y}_i$ is no longer negligible and MIMO Kelly's Test becomes more similar to the adaptive MIMO GLRT-LQ test.

2.6.3.2 P_d - Non-Gaussian Interference

Fig. 2.19 and Fig. 2.20 show the detection performance for the adaptive MIMO GLRT-LQ with FPE, the MIMO AMF with SCM and MIMO Kelly's Test when the texture has Gamma and Weibull distribution, respectively. The stationary target model is considered in all cases.

As expected, the adaptive MIMO GLRT-LQ performs much better than the MIMO AMF and MIMO Kelly's Test when the interference is impulsive. As mentioned in the previous section, MIMO Kelly's Test resembles the adaptive MIMO GLRT-LQ when $N_{s,i}$ is small as $N_{s,i} + \mathbf{y}_i^{\dagger}\widehat{\mathbf{M}}_{SCM,i}^{-1}\mathbf{y}_i \approx y_i^{\dagger}\widehat{\mathbf{M}}_{SCM,i}^{-1}\mathbf{y}_i$. Thus MIMO Kelly's Test is robust to the variations of interference power. However, when $N_{s,i}$ is large, MIMO Kelly's Test can no longer take into account the variations. Hence, MIMO Kelly's Test actually has better detection performance when $N_{s,i}$ is small. Note however that it still suffers much loss in detection performance compared to the adaptive MIMO GLRT-LQ as the SCM is no longer the ML estimate under non-Gaussian interference. The detection performance of the MIMO AMF is much worse than that of the other two detectors.

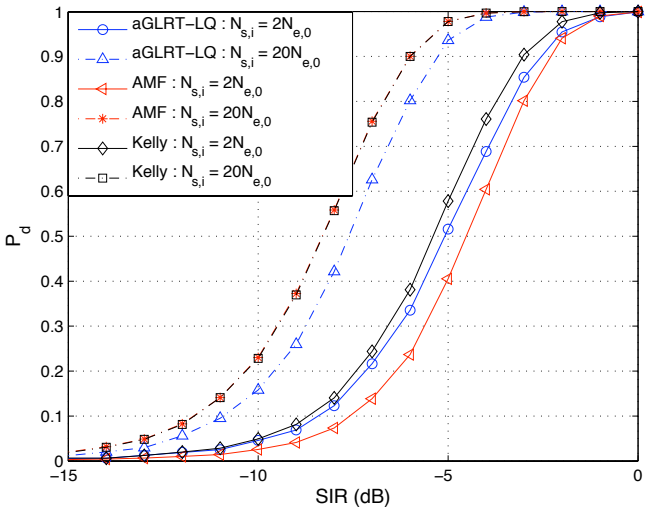

Figure 2.18: P_d against $\mathrm{SIR}_{\mathrm{pre}}$ for the adaptive MIMO GLRT-LQ using FPEs, the MIMO AMF using SCM and MIMO Kelly's Test with Gaussian interference. $P_{fa} = 0.001$. Stationary target model.

When the interference is less impulsive, the detection performance of the detectors becomes more similar but the adaptive MIMO GLRT-LQ still works the best, followed by MIMO Kelly's Test. As expected, the performance of MIMO Kelly's Test is more similar to that of the adaptive MIMO GLRT-LQ when $N_{s,i}$ is small while it is near to that of the MIMO AMF when $N_{s,i}$ is large.

2.7 Summary

A new MIMO Gaussian detector which takes into consideration possible correlation between subarrays has been derived. This new detector is robust with respect to the interference parameters as its statistical property under H_0 is the same no matter if there is correlation between subarrays or not. The adaptive version of this detector is also derived based on Kelly's Test.

The detection performance of these detectors are studied considering several different parameters, e.g. the effective number of subarrays K_e, the effective number of elements N_e, as well as the number of secondary data N_s. Having similar number of transmit and receive elements maximizes N_e, independent of the number of transmit and receive subarrays. This in turn maximizes the SIR gain. While having larger K_e increases robustness against target fluctuations, it also increases the threshold required to maintain the same P_{fa}, resulting in a loss of detection performance for the same SIR. For the adaptive detector, the loss factor l_f which arises due to the estimation of the covariance matrix depends on K_e, N_e and N_s. Increasing K_e and N_s and decreasing N_e result in less loss.

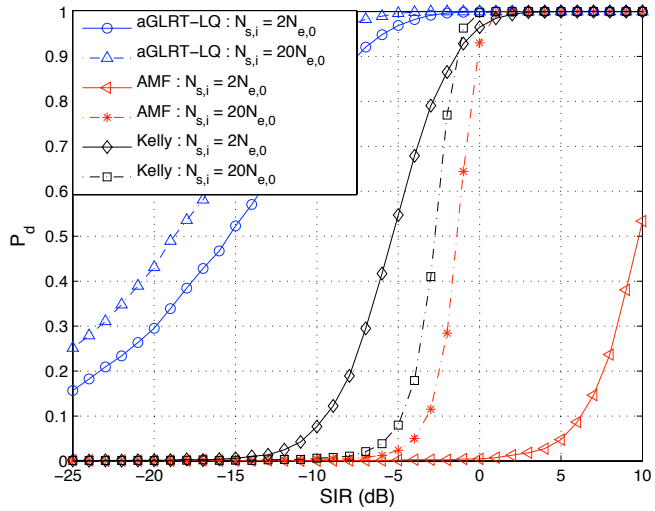

(a) $a = 0.5$

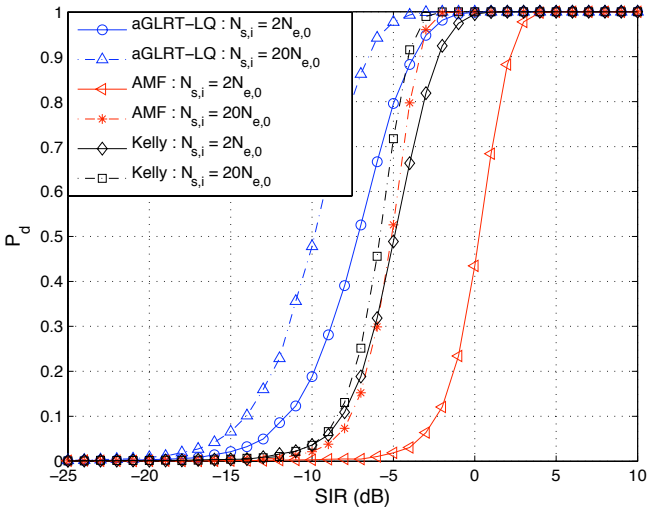

(b) $a = 2$

Figure 2.19: P_d against SIR_{pre} for the adaptive MIMO GLRT-LQ using FPEs, the MIMO AMF using SCM and MIMO Kelly's Test with K-distributed interference. $P_{fa} = 0.001$. Stationary target model.

The CFAR GLRT-LQ detector for detection under non-Gaussian interference has been extended to the MIMO case. A closed-form expression is also derived for the P_{fa} of the MIMO GLRT-LQ under the assumption that all subarrays contain the same number of elements. Compared to the MIMO OGD detector, this detector shows significant improvements in detection performance under non-Gaussian interference especially under very impulsive interference. It has a slight loss in

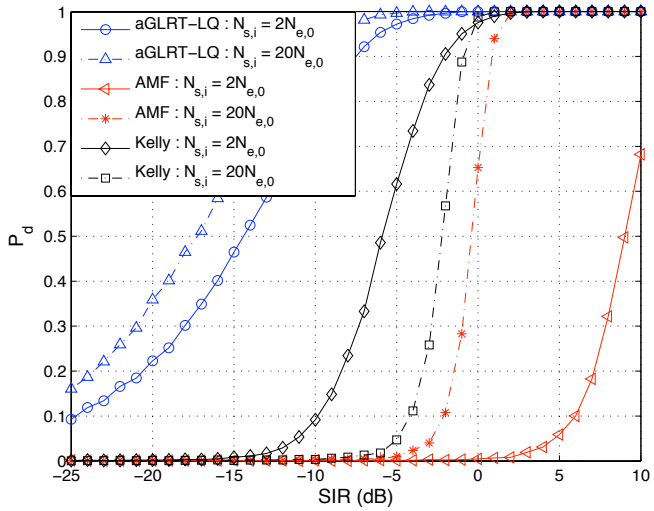

(a) $b = 0.658$

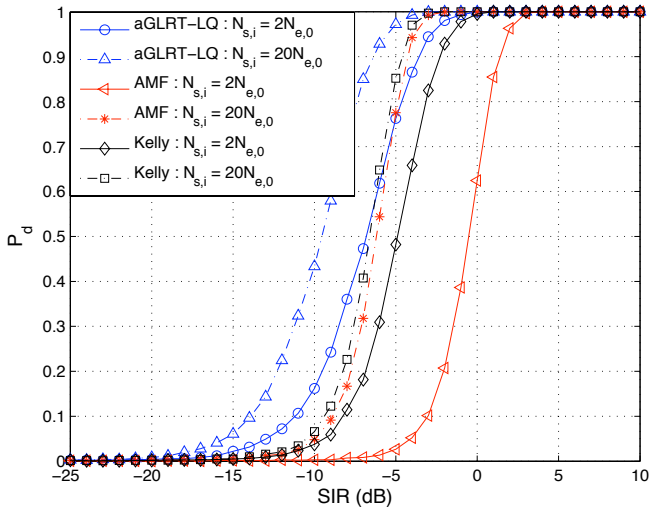

(b) $b = 1.763$

Figure 2.20: P_d against SIR_{pre} for the adaptive MIMO GLRT-LQ using FPEs, the MIMO AMF using SCM and MIMO Kelly's Test with Weibull-textured interference. $P_{fa} = 0.001$. Stationary target model.

performance when the interference is Gaussian.

Next, the adaptive version of this new detector is considered. The FPE is used to estimate the covariance matrix as the SCM no longer works under non-Gaussian interference. The theoretical performance of the adaptive version is shown to be texture-CFAR and matrix-CFAR by considering one subarray. The adaptive MIMO GLRT-LQ performs much better than MIMO Kelly's Test and the MIMO AMF

under impulsive non-Gaussian interference. It has comparable performance under Gaussian interference.

Chapter 3

Application: STAP

This chapter is organized as follows. The signal model for SISO-STAP is described in Section 3.1.1. Note that this is equivalent to what is called coherent MIMO-STAP in the literature. It is an extension of the classical monostatic STAP signal model. Transmit angle is included on top of the receive angle. This is due to the fact that there are several transmitters, each sending a different waveform such that the transmit angle can be determined. Furthermore, the radar can be in a bistatic configuration although we consider monostatic configurations here.

In Section 3.1.2, we formulate the detection problem and recall two well-known optimum CFAR detectors: the OGD for the non-adaptive case and the Kelly's Test for the adaptive case. In Section 3.1.3, the expressions for CRBs for SISO-STAP after detection are derived.

Next, we consider different configurations in Section 3.1.4. Given a fixed number of elements available, the configuration which will maximize the effective number of elements as well as the effective aperture size is presented. On top of that, the effects on clutter rank, as well as the width and number of clutter ridges, due to the spacing between elements and the velocity of the radar are investigated. The rank of the clutter covariance matrix is important as it determines the minimum number of secondary data needed to estimate the covariance matrix when it is unknown and reduced-rank algorithms are used. In Section 3.1.5, we study the detection and estimation performance for the different configurations compared to that for the classical STAP case.

In Section 3.2, MISO configurations are applied to STAP. The main advantage of using MISO configurations is its robustness to target RCS and velocity fluctuations with respect to aspect angle. The signal model for MISO-STAP is presented in Section 3.2.1. The model that is adopted is one where there is only one receive subarray and several widely separated transmit elements. As there is only one transmit element at each location, there is no transmit steering vector. The performance metric SIR loss for STAP is also extended to the MISO-STAP case.

The configurations and parameters considered are given in Section 3.2.3. In Section 3.2.4, we compare the detection performance of MISO-STAP with different number of transmit elements. We also study the detection performance of MISO-STAP and SISO-STAP given the same number of elements.

The contributions in this chapter are then summarized in Section 3.3.

3.1 SISO-STAP

3.1.1 Signal Model

We consider the coherent MIMO configuration [5], i.e. there is only one transmit and one receive subarray. They can be co-located or in a bistatic configuration. Let there be N transmit elements and M receive elements. The elements within the subarray are assumed to be closely-spaced such that the target RCS is the same. Previously in Chapter 2, we considered only single-pulse detection. Here, detection is done over a CPI with L pulses such that we have an additional time dimension as well as an additional parameter: Doppler frequency f_d.

It is well-known that most orthogonal waveforms are sensible to Doppler shifts, i.e. they cannot maintain their orthogonality when there is Doppler shift. As discussed in Chapter 1, it is thus more interesting to apply MIMO-STAP techniques to low frequency applications where the Doppler shifts are small. Moreover, due to the clutter mitigation requirements of GMTI, the radar is particularly sensitive to waveform characteristics, requiring similar clutter response from each waveform [62]. However, it is not within the scope of this thesis to study waveform characteristics. Assume here that pulse waveforms which maintain *sufficient* orthogonality under a variety of mutual delays and Doppler shifts are available such that the received signal can be separated after range matched filtering. The received signal can be expressed as:

$$\begin{aligned} \mathbf{y} &= ae^{j\phi}\mathbf{a}(\theta_r) \otimes \mathbf{b}(\theta_t) \otimes \mathbf{v}(f_d) + \mathbf{c} + \mathbf{n}, \\ &= ae^{j\phi}\mathbf{p} + \mathbf{c} + \mathbf{n}. \end{aligned}$$

The target part consists of $ae^{j\phi}\mathbf{p}$ where $ae^{j\phi}$ is the complex target RCS. Note that it is assumed that the target remains in the cell-under-test during the CPI and that the target RCS does not change from pulse to pulse. The receive, transmit and Doppler steering vectors are as follows:

$$\begin{aligned} \mathbf{a}(\theta_r) &= \left[1 \ \cdots \ \exp(j2\pi\frac{(M-1)d_r}{\lambda}\sin\theta_r)\right]^T, \\ \mathbf{b}(\theta_t) &= \left[1 \ \cdots \ \exp(j2\pi\frac{(N-1)d_t}{\lambda}\sin\theta_t)\right]^T, \\ \mathbf{v}(f_d) &= [1 \ \cdots \ \exp(j2\pi(L-1)\mathrm{PRI}\cdot f_d)]^T, \end{aligned}$$

where θ_r, θ_t and f_d are the receive angle, transmit angle and Doppler frequency, respectively. λ is the wavelength of the radar and PRI is the Pulse Repetition Interval. d_r and d_t are the inter-element spacing for the receive and transmit subarrays, respectively.

In the case where the transmit and receive subarray are co-located, the transmit and receive angles are the same: $\theta_r = \theta_t = \theta$. Hence the steering vector can be expressed as:

$$\begin{aligned} \mathbf{p} &= \mathbf{a}(\theta) \otimes \mathbf{b}(\theta) \otimes \mathbf{v}(f_d), \\ &= \mathbf{s}(\theta) \otimes \mathbf{v}(f_d). \end{aligned}$$

Note that f_d is the relative Doppler frequency measured by the radar. Due to the motion of the STAP platform, the actual target Doppler frequency f_t for the monostatic case is given by:

$$f_t = f_d + \frac{2v}{\lambda}\sin\theta,$$

where v is the velocity of the radar. Hence, we can express the Doppler steering vector as $\mathbf{v}(\theta, f_t)$.

The interference part consists of clutter $\mathbf{c}$ and noise $\mathbf{n}$. $\mathbf{c}$ is a MNLx1 vector containing clutter returns and $\mathbf{c} \sim \mathcal{CN}(\mathbf{0}, \mathbf{M}_c)$. $\mathbf{M}_c$ is the Clutter Covariance Matrix (CCM) and is of low rank. The low-rank nature of the CCM comes from the fact that in the virtual array aperture, there is a repeat of the virtual locations of the radar elements. Its rank depends on the configuration and will be discussed later in Section 3.1.4.

$\mathbf{n}$ is a MNLx1 vector containing thermal noise in the receive channels such that $\mathbf{n} \sim \mathcal{CN}(\mathbf{0}, \mathbf{M}_n)$ where $\mathbf{M}_n$ is the noise covariance matrix. When the thermal noise is uncorrelated, $\mathbf{M}_n$ is simply $\sigma^2\mathbf{I}$ where σ^2 is the noise power. In the case where the thermal noise is correlated, $\mathbf{n}$ becomes Gaussian colored noise and its covariance matrix is not the scaled identity matrix anymore. For identifiability considerations, we consider uncorrelated noise here.

We denote $\mathbf{M}$ as the overall interference covariance matrix:

$$\mathbf{M} = \mathbf{M}_c + \sigma^2\mathbf{I}.$$

Note that $\mathbf{M}$ is still of full rank due to the contribution from noise. However, as clutter is in general much stronger than noise, $\mathbf{M}$ has most of its power concentrated within a few DoF (corresponding to the rank of the CCM) instead of being distributed over all DoFs like in the full-rank interference covariance matrix used in Chapter 2.

3.1.2 Detection

We recall here briefly the optimum detectors when the interference covariance matrix is known and unknown. As the coherent MIMO has only one effective subarray, the optimum detectors derived in Section 2.3 (non-adaptive) and Section 2.4 (adaptive) reduce to those for the classical case: OGD and Kelly's Test, respectively. However, due to the motion of the STAP platform, there is a coupling between the angle and Doppler frequency of each clutter patch seen by the radar. Hence, the clutter power is concentrated along the clutter ridge which reflects the coupling. Due to the localized nature of the clutter, detection performance varies greatly depending on the target location and velocity.

As in Chapter 2, the detection problem can be expressed as the following binary hypothesis test:

$$\begin{cases} \mathrm{H}_0: & \mathbf{y} = \mathbf{c} + \mathbf{n}, \\ \mathrm{H}_1: & \mathbf{y} = ae^{j\phi}\mathbf{p} + \mathbf{c} + \mathbf{n}. \end{cases}$$

Under the null hypothesis H_0, the target is absent and the received signal contains only interference. Under the alternative hypothesis H_1, the target is present, resulting in a deterministic signal on top of the interference in the received signal.

Two important measures for detection performance are the probability of false alarm P_{fa} and the probability of detection P_d. For a given detector $\Lambda(\mathbf{y})$, P_{fa} is the probability of choosing H_1 when the target is absent (H_0):

$$P_{fa} = P\left(\Lambda(\mathbf{y}) > \lambda | H_0\right),$$

while P_d is the probability of correctly choosing H_1 when the target is present:

$$P_d = P\left(\Lambda(\mathbf{y}) > \lambda | H_1\right).$$

3.1.2.1 Optimum Detection

When the interference parameters are known, the optimum CFAR detector is the well-known OGD which can be expressed as:

$$\Lambda(\mathbf{y}) = \frac{|\mathbf{p}^\dagger \mathbf{M}^{-1}\mathbf{y}|^2}{\mathbf{p}^\dagger \mathbf{M}^{-1}\mathbf{p}}.$$

Its distribution is:

$$\Lambda(\mathbf{y}) \overset{d}{=} \begin{cases} H_0: & \chi_2^2(0), \\ H_1: & \chi_2^2(2a^2\mathbf{p}^\dagger \mathbf{M}^{-1}\mathbf{p}). \end{cases}$$

Note that this detector is CFAR as it does not depend on the interference covariance matrix under H_0. Under H_1, it depends on $2a^2\mathbf{p}^\dagger \mathbf{M}^{-1}\mathbf{p}$ which is equivalent to two times the post-processing SIR. In Chapter 2, the interference power is distributed evenly spatially. In the case of STAP, due to the highly localized nature of the clutter power (along the clutter ridges) and as clutter is much stronger than noise, the effective SIR varies significantly according to the location and velocity of the target.

Assuming that the CCM has rank r, it can be expressed in terms of a $MNLxr$ matrix $\mathbf{v}$:

$$\mathbf{M}_c = \mathbf{V}\mathbf{V}^\dagger,$$

where each column of $\mathbf{V}$ contains the eigenvector of $\mathbf{M}_c$ multiplied by the square-root of the corresponding eigenvalues (only for the non-zero eigenvalues). Using the Matrix Inversion Lemma [96], $\mathbf{M}^{-1}$ can be expressed as:

$$\mathbf{M}^{-1} = \frac{1}{\sigma^2}\mathbf{I}_{MNL} - \frac{1}{\sigma^2}\mathbf{V}(\mathbf{V}^\dagger\mathbf{V} + \sigma^2\mathbf{I}_r)^{-1}\mathbf{V}^\dagger,$$

where $\mathbf{I}_n$ stands for the identity matrix of size n. The post-processing SIR becomes:

$$\mathrm{SIR}_{\mathrm{post}} = a^2\mathbf{p}^\dagger \mathbf{M}^{-1}\mathbf{p} = \frac{a^2}{\sigma^2}MNL - \frac{a^2}{\sigma^2}\mathbf{p}^\dagger\mathbf{V}(\mathbf{V}^\dagger\mathbf{V} + \sigma^2\mathbf{I}_r)^{-1}\mathbf{V}^\dagger\mathbf{p}.$$

When the target is far from the clutter i.e. the target subspace is almost orthogonal to the clutter subspace, $\mathbf{V}^\dagger\mathbf{p} \approx 0$ and the SIR tends towards its maximum attainable value: $\frac{a^2}{\sigma^2}MNL$. This is the SIR obtained when there is only noise and $\frac{a^2}{\sigma^2}$ is the preprocessing SNR (per element per pulse). As the clutter power is much higher than that of noise, SIR can also be expressed as a projection into the orthogonal subspace of the clutter:

$$\text{SIR}_{\text{post}} \approx \frac{a^2}{\sigma^2}\mathbf{p}^\dagger(\mathbf{I}_{MNL} - \mathbf{V}(\mathbf{V}^\dagger\mathbf{V})^{-1}\mathbf{V}^\dagger)\mathbf{p}.$$

When the target is near to the clutter, the SIR becomes very small.

A performance metric that is useful for illustrating this is the SIR loss which is defined as the loss in post-processing SIR as compared to the ideal case where there is only noise:

$$\begin{aligned} \text{SIR loss} &= \frac{a^2\mathbf{p}^\dagger\mathbf{M}^{-1}\mathbf{p}}{\frac{a^2}{\sigma^2}MNL}, \\ &= \frac{\sigma^2\mathbf{p}^\dagger\mathbf{M}^{-1}\mathbf{p}}{MNL}. \end{aligned} \tag{3.1}$$

3.1.2.2 Adaptive Detection

In the case where the interference parameters are unknown, we assume that we have access to N_s i.i.d. secondary data to estimate $\mathbf{M}$: $\mathbf{y}(1), \ldots, \mathbf{y}(N_s)$. The optimum adaptive detector is the Kelly's Test [21]:

$$\hat{\Lambda}(\mathbf{y}) = \frac{|\mathbf{p}^\dagger\widehat{\mathbf{M}}_{\text{SCM}}^{-1}\mathbf{y}|^2}{(\mathbf{p}^\dagger\widehat{\mathbf{M}}_{\text{SCM}}^{-1}\mathbf{p})(N_r + \mathbf{y}^\dagger\widehat{\mathbf{M}}_{\text{SCM}}^{-1}\mathbf{y})},$$

where $\widehat{\mathbf{M}}_{\text{SCM}}$ is the SCM of $\mathbf{M}$ estimated using N_s secondary data:

$$\widehat{\mathbf{M}}_{\text{SCM}} = \frac{1}{N_s}\sum_{i=1}^{N_s}\mathbf{y}_i\mathbf{y}_i^\dagger.$$

Its distribution [89] is:

$$\hat{\Lambda}(\mathbf{y}) \overset{d}{=} \begin{cases} \text{H}_0: & \beta_{1,N_s-MNL+1}(0), \\ \text{H}_1: & \beta_{1,N_s-MNL+1}(2a^2\mathbf{p}^\dagger\mathbf{M}^{-1}\mathbf{p}\cdot l), \end{cases}$$

where $l \sim \beta_{N_s-MNL+2,MNL-1}(0)$ is the loss factor due to the estimation of the covariance matrix. As discussed previously in Section 2.4.2, the mean or expected value of l is $E(l_f) = \frac{N_s-MNL+2}{N_s+1}$. To limit the loss to 3 dB, i.e. $E(l_f) > 0.5$, we need $N_s > 2MNL - 3$ which is the Reed-Mallet-Brennan's rule [22]. As this loss factor acts upon the SIR, the mean SIR loss in the adaptive case can be considered to be:

$$\begin{aligned} \text{mean SIR loss} &= E(l_f)\cdot\frac{\sigma^2\mathbf{p}^\dagger\mathbf{M}^{-1}\mathbf{p}}{MNL}, \\ &= \frac{N_s - MNL + 2}{(N_s+1)MNL}\cdot\sigma^2\mathbf{p}^\dagger\mathbf{M}^{-1}\mathbf{p}. \end{aligned}$$

Note that this is relevant only in the case where the Kelly's Test is used as detector and not for other processing techniques such as reduced-rank algorithms.

3.1.3 Estimation

As mentioned in the previous section, the optimum detectors for the coherent MIMO case are similar to those for the classical phased array. However, the main advantage is the increase in angular resolution, i.e. its estimation performance. In estimation theory and statistics [37], the CRB expresses a lower bound on the variance of estimators of a deterministic parameter. For the general complex Gaussian case where $\mathbf{y} \sim \mathcal{CN}(\boldsymbol{\mu}(\boldsymbol{\Theta}), \mathbf{M}(\boldsymbol{\Theta}))$, the Fisher Information Matrix (FIM) is given by:

$$\begin{aligned}[\mathbf{J}(\boldsymbol{\Theta})]_{i,i'} &= \operatorname{tr}\left[\mathbf{M}(\boldsymbol{\Theta})^{-1}\frac{\partial \mathbf{M}(\boldsymbol{\Theta})}{\partial \Theta_i}\mathbf{M}(\boldsymbol{\Theta})^{-1}\frac{\partial \mathbf{M}(\boldsymbol{\Theta})}{\partial \Theta_{i'}}\right] \\ &\quad +2\Re\left[\frac{\partial \boldsymbol{\mu}^{\dagger}(\boldsymbol{\Theta})}{\partial \Theta_i}\mathbf{M}(\boldsymbol{\Theta})^{-1}\frac{\partial \boldsymbol{\mu}(\boldsymbol{\Theta})}{\partial \Theta_{i'}}\right].\end{aligned}$$

We can separate the parameters to be estimated as the signal parameters $\boldsymbol{\Theta_S}$ and the interference parameters $\boldsymbol{\Theta_I}$:

$$\boldsymbol{\Theta} = [\boldsymbol{\Theta_S} \;\; \boldsymbol{\Theta_I}].$$

Here we are under H_1, i.e. $\mathbf{y} = ae^{j\phi}\mathbf{p} + \mathbf{c} + \mathbf{n}$ and $\mathbf{y} \sim \mathcal{CN}(\boldsymbol{\mu}(\boldsymbol{\Theta_S}), \mathbf{M}(\boldsymbol{\Theta_I}))$. As $\boldsymbol{\mu}$ depends only on the signal parameters and $\mathbf{M}$ depends only on the interference parameters, the signal and interference parameters are disjoint, i.e. the CRB for $\boldsymbol{\Theta_S}$ remains the same whether $\mathbf{M}$ is known or not. To obtain the CRB for $\boldsymbol{\Theta_S}$, we need to consider only the upper left block of $\mathbf{J}(\boldsymbol{\Theta})$, denoted as $\mathbf{J}(\boldsymbol{\Theta_S})$.

As estimation is done after detection, we assume that a and ϕ are known such that $\boldsymbol{\Theta_S} = [\theta \;\; f_t]$. Defining $\mathbf{d}_s = \frac{\partial \mathbf{p}}{\partial \theta}$ and $\mathbf{d}_f = \frac{\partial \mathbf{p}}{\partial f_t}$, we get:

$$\mathbf{J}(\boldsymbol{\Theta_S}) = 2a^2\begin{bmatrix} \mathbf{d}_s{}^{\dagger}\mathbf{M}^{-1}\mathbf{d}_s & \Re(\mathbf{d}_s{}^{\dagger}\mathbf{M}^{-1}\mathbf{d}_f) \\ \Re(\mathbf{d}_s{}^{\dagger}\mathbf{M}^{-1}\mathbf{d}_f) & \mathbf{d}_f{}^{\dagger}\mathbf{M}^{-1}\mathbf{d}_f \end{bmatrix}.$$

As $\mathbf{J}(\boldsymbol{\Theta_S})$ is a 2x2 matrix, inversion is straightforward and we obtain the CRB for θ and f_t:

$$\begin{aligned}\mathrm{CRB}_{\theta\theta} &= \frac{1}{2a^2}\left(\frac{\mathbf{d}_f{}^{\dagger}\mathbf{M}^{-1}\mathbf{d}_f}{(\mathbf{d}_s{}^{\dagger}\mathbf{M}^{-1}\mathbf{d}_s)(\mathbf{d}_f{}^{\dagger}\mathbf{M}^{-1}\mathbf{d}_f) - \Re(\mathbf{d}_s{}^{\dagger}\mathbf{M}^{-1}\mathbf{d}_f)^2}\right), \\ \mathrm{CRB}_{f_t f_t} &= \frac{1}{2a^2}\left(\frac{\mathbf{d}_s{}^{\dagger}\mathbf{M}^{-1}\mathbf{d}_s}{(\mathbf{d}_s{}^{\dagger}\mathbf{M}^{-1}\mathbf{d}_s)(\mathbf{d}_f{}^{\dagger}\mathbf{M}^{-1}\mathbf{d}_f) - \Re(\mathbf{d}_s{}^{\dagger}\mathbf{M}^{-1}\mathbf{d}_f)^2}\right).\end{aligned}$$

Remark 3.1 (On the non-singularity of $\mathbf{J}(\boldsymbol{\Theta_S})$)**.** $\mathbf{J}(\boldsymbol{\Theta_S})$ *is singular when its determinant is equal to zero:*

$$\begin{aligned}(\mathbf{d}_s{}^{\dagger}\mathbf{M}^{-1}\mathbf{d}_s)(\mathbf{d}_f{}^{\dagger}\mathbf{M}^{-1}\mathbf{d}_f) - \Re(\mathbf{d}_s{}^{\dagger}\mathbf{M}^{-1}\mathbf{d}_f)^2 = 0, \\ \frac{\Re(\mathbf{d}_s{}^{\dagger}\mathbf{M}^{-1}\mathbf{d}_f)}{\sqrt{(\mathbf{d}_s{}^{\dagger}\mathbf{M}^{-1}\mathbf{d}_s)(\mathbf{d}_f{}^{\dagger}\mathbf{M}^{-1}\mathbf{d}_f)}} = 1.\end{aligned}$$

This implies that $\mathbf{d}_s$ *and* $\mathbf{d}_f$ *are collinear which is not the case due to the structure of the steering vector* $\mathbf{p}$ *and its dependence on* θ *and* f_t.

In the case where the estimation of the target RCS is of interest for classification purposes etc, $\boldsymbol{\Theta}_{\boldsymbol{S}} = [\theta \;\; f_t \;\; a \;\; \phi]$. This is also the case when detection and estimation are done simultaneously. The resulting FIM and CRBs are given in Appendix C.1. Estimating more parameters will always worsen the performance except when the parameters are independent.

In Fig. 3.1, the CRB for θ and f_t are plotted against the normalized Doppler frequency $\omega_t = f_t \cdot \text{PRI}$. Here, we see clearly the degradation of estimation performance when a and ϕ are estimated on top of θ and f_t (for Config 3c as described in Section 3.1.4). When a and ϕ are not estimated, we see that the CRB for both f_t and θ are lower, indicating a better resolution. More importantly, the peak in the CRB due to the presence of clutter is narrower when a and ϕ are not estimated, especially for θ.

It is interesting to note that estimation after detection seems to separate the SIR loss due to clutter cancellation and the loss in resolution due to the presence of clutter. The difference in CRB levels for the two cases corresponds approximately to the SIR loss due to clutter cancellation. This means that while a slow-moving target (at say $\omega_t = 0.02$) is more difficult to detect due to a SIR loss of -9 dB (according to Fig. 3.8), its direction and velocity can be estimated with no or little loss in resolution. However, at very low ω_t, estimation is no longer accurate due to the presence of clutter. Hence, it might be possible to reduce MDV further by lowering detection threshold to detect slower targets whose parameters can still be estimated accurately. SNR gain can then be further increased by additional processing between coherent processing intervals, similarly to the Synthetic Aperture Radar (SAR).

3.1.4 Configurations

3.1.4.1 Number of transmit and receive elements

We have discussed in Section 2.2 that one advantage of transmit diversity in MIMO radars is that it can increase the effective (virtual) number of elements $N_e = MN$ such that it is larger than the number of physical elements $N_p = M + N$. It is also noted in Remark 2.1 that the maximum effective number of elements is achieved when the number of transmit element is equal to the number of receive element (when N_p is even).

Moreover, the effective aperture size is given by:

$$L_a = (N-1)d_t + (M-1)d_r.$$

We know that if $d_r = \frac{\lambda}{2}$, choosing $d_t = Md_r$ will maximize the aperture size while maintaining critical sampling [38]. In this case, we will have an aperture size of $L_a = [(N-1)M + (M-1)]\frac{\lambda}{2} = (MN-1)\frac{\lambda}{2}$. This corresponds to a virtual array with MN closely-spaced elements while using only $N + M$ elements. The virtual

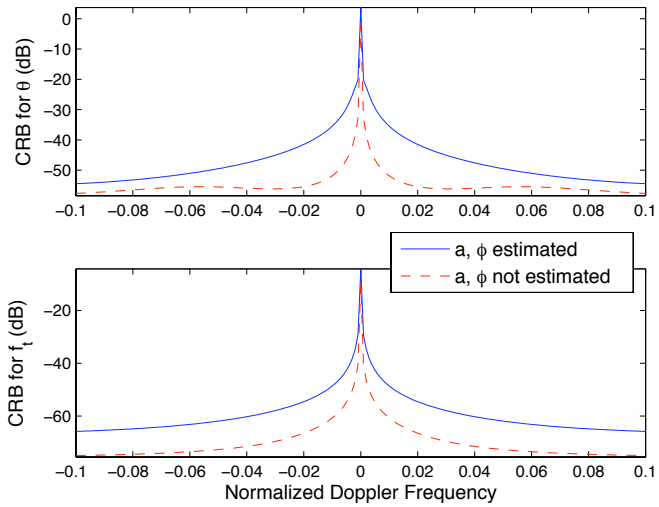

Figure 3.1: CRB in dB for θ (top) and f_t (bottom) for the case where a and ϕ are estimated (blue solid line) and not estimated (red dashed line). $\beta = 2$.

array is simply a spatial convolution of the transmit elements' physical positions with the receive elements' physical positions.

Remark 3.2. *Given a fixed number of physical elements N_p, the maximum possible aperture size given critical sampling is $L_a^{max} = (N_e^{max} - 1)\frac{\lambda}{2} \leq (\frac{{N_p}^2}{4} - 1)\frac{\lambda}{2}$, more precisely:*

$$L_a^{max} = \begin{cases} (\frac{{N_p}^2}{4} - 1)\frac{\lambda}{2}, & N_p \text{ even}, \\ (\frac{{N_p}^2 - 5}{4})\frac{\lambda}{2} < (\frac{{N_p}^2}{4} - 1)\frac{\lambda}{2}, & N_p \text{ odd}. \end{cases}$$

Remark 3.2 results directly from Remark 2.1. Let there be $N_p = 10$ physical elements. We consider 4 configurations which are summarized in Table 3.1 and illustrated in Fig. 3.2. Config 1 is the classical phased array and is included for comparison. The variations of N_e and L_a with N are shown in Fig. 3.3. We see that Config 3 maximizes both N_e and L_a, according to Remarks 2.1 and 3.2.

Note that in the power unlimited case (as described in Section 2.2), i.e. each transmit element transmits the same amount of energy, there is no difference between Config 2 and 4 and exchanging the configurations of receive and transmit subarrays does not change its performance. However, in the power limited case where the total transmitted energy remains the same, Config 2 is more advantageous than Config 4.

3.1.4.2 Spacing between transmit and receive elements

After we have decided on the distribution between the transmit and receive elements, we still have other design parameters like the inter-element spacing that can

Config	N	M	N_e	L_a/λ
1	1	9	9	4
2	2	8	16	7.5
3	5	5	25	12
4	8	2	16	7.5

Table 3.1: Element distribution configurations for MIMO-STAP.

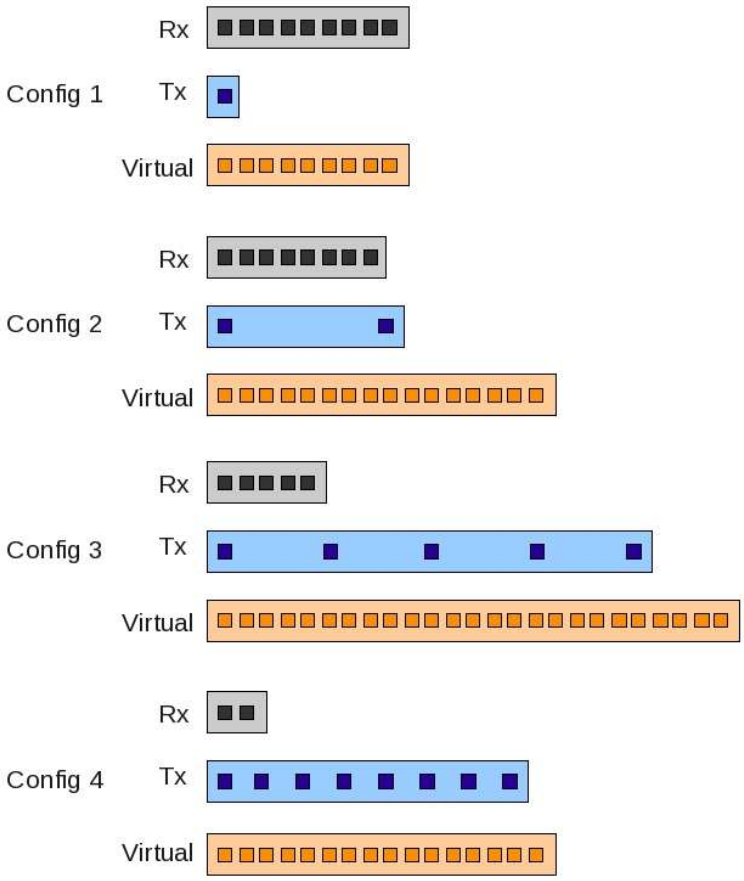

Figure 3.2: Element distribution configurations for MIMO-STAP.

be exploited to improve the detection and estimation performance. These parameters can also be used to reduce the rank of the CCM.

Before we present the different configurations, we start by introducing the Generalized MIMO Brennan's Rule which can be used to estimate the rank of the CCM in the case where the elements are not necessarily spaced at half wavelength.

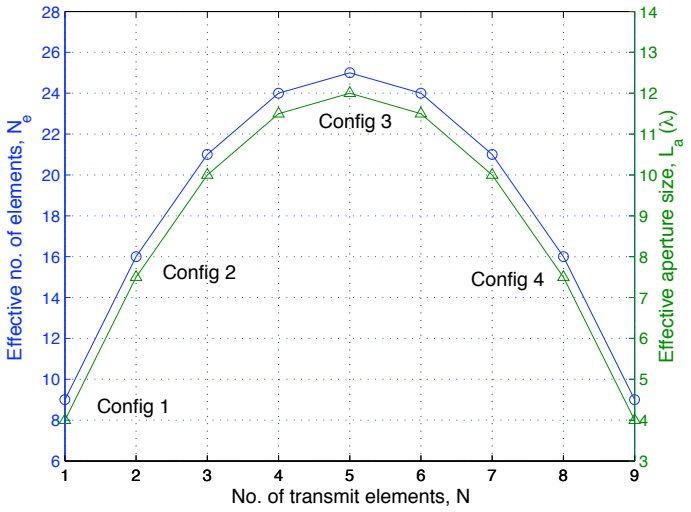

Figure 3.3: Variation of N_e and L_a with N. $N_p = 10$.

Theorem 3.1 (Generalized MIMO Brennan's Rule [J2])**.** *Define α, β and γ as below:*

$$\begin{aligned} \alpha &= \frac{d_r}{\lambda/2}, \\ \beta &= \frac{2v\mathrm{PRI}}{\lambda/2}, \\ \gamma &= \frac{d_t}{\lambda/2}. \end{aligned}$$

In the case where α, β and γ are integers, the rank of the CCM r is given by the number of distinct (integer) values N_d in:

$$m\alpha + n\gamma + l\beta \quad \forall \quad \begin{cases} m = 0, \ldots, M-1, \\ n = 0, \ldots, N-1, \\ l = 0, \ldots, L-1. \end{cases}$$

The proof of the theorem is presented in Appendix C.2.

Remark 3.3. *When α, β and γ are not integers, only N_d eigenvalues of $\mathbf{M}_c$ are significant such that the rank of $\mathbf{M}_c$ is approximated by N_d [39].*

Remark 3.4.

1. *When $\alpha = 1$, i.e. $d_r = \lambda/2$, we obtain the MIMO extension of Brennan's Rule as derived in [39].*

2. *If $\min(\alpha, \beta, \gamma) = 1$, then $N_d = (M-1)\alpha + (N-1)\gamma + (L-1)\beta + 1$.*

3. *If* α, β *and* γ *are divisible by* $\min(\alpha, \beta, \gamma)$, *then* $N_d = \frac{(M-1)\alpha+(N-1)\gamma+(L-1)\beta}{\min(\alpha,\beta,\gamma)} + 1$.

Consider the virtual array described in Section 3.1.4.1. Due to the sensor motion, the resulting synthetic aperture of the virtual array is extended, as in the case of SAR. The clutter rank is then basically the number of positions that are occupied by the virtual array. For ease of presentation, we consider a simple case where $N = M = 2$ and $L = 4$. In Fig. 3.4, the position of the virtual array at each pulse as well as the position of the final synthetic array are shown. In the first case (top), there are no spatial and Doppler ambiguity and the element spacing is $\lambda/2$. The virtual array moves by one element spacing between pulses, resulting in a synthetic aperture size of 3λ. The rank of the clutter is 7. With Doppler ambiguity $\beta = 2$ (middle), the virtual array moves by two element spacings between pulses and there is less overlap of the array. Hence, the rank increases to 10 and the synthetic aperture size is now 4.5λ. If we introduce spatial ambiguity as well (bottom), this causes the positions occupied to overlap. The resulting clutter rank is then reduced to 7 and the synthetic aperture size is further increased to 6λ.

In Fig. 3.5, we have plotted the clutter ridge for different α and γ while keeping $\beta = 2$. Config 3 is considered here. The values of α and γ as well as the rank of $\mathbf{M}_c$ are shown in Table 3.2. The configurations are also illustrated in Fig. 3.6.

One problem with MIMO-STAP is the increase in clutter rank. However, as discussed earlier, when there is ambiguity in the Doppler domain ($\beta = 2$), it can be interesting to introduce ambiguity in the spatial domain as well to reduce the width of the clutter ridge and clutter rank (Config b and d). Additional clutter ridges caused by spatial ambiguity occur at the same place as those caused by Doppler ambiguity, hence there is no increase in number of clutter ridges. The reduced clutter rank also reduces the number of secondary data needed to estimate the CCM. Many reduced-rank algorithms can also be effectively implemented when the clutter rank is low. Note that the rank for Config b and d can be obtained directly according to point 3 of Remark 3.4.

Config	α	γ	rank($\mathbf{M}_c$)
a	1	1	39
b	2	2	24
c	1	αM=5	55
d	2	αM=10	40

Table 3.2: Element spacing configurations for MIMO-STAP, using Config 3 as example.

For ease of comparison, the effective aperture size (L_a/λ) for all configurations are given in Table 3.3.

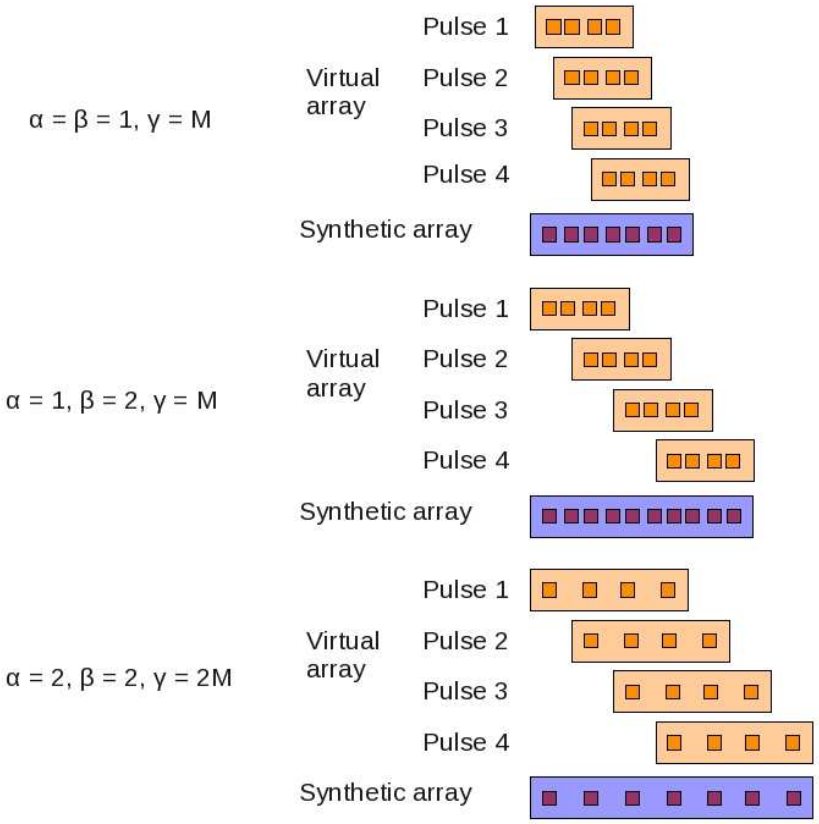

Figure 3.4: The virtual array and resulting synthetic array with no Doppler and spatial ambiguities (top), only Doppler ambiguity (middle) and both Doppler and spatial ambiguities (bottom). $N = M = 2$ and $L = 4$.

Config		Element Spacing			
		a	b	c	d
Element Distribution	1	4	8	4	8
	2	4	8	7.5	15
	3	4	8	12	24
	4	4	8	7.5	15

Table 3.3: Effective aperture size (L_a/λ) for all configurations.

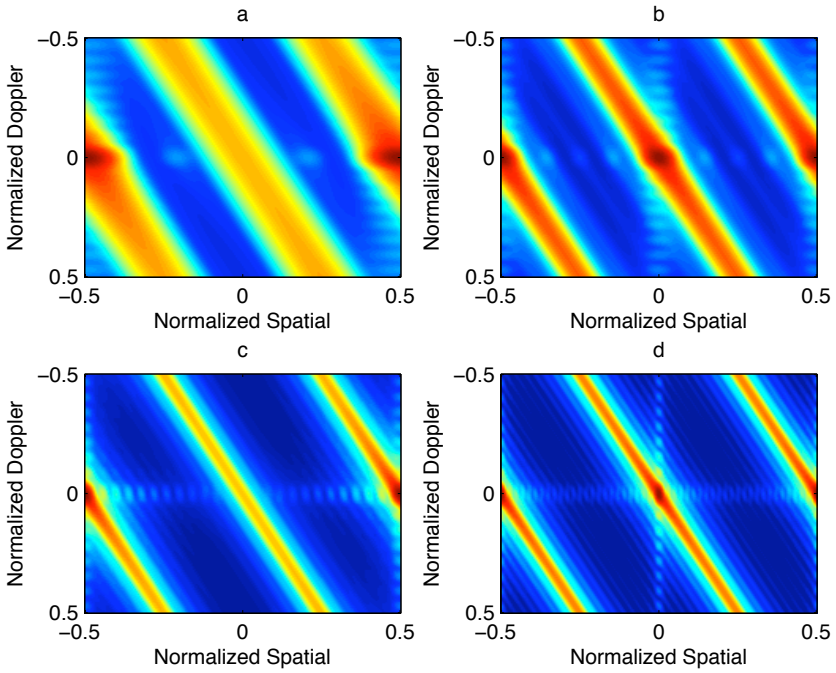

Figure 3.5: Clutter ridge for Config a (top left), Config b (top right), Config c (bottom left), Config d (bottom right). Config 3 and $\beta = 2$.

3.1.5 Simulation Results

The following parameters of simulation are considered. Both the receive and transmit subarrays are located at the origin. We consider two targets with normalized Doppler frequency $\omega_t = 0.01$ (T1) and 0.2 (T2), respectively. This enables us to compare the detection performance of the different configurations with and without clutter. For both targets, the target range is 70 km and $\theta = 0$.

The operating frequency of the radar is 15 MHz ($\lambda = 20$ m) and the PRI is 5 s. The radar is assumed to be moving at 5 m/s such that $\beta = 2$. The SNR per element per pulse is given by $\text{SNR} = \frac{a^2}{\sigma^2}$. P_{fa} is set to be 10^{-3} and $N_{MC} = 10^4$.

The number of pulses is $L = 16$. Note that as a rule of thumb, the number of pulses should be chosen such that it is bigger than the effective number of elements. This ensures that the full effective aperture is utilized. However, this is not always possible, especially when the target is moving and when range resolution is high. Here, we use $L = 16 < 25 = N_e^{max}$ to illustrate this limitation.

The clutter covariance matrix is modeled by integration over 180° of azimuth angles (front lobe of the receive subarray), considering isotropic antenna elements and classical power budget equation for clutter with constant reflectivity. The Clutter-to-Noise Ratio (CNR) is 60 dB per element per pulse.

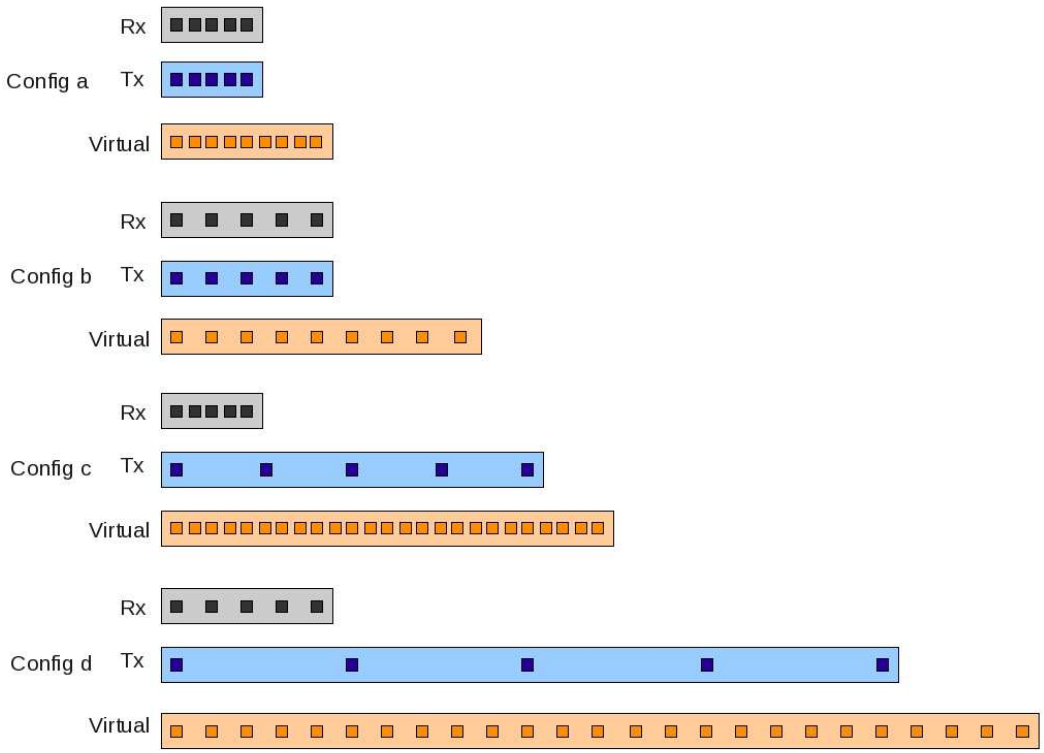

Figure 3.6: Element spacing configurations for MIMO-STAP, using Config 3 as example.

3.1.5.1 Detection Performance

In Fig. 3.7, we have the P_d against SNR for Config 1-4 (see Table 3.1 and Fig. 3.2 for configurations). As explained in Section 3.1.4, the curves for Config 2 and 4 coincide. As the Doppler frequency for target 2 is far from that of the clutter, the final SIR is approximately equal to SNR x MNL. We see that the MIMO configurations (Config 2-4) give us better detection performance than the classical STAP configuration (Config 1) as these configurations have larger MNL.

Due to SIR loss from clutter cancellation, the detection curves for target 1 are shifted to the right by approximately 22.5 dB, 18 dB and 15 dB for Config 1,2 (and 4) and 3, respectively. These values correspond to the SIR loss as defined in Eqn. (3.1) and shown in Fig. 3.8. The MIMO configurations have smaller SIR loss as larger MNL also increases the virtual aperture size (see Table 3.1) which in turn reduces the width of the clutter ridge. Hence, for target 1, the differences in performance are even more obvious.

Fig. 3.9 gives the P_d for different ω_t when SNR = 0 dB. Once again, we see that the MIMO configurations limit the loss in performance detection even for low ω_t. At $P_d = 0.9$, the MDV for Config 2 (and 4) is less than half of that for Config 1 while the MDV of Config 3 is only one quarter of that for Config 1.

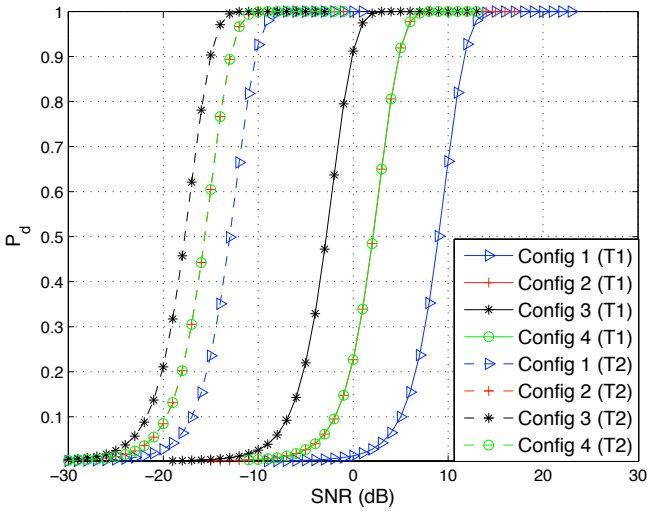

Figure 3.7: P_d against SNR for Config 1-4. In all cases, $\theta = 0$ and Config c.

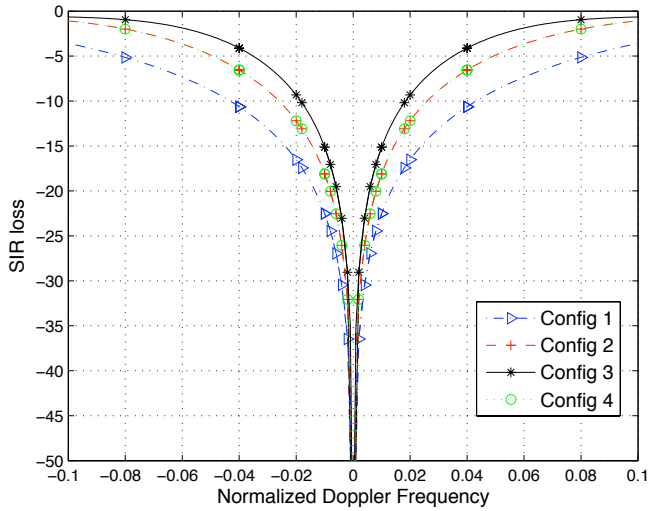

Figure 3.8: SIR Loss against ω_t for Config 1-4. In all cases, $\theta = 0$ and Config c.

Fig. 3.10 shows the corresponding P_d against SNR plot for Config a-d (see Table 3.2 and Fig. 3.6 for configurations). Here, MNL is the same (Config 3). Thus, we see that the detection performance for target 2 is almost the same for all configurations except for Config a which suffers a slight SIR loss of about 1 dB even at $\omega_t = 0.2$. For target 1, the differences in detection performance come from the differences in virtual aperture size L_a due to the spacing between the elements as shown in Table 3.3. We see that having the transmit elements spaced at $\gamma = \alpha M$ (Config c and d) is much better than having them spaced at $\gamma = \alpha$ (Config a and

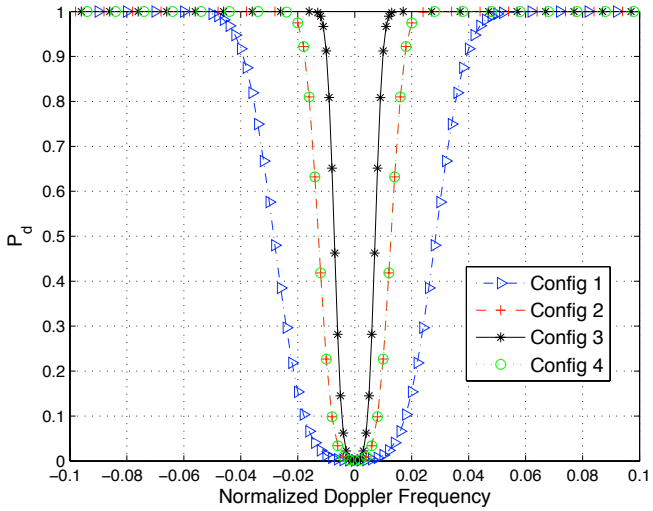

Figure 3.9: P_d against ω_t for Config 1-4. In all cases, $\theta = 0$, SNR $= 0$ dB and Config c.

b). According to Fig. 3.11, the SIR loss for target 1 is 24.5 dB, 19 dB, 15 dB and 12.5 dB for Config a, b, c and d, respectively. In the case where there is Doppler ambiguity $\beta > 1$ ($\beta = 2$ in this case), it can be further exploited to improve the detection performance (compare Config c and d).

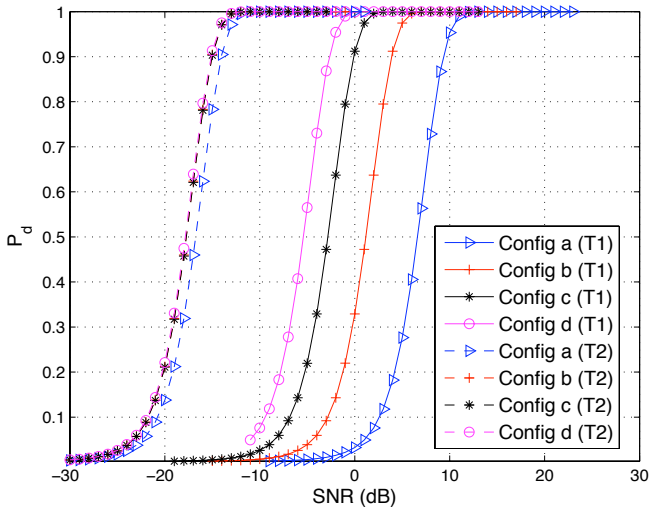

Figure 3.10: P_d against SNR for Config a-d. In all cases, $\theta = 0$ and Config 3.

Fig. 3.12 gives the P_d for different ω_t when SNR $= 0$ dB. The sparse configurations are able to reduce the MDV due to larger L_a: at $P_d = 0.9$, the MDV for Config c and d are about one third of that for Config a and about half of that for Config b.

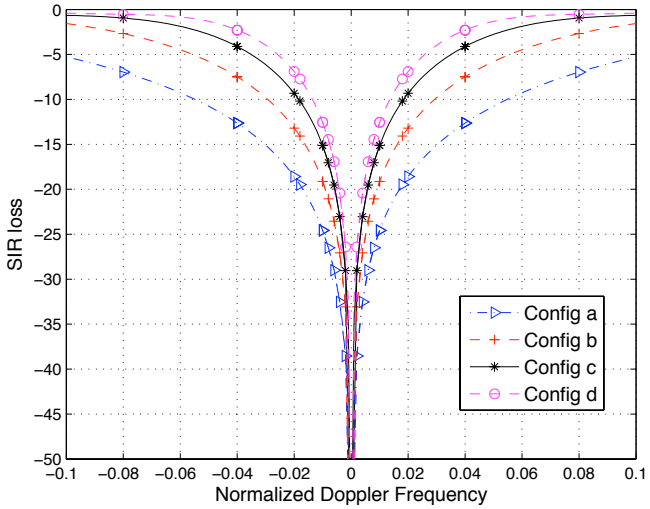

Figure 3.11: SIR Loss against ω_t for Config a-d. In all cases, $\theta = 0$ and Config 3.

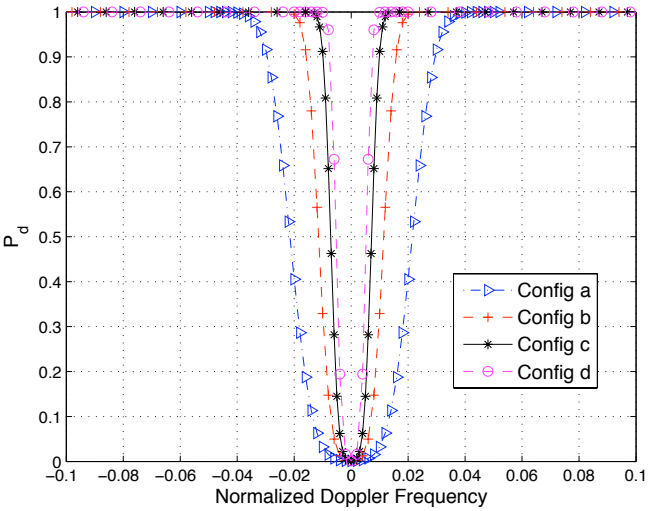

Figure 3.12: P_d against ω_t for Config a-d. In all cases, $\theta = 0$, SNR $= 0$ dB and Config 3.

3.1.5.2 Adaptive Detection Performance

In Fig. 3.13, we have the P_d against SNR for Config 1-4. Here, $\mathbf{M}$ is unknown and has to be estimated. This causes a degradation in detection performance for all configurations. Assume that we have only $N_s = 500$ secondary data. From Table 3.4, we see that with $N_s = 500$, $E(l_f)$ for Config 1 is more than 0.71 while it is only 0.20 for Config 3. This is because the size of $\mathbf{M}$ is larger for Config 3 and more secondary data is required for estimation. Indeed, it can be seen in Fig 3.14 that Config 3 is the most affected by the estimation of the covariance matrix due

to its deficiency in secondary data, especially for targets far from the clutter notch. This is why its detection performance is the worst for target 2. However, Config 3 still has a narrower clutter notch than Config 1 and similar to that of Config 2 and 4. Hence, for target 1 with small ω_t, Config 3 is still the best due to its large N_e and L_a. However, its advantage over Config 2 and 4 has diminished.

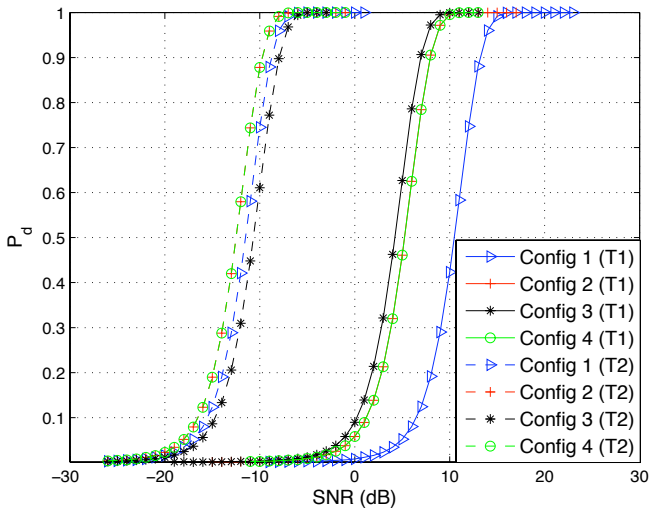

Figure 3.13: P_d against SNR for Config 1-4. In all cases, $\theta = 0$ and Config c. $N_s = 500$.

Config	N_s needed to have $E(l_f) = 0.5$	N_s/MNL	$E(l_f)$ for $N_s = 500$
1	285	3.47	0.71
2	509	1.95	0.49
3	797	1.25	0.20
4	509	1.95	0.49

Table 3.4: Required N_s for $E(l_f) = 0.5$, N_s/MNL and $E(l_f)$ for different configurations.

P_d against ω_t for Config 1-4 is plotted in Fig. 3.15. Compared to Fig. 3.9, we see that the MDV has increased for all the four configurations when the covariance matrix has to be estimated. Although Config 3 still has the best MDV, it no longer has much advantage over Config 2 and 4 ($\omega_t = 0.023$ compared to $\omega_t = 0.025$ for Config 2 and 4 at $P_d = 0.9$) as it is penalized by the deficiency in secondary data.

Next, we look at the corresponding plots for Config a-d (Config 3). In Fig. 3.16, the estimation of covariance matrix results in a loss of about 7 dB in detection performance for all configurations. The loss is the same as the configurations have the same MNL and N_s and hence the same $E(l_f)$. The loss of 7 dB corresponds

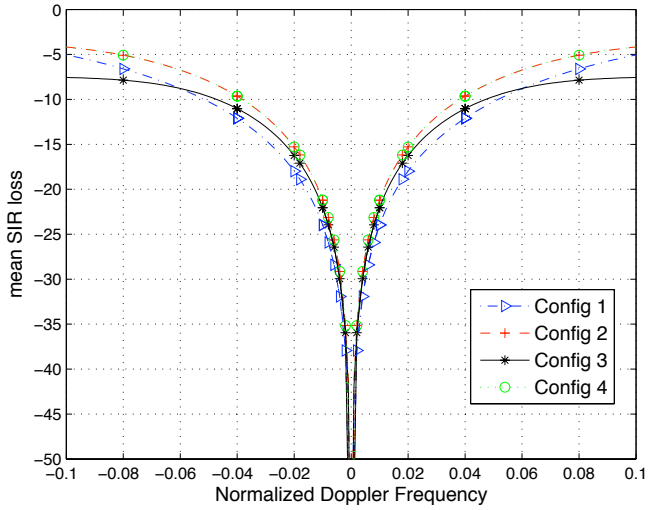

Figure 3.14: Mean SIR Loss against ω_t for Config 1-4. In all cases, $\theta = 0$ and Config c. $N_s = 500$.

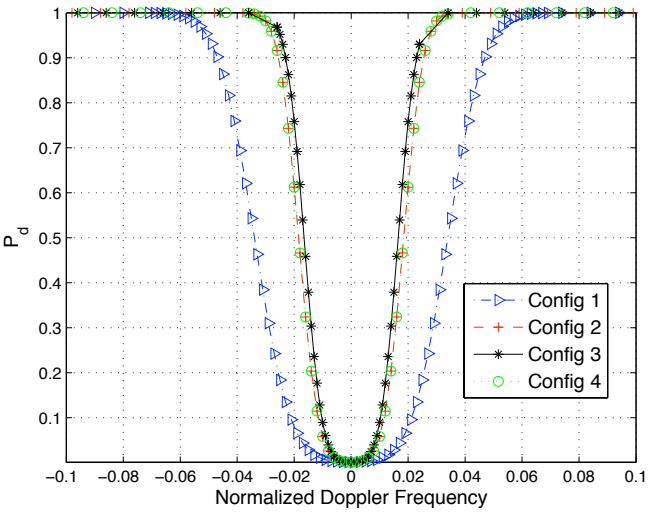

Figure 3.15: P_d against ω_t for Config 1-4. In all cases, $\theta = 0$, SNR = 0 dB and Config c. $N_s = 500$.

to $E(l_f) = 0.20$ as given in Table 3.4. Similarly, we see an additional loss of 7 dB in the mean SIR loss of Config a-d in Fig. 3.17 as compared to Fig. 3.11 for the optimum detection case.

In Fig. 3.12, the MDV for the adaptive detector is about 2.3 times the MDV for the non-adaptive detector, for $P_d = 0.9$ and for all configurations. Again, this is because all the configurations have the same MNL and N_s and the Kelly's Test

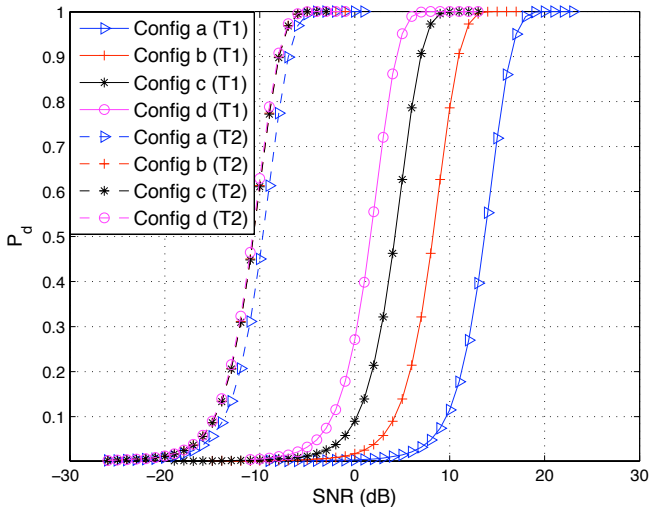

Figure 3.16: P_d against SNR for Config a-d. In all cases, $\theta = 0$ and Config 3. $N_s = 500$.

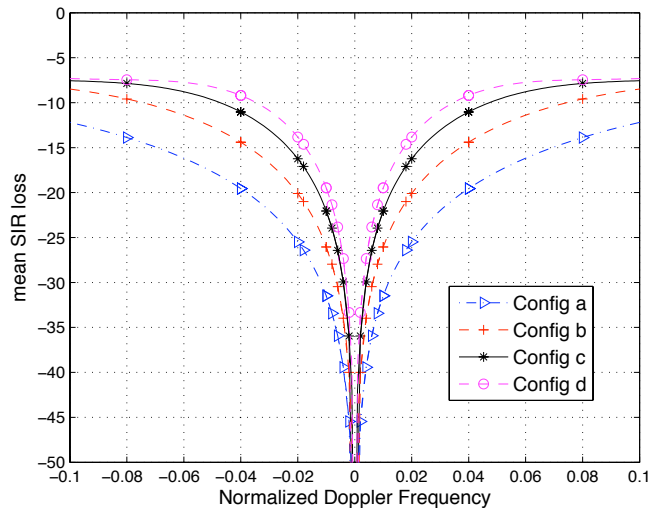

Figure 3.17: Mean SIR Loss against ω_t for Config a-d. In all cases, $\theta = 0$ and Config 3. $N_s = 500$.

does not take into account the structure of $\mathbf{M}$. While the Kelly's Test is optimum and the SCM is the ML estimate of the covariance matrix, it might not be the best option when there are not enough secondary data as the detector suffers a big loss l due to the bad estimation of the covariance matrix. It might also be better to choose Config 2 which requires fewer secondary data than Config 3.

However, with prior knowledge of the structure of $\mathbf{M}$, we can improve the matrix estimation especially if N_s is small. From Theorem 3.1, we know that the clutter

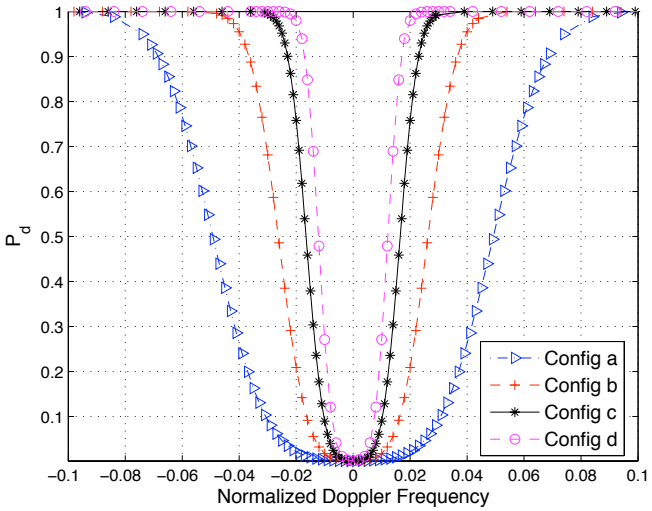

Figure 3.18: P_d against ω_t for Config a-d. In all cases, $\theta = 0$, SNR = 0 dB and Config 3. $N_s = 500$.

covariance matrix is generally of low rank ($N_d \ll MNL$), especially when configurations like Config b and d are used. Hence the interference covariance matrix has N_d significant eigenvalues while the remaining $MNL - N_d$ eigenvalues are much smaller and equal, corresponding to the noise power. As shown in [97], the required number of secondary data can be reduced to be twice the rank of the CCM i.e. $2N_d$. This is very important as it is difficult to have access to sufficient secondary data in practice, especially when MNL is large.

3.1.5.3 Estimation Performance

First, we compare the different configurations (Config 1-4, see Table 3.1) for the *optimum* case (Config c), i.e. $\alpha = 1$ and $\gamma = M$. $\beta = 2$ in this case. In Fig. 3.19, the CRBs for θ and f_t are plotted in dB against the normalized Doppler frequency ω_t. Once again, the curves for Config 2 and Config 4 overlap, hence the curve for Config 2 is not visible. In general, we see that the CRB is low when it is far from the clutter ridge while it becomes much higher at the clutter ridge ($\omega_t = 0$) due to the presence of strong clutter. Config 3 gives the lowest CRB in general, i.e. better estimation accuracy. At CRB = -50 dB (for f_t), the minimum ω_t for Config 3 is about one quarter of that for Config 1, indicating a much smaller MDV. More importantly, all the MIMO configurations (Config 2-4) show improvement in estimation performance over the classical STAP configuration (Config 1).

Next, we compare for Config 2 and 3 the effects of changing the different parameters according to Table 3.2. Note that there is no additional clutter peak due to grating lobes even though $\alpha > 1$ and $\gamma > 1$ because the parameters are chosen such that the clutter slopes coincide with that due to $\beta = 2$. According to Table 3.3,

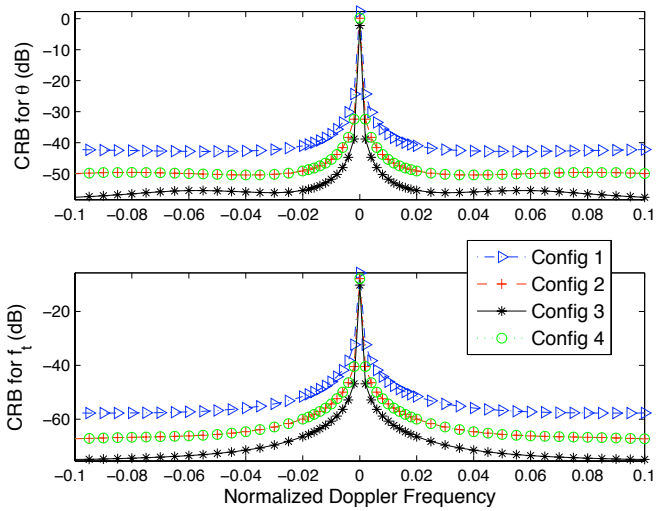

Figure 3.19: CRB in dB for θ (top) and f_t (bottom) for Config 1-4. $\beta = 2$.

Config 2 and 3 have the same effective aperture size L_a under Config a and b, i.e. equal spacings between transmit and receive elements while Config c and d bring out the advantages of equal N and M: L_a is much larger for Config 3 than Config 2. Surprisingly, for Config 2, L_a is slightly better for Config b than c which is the optimum configuration when $\beta = 1$.

In Fig. 3.20, we have the CRB in dB for θ and f_t for Config 2 and Config 3. The improvements in CRB are proportional to the improvements in L_a from Table 3.3. With large L_a, the angular resolution cells are smaller, hence there are more resolution cells between clutter and the target within the same Doppler bin, making clutter suppression easier. The improvements in CRB are more significant for θ than in f_t.

3.2 MISO-STAP

In the previous sections, we have studied the possibility of using SISO configurations to improve detection performance and MDV. However, with only one antenna system, it is vulnerable to the changes in direction of the target motion as well as target RCS fluctuations. Hence, in this section, we consider the feasibility of using spatial diversity to overcome these difficulties.

3.2.1 Signal Model

Consider that there is one receive subarray with closely-spaced elements for direction-finding. Due to the angle-Doppler dependence of the clutter, high angular resolution will keep the clutter within a smaller angle-Doppler space, hence increasing usable angle-Doppler space. Let there be K_e transmit subarrays each containing

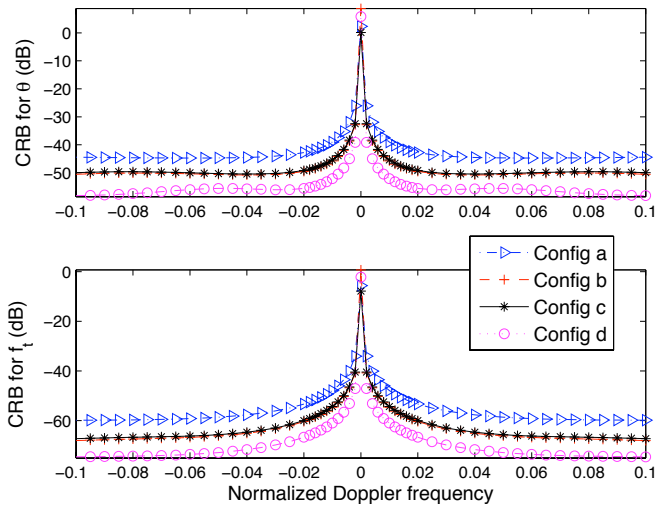

(a) Config 2

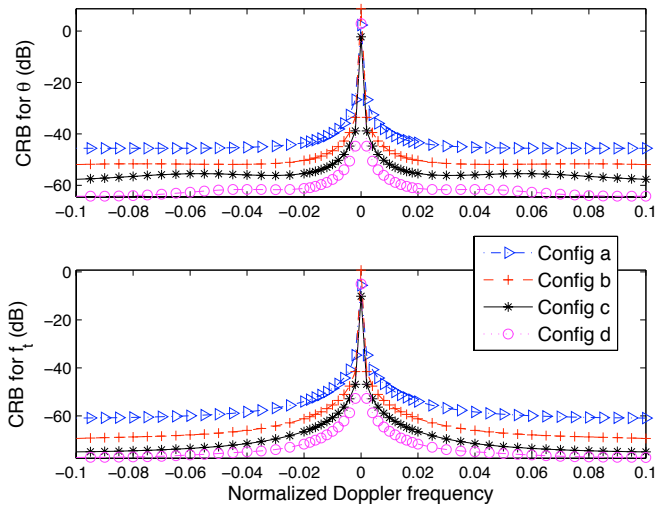

(b) Config 3

Figure 3.20: CRB in dB for θ (top) and f_t (bottom) for Config a-d. $\beta = 2$.

only one element. These subarrays are widely separated to ensure that the clutter returns are uncorrelated. Each transmit-receive subarray pair is in a bistatic configuration and the target RCS seen by each subarray pair is also different, given by $\boldsymbol{\alpha} = [a_1 e^{j\phi_1} \ \cdots \ a_{K_e} e^{j\phi_{K_e}}]^T$. It is assumed that the target remains in the cell-under-test during the CPI and that the target RCS does not change from pulse to pulse although it is different for each subarray.

Assume here that pulse waveforms which maintain sufficient orthogonality under different delays and Doppler shifts are available such that the received signal can

be separated after range matched filtering. Let there be L pulses in each CPI for all subarrays. The received signal can be expressed as:

$$\begin{aligned}\mathbf{y}_i &= a_i e^{j\phi_i}\mathbf{a}(\theta_r) \otimes \mathbf{v}(f_{d,i}) + \mathbf{c}_i + \mathbf{n}_i, \\ &= a_i e^{j\phi_i}\mathbf{p}_i + \mathbf{c}_i + \mathbf{n}_i,\end{aligned}$$

where $\mathbf{p}_i$ is the steering vector for the i-th subarray, containing the receive and Doppler steering vectors. Note that there is no transmit steering vector as there is only one transmit element in each subarray.

The receive steering vector is the same for all subarrays as there is only one receive subarray:

$$\mathbf{a}(\theta_r) = \left[1 \ \cdots \ \exp(j2\pi\frac{(M-1)d_r}{\lambda}\sin\theta_r)\right]^T,$$

where θ_r is the receive angle, λ is the wavelength of the radar and PRI is the Pulse Repetition Interval. d_r is the inter-element spacing for the receive subarray.

On the other hand, the Doppler steering vector varies from subarray to subarray:

$$\mathbf{v}(f_{d,i}) = [1 \ \cdots \ \exp(j2\pi(L-1)\mathrm{PRI}\cdot f_{d,i})]^T,$$

and $f_{d,i}$ is the Doppler frequency for the i-th subarray. Note that $f_{d,i}$ is different for each subarray due to the relative position and velocity of the transmit and receive subarrays with respect to the target.

As in Section 3.1.1, the interference part consists of clutter $\mathbf{c}_i$ and noise $\mathbf{n}_i$. $\mathbf{c}_i$ is a MLx1 vector containing clutter returns and $\mathbf{c}_i \sim \mathcal{CN}(\mathbf{0}, \mathbf{M}_{c,i})$. $\mathbf{M}_{c,i}$ is the CCM for the i-th subarray and is of low rank. $\mathbf{n}_i$ is a MLx1 vector containing uncorrelated thermal noise for the i-th subarray such that $\mathbf{n}_i \sim \mathcal{CN}(\mathbf{0}, \sigma_i^2\mathbf{I})$. We assume here for simplicity that the noise power in all subarrays is identical such that $\sigma_i^2 = \sigma^2$ for all i. The overall interference covariance matrix of the i-th subarray is thus:

$$\mathbf{M}_i = \mathbf{M}_{c,i} + \sigma^2\mathbf{I}.$$

3.2.2 Detection

As the interference received in the different subarrays are uncorrelated and Gaussian, the optimum detector is the MIMO OGD, given by Eqn. (2.8):

$$\ln\Lambda(\mathbf{y}) = \sum_{i=1}^{K_e}\frac{|\mathbf{p}_i^\dagger\mathbf{M}_i^{-1}\mathbf{y}_i|^2}{\mathbf{p}_i^\dagger\mathbf{M}_i^{-1}\mathbf{p}_i}.$$

In Section 2.3, we have derived the general version of MIMO OGD in the sense that it does not require the subarrays to be independent. The detector is **M**-CFAR and no assumption is made on the steering vector. In fact, it has the same structure

in Section 2.3 as in this section but with different parameters. Thus, the statistical properties are similar:

$$\ln \Lambda(\mathbf{y}) \overset{d}{=} \begin{cases} \mathrm{H}_0: & \frac{1}{2}\chi^2_{2K_e}(0), \\ \mathrm{H}_1: & \frac{1}{2}\chi^2_{2K_e}(2\sum_{i=1}^{K_e} a_i^2 \mathbf{p}_i^\dagger \mathbf{M}_i^{-1}\mathbf{p}_i). \end{cases}$$

In Section 3.1.2.1, we presented the standard performance metric used to measure SIR loss under clutter compared to the ideal case where there is only noise. In the case of MISO-STAP, the clutter notch for each subarray occurs at different Doppler frequencies. Hence, it is necessary to use the MIMO version of this performance metric to obtain the overall performance of the radar. The MIMO version of SIR loss is given by:

$$\text{SIR loss} = \sigma^2 \frac{\sum_{i=1}^{K_e} a_i^2 \mathbf{p}_i^\dagger \mathbf{M}_i^{-1}\mathbf{p}_i}{\sum_{i=1}^{K_e} a_i^2 ML}.$$

Note that the target power does not cancel out as in the case of SISO-STAP, that is to say that the SIR loss depends on the distribution of the target RCS. If the target RCS is high where the clutter is weak and low where the clutter is strong, SIR loss will be small and vice versa. We see also that SIR loss depends on geometry gain, given by $\mathbf{p}_i^\dagger \mathbf{M}_i^{-1}\mathbf{p}_i$ and on diversity gain, given by $\sum_{i=1}^{K_e} a_i^2$.

If the target power is equal for all subarrays such that $a_i^2 = a^2 \ \ \forall\ i$, we obtain:

$$\begin{aligned} \text{SIR loss} &= \sigma^2 \frac{\sum_{i=1}^{K_e} a^2 \mathbf{p}_i^\dagger \mathbf{M}_i^{-1}\mathbf{p}_i}{K_e a^2 ML}, \\ &= \frac{\sigma^2}{K_e} \frac{\sum_{i=1}^{K_e} \mathbf{p}_i^\dagger \mathbf{M}_i^{-1}\mathbf{p}_i}{ML}, \end{aligned} \tag{3.2}$$

which is equivalent to the average SIR loss for each subarray. Similarly, if the target RCS follows a complex Rayleigh distribution (from subarray to subarray), then its variance is given by σ_t^2 and we will have the same expression for SIR loss as in Eqn. (3.2).

3.2.3 Simulation Configurations and Parameters

Let there be a receive subarray at the origin with $M = 8$ elements, spaced at half-wavelength. We consider 3 cases: $K_e = 1, 2, 5$. $K_e = 1$ is the classical phased array and is included for comparison. The number of pulses is $L = 16$ so that Doppler frequency can be estimated as well. There is only one element in each transmit subarray. The transmit subarrays are assumed to be sufficiently far apart such that the clutter returns are independent for each subarray. For simplicity, they are placed at uniformly spaced angles in the same hemisphere as the receive subarray and are equidistant from the target as shown in Fig. 3.21 for the case of $K_e = 5$.

The position and velocity of the receive and transmit subarrays, as well as that for the target, are shown in Table 3.5. As before, the operating frequency of the

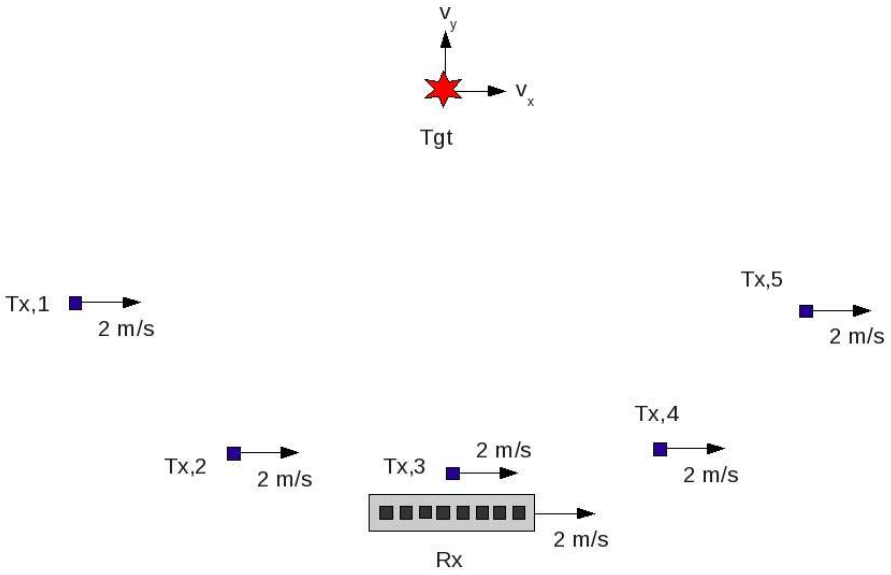

Figure 3.21: Simulation configuration for MISO-STAP ($K_e = 5$).

Receive x-position (km)	0
Receive y-position (km)	0
Receive x-velocity (m/s)	2
Receive y-velocity (m/s)	0
Transmit x-position (km)	$70 \cdot \cos((-K_e : -1)\frac{\pi}{K_e+1})$
Transmit y-position (km)	$70 \cdot \sin((-K_e : -1)\frac{\pi}{K_e+1})$
Transmit x-velocity (m/s)	2
Transmit y-velocity (m/s)	0
Target x-position (km)	0
Target y-position (km)	70

Table 3.5: Simulation configuration for MISO-STAP.

radar is 15 MHz ($\lambda = 20$m). The SNR per element per pulse is given by SNR $= \frac{a^2}{\sigma^2}$. $P_{fa} = 0.001$ is used and $N_{MC} = 10^4$ runs are done for the simulations.

As before, the clutter covariance matrix is modeled by integration over 180° of azimuth angles (front lobe of the receive subarray), considering isotropic antenna elements and classical power budget equation for clutter with constant reflectivity. However, note that the isorange is now elliptic and different for each subarray. For

simplicity, we consider that the CNR is the same for all subarrays: 60 dB per element per pulse.

To demonstrate the robustness of the MISO-STAP configuration against the dependence of target RCS and variation of LOS speed on aspect angle, we consider two targets with different absolute speeds: 0.1 m/s (target 1) and 1.5 m/s (target 2). However, their directions vary randomly accordingly to an uniform distribution between 0 and 2π. Their RCS as seen by each subarray pair are represented by a Gaussian distribution:

$$\boldsymbol{\alpha} \sim \mathcal{CN}(\mathbf{0}, \sigma_t^2 \mathbf{I}),$$

where σ_t^2 is the power of the target. This RCS model is the same as that adopted in Chapter 2.

3.2.4 Simulation Results

In Fig. 3.22, we have the P_d against SNR curves for $K_e = 1, 2, 5$ and for the two targets as described in Section 3.2.3. $P_{fa} = 0.001$ is used. $K_e = 1$ is the classical STAP. For both targets, the detection performance is better for larger K_e despite the fact that higher threshold is required to maintain the same P_{fa} (see Appendix B.2). This is mainly due to increased N_e with increased K_e but it is also due to spatial diversity. With spatial diversity, the fluctuations of target RCS are averaged out. Moreover, due to the diversity of LOS directions, it is impossible for a moving target to have zero LOS speed for all antennas simultaneously. This explains why the detection curves for $K_e = 2, 5$ converge much faster to one than that for $K_e = 1$.

Interestingly, the improvement in detection performance is significant between $K_e = 1$ and $K_e > 1$ but much smaller between $K_e = 2$ and $K_e = 5$. With only two subarrays ($K_e = 2$), we are able to achieve much of the geometry and diversity gain.

Although it is not apparent from the detection curves, having spatial diversity also means that the full target velocity can be determined uniquely as each subarray detects the target with a different velocity, corresponding to the projection of the target's actual velocity to different LOS directions.

In Fig. 3.23, we have plotted the SIR loss against x and y velocities (denoted as v_x and v_y, respectively) for $K_e = 1, 2, 5$. Note that we consider $\theta_r = 0$ for all cases. We see that there are K_e clutter notches and these clutter notches lie in the XLOS direction of the corresponding subarray, as illustrated in Fig. 3.24 for $K_e = 2$. The performance of MISO-STAP is very *configuration-dependent*, not only on the number of subarrays and elements but also on the relative position of each subarray. Even with the same number of subarrays and elements, we can change the slope of the clutter notches by changing the relative position of each subarray.

Note that in this simulation, we consider that the target follows a complex Rayleigh distribution such that the SIR loss for MISO as given in Eqn. (3.2), is simply an average of the SIR loss for each subarray, as explained in Section 3.2.2. Thus, there are K_e clutter notches but these notches are shallower than in the SISO case. However, this means also that MISO suffers a slight performance loss

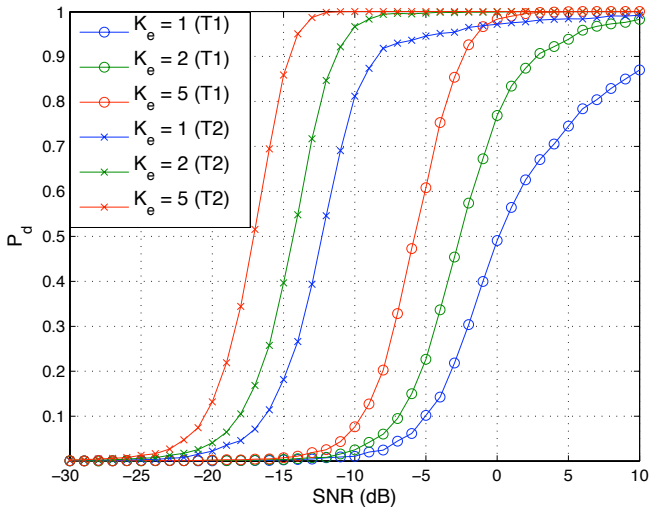

Figure 3.22: P_d against SNR for MISO-STAP with $K_e = 1, 2, 5$. In all cases, $\theta_r = 0$.

of several dBs outside the clutter notches. It might be interesting to consider a two-step detection algorithm e.g. M-out-of-N detection scheme, so as to exclude the contribution of subarrays whose clutter notch cancels out the target signal.

Next, we compare the detection performance of the MISO-STAP radar with $K_e = 2$ and the SISO-STAP radar with $N = 2$ (Config 2c as presented in Section 3.1.4). Both radar systems have a receive subarray with 8 elements spaced at half wavelength and 2 transmit elements. In the MISO case, the transmit elements are placed far apart according to Table 3.5 while in the SISO case, the transmit elements are placed $M \cdot \frac{\lambda}{2} = 4\lambda$ apart. Note that both configurations have the same number of physical elements $N_p = 10$ and effective number of elements $N_e = 16$.

In Fig. 3.25, we have plotted the P_d against SNR curves for MISO case ($K_e = 2$) and SISO ($N = 2$) and for the two targets described in Section 3.2.3. As expected, the detection performance is better for the SISO case at low P_d because of the improved resolution. However, the SISO configuration is not robust to fluctuations of target RCS and changes in direction of target motion such that its P_d converges slowly to one. Hence, the MISO case performs better at high P_d.

3.3 Summary

The detection and estimation performance of SISO-STAP are studied in terms of the detection probabilities for a fixed P_{fa} when $\mathbf{M}$ is known and unknown, as well as the CRB. Different configurations are considered. Given a fixed number of elements available, the distribution of the elements between the transmit and receive subarrays is varied (Config 1-4). It is found that when the number of transmit and receive elements is the same, the effective number of elements N_e and the effective

aperture size (for critical sampling) are maximized. The spacings between transmit and receive elements are then varied (Config a-d) to further increase the effective aperture size. The MIMO Brennan's rule is also generalized such that the spacings between transmit and receive elements are not necessarily at half wavelength. Using the generalized MIMO Brennan's rule, we also found that the sparse configurations (Config b and d) are able to reduce the rank of the CCM.

When the target is far from the clutter, maximizing N_e and thus SIR gain improves detection and estimation performance. However, when the target is near to the clutter, it is more important to maximize the effective aperture size as it will reduce SIR loss and hence reduce MDV.

A preliminary study is done on the application of MISO configurations to STAP (MISO-STAP). The setup considered consists of a single receive subarray and several transmit elements. Due to the angular diversity offered by MISO-STAP, the radar is robust against the fluctuations of target RCS and the dependence of the target velocity with respect to the aspect angle.

A comparison between MISO and SISO configurations is made in terms of detection probabilities, given the same N_p and N_e. The SISO configuration is better than the MISO configuration in general due to improved resolution. However, the MISO configuration is more robust to fluctuations of target RCS and target velocity directions, resulting in better performance at high P_d.

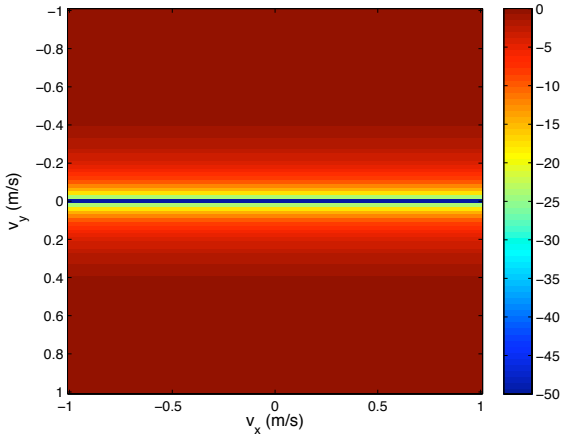

(a) $K_e = 1$

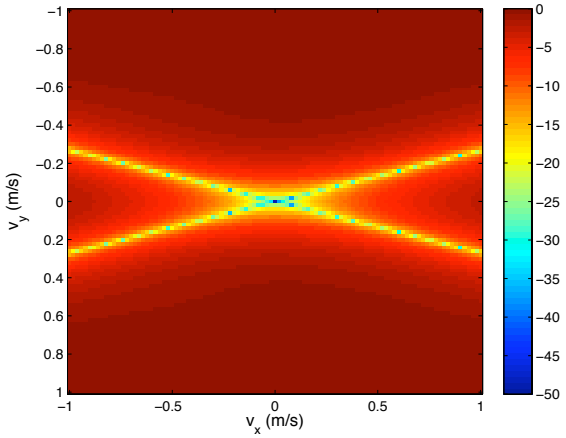

(b) $K_e = 2$

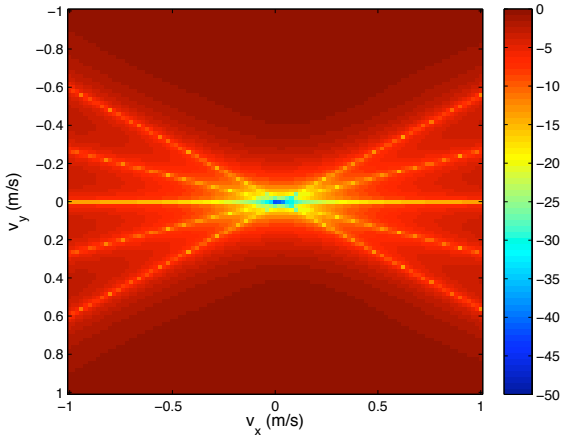

(c) $K_e = 5$

Figure 3.23: SIR loss in dB for different velocities in x and y directions for MISO-STAP with $K_e = 1, 2, 5$. In all cases, $\theta_r = 0$.

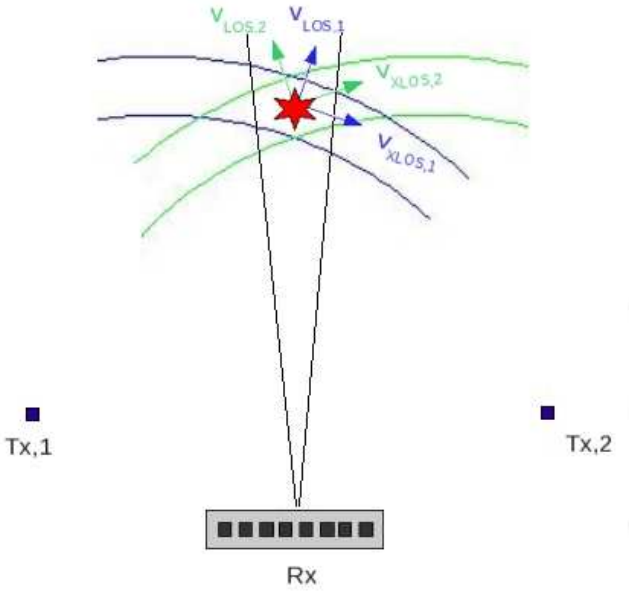

Figure 3.24: Illustration of the different LOS and XLOS velocities for different subarrays. $K_e = 2$.

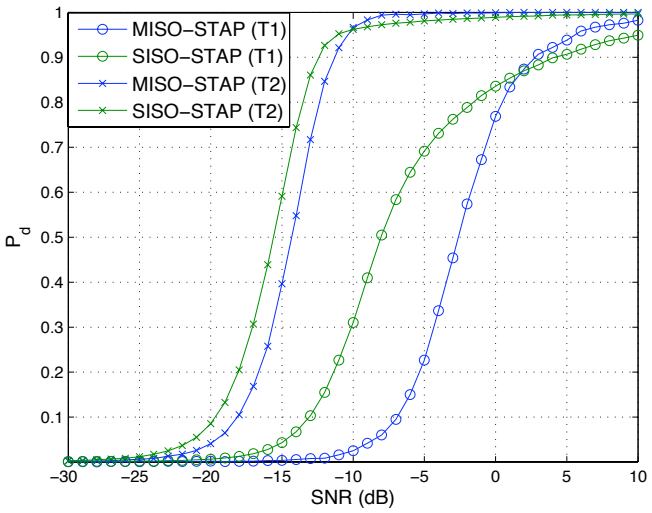

Figure 3.25: P_d against SNR for MISO-STAP with $K_e = 2$ and for SISO-STAP with $N = 2$. In both cases, $\theta_r = 0$.

Conclusions and Future Works

Conclusions

Gaussian Detector

A new MIMO Gaussian detector which takes into consideration possible correlation between subarrays has been derived. It becomes the classical MIMO OGD when the subarrays are uncorrelated such that the covariance matrix is block diagonal. This new detector is robust with respect to the interference parameters as its statistical property under H_0 is the same no matter if there is correlation between subarrays or not, i.e. the detector is **M**-CFAR. The adaptive version of this detector is also derived based on Kelly's Test. Finally, the **M**-CFAR property of the detector is verified using Monte-Carlo simulations. This new detector is interesting due to its robustness.

The properties of the detector are studied considering several different parameters, e.g. the effective number of subarrays K_e and the effective number of elements N_e. Having similar number of transmit and receive elements maximizes N_e, independent of the number of transmit and receive subarrays. It is important to maximize N_e as it affects the SIR gain. While having a larger K_e increases robustness against target fluctuations, it also increases the threshold required to maintain the same P_{fa}, resulting in a loss of detection performance for the same SIR. Monte-Carlo simulations are carried out to compare the detection performance for different K_e and N_e, as well as the degradation of the detection performance due to target fluctuations, modeled similarly to that of the well-known Swerling I target.

For the adaptive version, we discussed the loss factor l_f which arises due to the estimation of the covariance matrix and the number of secondary data N_s required for satisfactory detection performance. From the statistical distribution of l_f, it can be seen that given a fixed N_s, it might be better to choose a smaller N_e and a bigger K_e to reduce loss. To limit the loss to 3 dB, we need $N_s > 2N_e - 2K_e - 1$, providing $N_s \geq N_e$ is fulfilled such that the SCM is of full rank. Monte-Carlo simulations are then carried out to compare the detection performance for different K_e, N_e and N_s.

Non-Gaussian Detector

The CFAR GLRT-LQ detector for detection under non-Gaussian interference has been extended to the MIMO case where all subarrays are considered jointly as a system such that only one detection threshold is used. Theoretical performance for the new detector, MIMO GLRT-LQ, is also derived and validated using Monte Carlo simulations. Detection performance is then analyzed through simulations. Compared to the classical MIMO OGD detector, the new detector shows significant

improvements in detection performance under non-Gaussian interference especially under very impulsive interference. It has a slight loss in performance when the interference is Gaussian. This is expected since the MIMO OGD is the optimum detector under Gaussian interference. However, the robustness of the MIMO GLRT-LQ detector under non-Gaussian interference more than compensates this slight loss under Gaussian interference. The degradation of the detection performance due to target fluctuations was also investigated through simulations.

Next, the adaptive version of this new detector is considered. The FPE is used to estimate the covariance matrix as the classical SCM no longer works under non-Gaussian interference. The adaptive version is shown to be texture-CFAR and matrix-CFAR theoretically for the case where there is only one subarray. On top of that, the detection performance tends to that of the case where the covariance matrix is known when the number of secondary data is large. Due to the complexity of equations, the case where there is more than one subarray is studied only empirically using simulations.

The detection performance of the adaptive MIMO GLRT-LQ using FPE is then compared to the MIMO AMF using SCM and the MIMO Kelly's Test through simulations. As expected, the new detector performs much better under non-Gaussian interference, especially when the interference is very impulsive. Due to the similarity in structure between the MIMO Kelly's Test and the adaptive MIMO GLRT-LQ especially when there are few secondary data, the MIMO Kelly's Test suffers less loss in detection performance than the MIMO AMF under non-Gaussian interference. Moreover, the adaptive MIMO GLRT-LQ has comparable performance under Gaussian interference.

The main conclusion is that it is always preferable to use the adaptive MIMO GLRT-LQ with FPE regardless of the interference distribution because of the robustness of these tools with respect to the covariance matrix and the texture. Even in the case where the interference is Gaussian for all subarrays, the interference power for each subarray is expected to be different such that the texture is different and deterministic. Hence it is still better to use the new MIMO non-Gaussian detector.

SISO-STAP

In the first part of Chapter 3, we studied the detection and estimation performance of monostatic coherent MIMO-STAP (SISO-STAP) for different configurations in terms of the detection probabilities for a fixed P_{fa} when the interference parameters are known and unknown, as well as the CRB which give the lower bounds of the variances of estimators of deterministic parameters. We consider different configurations. Given a fixed number of elements available, the distribution of the elements between the transmit and receive subarrays is varied (Config 1-4). It is found that when the number of transmit and receive elements is the same, the effective number of elements N_e and the effective aperture size (for critical sampling) are maximized. The spacings between the transmit and receive elements are then varied (Config

a-d) to further increase the effective aperture size. The MIMO Brennan's rule is also generalized such that the spacings between the transmit and receive elements are not necessarily at half wavelength.

For the detection part, maximizing N_e increases P_d for a fixed P_{fa} when the target is far from clutter as the SIR gain is almost proportional to N_eL. On the other hand, when the target is located close to the clutter ridge, maximizing L_a is more important as it will reduce SIR loss and hence reduce MDV for a given P_d and P_{fa}. Use of sparse configurations with ambiguities (Config d) can further increase L_a and hence reduce MDV. It will not cause additional ambiguities if the spatial ambiguities are chosen to coincide with the Doppler ambiguities.

However, when N_e is large, more secondary data is needed to estimate $\mathbf{M}$ and it might not be possible to have access to such a big number of secondary data. In such a case, it might be better to select a configuration with a slightly smaller N_e. Moreover, using the generalized MIMO Brennan's rule, we also found that the sparse configurations (Config b and d) are able to reduce the rank of the CCM. The reduced rank can be exploited to reduce the number of secondary data required by using reduced-rank algorithms.

For the estimation part, the CRBs and MDV are lower if we do not estimate the target RCS simultaneously (for target identification and classification). Moreover, increase in L_a improves estimation in two ways: better accuracy in general, especially far from clutter and reduced MDV. The bounds can be further lowered without causing additional ambiguities by increasing the element spacing in certain ways.

MISO-STAP

In the second part of Chapter 3, a preliminary study is done on the application of MISO configurations to STAP (MISO-STAP). The setup considered consists of a single receive subarray and several transmit elements. This setup is interesting as it can easily be achieved by adding single transmit elements to existing STAP systems.

Due to the angular diversity offered by MISO-STAP, the radar is robust against the fluctuations of target RCS and the dependence of the target velocity with respect to the aspect angle. The performance of MISO-STAP depends not only on the number of subarrays and elements but also on the relative position of each subarray. This is because the slopes of the clutter notches depend on the relative positions of the subarrays.

A comparison between MISO and SISO configurations is made in terms of detection probabilities, given the same N_p and N_e. The SISO configuration is better than the MISO configuration in general due to improved resolution, however its probability of detection converges slowly to one as it is not robust to fluctuations of target RCS and target velocity directions. Hence, for high P_d, MISO performs better than the SISO configuration.

Future Works

MIMO radar signal processing is still a relatively new topic and there is still much work to be done. Some possible continuations to this thesis are proposed below.

- Signal Model:
  The signal model can be further developed in the following ways:
  - Include waveform information:
    It is more realistic as perfect orthogonal waveforms do not exist. In order to study the effects due to non-orthogonality of the waveforms on detection and estimation performance, it is necessary to include them in the signal model. Moreover, the signal model with waveform information can be used to design waveforms by imposing certain constraints.
  - Include range information:
    This will make the signal model more complete and enables us to study the irregular resolution cells arising from multistatic configurations.
  - Fluctuating models for target:
    Currently, the target RCS is assumed to be deterministic though different for each subarray in the derivation of the detector. As explained in Section 2.3.4.3, it can also be extended to the stochastic case by averaging P_d over the PDF of $\boldsymbol{\alpha}$. However, this does not result in a closed-form solution. It might be better to model target RCS directly as a random variable. This will cause a slight change in the statistical properties of the detector and give the closed-form expression of P_d for the stochastic case.
  - Use of tensors for representation and calculations:
    Due to the multi-dimensional nature of MIMO signal processing, it might be more efficient to use tensors to represent the signals instead of stacking received signals to form a long vector.

- Target classification:
  In the case of widely separated subarrays, the target RCS seen by each subarray is different and dependent on the aspect angle. Hence, with a sufficient number of subarrays, it is possible to obtain a rough RCS diagram of the target, enabling classification.

- Two-step detection and estimation algorithm:
  Currently, for the MIMO OGD, the detector is simply the sum of the detectors for each individual subarray. A two-step algorithm can be used to perform the hypothesis testing using only the P best subarrays in terms of SIR. Alternatively, adaptive weighting can be introduced to penalize subarrays with low SIR. This is particularly useful for MISO-STAP to exclude or reduce the contribution of subarrays whose clutter notch cancels out the target signal. Similarly, only subarrays with high SIR should be used for estimation.

- Experiments:
  Experiments have to be done to validate the theoretical and simulation results obtained in this thesis on Gaussian and non-Gaussian detectors, as well as MIMO-STAP.

- Low-rank methods for STAP:
  As mentioned in Chapter 3, the reduced rank of sparse configurations (config b and d) can be exploited by the application of low-rank methods to estimate the covariance matrix. Many low-rank methods exist already for classical STAP and it is interesting to extend these methods to the MIMO case.

- Diagonal loading:
  One of the main problems of MIMO detection is the increased dimension of the interference covariance matrix such that many secondary data are required for a good estimate of the matrix. However, due to the intrinsic nature of MIMO configurations, it is often difficult to have sufficient i.i.d. secondary data. Classical methods such as diagonal loading can be considered to improve performance when there are insufficient secondary data. It is interesting to derive adaptive methods to find the optimum loading factor for MIMO.

- Estimation bounds:
  In Chapter 3, the CRB for SISO-STAP is studied for a fixed SIR so as to see the dependence of the CRB on the azimuth angle due to the presence of the clutter ridge. However, it is also important to study the threshold SIR which defines the threshold where the estimator's performance approaches the CRB. At low SIR, the variance of the estimator is poor and far from CRB as the interference is of sufficient strength to cause the estimator to be confused by any large near ambiguities of the angle estimation statistic. Moreover, other bounds can be considered instead of the CRB which does not have very tight bounds.

Appendix A

Generalities

This appendix recalls the PDF of the main distributions used in this thesis.

A.1 Complex Gaussian Distribution

The PDF of a complex Gaussian random variable x with a mean of μ and a variance of σ^2 is given by:

$$f(x) = \frac{1}{\pi\sigma^2} \exp\left(-\frac{|x-\mu|^2}{\sigma^2}\right),$$

while the PDF of a complex multivariate Gaussian random vector $\mathbf{x}$ with a mean of $\boldsymbol{\mu}$ and a covariance matrix of $\mathbf{M}$ is given by:

$$f(\mathbf{x}) = \frac{1}{\pi^k \|\mathbf{M}\|} \exp\left(-(\mathbf{x}-\boldsymbol{\mu})^\dagger \mathbf{M}^{-1}(\mathbf{x}-\boldsymbol{\mu})\right).$$

A.2 Chi-square Distribution

The PDF of the chi-square distribution with k DoFs is given by:

$$f(x) = \begin{cases} \frac{1}{2^{k/2}\Gamma(k/2)}\, x^{k/2-1} e^{-x/2}, & x \geq 0, \\ 0, & \text{otherwise}, \end{cases}$$

where $\Gamma(z)$ is the Gamma function: $\Gamma(z) = \int_0^\infty t^{z-1} e^{-t} dt$ [86].

A.3 Uniform Distribution

The PDF of the uniform distribution with parameters a and b is given by:

$$f(x) = \begin{cases} \frac{1}{b-a} & a \leq x \leq b, \\ 0 & x < a \ \text{ or } \ x > b. \end{cases}$$

A.4 Beta and Beta Prime Distribution

The PDF of a Beta distributed random variable $x \sim \beta_{a,b}$ is given by:

$$f(x) = \frac{\Gamma(a+b)}{\Gamma(a)\Gamma(b)} x^{a-1}(1-x)^{b-1} \mathbb{1}_{[0,1]}(x),$$

where $\mathbb{1}_{[0,1]}(x)$ is the indicator function of x on the interval $[0,1]$.

The PDF of a Beta Prime distributed random variable $x \sim \beta'_{a,b}$, as defined in [86] is:

$$f(x) = \frac{\Gamma(a+b)}{\Gamma(a)\Gamma(b)} \frac{x^{a-1}}{(1+x)^{a+b}}, \quad x > 0.$$

A.5 F-Distribution

The PDF of an F-distributed random variable x with parameters a and b is given by:

$$f(x) = \frac{\Gamma(\frac{a+b}{2})}{\Gamma(\frac{a}{2})\Gamma(\frac{b}{2})} \frac{1}{x} \left(\frac{ax}{ax+b}\right)^{\frac{a}{2}} \left(1 - \frac{ax}{ax+b}\right)^{\frac{b}{2}}.$$

A.6 Gamma Distribution

The PDF and the statistical mean of the Gamma distribution with parameters a and b are given by:

$$\begin{aligned} p(x) &= \frac{1}{b^a \Gamma(a)} x^{a-1} e^{-x/b}, \\ E(x) &= ab. \end{aligned}$$

A.7 Weibull Distribution

The PDF and the statistical mean of the Weibull distribution with parameters a and b are given by:

$$\begin{aligned} p(x) &= \frac{b}{a} \left(\frac{x}{a}\right)^{b-1} e^{-(\frac{x}{a})^b}, \\ E(x) &= a\Gamma\left(1 + \frac{1}{b}\right). \end{aligned}$$

Appendix B

Appendices for Chapter 2

B.1 Maximum Effective Number of Elements

Let the total number of physical elements be N_p such that:

$$\begin{aligned} N_p &= \sum_{n=1}^{\tilde{N}} N_n + \sum_{m=1}^{\tilde{M}} M_m, \\ &= N_{tx} + N_{rx}, \end{aligned}$$

where N_{tx} and N_{rx} are the physical number of transmit elements and receive elements, respectively. The effective number of elements is then given by:

$$\begin{aligned} N_e &= \sum_{n=1}^{\tilde{N}} \sum_{m=1}^{\tilde{M}} N_n M_m, \\ &= \sum_{n=1}^{\tilde{N}} N_n \sum_{m=1}^{\tilde{M}} M_m, \\ &= N_{tx} N_{rx}, \\ &= N_{tx}(N_p - N_{tx}), \\ &= -\left(N_{tx} - \frac{N_p}{2}\right)^2 + \frac{N_p^2}{4}. \end{aligned}$$

To maximize N_e, we need to minimize $-\left(N_{tx} - \frac{N_p}{2}\right)^2$. When N_p is even, $N_e^{max} = \frac{N_p^2}{4}$ and $N_{tx} = N_{rx} = \frac{N_p}{2}$. When N_p is odd, $N_e^{max} = \frac{N_p^2}{4} - \frac{1}{4}$ while $N_{tx} = \frac{N_p+1}{2}$ and $N_{rx} = \frac{N_p-1}{2}$ or vice versa.

B.2 Detection threshold increases with DoF

If the detector follows a chi-square distribution: $\Lambda(\mathbf{y}) \sim \chi^2_{2K_e}(0)$, we have for a given P_{fa} and λ:

$$\begin{aligned} P_{fa} &= P(\Lambda(\mathbf{y}) > \lambda | \mathrm{H}_0), \\ &= \frac{\Gamma(K_e, \lambda)}{\Gamma(K_e)}, \end{aligned}$$

where $\Gamma(n, a)$ and $\Gamma(n)$ are the upper incomplete Gamma function and Gamma function, respectively. After modifying Eqn. (6.5.22) in [86], we have:

$$\Gamma(K_e, \lambda) = (K_e - 1)\Gamma(K_e - 1, \lambda) + \lambda^{K_e - 1} e^{-\lambda}.$$

As K_e is an integer, $\Gamma(K_e) = (K_e - 1)!$ and hence:

$$\frac{\Gamma(K_e, \lambda)}{\Gamma(K_e)} = \frac{\Gamma(K_e - 1, \lambda)}{\Gamma(K_e - 1)} + \frac{\lambda^{K_e - 1} e^{-\lambda}}{\Gamma(K_e)}.$$

As the second term on the right hand side is positive, it means that given the same detection threshold λ, P_{fa} is bigger for bigger K_e. To keep P_{fa} constant, λ will have to be increased for bigger K_e.

B.3 Alternative MIMO Kelly's Test

B.3.1 Derivation

We recall here the MIMO Kelly's Test when the subarrays are independent:

$$\hat{\Lambda}(\mathbf{y}) = \prod_{i=1}^{K_e} \left[1 - \frac{|\mathbf{p}_i^\dagger \widehat{\mathbf{M}}_{SCM,ii}^{-1} \mathbf{y}_i|^2}{(\mathbf{p}_i^\dagger \widehat{\mathbf{M}}_{SCM,ii}^{-1} \mathbf{p}_i)(N_{s,i} + \mathbf{y}_i^\dagger \widehat{\mathbf{M}}_{SCM,ii}^{-1} \mathbf{y}_i)} \right]^{-N_{s,i}}. \tag{B.1}$$

Given $N_{s,i}$ i.i.d. secondary data for the i-th subarray, the SCM of the i-th subarray $\mathbf{M}_{ii}$ is given by:

$$\widehat{\mathbf{M}}_{SCM,ii} = \frac{1}{N_{s,i}} \sum_{l=1}^{N_{s,i}} \mathbf{z}_i(l)\mathbf{z}_i(l)^\dagger.$$

Using $\widehat{\mathbf{M}}_{SCM,ii}$, we can define the matrices $\mathbf{T}_{0,i}$ and $\mathbf{T}_{1,i}$ as below:

$$\begin{aligned}
\mathbf{T}_{0,i} &= \frac{1}{N_{s,i}+1} \left(\mathbf{y}_i \mathbf{y}_i^\dagger + N_{s,i} \widehat{\mathbf{M}}_{SCM,ii} \right), \\
\mathbf{T}_{1,i} &= \frac{1}{N_{s,i}+1} \left((\mathbf{y}_i - \alpha_i \mathbf{p}_i)(\mathbf{y}_i - \alpha_i \mathbf{p}_i)^\dagger + N_{s,i} \widehat{\mathbf{M}}_{SCM,ii} \right).
\end{aligned}$$

Under H_0 and H_1, the likelihood functions are given by:

$$\begin{aligned}
f(\mathbf{y}_i, \mathbf{z}_i(1), \ldots, \mathbf{z}_i(N_{s,i})|\mathrm{H}_0) &= \left[\frac{1}{\pi^{N_{e,i}} \|\mathbf{M}_{ii}\|} \exp\left(-\mathrm{tr}(\mathbf{M}_{ii}^{-1} \mathbf{T}_{0,i}) \right) \right]^{N_{s,i}+1}, \\
f(\mathbf{y}_i, \mathbf{z}_i(1), \ldots, \mathbf{z}_i(N_{s,i})|\mathrm{H}_1) &= \left[\frac{1}{\pi^{N_{e,i}} \|\mathbf{M}_{ii}\|} \exp\left(-\mathrm{tr}(\mathbf{M}_{ii}^{-1} \mathbf{T}_{1,i}) \right) \right]^{N_{s,i}+1}.
\end{aligned}$$

Maximizing with respect to $\mathbf{M}_{ii}$, we obtain:

$$\begin{aligned}
\max_{\mathbf{M}_{ii}} f(\mathbf{y}_i, \mathbf{z}_i(1), \ldots, \mathbf{z}_i(N_{s,i})|\mathrm{H}_0) &= f(\mathbf{y}_i, \mathbf{z}_i(1), \ldots, \mathbf{z}_i(N_{s,i})|\mathrm{H}_0)|_{\widehat{\mathbf{M}}_{ii} = \mathbf{T}_{0,i}}, \\
&= \left[\frac{1}{(\pi e)^{N_{e,i}} \|\mathbf{T}_{0,i}\|} \right]^{N_{s,i}+1}, \\
\max_{\mathbf{M}_{ii}} f(\mathbf{y}_i, \mathbf{z}_i(1), \ldots, \mathbf{z}_i(N_{s,i})|\mathrm{H}_1) &= f(\mathbf{y}_i, \mathbf{z}_i(1), \ldots, \mathbf{z}_i(N_{s,i})|\mathrm{H}_1)|_{\widehat{\mathbf{M}}_{ii} = \mathbf{T}_{1,i}}, \\
&= \left[\frac{1}{(\pi e)^{N_{e,i}} \|\mathbf{T}_{1,i}\|} \right]^{N_{s,i}+1}.
\end{aligned}$$

As the subarrays are independent, the adaptive detector can be written as:

$$\begin{aligned}
\hat{\Lambda}(\mathbf{y}) &= \prod_{i=1}^{K_e} \frac{\max\limits_{\mathbf{M}_{ii}, \alpha_i} f(\mathbf{y}_i, \mathbf{z}_i(1), \ldots, \mathbf{z}_i(N_{s,i})|\mathrm{H}_1)}{\max\limits_{\mathbf{M}_{ii}} f(\mathbf{y}_i, \mathbf{z}_i(1), \ldots, \mathbf{z}_i(N_{s,i})|\mathrm{H}_0)}, \\
&= \prod_{i=1}^{K_e} \left[\frac{\|\mathbf{T}_{0,i}\|}{\min\limits_{\alpha_i} \|\mathbf{T}_{1,i}\|} \right]^{N_{s,i}}.
\end{aligned}$$

Using Eqn. (2.13), Eqn. (2.14) and Eqn. (2.6), we obtain Eqn. (B.1).

B.3.2 Statistical Properties

Eqn. (B.1) can also be expressed as a product of the detectors for each subarray:

$$\hat{\Lambda}(\mathbf{y}) = \prod_{i=1}^{K_e} \left[\frac{1}{1-\hat{\Lambda}_i} \right]^{N_{s,i}},$$

where

$$\hat{\Lambda}_i = \frac{|\mathbf{p}_i^\dagger \widehat{\mathbf{M}}_{SCM,ii}^{-1} \mathbf{y}_i|^2}{(\mathbf{p}_i^\dagger \widehat{\mathbf{M}}_{SCM,ii}^{-1} \mathbf{p}_i)(N_{s,i} + \mathbf{y}_i^\dagger \widehat{\mathbf{M}}_{SCM,ii}^{-1} \mathbf{y}_i)} \sim \beta_{1,N_{s,i}-N_{e,i}+1}.$$

Let all subarrays have the same length $N_{e,0}$ and the same number of secondary data $N_{s,0}$ such that:

$$\hat{\Lambda}_i \sim \beta_{1,N_{s,0}-N_{e,0}+1} \quad \forall\ i = 1, \ldots, K_e.$$

Following the same steps as in Appendix B.5, we obtain the probability of false alarm:

$$P_{fa} = \eta^{-(N_{s,0}-N_{e,0}+1)} \sum_{k=0}^{K_e-1} \frac{(N_{s,0}-N_{e,0}+1)^k}{k!} (\ln \eta)^k.$$

B.4 Proof of Theorem on loss factor when $N_e = K_e$

When there is only 1 element per subarray, $\mathbf{P} = \mathbf{I}$ and Eqn. (2.15) becomes:

$$\begin{aligned}\hat{\Lambda}(\mathbf{y}) &= \frac{\mathbf{y}^\dagger \widehat{\mathbf{M}}_{SCM}^{-1}\mathbf{y}}{N_s + \mathbf{y}^\dagger \widehat{\mathbf{M}}_{SCM}^{-1}\mathbf{y}}, \\ &= \frac{\mathbf{y}^\dagger \bar{\mathbf{M}}_{SCM}^{-1}\mathbf{y}}{1 + \mathbf{y}^\dagger \bar{\mathbf{M}}_{SCM}^{-1}\mathbf{y}},\end{aligned}$$

where $\bar{\mathbf{M}}_{SCM} = N_s\widehat{\mathbf{M}}_{SCM} \sim \mathcal{CW}(N_s, N_e, \mathbf{M})$.

Let us define the matrix $\mathbf{C} = \mathbf{M}^{-1/2}\bar{\mathbf{M}}_{SCM}\mathbf{M}^{-1/2}$ and according to [98], $\mathbf{C} \sim \mathcal{CW}(N_s, N_e, \mathbf{I})$. Consider the whitened signal $\mathbf{x} = \mathbf{M}^{-1/2}\mathbf{y}$, we next perform an unitary transformation on $\mathbf{x}$ by $\mathbf{U}$ which is defined as:

$$\mathbf{U} = \left[\frac{\mathbf{x}}{\sqrt{\mathbf{x}^\dagger\mathbf{x}}},\ \tilde{\mathbf{U}}\right],$$

where $\tilde{\mathbf{U}}^\dagger\mathbf{x} = \mathbf{0}$. The transformed variable can be expressed using $\mathbf{e}_1^\dagger = [1\ 0\ \cdots\ 0]$:

$$\mathbf{U}^\dagger\mathbf{x} = \sqrt{\mathbf{x}^\dagger\mathbf{x}}\mathbf{e}_1,$$

and the detector becomes:

$$\begin{aligned}\hat{\Lambda}(\mathbf{x}) &= \frac{\mathbf{x}^\dagger\mathbf{x}\mathbf{e}_1^\dagger\mathbf{G}^{-1}\mathbf{e}_1}{1 + \mathbf{x}^\dagger\mathbf{x}\mathbf{e}_1^\dagger\mathbf{G}^{-1}\mathbf{e}_1}, \\ &= \frac{\mathbf{x}^\dagger\mathbf{x}\ g_{11}}{1 + \mathbf{x}^\dagger\mathbf{x}\ g_{11}},\end{aligned}$$

where $\mathbf{G} = \mathbf{U}^\dagger\mathbf{C}\mathbf{U} \sim \mathcal{CW}(N_s, N_e, \mathbf{I})$ and g_{11} is the top left element of $\mathbf{G}^{-1}$. Using Theorem 1 in [89], we find that the distribution of g_{11} is $\chi^2_{2(N_s-N_e+1)}$ and it is independent from $\mathbf{x}$.

Under H_0, $\mathbf{x} \sim \mathcal{CN}(\mathbf{0}, \mathbf{I})$ such that $\mathbf{x}^\dagger\mathbf{x} \sim \chi^2_{2N_e}(0) = \chi^2_{2K_e}(0)$. Under H_1, $\mathbf{x} \sim \mathcal{CN}(\mathbf{M}^{-1/2}\boldsymbol{\alpha}, \mathbf{I})$ such that $\mathbf{x}^\dagger\mathbf{x} \sim \chi^2_{2K_e}(2\boldsymbol{\alpha}^\dagger\mathbf{M}^{-1}\boldsymbol{\alpha}) = \chi^2_{2K_e}(2\mathrm{SIR}_{\mathrm{post}})$. Hence the distribution of the detector can be described as:

$$\hat{\Lambda}(\mathbf{y}) \overset{d}{=} \begin{cases} \mathrm{H}_0: & \beta_{K_e, N_s-N_e+1}(0), \\ \mathrm{H}_1: & \beta_{K_e, N_s-N_e+1}(2\mathrm{SIR}_{\mathrm{post}}). \end{cases}$$

Therefore, l_f is equal to one.

B.5 Proof of Theorem on P_{fa} of Non-Gaussian Detector

We recall that under H_0, the detector for the i-th subarray under *Gaussian* interference can be expressed in terms of an F-statistics:

$$1 - \frac{1}{\Lambda_i(\mathbf{y}_i)} = \frac{|\mathbf{p}_i^\dagger \mathbf{M}_i^{-1} \mathbf{y}_i|^2}{(\mathbf{p}_i^\dagger \mathbf{M}_i^{-1} \mathbf{p}_i)(\mathbf{y}_i^\dagger \mathbf{M}_i^{-1} \mathbf{y}_i)} \stackrel{d}{=} \frac{t_i}{t_i + 1},$$

where $(N_{e,i} - 1)t_i$ is a centralized F-distributed random variable with parameters $a = 2$ and $b = 2N_{e,i} - 2$. Assuming that all the subarrays have the same number of effective elements $N_{e,0}$, the random variable becomes $t_i' = (N_{e,0} - 1)t_i$. The PDF of t_i' is given in Appendix A.5. As a and b are both positive integers, the PDF can be simplied to:

$$f(t_i') = \left(\frac{N_{e,0} - 1}{t_i' + N_{e,0} - 1} \right)^{N_{e,0}}.$$

Each $\Lambda_i(\mathbf{x}_i)$ can also be expressed in terms of t_i':

$$\Lambda_i(\mathbf{x}_i) = \frac{1}{1 - \frac{t_i}{t_i + 1}} = 1 + t_i = 1 + \frac{t_i'}{N_{e,0} - 1}.$$

Let $u_i = \Lambda_i(\mathbf{x}_i)$ such that $t_i' = (u_i - 1)(N_{e,0} - 1)$,

$$\begin{aligned} f(u_i) &= f(t') \cdot \left| \frac{dt_i'}{du_i} \right|, \\ &= (N_{e,0} - 1) u_i^{-N_{e,0}}. \end{aligned}$$

In order to find the PDF for $u = \prod_{i=1}^{K_e} u_i$, we consider the bijective function from $(u_1, \ldots, u_{K_e})$ to $(u, v_1, \ldots, v_{K_e - 1})$ where:

$$\begin{aligned} u &= \prod_{i=1}^{K_e} u_i \in [1, +\infty), \\ v_1 &= u_1 \in [1, u], \\ v_i &= u_i \in [1, v_{i-1}] \quad i = 2, \ldots, K_e - 1. \end{aligned}$$

To obtain the PDF of u, we perform a change of variable (J denotes Jacobian):

$$\begin{aligned}
f_1(u_1,\ldots,u_{K_e}) &\equiv \prod_i^{K_e} f(u_i), \\
&= (N_{e,0}-1)^{K_e} u^{-N_{e,0}}, \\
f_2(u,v_1,\ldots,v_{K_e-1}) &\equiv \mathbb{1}_{u\geq v_1\geq\cdots\geq u_{K_e-1}\geq 1} f_1(u_1,\ldots,u_{K_e})|J|^{-1}, \\
&= (N_{e,0}-1)^{K_e} u^{-N_{e,0}} \frac{1}{\prod_{i=1}^{K_e-1} v_i}, \\
f_3(u,v_1,\ldots,v_{K_e-2}) &\equiv \mathbb{1}_{u\geq v_1\geq\cdots\geq u_{K_e-2}\geq 1} \int_1^{v_{K_e-2}} f_2(u,v_1,\ldots,v_{K_e-1}) dv_{K_e-1}, \\
&= (N_{e,0}-1)^{K_e} u^{-N_{e,0}} \frac{\ln v_{K_e-2}}{\prod_{i=1}^{K_e-2} v_i}, \\
f_4(u,v_1,\ldots,v_{K_e-3}) &\equiv \mathbb{1}_{u\geq v_1\geq\cdots\geq u_{K_e-3}\geq 1} \int_1^{v_{K_e-3}} f_3(u,v_1,\ldots,v_{K_e-2}) dv_{K_e-2}, \\
&= (N_{e,0}-1)^{K_e} u^{-N_{e,0}} \frac{1}{2} \frac{(\ln v_{K_e-3})^2}{\prod_{i=1}^{K_e-3} v_i}, \\
&\vdots \\
f_{K_e}(u) &\equiv \int_1^u f_{K_e-1}(u,v_1) dv_1, \\
&= (N_{e,0}-1)^{K_e} u^{-N_{e,0}} \frac{1}{(K_e-1)!} (\ln u)^{K_e-1}.
\end{aligned}$$

To obtain the P_{fa}, we integrate $f_{K_e}(u)$ from the threshold λ to infinity:

$$\begin{aligned}
P_{fa} &= \int_\lambda^\infty f_{K_e}(u) du, \\
&= \lambda^{-N_{e,0}+1} \sum_{k=0}^{K_e-1} \frac{(N_{e,0}-1)^k}{k!} (\ln\lambda)^k.
\end{aligned}$$

B.6 On P_{fa} of Adaptive Non-Gaussian Detector

To find the P_{fa}, we begin with the case where $K_e = 1$. The adaptive detector is given by:

$$\hat{\Lambda}_1(\mathbf{y}_1) = \left[\frac{|\mathbf{p}_1^\dagger \widehat{\mathbf{M}}_{FP,1}^{-1} \mathbf{y}_1|^2}{(\mathbf{p}_1^\dagger \widehat{\mathbf{M}}_{FP,1}^{-1} \mathbf{p}_1)(\mathbf{y}_1^\dagger \widehat{\mathbf{M}}_{FP,1}^{-1} \mathbf{y}_1)} \right]^{-1}.$$

and its distribution is:

$$\hat{\Lambda}_1(\mathbf{y}_1) \overset{d}{=} 1 + B_1 | l_{f,1}, \qquad \begin{cases} B_1 | l_{f,1} \sim \beta'_{1, n_{a,1}-1}, \\ l_{f,1} \sim \beta_{n_{a,1}, n_{b,1}-n_{a,1}-1}, \end{cases}$$

where

$$\begin{aligned} n_{a,1} &= \frac{N_{e,1}}{N_{e,1}+1} N_{s,1} - N_{e,1} + 2, \\ n_{b,1} &= \frac{N_{e,1}}{N_{e,1}+1} N_{s,1} + 2. \end{aligned}$$

Using the PDF of the beta and beta prime distribution given in Appendix A.4, we obtain the PDF of B_1:

$$\begin{aligned} f(B_1) &= \int_0^1 \frac{\Gamma(n_{a,1})\Gamma(n_{b,1}-1)}{\Gamma(n_{a,1}-1)\Gamma(n_{a,1})\Gamma(n_{b,1}-n_{a,1}-1)} \cdot \frac{(1-N_{e,1})^{n_{b,1}-n_{a,1}-1} l_{f,1}^{n_{a,1}-1}}{(1+B_1(1-l_{f,1}))^{n_{a,1}}} dl_{f,1}, \\ &= \frac{\Gamma(n_{b,1}-1)(1+B_1)^{-n_{a,1}}}{\Gamma(n_{a,1}-1)\Gamma(n_{b,1}-n_{a,1}-1)} \int_0^1 \frac{l_{f,1}^{n_{a,1}-1}(1-l_{f,1})^{n_{b,1}-n_{a,1}-1}}{\left(1-\frac{B_1}{1+B_1} l_{f,1}\right)^{n_{a,1}}} dl_{f,1}, \\ &= \frac{\Gamma(n_{b,1}-1)(1+B_1)^{-n_{a,1}}}{\Gamma(n_{a,1}-1)\Gamma(n_{b,1}-n_{a,1}-1)} \cdot \frac{\Gamma(n_{a,1})\Gamma(n_{b,1}-n_{a,1})}{\Gamma(n_{b,1})} \\ &\quad \text{x } {}_2\mathrm{F}_1\left(n_{a,1}, n_{a,1}, n_{b,1}, \frac{B_1}{1+B_1}\right), \\ &= \frac{(n_{a,1}-1)(n_{b,1}-n_{a,1}-1)}{(n_{b,1}-1)(1+B_1)^{n_{a,1}}} \; {}_2\mathrm{F}_1\left(n_{a,1}, n_{a,1}, n_{b,1}, \frac{B_1}{1+B_1}\right), \end{aligned}$$

where ${}_2\mathrm{F}_1(a,b,c,x)$ is the hypergeometric function as defined in [86]:

$${}_2\mathrm{F}_1(a,b,c,x) = \frac{\Gamma(c)}{\Gamma(b)\Gamma(c-b)} \int_0^1 \frac{t^{b-1}(1-t)^{c-b-1}}{(1-tx)^a} dt.$$

Letting $\hat{\Lambda}_1(\mathbf{y}_1) = u_1 = 1 + B_1$, the PDF becomes:

$$f(u_1) = \frac{(n_{a,1}-1)(n_{b,1}-n_{a,1}-1)}{(n_{b,1}-1)} u_1^{-n_{a,1}} \; {}_2\mathrm{F}_1\left(n_{a,1}, n_{a,1}, n_{b,1}, 1-\frac{1}{u_1}\right). \tag{B.2}$$

To obtain the P_{fa}, we integrate the PDF from λ to ∞:

$$P_{fa} = \int_\lambda^\infty f(u_1) du_1.$$

Through a change of variable $x = 1 - \frac{1}{u_1}$ and the Euler Transformation for hypergeometric functions (Eqn. (15.3.4) in [86]), we get:

$$P_{fa} = \int_{1-1/\lambda}^{1} \frac{(n_{a,1}-1)(n_{b,1}-n_{a,1}-1)}{(n_{b,1}-1)}(1-x)^{n_{a,1}}{}_2\mathrm{F}_1(n_{a,1}, n_{a,1}, n_{b,1}, x)\frac{1}{(1-x)^2}dx,$$
$$= \int_{1-1/\lambda}^{1} \frac{(n_{a,1}-1)(n_{b,1}-n_{a,1}-1)}{(n_{b,1}-1)}{}_2\mathrm{F}_1\left(n_{a,1}, n_{b,1}-n_{a,1}, n_{b,1}, \frac{x}{x-1}\right)\frac{1}{(1-x)^2}dx.$$

Consider the hypergeometric function $F = {}_2\mathrm{F}_1(n_{a,1}-1, n_{b,1}-n_{a,1}-1, n_{b,1}-1, \frac{x}{x-1})$, the derivative of F is then:

$$\frac{dF}{dx} = \frac{(n_{a,1}-1)(n_{b,1}-n_{a,1}-1)}{(n_{b,1}-1)}{}_2\mathrm{F}_1\left(n_{a,1}, n_{b,1}-n_{a,1}, n_{b,1}, \frac{x}{x-1}\right)\frac{-1}{(1-x)^2}.$$

Using this derivative, we can obtain the final expression for P_{fa}:

$$\begin{aligned} P_{fa} &= \int_{1-1/\lambda}^{1} -\frac{dF}{dx}dx, \\ &= {}_2\mathrm{F}_1(n_{a,1}-1, n_{b,1}-n_{a,1}-1, n_{b,1}-1, 1-\lambda). \end{aligned} \tag{B.3}$$

From Eqns. (B.2) and (B.3), we see that the distribution of the detector and the P_{fa}, respectively, depends only on $N_{s,1}$ and $N_{e,1}$. This means that the adaptive detector is also CFAR.

As $N_{s,1} \to \infty$, $n_{a,1} - 1 \approx n_{b,1} - 1$. Using the identity given by Eqn. (15.1.8) in [86], ${}_2\mathrm{F}_1(a, b, b, z) = {}_2\mathrm{F}_1(b, a, b, z) = (1-z)^{-a}$, we see that, asymptotically, P_{fa} tends to

$$P_{fa} \to \lambda^{-(n_{b,1}-n_{a,1}-1)} = \lambda^{-N_{e,1}+1},$$

which is the same expression as that for the case where the covariance matrix is known and $K_e = 1$.

We now proceed to the general case where $K_e \geq 1$. As before, we consider the product of all the individual detection tests for each subarray $u = \prod_{i=1}^{K_e} u_i$. The joint density function is given by:

$$f(u_1, \ldots, u_{K_e}) = \prod_{i=1}^{K_e} \frac{(n_{a,i}-1)(n_{b,i}-n_{a,i}-1)}{(n_{b,i}-1)} u_i^{-n_{a,i}}{}_2\mathrm{F}_1\left(n_{a,i}, n_{a,i}, n_{b,i}, 1-\frac{1}{u_i}\right).$$

Due to the complexity of the above expression, the PDF of $f(u)$ and consequently P_{fa} has not been obtained analytically.

Appendix C

Appendices for Chapter 3

C.1 Derivation of Cramér-Rao Bounds

When $\mathbf{\Theta_S} = [\theta \quad f_t \quad a \quad \phi]$, $\mathbf{J}(\mathbf{\Theta_S})$ becomes:

$$2\left[\begin{array}{cc|cc} a^2\mathbf{d}_s{}^\dagger\mathbf{M}^{-1}\mathbf{d}_s & a^2\Re(\mathbf{d}_s{}^\dagger\mathbf{M}^{-1}\mathbf{d}_f) & a\Re(\mathbf{p}^\dagger\mathbf{M}^{-1}\mathbf{d}_s) & a^2\Im(\mathbf{p}^\dagger\mathbf{M}^{-1}\mathbf{d}_s) \\ a^2\Re(\mathbf{d}_s{}^\dagger\mathbf{M}^{-1}\mathbf{d}_f) & a^2\mathbf{d}_f{}^\dagger\mathbf{M}^{-1}\mathbf{d}_f & a\Re(\mathbf{p}^\dagger\mathbf{M}^{-1}\mathbf{d}_f) & a^2\Im(\mathbf{p}^\dagger\mathbf{M}^{-1}\mathbf{d}_f) \\ \hline a\Re(\mathbf{p}^\dagger\mathbf{M}^{-1}\mathbf{d}_s) & a\Re(\mathbf{p}^\dagger\mathbf{M}^{-1}\mathbf{d}_f) & \mathbf{p}^\dagger\mathbf{M}^{-1}\mathbf{p} & 0 \\ a^2\Im(\mathbf{p}^\dagger\mathbf{M}^{-1}\mathbf{d}_s) & a^2\Im(\mathbf{p}^\dagger\mathbf{M}^{-1}\mathbf{d}_f) & 0 & a^2\mathbf{p}^\dagger\mathbf{M}^{-1}\mathbf{p} \end{array}\right], \\ = \left[\begin{array}{c|c} \mathbf{A} & \mathbf{B}^T \\ \hline \mathbf{B} & \mathbf{C} \end{array}\right].$$

By the Partitioned Matrix Lemma [96], the top left block of $\mathbf{J}(\mathbf{\Theta_S})^{-1}$ is given by the inverse of the Schur's Complement of $\mathbf{A}$: $\mathbf{A} - \mathbf{B}^T\mathbf{C}^{-1}\mathbf{B}$. The CRBs can be simplied to be:

$$\begin{aligned} \mathrm{CRB}_{\theta\theta} &= \frac{1}{\eta}\left(\mathbf{d}_f{}^\dagger\mathbf{M}^{-1}\mathbf{d}_f - \frac{|\mathbf{p}^\dagger\mathbf{M}^{-1}\mathbf{d}_f|^2}{\mathbf{p}^\dagger\mathbf{M}^{-1}\mathbf{p}}\right), \\ \mathrm{CRB}_{f_tf_t} &= \frac{1}{\eta}\left(\mathbf{d}_s{}^\dagger\mathbf{M}^{-1}\mathbf{d}_s - \frac{|\mathbf{p}^\dagger\mathbf{M}^{-1}\mathbf{d}_s|^2}{\mathbf{p}^\dagger\mathbf{M}^{-1}\mathbf{p}}\right), \end{aligned}$$

where η is the determinant of $(\mathbf{A} - \mathbf{B}^T\mathbf{C}^{-1}\mathbf{B})$.

Note that the CRBs have the same form as those derived in [99]. However in [99], $\mathrm{CRB}_{f_df_d}$ is derived instead of $\mathrm{CRB}_{f_tf_t}$. We can easily obtain $\mathrm{CRB}_{f_df_d}$ by:

$$\mathrm{CRB}_{f_df_d} = \left[\frac{\partial\theta}{\partial f_t} \quad \frac{\partial f_d}{\partial f_t}\right] \cdot \begin{bmatrix} \mathrm{CRB}_{\theta\theta} & \mathrm{CRB}_{\theta f_t} \\ \mathrm{CRB}_{\theta f_t} & \mathrm{CRB}_{f_tf_t} \end{bmatrix} \cdot \begin{bmatrix} \frac{\partial\theta}{\partial f_t} \\ \frac{\partial f_d}{\partial f_t} \end{bmatrix}.$$

Similarly, we can get the bottom right block of $\mathbf{J}(\mathbf{\Theta_S})^{-1}$ by finding the inverse of the Schur's Complement of $\mathbf{C}$: $\mathbf{C} - \mathbf{B}\mathbf{A}^{-1}\mathbf{B}^T$. Applying the Matrix Inversion Lemma [96], the bottom right block of $\mathbf{J}(\mathbf{\Theta_S})^{-1}$ is given by:

$$\mathbf{C}^{-1} + \mathbf{C}^{-1}\mathbf{B}(\mathbf{A} - \mathbf{B}^T\mathbf{C}^{-1}\mathbf{B})^{-1}\mathbf{B}^T\mathbf{C}^{-1}.$$

As the terms in $(\mathbf{A}-\mathbf{B}^T\mathbf{C}^{-1}\mathbf{B})^{-1}$ can be expressed in terms of $\mathrm{CRB}_{\theta\theta}$, $\mathrm{CRB}_{f_tf_t}$ and $\mathrm{CRB}_{\theta f_t}$, we can express the CRBs for a and ϕ in terms of these bounds:

$$\begin{aligned}
\mathrm{CRB}_{aa} &= \frac{1}{2\mathbf{p}^\dagger\mathbf{M}^{-1}\mathbf{p}} + \frac{a^2}{(\mathbf{p}^\dagger\mathbf{M}^{-1}\mathbf{p})^2}\Big(\Re(\mathbf{p}^\dagger\mathbf{M}^{-1}\mathbf{d}_s)^2\cdot\mathrm{CRB}_{\theta\theta} \\
&\quad + \Re(\mathbf{p}^\dagger\mathbf{M}^{-1}\mathbf{d}_f)^2\cdot\mathrm{CRB}_{f_tf_t} + 2\Re(\mathbf{p}^\dagger\mathbf{M}^{-1}\mathbf{d}_s)\ \Re(\mathbf{p}^\dagger\mathbf{M}^{-1}\mathbf{d}_f)\cdot\mathrm{CRB}_{\theta f_t}\Big), \\
\mathrm{CRB}_{\phi\phi} &= \frac{1}{2a^2\mathbf{p}^\dagger\mathbf{M}^{-1}\mathbf{p}} + \frac{a^2}{(\mathbf{p}^\dagger\mathbf{M}^{-1}\mathbf{p})^2}\Big(\Im(\mathbf{p}^\dagger\mathbf{M}^{-1}\mathbf{d}_s)^2\cdot\mathrm{CRB}_{\theta\theta} \\
&\quad + \Im(\mathbf{p}^\dagger\mathbf{M}^{-1}\mathbf{d}_f)^2\cdot\mathrm{CRB}_{f_tf_t} + 2\Im(\mathbf{p}^\dagger\mathbf{M}^{-1}\mathbf{d}_s)\ \Im(\mathbf{p}^\dagger\mathbf{M}^{-1}\mathbf{d}_f)\cdot\mathrm{CRB}_{\theta f_t}\Big).
\end{aligned}$$

C.2 Proof of Generalized MIMO Brennan's Rule

The clutter returns contain contributions from N_c clutter patches located at the same range but different angles θ_i:

$$\mathbf{c} = \sum_{i=1}^{N_c} \mathbf{c}_i = \sum_{i=1}^{N_c} \alpha_i \mathbf{s}(\theta_i) \otimes \mathbf{v}(\theta_i, 0),$$

where α_i is the amplitude of the signal reflected by the i-th clutter patch and $\alpha_i \sim \mathcal{CN}(0, \sigma_{c,i}^2)$. Let $\mathbf{V}_c$ be the $MNLxN_c$ matrix containing the steering vectors $\mathbf{c}_i$ to each clutter patch and Σ_c a diagonal matrix containing the power of each patch $\sigma_{c,i}^2$, the clutter covariance matrix can be expressed as:

$$\mathbf{M}_c = \mathbf{V}_c \Sigma_c \mathbf{V}_c^{\dagger}.$$

As the number of clutter patches is large and Σ_c is positive definite, the rank of $\mathbf{M}_c$ is equal to that of $\mathbf{V}_c$. For the n-th transmit element, m-th receive element and l-th pulse, the clutter signal from the i-th clutter patch is given by:

$$\begin{aligned} & \alpha_i \exp(j2\pi(m\frac{d_r}{\lambda}\sin\theta_i + n\frac{d_t}{\lambda}\sin\theta_i + l\frac{2vPRI}{\lambda}\sin\theta_i)), \\ = \quad & \alpha_i \exp(j2\pi\frac{\sin\theta_i}{2}(m\alpha + n\gamma + l\beta)), \\ = \quad & \alpha_i \exp(j2\pi f_{s,i}(m\alpha + n\gamma + l\beta)). \end{aligned}$$

That is to say that each element in the i-th column of $\mathbf{V}_c$ can be expressed in terms of $f_{s,i}$. Note that to take into consideration spatial aliasing ($\min(\alpha, \gamma) > 1$) on top of Doppler aliasing ($\beta > 1$), $f_{s,i}$ is defined as $\frac{\sin\theta_i}{2}$ such that

$$-0.5 \leq f_{s,i} < 0.5.$$

When α, β and γ are integers, the number of distinct elements in each column of $\mathbf{V}_c$ is equal to the number of distinct (integer) values, N_d in:

$$m\alpha + n\gamma + l\beta, \quad \forall \quad \begin{cases} m = 0, \ldots, M-1, \\ n = 0, \ldots, N-1, \\ l = 0, \ldots, L-1. \end{cases}$$

Since $f_{s,i}$ is different for each clutter patch, the columns of $\mathbf{V}_c$ are linearly-independent. Hence, the clutter rank is given by $\min(N_d, N_c) = N_d$ as $N_c \gg N_d$.

Journals

[J1] C. Y. Chong, F. Pascal, J-P. Ovarlez, and M. Lesturgie, "MIMO radar detection in non-Gaussian and heterogeneous clutter," *IEEE J. of Selected Topics in Sig. Proc. : MIMO Radar and its Applications*, vol. 4, no. 1, pp. 115–126, Feb 2010.

[J2] C. Y. Chong, F. Pascal, and M. Lesturgie, "Comparisons of different coherent MIMO-STAP configurations by detection and estimation performance," *IEE Proc. Radar Sonar Navig. (submitted)*, 2011.

Conferences

[C1] C. Y. Chong, F. Pascal, J-P. Ovarlez, and M. Lesturgie, "Adaptive MIMO radar detection in non-Gaussian and heterogeneous clutter considering fluctuating targets," in *IEEE Statistical Signal Processing Workshop*, Cardiff, UK, Aug 2009.

[C2] C. Y. Chong, F. Pascal, and M. Lesturgie, "MIMO radar detection under non-Gaussian clutter," in *Radar Conference*, Bordeaux, France, Oct 2009.

[C3] C. Y. Chong, F. Pascal, J-P. Ovarlez, and M. Lesturgie, "Robust MIMO radar detection for correlated subarrays," in *IEEE Int. Conf. on Acoustics, Speech and Sig. Proc.*, Dallas, USA, Mar 2010.

[C4] C. Y. Chong, F. Pascal, J-P. Ovarlez, and M. Lesturgie, "Hybrid MIMO radar: Configurations and applications on STAP," in *2nd SONDRA Workshop*, Cargese, France, May 2010.

[C5] C. Y. Chong, F. Pascal, J-P. Ovarlez, and M. Lesturgie, "Properties of robust MIMO detector," in *European Sig. Proc. Conf.*, Aalborg, Denmark, Aug 2010.

[C6] C. Y. Chong, F. Pascal, and M. Lesturgie, "Estimation performance of coherent MIMO-STAP using Cramér-Rao bounds," in *IEEE Radar Conference*, Kansas City, USA, May 2011.

Bibliography

[1] J. Li and P. Stoica, *MIMO Radar Signal Processing*, Wiley, 1st edition, 2009.

[2] E. Fishler, A. Haimovich, R. Blum, L. Cimini, D. Chizhik, and R. Valenzuela, "Performance of MIMO radar systems: Advantages of angular diversity," in *Proc. 38th Asilomar Conference on Signals, Systems and Computers*, Pacific Grove, USA, Nov 2004, pp. 305–309.

[3] A. M. Haimovich, R. S. Blum, and L. J. Cimini Jr, "MIMO radar with widely separated antennas," *IEEE Sig. Proc. Magazine*, vol. 25, no. 1, pp. 116–129, Jan 2008.

[4] E. Fishler, A. Haimovich, R. Blum, and L. J. Cimini, "Spatial diversity in radars - models and detection performance," *IEEE Trans. Sig. Proc.*, vol. 54, no. 3, pp. 823–838, March 2006.

[5] J. Li and P. Stoica, "MIMO radar with colocated antennas," *IEEE Sig. Proc. Magazine*, vol. 24, no. 5, pp. 106–114, Sept 2007.

[6] N. H. Lehmann, E. Fishler, A. Haimovich, R. Blum, D. Chizhik, and L. Cimini, "Evaluation of transmit diversity in MIMO-radar direction finding," *IEEE Trans. Sig. Proc.*, vol. 55, no. 5, pp. 2215–2225, May 2007.

[7] L. Xu, J. Li, and P. Stoica, "Radar imaging via adaptive MIMO techniques," in *Proc. 14th European Signal Processing Conference*, Florence, Italy, Sept 2006.

[8] J. Li, "Multi-Input Multi-Output (MIMO) radar - diversity means superiority," Annual report, Office of Naval Research, Oct 2007.

[9] F. Daum and J. Huang, "MIMO radar: Snake oil or good idea?," *IEEE Aero. Elect. Sys. Magazine*, vol. 24, no. 5, pp. 8–12, May 2009.

[10] J. B. Billingsley, "Ground clutter measurements for surface-sited radar," Technical Report 780, MIT, Feb 1993.

[11] S. Watts, "Radar detection prediction in sea clutter using the compound K-distribution model," *IEE Proc. F*, vol. 132, no. 7, pp. 613–620, 1985.

[12] T. Nohara and S. Haykin, "Canada east coast trials and the K-distribution," *IEE Proc. F*, vol. 138, no. 2, pp. 82–88, 1991.

[13] A. Farina, A. Russo, and F. Scannapieco, "Radar detection in coherent weibull clutter," *IEEE Trans. Acoust. Speech. Sig. Proc.*, vol. 35, no. 6, pp. 893–895, June 1987.

[14] B. Picinbono, "Spherically invariant and compound Gaussian stochastic processes," *IEEE Trans. Inform. Theory*, pp. 77–79, Jan 1970.

[15] K. Yao, "A representation theorem and its applications to spherically invariant random processes," *IEEE Trans. Inform. Theory*, vol. 19, no. 5, pp. 600–608, Sept 1973.

[16] M. Rangaswamy, D. D. Weiner, and A. Ozturk, "Non-Gaussian vector identification using spherically invariant random processes," *IEEE Trans. Aero. Elect. Sys.*, vol. 29, no. 1, pp. 111–124, Jan 1993.

[17] E. Conte, M. Lops, and G. Ricci, "Asymptotically optimum radar detection in compound-Gaussian clutter," *IEEE Trans. Aero. Elect. Sys.*, vol. 31, no. 2, pp. 617–625, April 1995.

[18] F. Gini, "Sub-optimum coherent radar detection in a mixture of K-distributed and Gaussian clutter," *IEE Proc. Radar Sonar Navig.*, vol. 144, no. 1, pp. 39–48, Feb 1997.

[19] E. Jay, J-P. Ovarlez, D. Declercq, and P. Duvaut, "BORD: Bayesian optimum radar detector," *Sig. Proc.*, vol. 83, no. 6, pp. 1151–1162, June 2003.

[20] N. H. Lehmann, A. Haimovich, R. Blum, and L. Cimini, "MIMO-radar application to moving target detection in homogeneous clutter," in *Proc. Adaptive Sensor Array Processing Workshop*, Lexington, USA, June 2006.

[21] E. J. Kelly, "An adaptive detection algorithm," *IEEE Trans. Aero. Elect. Sys.*, vol. 22, no. 1, March 1986.

[22] I. S. Reed, J. D. Mallett, and L. E. Brennan, "Rapid convergence rate in adaptive arrays," *IEEE Trans. Aero. Elect. Sys.*, vol. 10, no. 6, pp. 853–863, Nov 1974.

[23] F. Gini and M. V. Greco, "Covariance matrix estimation for CFAR detection in correlated heavy tailed clutter," *Sig. Proc. , Special Section on Sig. Proc. with Heavy Tailed Distributions*, vol. 82, no. 12, pp. 1847–1859, Dec 2002.

[24] E. Conte, A. De Maio, and G. Ricci, "Recursive estimation of the covariance matrix of a compound-Gaussian process and its application to adaptive CFAR detection," *IEEE Trans. Sig. Proc.*, vol. 50, no. 8, pp. 1908–1915, Aug 2002.

[25] F. Pascal, Y. Chitour, J-P. Ovarlez, P. Forster, and P. Larzabal, "Covariance structure maximum-likelihood estimates in compound Gaussian noise: Existence and algorithm analysis," *IEEE Trans. Sig. Proc.*, vol. 56, no. 1, pp. 34–48, Jan 2008.

[26] F. Pascal, P. Forster, J-P. Ovarlez, and P. Larzabal, "Performance analysis of covariance matrix estimates in impulsive noise," *IEEE Trans. Sig. Proc.*, vol. 56, no. 6, pp. 2206–2217, June 2008.

[27] J. Ward, "Space-time adaptive processing for airborne radar," Tech. report, Lincoln Lab, MIT, Dec 1994.

[28] R. Klemm, *Principles of Space-Time Adaptive Processing*, IEE Publishing, 2002.

[29] J. R. Guerci, *Space-Time Adaptive Processing for Radar*, Artech House, 2003.

[30] C. Wolff, "Space-time adaptive processing (STAP)," Tech. Rep., http://www.radartutorial.eu/20.airborne/ab11.en.html, 2005.

[31] D. W. Bliss, K. W. Forsythe, S. K. Davis, G. S. Fawcett, D. J. Rabideau, L. L. Horowitz, and S. Kraut, "GMTI MIMO radar," in *Proc. 4th IEEE Waveform Diversity and Design Conf.*, Orlando, USA, Feb 2009.

[32] J. Kantor and S. K. Davis, "Airborne GMTI using MIMO techniques," in *IEEE Radar Conference*, Washington D. C., USA, May 2010.

[33] M. Xue, W. Roberts, J. Li, X. Tan, and P. Stoica, "MIMO radar sparse angle-Doppler imaging for ground moving target indication," in *IEEE Radar Conference*, Washington D. C., USA, May 2010.

[34] N. A. Goodman and D. Bruyere, "Optimum and decentralized detection for multistatic airborne radar," *IEEE Trans. Aero. Elect. Sys.*, vol. 43, no. 2, pp. 806–813, Apr 2007.

[35] W. L. Melvin, R. Hancock, M. Rangaswamy, and J. Parker, "Adaptive distributed radar," in *Radar Conference*, Bordeaux, France, Oct 2009.

[36] W. L. Melvin, "Adaptive moving target indication," in *Advances in Bistatic Radar*, Ed. N. Willis and H. Griffiths, Eds. Sci-Tech Publishing, 2007.

[37] S. M. Kay, *Fundamentals of Statistical Signal Processing: Estimation Theory*, Prentice Hall, 1993.

[38] D. W. Bliss and K. W. Forsythe, "Multiple-input multiple-output (MIMO) radar and imaging: Degrees of freedom and resolution," in *Proc. 37th IEEE Asilomar Conf. Signals, Systems, Computers*, Nov 2003.

[39] C-Y. Chen and P. P. Vaidyanathan, "MIMO radar space-time adaptive processing using prolate spheroidal wave functions," *IEEE Trans. Sig. Proc.*, vol. 56, no. 2, pp. 623–635, 2008.

[40] E. Fishler, A. Haimovich, R. Blum, L. Cimini, D. Chizhik, and R. Valenzuela, "MIMO radar: An idea whose time has come," in *Proc. IEEE Int. Conf. Radar*, Philadelphia, USA, Apr 2004, pp. 71–78.

[41] J. Li, P. Stoica, L. Xu, and W. Roberts, "On parameter identifiability of MIMO radar," *IEEE Sig. Proc. Letters*, vol. 14, no. 12, pp. 968–971, Dec 2007.

[42] T. Aittomaki and V. Koivunen, "Performance of MIMO radar with angular diversity under Swerling scattering models," *IEEE J. of Selected Topics in Sig. Proc. : MIMO Radar and its Applications*, vol. 4, no. 1, pp. 101–114, Feb 2010.

[43] Y. Abramovich, G. Frazer, and B. Johnson, "Non-causal adaptive spatial clutter mitigation in monostatic MIMO radar: Fundamental limitations," *IEEE J. of Selected Topics in Sig. Proc.*, vol. 4, no. 1, pp. 40–54, Feb 2009.

[44] G. J. Frazer, Y. I. Abramovich, and B. A. Johnson, "Multiple-iinput multiple-output over the horizon radar: Experimental results," *IET Radar Sonar Navig.*, vol. 3, no. 4, pp. 290–303, Aug 2009.

[45] M. Lesturgie, "Improvement of high-frequency surface waves radar performances by use of multiple-input multiple-output configurations," *IET Radar Sonar Navig.*, vol. 3, no. 1, pp. 49–61, Feb 2009.

[46] M. Skolnik, *Introduction to Radar Systems*, McGraw-Hill, 3rd edition, 2002.

[47] R. S. Blum, "Limiting case of a lack of rich scattering environment for MIMO radar diversity," *IEEE Sig. Proc.Letters*, vol. 16, no. 10, pp. 901–904, Oct 2009.

[48] Q. He, N. H. Lehmann, R. S. Blum, and A. M. Haimovich, "MIMO radar moving target detection in homogeneous clutter," *IEEE Trans. Aero. Elect. Sys.*, vol. 47, no. 3, pp. 1290–1301, July 2010.

[49] C. Du, J. S. Thompson, and Y. Petillot, "Predicted detection performance of MIMO radar," *IEEE Sig. Proc. Letters*, vol. 15, pp. 83–86, 2008.

[50] J. Tang, N. Li, Y. Wu, and Y. Peng, "On detection performance of MIMO radar: A relative entropy-basd study," *IEEE Sig. Proc. Letters*, vol. 16, no. 3, pp. 184–187, Mar 2009.

[51] Q. He, R. S. Blum, and A. M. Haimovich, "Noncoherent MIMO radar for location and velocity estimation: More antennas means better performance," *IEEE Trans. Sig. Proc.*, vol. 58, no. 7, pp. 3661–3680, July 2010.

[52] Q. He, R. S. Blum, H. Godrich, and A. M. Haimovich, "Target velocity estimation and antenna placement for MIMO radar with widely separated antennas," *IEEE J. of Selected Topics in Sig. Proc. : MIMO Radar and its Applications*, vol. 4, no. 1, pp. 79–100, Feb 2010.

[53] M. R. Bell, "Information theory and radar waveform design," *IEEE Trans. Inf. Theory*, vol. 39, no. 5, pp. 1578–1597, Sept 1993.

[54] A. De Maio and M. Lops, "Design principles of MIMO radar detectors," *IEEE Trans. Aero. Elect. Sys.*, vol. 43, no. 3, pp. 886–898, July 2007.

[55] A. De Maio, M. Lops, and L. Venturino, "Diversity-Integration tradeoffs in MIMO detection," *IEEE Trans. Sig. Proc.*, vol. 56, no. 10, pp. 5051–5061, Oct 2008.

[56] A. Aubry, M. Lops, A. M. Tulino, and L. Venturino, "On MIMO waveform design for non-Gaussian target detection," in *Radar Conference*, Bordeaux, France, Oct 2009.

[57] B. Tang, J. Tang, and Y. Peng, "MIMO radar waveform design in colored noise based on information theory," *IEEE Trans. Sig. Proc.*, vol. 58, no. 9, pp. 4684–4697, Sept 2010.

[58] X. Song, S. Zhou, and P. Willett, "Reducing the waveform cross correlation of MIMO radar with Space-Time Coding," *IEEE Trans. Sig. Proc.*, vol. 58, no. 8, pp. 4213–4224, Aug 2010.

[59] J. Tabrikian, "Performance bounds and techniques for target localization using MIMO radars," in *MIMO Radar Signal Processing*, J. Li and P. Stoica, Eds., pp. 153–191. Wiley, 2009.

[60] V. F. Mecca, D. Ramakrishnan, and J. L. Krolik, "MIMO radar space-time adaptive processing for multipath clutter mitigation," in *IEEE Sensor Array and Multichannel Sig. Proc. Workshop*, Jul 2006.

[61] B. Friedlander, "On the relationship between MIMO and SIMO radars," *IEEE Trans. Sig. Proc.*, vol. 57, no. 1, pp. 394–398, Jan 2009.

[62] K. W. Forsythe and D. W. Bliss, "MIMO radar waveform constraints for GMTI," *IEEE J. of Selected Topics in Sig. Proc. : MIMO Radar and its Applications*, vol. 4, no. 1, pp. 21–32, Feb 2010.

[63] D. J. Rabideau, "Doppler-offset waveforms for MIMO radar," in *IEEE Radar Conference*, Kansas City, USA, May 2011.

[64] Y. Yang and R. S. Blum, "MIMO radar waveform design based on mutual information and minimum mean-square error estimation," *IEEE Trans. Aero. Elect. Sys.*, vol. 43, no. 1, pp. 330–343, Jan 2007.

[65] Y. Yang and R. S. Blum, "Minimax robust MIMO radar waveform design," *IEEE J. of Selected Topics in Sig. Proc*, vol. 1, no. 1, pp. 147–155, Jun 2007.

[66] Y. Yang, R. S. Blum, Z. He, and D. R. Fuhrmann, "MIMO radar waveform design via alternating projection," *IEEE Trans. Sig. Proc*, vol. 58, no. 3, pp. 1440–1445, Mar 2010.

[67] J. Li, L. Xu, P. Stoica, K. W. Forsythe, and D. W. Bliss, "Range compression and waveform optimization for MIMO radar: A Cramér-Rao bound based study," *IEEE Trans. Sig. Proc.*, vol. 56, no. 1, pp. 218–232, Jan 2008.

[68] D. W. Bliss, K. W. Forsythe, and C. D. Richmond, "MIMO radar: Joint array and waveform optimization," in *Proc. 41st IEEE Asilomar Conf. Signals, Systems, Computers*, Nov 2007.

[69] G. San Antonio, D. R. Fuhrmann, and F. C. Robey, "MIMO radar ambiguity functions," *IEEE J. of Selected Topics in Sig. Proc.*, vol. 1, no. 1, pp. 167–177, Jun 2007.

[70] B. Friedlander, "Waveform design for MIMO radars," *IEEE Trans. Aero. Elect. Sys.*, vol. 43, no. 3, pp. 1227–1238, Jul 2007.

[71] D. R. Fuhrmann and G. S. Antonio, "Transmit beamforming for MIMO radar system using signal cross-correlation," *IEEE Trans. Aero. Elect. Sys.*, vol. 44, no. 1, pp. 171–186, Jan 2008.

[72] T. Aittomaki and V. Koivunen, "Signal covariance matrix optimization for transmit beamforming in MIMO radars," in *Proc. 41st IEEE Asilomar Conf. Signals, Systems, Computers*, Nov 2007.

[73] P. Stoica, J. Li, and Y. Xie, "On probing signal design for MIMO radar," *IEEE Trans. Sig. Proc.*, vol. 55, no. 8, pp. 4151–4161, Aug 2007.

[74] K. W. Forsythe and D. W. Bliss, "MIMO radar: Concepts, performance enhancements, and applications," in *MIMO Radar Signal Processing*, J. Li and P. Stoica, Eds., pp. 65–121. Wiley, 2009.

[75] L. Xu and J. Li, "Iterative Generalized-Likelihood Ratio Test for MIMO radar," *IEEE Trans. Sig. Proc.*, vol. 55, no. 6, pp. 2375–2385, June 2007.

[76] D. Nion and N. D. Sidiropoulos, "Tensor algebra and multidimensional harmonic retrieval in signal processing for MIMO radar," *IEEE Trans. Sig. Proc.*, vol. 58, no. 11, pp. 5693–5705, 2010.

[77] O. Bar-Shalom and A. J. Weiss, "Direct position determination using MIMO radar," in *Proc. 25th IEEE Convention of Electrical and Electronics Engineers in Israel*, Eilat, Israel, Dec 2008.

[78] C. R. Berger, B. Demissie, J. Heckenbach, P. Willett, and S. Zhou, "Signal processing for passive radar using OFDM waveforms," *IEEE J. of Selected Topics in Sig. Proc. : MIMO Radar and its Applications*, vol. 4, no. 1, pp. 226–238, Feb 2010.

[79] J. Bergin, S. McNeil, L. Fomundam, and P. Zulch, "MIMO phased-array for SMTI radar," in *IEEE Aerospace Conference*, Mar 2008.

[80] A. Hassanien and S. A. Vorobyov, "Phased-MIMO radar: a tradeoff between phased-array and MIMO radars," *IEEE Trans. Sig. Proc.* , vol. 58, no. 6, pp. 3137–3151, Jun 2010.

[81] H. Li and B. Himed, "Transmit subaperturing for MIMO radars with co-located antennas," *IEEE J. of Selected Topics in Sig. Proc. : MIMO Radar and its Applications*, vol. 4, no. 1, pp. 55–65, Feb 2010.

[82] D. R. Fuhrmann, J. P. Browning, and M. Rangaswamy, "Signaling strategies for the hybrid MIMO phased-array radar," *IEEE J. of Selected Topics in Sig. Proc. : MIMO Radar and its Applications*, vol. 4, no. 1, pp. 66–78, Feb 2010.

[83] A. De Maio, M. Lops, and L. Venturino, "Diversity-integration tradeoffs in MIMO detection," *IEEE Trans. Sig. Proc.*, vol. 56, no. 10, pp. 5051–5061, 2008.

[84] J. G. Proakis, *Digital Communications*, McGraw-Hill, 4th edition, 2000.

[85] K. B. Petersen and M. S. Pedersen, "The matrix cookbook," Tech report, http://matrixcookbook.com, Nov 2008.

[86] M. Abramowitz and I. A. Stegun, *Handbook of Mathematical Functions*, National Bureau of Standard AMS 55, 1st edition, June 1964.

[87] F. W. J. Olver, D. W. Lozier, R. F. Boisvert, and C. W. Clark, *NIST Handbook of Mathematical Functions*, Cambridge University Press, July 2010.

[88] L. L. Scharf and B. Friedlander, "Matched subspace detectors," *IEEE Trans. Sig. Proc.*, vol. 42, no. 8, pp. 2146–2157, Aug 1994.

[89] Kraut S, Scharf L L, and L T McWhorter, "Adaptive subspace detectors," *IEEE Trans. Sig. Proc.*, vol. 49, no. 1, Jan 2001.

[90] I. D. Olin, "Amplitude and temporal statistics of sea clutter," in *IEE Conference Publication 216 for Radar*, London, UK, Oct 1982.

[91] D. B. Trizna, "Statistics of low grazing angle radar sea scatter for moderate and fully developed ocean waves," *IEEE Trans. Ant. Prop.*, vol. 39, no. 12, pp. 1681–1690, Dec 1991.

[92] F. Gini, M. V. Greco, A. Farina, and P. Lombardo, "Optimum and mismatched detection against K-distributed plus Gaussian clutter," *IEEE Trans. Aero. Elect. Sys.*, vol. 34, no. 3, pp. 860–876, July 1998.

[93] F. A. Pentini, A. Farina, and F. Zirilli, "Radar detection of targets located in a coherent K distributed clutter background," *IEE Proc. F*, vol. 139, no. 3, pp. 238–245, June 1992.

[94] F. Pascal, J-P. Ovarlez, P. Forster, and P. Larzabal, "On a SIRV-CFAR detector with radar experimentations in impulsive noise," in *Proc. European Signal Processing Conference*, Florence, Italy, Sept 2006.

[95] F. C. Robey, D. R. Fuhrmann, E. J. Kelly, and R. Nitzberg, "A CFAR adaptive matched filter detector," *IEEE Trans. Aero. Elect. Sys.*, vol. 28, no. 1, pp. 208–216, Jan 1992.

[96] L. L. Scharf, *Statistical Signal Processing: Detection, Estimation and Time Series Analysis*, Addison-Wesley, 1st edition, 1991.

[97] G. Pailloux, J-P. Ovarlez, F. Pascal, and P. Forster, "Persymmetric adaptive radar detectors," *IEEE Trans. Aero. Elect. Sys. (to appear)*, 2011.

[98] T. W. Anderson, *An Introduction to Multivariate Statistical Analysis*, Wiley, 3rd edition, 2003.

[99] J. Ward, "Cramér-Rao bounds for target angle and Doppler estimation with Space-Time Adaptive Processing radar," in *Proc. 29th Asilomar Conference on Signals, Systems and Computers*, Pacific Grove, CA , USA, Nov 1995.

Signal Processing for MIMO Radars : Detection under Gaussian and non-Gaussian environments and application to STAP

A Multiple-Input Multiple Output (MIMO) radar can be broadly defined as a radar system employing multiple transmit waveforms and having the ability to jointly process signals received at multiple receive antennas. In terms of configurations, the antennas can be widely separated or co-located.

The first part of the thesis is on detection under Gaussian and non-Gaussian environments using a MIMO radar which contains several widely separated subarrays with one or more elements each. Two different situations are considered. Firstly, we consider that the interference is Gaussian but correlation between subarrays can arise due to insufficient spacing and the imperfect orthogonality of waveforms. Secondly, we consider that the interference is non-Gaussian, a situation which arises under sea and ground clutter and when the resolution is very high.

The second part is on the application of MIMO techniques to Space-Time Adaptive Processing (STAP). The coherent MIMO configuration is studied in terms of antenna element distribution and inter-element spacing to improve detection and estimation performance. A preliminary study is also done on the use of spatial diversity to improve detection stability w.r.t. target Radar Cross Section (RCS) fluctuations and velocity direction changes.

Keywords: MIMO, diversity, detection, Gaussian, non-Gaussian, adaptive, STAP, Cramér-Rao bound

Traitement du signal pour les radars MIMO: Détection en environnement gaussien et non gaussien et application au STAP

Un radar Multiple-Input Multiple-Output (MIMO) est celui où les émetteurs envoient des formes d'ondes différentes (orthogonales ou partiellement corrélées) qui peuvent être séparées à la réception. En outre, les émetteurs et récepteurs peuvent être colocalisés ou largement séparés.

La première partie de la thèse porte sur la détection dans des environnements gaussiens et non gaussiens en utilisant un radar MIMO, qui contient plusieurs sous-réseaux largement séparés avec un ou plusieurs éléments chacun. Deux situations différentes sont considérées. Premièrement, nous considérons que les interférences sont gaussiennes, mais une corrélation entre les sous-réseaux peut survenir en raison d'un espacement insuffisant et de l'orthogonalité imparfaite des formes d'ondes. Deuxièmement, nous considérons que les interférences sont non gaussiennes, une situation qui se présente quand il y a du fouillis de sol ou de mer et lorsque la résolution est très élevée.

La deuxième partie est dédiée à l'utilisation de techniques MIMO pour le Space-Time Adaptive Processing (STAP). La configuration MIMO cohérente est étudiée en changeant la distribution et l'espacement des éléments d'antenne pour améliorer les performances de détection et d'estimation. En outre, une étude préliminaire est également présentée sur l'utilisation de la diversité spatiale pour rendre le radar plus robuste aux fluctuations de la RCS et à la variation de la vitesse de la cible par rapport à l'angle d'incidence du signal émis et reçu.

Mots-clés : MIMO, diversité, détection, gaussien, non gaussien, adaptative, STAP, borne de Cramér-Rao